Synthesis of carbon nanotubes and their application in TiO_2 photocatalysis

by

Brian M. Everhart

B.S., Kansas State University, 2017

AN ABSTRACT OF A DISSERTATION

Submitted in partial fulfillment of the requirements for the degree

DOCTOR OF PHILOSOPHY

Tim Taylor Department of Chemical Engineering
Carl R. Ice College of Engineering

KANSAS STATE UNIVERSITY
Manhattan, Kansas

2022

Abstract

In the 21st century, scientists and engineers are tasked with furthering technological innovation while simultaneously achieving environmental sustainability. This necessitates the scalable development and implementation of advanced materials. The following work includes insight into the growth of single wall carbon nanotubes (SWCNTs) which are desired for a wide array of applications due to their exceptional, tunable properties. It also explores the use of composite materials comprised of CNTs and titanium dioxide (TiO_2) for environmental remediation applications. The research presented in this document establishes the ability of FTS-GP (Fischer Tropsch Synthesis Gas Precursor, a waste product of industrial processes) to generate water in situ via gas phase reaction of CO with H_2. The work demonstrates that this generated water is responsible for prolonged catalyst lifetime compared to a conventional precursor such as ethylene (C_2H_4). Experiments from both a conventional chemical vapor deposition (CVD) system and an autonomous research system (ARES) are supported by thermodynamic analysis, which together provide insight into the role of FTS-GP in generating on-site water during growth of SWNCT carpets. SWCNT growth is further investigated using Ru as a promoter to increase the selectivity of small-diameter SWCNTs (diameters below 1 nm). By performing over 200 growth experiments in ARES with different feedstocks and extensive multi-excitation Raman spectroscopic characterization, we demonstrate that the Ru-promoted Co catalyst doubles the selectivity of small-diameter SWCNTs (diameters below 1 nm) at 750 °C in comparison to Co, increasing to a factor of three at higher temperatures. Density functional theory (DFT) calculations with 13 and 55 atom Co_xRu_y clusters (ranging from 0 to 22% Ru content) reveal increases in cluster cohesive energies (E_C) with Ru content. As these findings are indicative of increases in melting temperature and reduction in atom mobility with Ru content, they are consistent with the presence

of ~10% Ru in our Co catalyst which increases sintering resistance and stability of small nanoparticles, resulting in high selectivity toward small-diameter SWCNTs.

After the discussion on SWCNT growth, the work in this document examines the fabrication of CNT-TiO_2 composite materials and their ability to efficiently eliminate airborne pollutants. It begins with the synthesis of CNT-TiO_2 composites and the role of CNTs in degradation of acetaldehyde, a representative volatile organic compound (VOC) in a batch reactor. The study indicates that a small amount of multi-walled carbon nanotubes (MWCNTs) increases catalyst performance compared to TiO_2, whereas the addition of CNTs beyond the optimum loading ratio of 1:100 (MWCNT:TiO_2) diminishes the effectiveness of the photocatalyst and the synergistic effect between MWCNTs and TiO_2. CNT-TiO_2 photocatalyst composites are subsequently implemented for degradation of NO_x in a continuous flow reactor. This study demonstrates the use of CNT-TiO_2 photocatalyst films for effective transformation of NO_x into nitrates. Using the objective figure of merit for NO_x abatement, $DeNO_x$ index, the catalyst performance in a laminar-flow reactor was evaluated under different conditions, including relative humidity (RH), initial NO_x concentration, reactor geometry (headspace distance), and state of the catalyst (fresh vs. recycled). Our results reveal CNT-TiO_2 significantly outperforms P25 in a humid environment despite exhibiting comparable NO conversion at low RH. In addition, mass transfer from the bulk airflow limits NO conversion when the reactor headspace is too large (>3 mm), due to limited diffusion of NO_x to the photocatalyst surface. The remarkable $DeNO_x$ activity of CNT-TiO_2 over a wide range of RH levels is rationalized based on the ratio of physisorbed-to-chemisorbed water on the photocatalyst surface and the effect of this physisorbed water in increasing the amount of superoxide ($O_2^{\bullet-}$) radicals generated.

Synthesis of carbon nanotubes and their application in TiO_2 photocatalysis

by

Brian M. Everhart

B.S., Kansas State University, 2017

A DISSERTATION

Submitted in partial fulfillment of the requirements for the degree

DOCTOR OF PHILOSOPHY

Tim Taylor Department of Chemical Engineering
Carl R. Ice College of Engineering

KANSAS STATE UNIVERSITY
Manhattan, Kansas

2022

Approved by:

Major Professor
Placidus B. Amama

Copyright

Abstract

In the 21st century, scientists and engineers are tasked with furthering technological innovation while simultaneously achieving environmental sustainability. This necessitates the scalable development and implementation of advanced materials. The following work includes insight into the growth of single wall carbon nanotubes (SWCNTs) which are desired for a wide array of applications due to their exceptional, tunable properties. It also explores the use of composite materials comprised of CNTs and titanium dioxide (TiO_2) for environmental remediation applications. The research presented in this document establishes the ability of FTS-GP (Fischer Tropsch Synthesis Gas Precursor, a waste product of industrial processes) to generate water in situ via gas phase reaction of CO with H_2. The work demonstrates that this generated water is responsible for prolonged catalyst lifetime compared to a conventional precursor such as ethylene (C_2H_4). Experiments from both a conventional chemical vapor deposition (CVD) system and an autonomous research system (ARES) are supported by thermodynamic analysis, which together provide insight into the role of FTS-GP in generating on-site water during growth of SWNCT carpets. SWCNT growth is further investigated using Ru as a promoter to increase the selectivity of small-diameter SWCNTs (diameters below 1 nm). By performing over 200 growth experiments in ARES with different feedstocks and extensive multi-excitation Raman spectroscopic characterization, we demonstrate that the Ru-promoted Co catalyst doubles the selectivity of small-diameter SWCNTs (diameters below 1 nm) at 750 °C in comparison to Co, increasing to a factor of three at higher temperatures. Density functional theory (DFT) calculations with 13 and 55 atom Co_xRu_y clusters (ranging from 0 to 22% Ru content) reveal increases in cluster cohesive energies (E_C) with Ru content. As these findings are indicative of increases in melting temperature and reduction in atom mobility with Ru content, they are consistent with the presence

of ~10% Ru in our Co catalyst which increases sintering resistance and stability of small nanoparticles, resulting in high selectivity toward small-diameter SWCNTs.

After the discussion on SWCNT growth, the work in this document examines the fabrication of CNT-TiO_2 composite materials and their ability to efficiently eliminate airborne pollutants. It begins with the synthesis of CNT-TiO_2 composites and the role of CNTs in degradation of acetaldehyde, a representative volatile organic compound (VOC) in a batch reactor. The study indicates that a small amount of multi-walled carbon nanotubes (MWCNTs) increases catalyst performance compared to TiO_2, whereas the addition of CNTs beyond the optimum loading ratio of 1:100 (MWCNT:TiO_2) diminishes the effectiveness of the photocatalyst and the synergistic effect between MWCNTs and TiO_2. CNT-TiO_2 photocatalyst composites are subsequently implemented for degradation of NO_x in a continuous flow reactor. This study demonstrates the use of CNT-TiO_2 photocatalyst films for effective transformation of NO_x into nitrates. Using the objective figure of merit for NO_x abatement, $DeNO_x$ index, the catalyst performance in a laminar-flow reactor was evaluated under different conditions, including relative humidity (RH), initial NO_x concentration, reactor geometry (headspace distance), and state of the catalyst (fresh vs. recycled). Our results reveal CNT-TiO_2 significantly outperforms P25 in a humid environment despite exhibiting comparable NO conversion at low RH. In addition, mass transfer from the bulk airflow limits NO conversion when the reactor headspace is too large (>3 mm), due to limited diffusion of NO_x to the photocatalyst surface. The remarkable $DeNO_x$ activity of CNT-TiO_2 over a wide range of RH levels is rationalized based on the ratio of physisorbed-to-chemisorbed water on the photocatalyst surface and the effect of this physisorbed water in increasing the amount of superoxide ($O_2^{\bullet-}$) radicals generated.

Table of Contents

List of Figures xii

List of Tables xxii

Acknowledgements xxiii

Chapter 1 – Introduction 1

1.1 Introduction 1

1.2 References 10

Chapter 2 - Efficient Growth of Carbon Nanotube Carpets Enabled by In-Situ Generation of Water 15

2.1 Introduction 15

2.2 Experimental Section 18

2.2.1 SWCNT Growth by FTS-GP CVD 18

2.2.2 Characterization 19

2.2.3 SWCNT Growth Investigations in ARES 20

2.3 Results and Discussion 21

2.3.1 Catalytic Performance at Different Temperatures 21

2.3.2 Thermodynamic Prediction of In-situ Generation of Water 27

2.3.3 Experimental Verification of Water Generation 31

2.3.4 Using ARES to Probe the Effect of Water Concentration 32

2.4 Conclusions 37

2.5 References 38

Chapter 3 - High-Throughput Experimentation for Selective Growth of Small-Diameter Single-Wall Carbon Nanotubes using Ru-Promoted Co Catalysts 44

3.1 Introduction 44

3.2 Experimental Section 47

3.2.1 Preparation of catalyst substrates 47

3.2.2 SWCNT growth in ARES 48

3.2.3 Computational analysis methods 51

3.3 Results 51

3.3.1 SWCNT growth in ARES using different feedstocks 51

3.3.2 Multi-excitation Raman spectroscopic characterization of SWCNTs grown with ethylene 60

3.3.3 DFT calculations 62

3.3.4 SWCNT growth in ARES using pure Ru or Co-Ru with a higher Ru amount 65

3.4 Discussion 67

3.5 Conclusions 69

3.6 References 71

Chapter 4 - Hydrothermal Synthesis of Carbon Nanotube-Titania Composites for Enhanced Photocatalytic Performance 78

4.1 Introduction 78

4.2 Experimental 80
4.2.1 Chemicals 80
4.2.2 CNT Oxidation 81
4.2.3 Catalyst Synthesis 81
4.2.4 Characterization 82
4.2.5 Photocatalytic Performance 83
4.3 Results and Discussion 84
4.3.1 Characterization of Photocatalysts 84
4.3.2 Photocatalytic activity 91
4.4 Conclusions 95
4.5 References 96
5.1 Introduction 101
5.2 Experimental 105
5.2.1 Oxidation of CNTs 105
5.2.2 Synthesis of CNT-TiO_2 hybrid photocatalyst 105
5.2.3 Coating of photocatalysts 106
5.2.4 Characterization of photocatalysts 106
5.2.5 Photocatalytic performance evaluation 108
5.3 Results and Discussion 110
5.3.1 Characterization of photocatalysts 110

5.3.2 Effect of humidity 113

5.3.3 Effect of initial concentration 118

5.3.4 Effect of headspace 120

5.3.5 Effect of photocatalyst stability and recycling 122

5.3.6 Photocatalytic mechanism of NO_x oxidation 123

5.4 Conclusions 130

5.5 References 131

Chapter 6 – Conclusions 137

Chapter 7 – Future Work 139

Appendix A – Supplementary Information for Chapter 2 141

Appendix B – Supplementary Information for Chapter 3 144

B.1 Analysis of C1 and C2 values in Equation (1) 149

B.2 References 159

Appendix C – Supplementary Information for Chapter 4 161

Appendix D – Supplementary Information for Chapter 5 164

List of Figures

Figure 2.1. Schematic illustration of onsite generation of water during CNT carpet growth via FTS-GP CVD. 17

Figure 2.2. SEM images of SWCNT carpets grown on Al_2O_3/Fe substrates at different temperatures after 90 min: (a) 650°C; (b) 700°C; (c) 750°C; and (d) 800°C. (e) Plots of SWCNT carpet height as a function of growth time for different growth temperatures; solid lines represent curve fitting of the radioactive decay model (Equation 1) to the experimental data shown in symbols. 22

Figure 2.3. Representative Raman spectra of SWCNT carpet samples (excitation at 633 nm) with their respective I_G/I_D ratios. 25

Figure 2.4. Growth rate-catalyst lifetime map of SWCNT carpets using supported monometallic catalyst showing a comparison of representative studies (in blue) including our results from FTS-GP CVD using an Fe catalyst (in green). E and F show the experimental and fitted lifetimes for FTS-GP CVD growth at 750°C, respectively; E and F and are assumed to be the limits of τo. The number indicates the reference for each datum. 27

Figure 2.5. Thermodynamic prediction of the concentration of water generated during FTS-GP CVD. (a) Profiles of partial pressures of water as functions of growth temperatures for different feed compositions of FTS-GP (5, 10, 20, and 30%) with Ar as balance over a broad temperature range (0 – 1750°C). Along these lines, ΔG of Reaction 1 is zero, i.e., it is in equilibrium. (b) Profiles of water concentrations (ppm) as functions of temperatures with data points corresponding to growth temperatures used during FTS-GP CVD [adapted from (a)]..... 30

Figure 2.6. Concentration of water produced via gas-phase reaction of FTS-GP in a batch reactor as a function of temperature. Plot of carpet height after 90 min of growth versus

temperature is included for comparison. The green shade shows the sweet spot for efficient carpet growth under the conditions used. 31

Figure 2.7. Plots of CNT yield as a function of growth time during CVD growth for different levels of water in ARES using FTS-GP (a) and ethylene (b) as feedstocks. The green solid lines represent curve fitting of the radioactive decay model (Equation 1) to the experimental data shown in symbols. 34

Figure 2.8. Growth kinetics parameters obtained by fitting the ARES growth curves with the radioactive decay model (Equation 1). (a) Plots of initial growth rate of SWCNTs as a function of water concentrations for FTS-GP and ethylene. (b) Plots of catalyst lifetime as a function of water concentrations for FTS-GP and ethylene. 35

Figure 3.1. Schematic illustration of ARES, a high throughput laser-induced CVD system capable of in-situ Raman spectroscopy. 49

Figure 3.2. Weighted average RBM frequency data acquired with 532 nm (a) and 633 nm (b) laser excitations at different growth temperature. (c) Approximation of the true RBM frequency distribution in each temperature bracket by averaging data in (a) and (b). (d) Mean of weighted average RBM frequency data in (c) for Co and Co-Ru. Histograms of relative frequency of RBM peaks as a function of peak location for Co and Co-Ru using 532 nm (e) and 633 nm (f) laser excitations; the relative frequency is the percentage of each RBM peak area to the total RBM peak area. 52

Figure 3.3. SEM images showing density of SWCNTs grown on Co (a) and Co-Ru (b) catalysts. Plots of selectivity toward small-diameter SWCNTs as a function of growth temperature using different feedstocks on Co (c) and Co-Ru (d) catalysts (calculated from Raman spectra acquired with 532 nm laser excitation). Heat/contour plots illustrating selectivity (in c and d) and

G-band area (proxy for abundance of SWCNT growth) versus growth temperature for Co (e) and Co-Ru (f) catalysts using growth results for ethylene and acetylene..... 55

Figure 3.4. Plots of SWCNT yield as a function of growth time using different feedstock-catalyst combinations: (a) ethylene and Co, (b) ethylene and Co-Ru, (c) acetylene and Co, and (d) acetylene and Co-Ru. The solid lines represent curve fitting of the radioactive decay model (Equation 1). Scatter plots of initial growth rate (e) and catalyst lifetime (f), obtained by fitting plots a-d to Equation 1, as a function of growth temperature. 59

Figure 3.5. Multi-excitation Raman spectra of SWCNTs grown on Co (a) and Co-Ru (b) catalysts; green shade highlights the small-diameter region (<1 nm). (c) Plots of selectivity averages for small-diameter SWCNTs on Co and Co-Ru catalysts. Data used for analysis were acquired with 532 nm and 633 nm laser excitations over four temperature ranges (650-699 °C, 700-749 °C, 750-799 °C, 800-849°C). (d) Histogram of average selectivity across temperature ranges for Co and Co-Ru catalysts. Error bars show standard deviations for the calculated average values. 61

Figure 3.6. (a) DFT optimization and calculation of cohesive energy, E_C, for13- and 55-atom clusters of Co and Co-Ru. a) Co13, Co12Ru (A) with adsorbed Ru atom, and Co12Ru (B) with Ru atom in the bulk region of the cluster. (b) Co55, Co49Ru6 (A-F), Co43Ru12, which contain 0, 6, and 12 Ru atoms, respectively. Configurations A through I were generated randomly and represent different arrangement scenarios for Ru on the cluster surface. Notably A represents the arrangement with the Ru atoms most separated from each other, D represents the arrangement with most symmetric Ru atom placement, and F represents the most segregated arrangement (notice all Ru atoms clustering together). 64

Figure 3.7. Heat plots of G-band intensity and small diameter SWCNT selectivity of growth experiments performed on a Co-Ru catalyst (20% Ru) with ethylene and the addition of 0 ppm (a) and 11ppm H_2O (b). (c) Representative Raman spectra of SWCNTs grown on pure Ru catalyst with ethylene in the absence and presence of water (11 ppm). (d) Representative Raman spectra of SWCNTs grown on pure Ru catalysts under conditions that maximize small-diameter SWCNT selectivity. 66

Figure 4.1. XRD patterns of TiO_2 and TiO_2-MWCNT nanocomposites. Peak labels have been included to correlate peaks to crystal phase (Anatase [A], Rutile [R], or Brookite [B]). 85

Figure 4.2. Low- and high-magnification SEM images of photocatalysts: TiO2 (a, b), TiO2/MWCNT-1% (c, d), TiO2/MWCNT-5% (e, f). 87

Figure 4.3. Carbon dispersion within photocatalysts. SEM images with EDS mapping of elemental carbon overlayed (a – d). EDS mapping of elemental carbon illustrating carbon dispersion (e – h). 88

Figure 4.4. TEM images of TiO2 particles on MWCNTs in the TiO_2/MWCNT-5% sample. 89

Figure 4.5. XPS high-resolution O 1s spectra of photocatalysts fitted using two asymmetric peakcomponents. 90

Figure 4.6. (a) Degradation curves of photocatalyst performance projection. Center lines indicatethe first order rate equation derived from the average degradation data for each catalyst. (b) Photocatalytic degradation of acetaldehyde as a function of UV illumination time. (c) Comparison of the average rate constants for the photocatalytic degradation of acetaldehyde using TiO2, TiO2/MWCNT-1%, and TiO2/MWCNT-5%. 92

Figure 4.7. Proposed mechanism for the role of CNTs in TiO_2 nucleation and dispersion duringhydrothermal synthesis of TiO_2/MWCNTs. 95

Figure 5.1. (a) Schematic illustration of the photocatalytic reactor setup. (b) Schematic illustration of the laminar-flow reactor configuration constructed according to ISO standards showing NO_x flow and oxidation on photocatalyst surface. (c) Overview of experiments conducted. 110

Figure 5.2. (a) XRD patterns for CNT-TiO_2 (red) and P25 (blue) photocatalysts. (b) UV-Vis spectra of CNT-TiO_2 (red) and P25 (blue) photocatalysts (inset: Tauc plots of the photocatalysts). SEM images of CNT-TiO_2 (c) and P25 (e), and corresponding EDS spectra and chemical composition including weight percentage of carbon for CNT-TiO_2 (d) and P25 (f)... 112

Figure 5.3. Representative NOx degradation profiles at over 2 hours using an initial NO_x concentration of 1000ppb at low humidity (10% RH) for NO (a), NO_2 (b), and NO_x (c); and at high humidity (50% RH) for NO (d), NO_2 (e), NO_x (f). Each degradation profile has four distinct regions: (1) initiation of NO_x flow indicated by the steep rise in relative concentration (~10 min), (2) NO_x equilibration with the lights off (~30 min), (3) degradation under illumination (~120 min), and (4) NO_x re-equilibration after lights are shut off (~10 min). 115

Figure 5.4. Profiles of NO, NO_2, and NO_x concentrations as a function of RH: (a) initial NOx concentrations, (b) reduction in relative concentrations for P25, and (c) reduction in relative concentrations for CNT-TiO_2. (d) $DeNO_x$ index for P25 and CNT-TiO_2 as a function of RH. (e) NO conversion and NO_x storage selectivity at low and high RH for each catalyst. Experiments were performed at 1000ppb initial NO_x concentration. 116

Figure 5.5. Reduction in relative concentration profiles of NO, NO_2, and NO_x versus initial NOx concentration at low RH (10%) for P25 (a) and CNT-TiO_2 (b) and high RH (50%) for P25

(c) and CNT-TiO_2 (d). (e) DeNOx index for P25 and CNT-TiO_2 as a function of initial concentration for 10% RH (e) and 50% RH (f). 119

Figure 5.6. $DeNO_x$ index for P25 and CNT-TiO_2 as a function of reactor headspace distance for low RH (10%) (a) and high RH (50%) (b). (c) NO conversion and NOx storage selectivity corresponding to (a). (d) NO conversion and NOx storage selectivity for photocatalytic reactions performed at different flow rates using a headspace distance of 3mm at 10% RH. Flow rates in Figure (d) were chosen to equate residence times in Figure (c). 121

Figure 5.7. (a) $DeNO_x$ index for pristine and recycled P25 and CNT-TiO_2 catalysts at 10% RH and 50% RH levels. (b) NO_x storage selectivity for pristine and recycled P25 and CNT-TiO_2 catalysts at 10% RH and 50% RH levels. 123

Figure 5.8. (a-b) EPR spectra of DMPO-hydroxyl radical spin adducts produced from P25 and CNT-TiO_2 catalysts in (a) aqueous dispersion (0.2 mg/mL) and (b) water containing ethanol (1%, v/v, 0.2 mg/mL) after 5 minutes of UV irradiation. (c) TGA profiles of P25 and CNT-TiO_2 catalysts obtained using a ramp rate of 5°C /min under air flow; (d) zoom-in version of (c) showing the temperature range of interest associated with desorption of physisorbed water. High-resolution XPS O 1s spectra of P25 (e) and CNT-TiO_2 (f) catalysts. 126

Figure 5.9. Schematic illustration of the role of CNT in improving NO_2 conversion on CNT-TiO_2 in a humid environment. The relatively higher adsorbed water content on CNT-TiO_2 compared to the predominantly OH radical dominant oxidation of NO_x on P25 is hypothesized to increase stability and activity of superoxide radicals. 129

Figure A2.1. SWCNT yield as a function of growth temperature in ARES. 142

Figure A2.2. Post-growth Raman spectra (excitation wavelength 633 nm) collected from the ARES micropillars for SWCNT growth experiments performed using C_2H_4 (a) and FTS-GP (b) for varying amounts of H_2O. 142

Figure A2.3. SWCNT yield and catalyst lifetime for different feedstocks and compositions in the absence of additional water at 825°C in ARES. 143

Figure B3.1. Representative Raman spectra and peak fitting for SWCNTs grown on Co (a) – (b) and Co-Ru (c) – (d) using acetylene as the feedstock. For spectra acquired with 532 nm (a and c) excitation, the small-diameter SWCNT selectivity of Co in (a) is 0.293 (T = 750°), while the selectivity of Co-Ru in (c) is 0.485 (T = 770°). For spectra acquired with 633 nm laser (b and d), the small-diameter SWCNT selectivity of Co in (c) is 0.364 (T = 750°), while the selectivity of Co-Ru in (d) is 0.646 (T = 770°). 146

Figure B3.2. Relative frequency of RBM peaks obtained by averaging Raman data from 532 nm and 633 nm laser excitations shown in Figures 2(e) – (f) versus peak position using 20 cm^{-1} (a) and 50 cm^{-1} (b) brackets. 147

Figure B3.3. Relative frequency of RBM peaks for Co (a-b) and Co-Ru (c-d) versus peak position using Raman data from 532 nm and 633 nm laser excitations at different growth temperature ranges. 147

Figure B3.4. Relative frequency of RBM peaks for growth on Co (a-b) and Co-Ru (c-d) versus peak position using ethylene, acetylene, and FTS-GP precursors. Data are shown for 532 nm and 633 nm laser excitations. 148

Figure B3.5. (a) – (b) Difference in selectivity towards small-diameter SWCNTs for the different feedstocks on Co and Co-Ru; data were calculated from Raman spectra acquired with 633 nm laser excitation. 148

Figure B3.6. The effect of different C_1 and C_2 values on the average small-diameter selectivity at different growth temperatures for Co (a) and Co-Ru (b). (c) Average selectivity using the four sets of C_1 and C_2 values for Co and Co-Ru. 151

Figure B3.7. Data used in Figure 3 (c) separated to show small-diameter selectivity for growth performed with ethylene and acetylene as feedstocks: (a) data from 532nm Raman excitation; (b) data from 633nm Raman excitation. (c) Averaged data from spectra acquired using 532nm and 633nm excitation. (d) Histogram of average selectivity across temperature ranges for Co and Co-Ru catalysts. Error bars show standard deviations for the calculated average values. 152

Figure B3.8. Multi-excitation Raman spectra of SWCNTs grown on Co (a) and Co-Ru (b) catalysts using acetylene as the feedstock; the green shade highlights the small-diameter region (<1 nm). 153

Figure B3.9. Selectivity data used in Figure 3 (c) separated based on their excitation wavelength: (a) 532 nm, and (b) 633 nm. 153

Figure B3.10. AFM images of as-deposited catalyst films and annealed in H_2/Ar for 0 min (a and b), 3 min (c and d), 10 min (e and f), and 30 min (g and h) for Co (left panel) and Co-Ru (right panel). A plot of RMS roughness obtained from the images as a function of annealing time (i). Films were deposited on Si substrates and annealed in a regular hot-wall CVD. 154

Figure B3.11. Small-diameter selectivity of SWCNTs grown on IBS/e alumina-supported Co and Co-Ru catalysts for the different feedstocks as a function of temperature. (a) – (b) Selectivity calculated from Raman spectra acquired with 532 nm excitation. (c) – (d) Selectivity calculated from Raman spectra acquired with 633 nm excitation. 155

Figure B3.12. Heat plots illustrating the small-diameter SWCNT selectivity and G-band area (representing abundance of growth) versus temperature for growth on IBS/e alumina-supported Co and Co-Ru catalysts. Plots for growth using ethylene and acetylene on Co (a) and Co-Ru (b). Plots for growth using FTS-GP on Co (c) and Co-Ru (d). 156

Figure B3.13. (a) Plots of average selectivity towards small-diameter SWCNTs on IBS/e alumina-supported Co and Co-Ru catalysts versus growth temperature: (a) data acquired with 532nm excitation; (b) data acquired with 633 nm excitation. (c) Average selectivity for combined data acquired with 532 nm and 633 nm excitations. (d) Histogram of average selectivity across temperature ranges for Co and Co-Ru catalysts. Error bars show standard deviations for the calculated average values. 157

Figure B3.14. Data adapted from Figure S8 to compare average small-diameter SWCNT selectivity for growth with ethylene and acetylene on Co and Co-Ru catalysts supported on IBS/e alumina: (a) data acquired with 532 nm excitation; (b) data acquired with 633 nm excitation. (c) Average selectivity for combined data acquired with 532 nm and 633 nm excitations. (d) Histogram of average selectivity across temperature ranges for Co and Co-Ru catalysts. Error bars show standard deviations for the calculated average values. 158

Figure C4.1. Raman spectra of TiO_2, TiO_2/MWCNT-1%, and TiO_2/MWCNT-5% using 514 nm laser excitation. 161

Figure C4.2. Adsorption-desorption isotherms of TiO_2, TiO_2/MWCNT-1%, and TiO_2/MWCNT-5% photocatalysts. 162

Figure C4.3. UV-Vis absorbance spectra of TiO_2, TiO_2/MWCNT-1%, TiO_2/MWCNT-5%, and P25 as a reference sample. 163

Figure D5.1. (a) An SEM image of CNT-TiO_2 microstructure. (b) XRD profiles of individual CNT-TiO_2 batches prior to mixing. (c) Raman spectra confirming the presence of the crystal phases observed in XRD. 164

Figure D5.2. Optical microscopic images and N_2 adsorption-desorption isotherms for P25 and CNT-TiO_2 catalysts. 165

Figure D5.3. Absolute (a-b) and relative (c-d) humidity of major cities across the globe and in the US specifically. Temperature data used to convert relative humidity to absolute values has been included in (e-f). 169

Figure D5.4. NO conversion and NOx storage selectivity for both P25 and CNT-TiO2 as a function of initial NOx concentration for low humidity (a) and (c) as well as high humidity (b) and (d). These figures show that NO conversion is dependent on initial concentration. 170

Figure D5.5. NO conversion and NOx storage selectivity for both P25 and CNT-TiO2 as a function of reactor headspace for low humidity (a) and (c) as well as high humidity (b) and (d). These figures show that NO conversion is highly dependent on reactor headspace, with a maximum conversion occurring at 5mm..... 171

Figure D5.6. EPR results for P25 and CNT-TiO2 using (a) 0.2 mg/mL SDS surfactant and 15 minutes of sonication time. Results indicate that SDS does not contribute to the DMPO-OH radical measurement. Figure (b) shows EPR results without the addition of SDS. Figure (c) shows EPR results using SDS and long sonication times (120 minutes). 172

Figure D5.7. Photoluminescence spectra of P25 and CNT-TiO_2 catalyst powders..... 173

Figure D5.8. (a) NO conversion, storage selectivity, and (b) $DeNO_x$ of catalyst films containing different amounts of P25. (c) low magnification images of the respective catalyst films. 174

List of Tables

Table 2.1. Summary of fitting parameters (β and τ) and goodness of fit, modeled by the radioactive decay model (Equation 1), for different growth temperatures. 23

Table 4.1. Summary of catalyst properties. 86

Table 4.2. Summary of results of deconvolution of high-resolution XPS O 1s spectrum of TiO_2 and TiO_2/MWCNT composites using peak components with asymmetric line shapes. 91

Table 5.1. Catalyst powder characterization 113

Table A2.1. Predicted amount of water generated during FTS-GP CVD at different growth temperatures for different fractions of FTS-GP in the feed. 141

Table B3.1. Average values of the fitting parameters (ν and τ) from Figure 4. 144

Table B3.2. G-band integrated area and small-diameter SWCNT selectivity as functions of temperature for growth on Co and Co-Ru as shown in Figure 3.3. 145

Table C4.1. Summary of phase composition of photocatalysts: calculated ratio of anatase and rutile determined from Equation 1 and the phase composition determined via RIR method. 161

Table D5.1. Thickness measurements for P25 and CNT-TiO_2 catalyst films using optical microscopy. 166

Table D5.2. Total catalyst mass for P25 and CNT-TiO_2 catalyst films. 166

Table D5.3. Relative NO, NO_2, and NO_x degradation percentages for P25 and CNT-TiO_2 catalysts at different humidity levels, shown in Figure 4. 167

Table D5.4. Relative NO, NO_2, and NO_x degradation percentages for P25 and CNT-TiO_2 catalysts at different initial concentration for a) 50% and 10% relative humidity, shown in Figure 5 168

Acknowledgements

I would like to express my sincere gratitude to my advisor, Dr. Placidus B. Amama, for all his support and guidance throughout my Ph.D. I began working under Dr. Amama as an undergraduate researcher and was so inspired by his passion for research that I decided to continue my education under his guidance. I am indebted to him for his support through all the highs and lows of graduate school, as well as the opportunities his mentorship has provided. Many thanks to all my committee members, Dr. James H. Edgar, Dr. Keith Hohn, Dr. Bin Liu, and Dr. Jun Li for their professional guidance and help. I would like to give special thanks to Dr. Benji Maruyama and all his group members at the Air Force Research Lab at Wright Patterson Air Force Base. Without their collaboration and advisement, my work on carbon nanotube synthesis would not have been possible. I'm grateful for the professional experience and mentorship I have received though working with them. I am thankful to all my research group members here at K-State whose work contributed to the success of our research projects. I thank Montgomery Baker-Fales, who first introduced me to Dr. Amama and contributed greatly to the foundation of my work as a graduate student. I also want to acknowledge Bailey McAuley, who provided invaluable help when constructing and troubleshooting our flow reactor system. I share my appreciation for Dr. Haider Almkhelfe and Ahmed Al Mayyahi for their continued guidance and collaboration, respectively. I would also like to thank all the other members of the Chemical Engineering Department who have guided me in me in all the aspects of graduate school which may be taken for granted, including help with purchase orders, financial questions, and travel documentation.

I must thank my parents, Mr. Steven Everhart and Mrs. Lisa Everhart, and my sister, Ms. Emily Everhart, whose unconditional love and support have provided constant reassurance

during my studies. Completing my Ph.D. has been both the greatest challenge and greatest accomplishment of my life. Finally, I would like to extend my gratitude to all of my friends who have supported me through this journey. I am extremely appreciative to you all and am proud to share in my successes with you.

Chapter 1 – Introduction

1.1 Introduction

The 2018 Environmental Performance Index indicated that one of the greatest environmental threats to public health is poor air quality; 65% of all "life-years" lost can be attributed to inadequate air quality as a result of cardiovascular disease and lung cancer among other severe health complications.[1, 2] The environmental protection agency has set air quality standards for six air pollutants, which include: ozone (O_3), carbon monoxide (CO), lead (Pb), sulfur dioxide (SO_2), nitrogen dioxide (NO_x), and particulate matter (PM).[3] Lead has seen drastic reductions in most urban areas, as airborne lead pollution has decreased by over 98% since 1980 largely due to the elimination of lead from paint and gasoline.[4] Sulfur dioxide and carbon monoxide concentrations have also been significantly mitigated as the result of cleaner fuels, improvements in flue gas scrubbing, and improved catalytic converters in vehicles.[5, 6] Thus far, mitigation efforts targeting PM, NO_x, and O_3 have been less successful. Most major urban centers have concentrations of particulates that are above the recommended World Health Organization Air Quality Guideline of 10 micrograms per cubic meter ($\mu g/m^3$).[7] The most significant sources of particulate matter are vehicle exhaust and coal combustion for electricity production, with traffic being considered as the most significant source of particulate pollution in cities. NO_x itself is not only harmful at concentrations as low as 21 ppb ($40ug/m_3$), but it also reacts in atmosphere to generate tropospheric ozone, resulting in smog and even contributes to particulate matter (PM2.5) pollution concentrations via formation of nitrate aerosols.[2, 8-11] NO_x is a generic term including seven different compounds but is generally represented by nitrogen monoxide (NO) and dioxide (NO_2). Over 90% of all atmospheric NO_x originates from anthropogenic sources, including energy

production and distribution, and energy use in industry. The majority of tropospheric ozone (O_3) comes indirectly from the reaction of NO_x with other pollutants, such as volatile organic compounds (VOC's). These precursors, after emission, react in the presence of sunlight to produce ozone, which remain in the atmosphere where it can spread over large distances.[12-15] In order to mitigate these pollutants, several strategies have been researched or implemented, including selective catalytic reduction (SCR) of NO_x from flue gas and vehicle exhaust, particulate filtration devices, and photocatalysis.[16-21]

Photocatalysis, first discovered by Fujishima and Honda in 1972, enabled the ultraviolet light-assisted splitting of water to generate oxygen and hydrogen.[22] Photocatalysis utilizes a semiconductive material—such as titanium dioxide, zinc oxide, and cadmium sulfide—capable of absorbing photons, thereby creating an electronically viable reaction pathway.[23] As with any semiconductor, there is an associated band gap separating the conduction band from the valence band. When an electron is excited, it enters the conduction band, leaving behind a positively charged hole in the valence band. The hole oxidizes water vapor (H_2O), generating hydroxyl radicals ($OH^{\bullet}$), while the excited electron can react with molecular oxygen (O_2) to generate superoxide radicals ($O_2^{\bullet-}$). These radicals can then react with pollutant adsorbed onto the surface of the photocatalyst, leading to degradation of the pollutant. During this excitation process, however, the excited electrons can also return to the resulting holes in the valence band without partaking in these reduction and oxidation reaction.[24] This process, referred to as recombination, hinders the rate of pollutant degradation.

Materials with large band gaps, such as TiO_2 (3.2 eV for anatase), perform significantly better than low band gap semiconductors as photocatalysts because a larger band gap results in higher free energy of photogenerated charge carriers.[25] Pollutants have a certain redox potential,

representing the energy required to degrade them. The large band gap of TiO_2 gives the photocatalyst strong redox potential, making it capable of degrading a wide array of pollutants while also increasing its electrochemical stability. High stability prevents TiO_2 from degrading due to exposure to high energy photons.[26] Too large of a band gap, however, requires illumination from ultraviolet light to excite electrons to the conduction band. Despite the many advantages of TiO_2, including its relative nontoxicity and high photocatalytic activity,[27, 28] TiO_2 suffers from two fundamental limitations: (1) fast recombination of holes and electrons, decreasing its quantum efficiency; and (2) an intrinsic bandgap that confines its photoactivity to the UV range, which makes up only ~5% of the total solar spectrum.[29] In an effort to overcome these problems, researchers have explored a number of modification approaches[30-33] and recently turned to carbon nanotubes (CNTs) and other carbon nanomaterials.[34-37]

At the most basic level, a CNT can be characterized as a graphene sheet rolled-up to form a tube. Single-wall CNTs (SWCNTs) are comprised of a single layer of graphene, while a multiwalled CNT (MWCNT) is comprised of two or more layers. Since their discovery by Iijima in 1991,[38] they have continued to attract great attention due to their excellent material properties, including high mechanical strength, excellent electrical and thermal conductivity.[39-44] This unique combination of properties enables the application of CNTs in a plethora of applications, including lightweight electronics, sensing devices, high strength building materials, and environmental remediation.[45-51] For their realization in many of these applications, scalability is required. Furthermore, CNT properties are largely dependent on their geometry, necessitating uniform CNTs with similar properties for successful incorporation into an application. Controlling growth of CNTs requires optimization of a multi-parameter space including, but not limited to, catalyst material, catalyst thickness, temperature, pressure, carbon precursor, and gaseous additives. The

development of an efficient technique for controlled synthesis of CNTs remains a major challenge for the industrial application of CNTs.

The number of concentric tubes is not the only differentiator between CNTs. The graphene sheets comprising these tubes can also be rolled at different angles, forming different CNT chiralities which strongly influence electronic properties.[39, 52] While MWCNTs are metallic in their ability to conduct electrons, SWCNTs can be either metallic (m-SWCNT) or semiconducting (s-SWCNT), depending on their chiral angle. CNT chiral angle ranges from $\theta = 0°$ zig-zag CNTs up to $\theta = 30°$ for armchair SWCNTs. SWCNTs grown via a standard chemical vapor deposition (CVD) growth can be comprised of many different chiralities.[53] In a standard distribution of as-grown SWCNTs, roughly two-thirds are semi-conducting while the rest are metallic. While diameter has a small influence on the properties of m-SWCNTs, such as tensile strength, s-SWCNTs are strongly influenced by diameter, as their band gap is inversely proportional to diameter. A diameter of 1nm correlates to an s-SWCNT band gap of roughly 0.7 eV. As the diameter increases, the band gap continues to drop until the tubes are considered semi-metallic in nature.[54] For this reason, applications requiring s-SWCNTs necessitate small diameters. Thus far, efforts to reduce the diameter of SWCNTs have been limited, particularly on supported growth. When breakthroughs in synthesis enable scalable growth of small-diameter SWCNTs, widespread application will be realized. One such field is heterogeneous photocatalysis.

Both metallic and semiconducting CNTs are of interest as photocatalyst supports and have inspired two mechanisms. First, incorporating metallic CNTs into TiO_2 composites can result in synergetic effects such as minimizing charge recombination via electron transfer to CNTs acting as “electron sinks.” Second, s-SWCNTs can induce visible light response through red-shifts in the absorption spectra into the visible region.[34-36, 55-57] The work presented in this document focuses

on the first mechanism. Frequently, excited electrons recombine with their corresponding holes in the valence band before oxidation and reduction reactions can occur, preventing generation of radical species and inhibiting the photocatalytic degradation of adsorbed pollutants. This rapid recombination of electron-hole pairs greatly reduces quantum efficiency, defined as the fraction of excited electron/hole pairs that partake in redox reactions compared to the total number adsorbed photons.[58, 59] Accomplishing this goal requires substantial progress in both scalable growth of CNTs with controlled structural and electronic properties and design of TiO_2-CNT photocatalyst composites for efficient mitigation of ambient air pollutants. Each of these fields has several limitations which must be overcome for application of CNT-TiO_2 photocatalyst materials in pollution mitigation.

The *goal of this study* is to conduct fundamental investigations that will lead to the development of rational principles for controlled growth of SWCNTs and fabrication of CNT-TiO_2 composite materials with superior activity in the degradation of a variety of gas-phase pollutants than conventional photocatalysts. Our strategy for achieving this goal involves the use the Autonomous Research System (ARES), an automated, high throughput, laser-induced chemical vapor deposition system with in situ Raman spectral feedback. This system allows the user to perform hundreds of experiments in a short period of time, effectively finding the ideal conditions for improved control of SWCNT growth which can be applied to conventional CVD and future upscaling efforts. This work will also investigate the mechanisms by which CNT-TiO_2 photocatalysts enable superior oxidation of gas-phase pollutants relative to the current standard material, TiO_2. Batch and continuous flow reactor systems will be implemented for evaluation of catalyst performance. Degradation profiles and rate laws will be analyzed to determine catalyst

performance. The research presented in this document advances each of these fields and is divided into the following objectives:

- Develop a fundamental understanding of SWCNT growth from FTS-GP, a gaseous product mixture from the Fischer Tropsch synthesis process, which enables efficient growth with record catalyst lifetimes. The hypothesis of this task is that FTS-GP enables in-situ generation of water, which can prevent deposition of amorphous carbon thereby extending catalyst lifetimes.
- Utilize rapid experimentation to probe conditions for growth of small-diameter SWCNTs using high-melting-point transition metal catalyst promoters. The hypothesis of this task is that the high-melting-point promoter will reduce catalyst sintering, thereby producing smaller SWCNT diameters compared to conventional catalysts. The small-diameter s-SWCNTs would have bandgaps favorable for photocatalysis. Rapid experimentation allows for efficient exploration of the SWCNT growth parameter space.
- Design efficient CNT-TiO_2 photocatalysts which effectively degrade gas phase pollutants. The hypothesis for this task is that intimate contact between CNTs and TiO_2 can improve the photocatalytic efficiency of composite films when compared to pure TiO_2 by increasing the concentration of radicals generated due to the enhanced separation of photogenerated electrons and holes.
- Develop a fundamental understanding of the mechanism for enhanced photocatalytic oxidation of NO_x using CNT-TiO_2 photocatalyst films under practical conditions. NO_x oxidation involves a complex system of reaction pathways which is not yet well-understood; we hypothesize that improved radical generation using CNT-TiO_2

photocatalysts will improve the complete oxidation of NO_x to nitrates under real world conditions, such as elevated humidity levels.

The research in this work is expected to provide a foundation for scalable growth of SWCNTs and improve understanding of CNT-TiO_2 composites in gas phase photocatalysis. The work completed in this study is expected to have broad applicability: (1) provide insight into scalable growth of small-diameter SWCNTs and (2) establish a basis for improving photocatalyst performance using CNT-TiO_2 composites.

Chapter 2 investigates the ability of the growth precursor FTS-GP (Fischer Tropsch Synthesis Gas Precursor) to generate water via gas phase reaction of CO with H_2. The study also demonstrates that the water generated is responsible for the prolonged catalyst lifetime with Fe catalysts compared to a conventional precursor such as ethylene (C_2H_4). Experiments from both CVD and ARES systems contribute to understanding the role of FTS-GP in generating on-site water during growth of SWNCT carpets. These results are supported by thermodynamic analysis, which show that the concentration of water generated in situ decreases with increasing reactor temperature.

Chapter 3 builds upon the understanding gained from experiments performed in ARES in Chapter 2 and investigates the use of Ru as a promoter for the growth of small-diameter SWCNTs. By performing over 200 growth experiments in ARES with different feedstocks and extensive multi-excitation Raman spectroscopic characterization, we demonstrate that the Ru-promoted Co catalyst nearly doubles the selectivity of small-diameter SWCNTs (diameters below 1 nm) at 750 °C in comparison to Co. At higher temperatures between 800 and 850 °C, Ru stabilizes Co catalyst nanoparticles and increases the selectivity of small-diameter SWCNTs by almost a factor of three. Results reveal that SWCNT diameters are not only dependent on catalyst properties but also on

the type of feedstock as selectivity toward small diameter SWCNTs decreases in the following order: ethylene > acetylene > FTS-GP. Density functional theory calculations with 13 and 55 atom Co_xRu_y clusters (ranging from 0 to 22% Ru content) reveal increases in cluster cohesive energies (EC) with Ru content, irrespective of the exact location of Ru atoms in the clusters. As these findings are indicative of increases in melting temperature and reduction in atom mobility with Ru content, they are consistent with the presence of ~10% Ru in our Co catalyst, increasing sintering resistance, stability of small nanoparticles, and the observed high selectivity toward small-diameter SWCNTs.

While Chapter 2 and Chapter 3 focus on methods for scalable growth of small-diameter SWCNTs, Chapter 4 and Chapter 5 delve into the role of CNTs in photocatalyst composites. Both chapters focus on the mechanism of photocatalytic activity enhancement using metallic CNTs. Multi-walled CNTs have been utilized in this work because they are metallic. Chapter 4 focuses on CNT-TiO_2 composites and their role in degradation of acetaldehyde, a representative VOC (volatile organic compound), in a batch reactor. Nanosized, well-dispersed titania particles were synthesized via a hydrothermal method using MWCNTs as structural modifiers during the nucleation process to decrease aggregation. The study indicates that a small amount of CNTs increase catalyst performance compared to TiO_2, but the addition of CNTs beyond the optimum loading ratio of 1:100 (MWCNT:TiO_2) diminishes the effectiveness of the photocatalyst and the synergistic effect between MWCNTs and TiO_2. The primary mechanism for photocatalytic activity enhancement in TiO_2/MWCNT-1% is thought to be due to increased porosity, hydroxyl enrichment on the surface, and high dispersion of TiO_2 particles.

Chapter 5 builds upon the understanding gained in Chapter 1 to explore the use of CNT-TiO_2 photocatalyst composites for oxidation of NO_x in a continuous flow reactor. Although many

different photocatalysts exhibit improved NO conversion to NO_2, the performance in the oxidation of NO_2, the more toxic form of NOx, to nitrate remains a challenge; in addition, the performance of hybrid photocatalysts under practical conditions is unclear. This study demonstrates the use of CNT-TiO_2 photocatalyst films for effective transformation of NO_x into nitrates. Using the objective figure of merit for NO_x abatement, $DeNO_x$ index, the catalyst performance in a laminar-flow reactor was evaluated under simulated conditions that are relevant in abating NOx. The conditions probed include relative humidity (RH), initial NOx concentration, reactor geometry (headspace distance), and state of the catalyst (fresh vs. recycled). Our results reveal CNT-TiO_2 significantly outperforms P25 in a humid environment despite exhibiting comparable NO conversion at low RH. This disparity becomes even more pronounced when recycled photocatalyst films are used. In addition, mass transfer from the bulk airflow limits NO conversion when the reactor headspace is too large (>3 mm), due to limited diffusion of NO_x to the photocatalyst surface. Our findings highlight the importance of headspace distance, a parameter that has mostly been overlooked in reactor design for photocatalytic oxidation of NO_x, but which dictates the optimal catalyst configuration for flue gas treatment. The remarkable $DeNO_x$ activity of CNT-TiO_2 over a wide range of RH levels is rationalized based on the ratio of physisorbed-to-chemisorbed water on the photocatalyst surface and the effect of this physisorbed water in increasing the amount of superoxide ($O_2^{\bullet-}$) radicals generated.

1.2 References

1. Erickson, L. E.; Griswold, W.; Maghirang, R. G.; Urbaszewski, B. P., Air Quality, Health and Community Action. *J. Environ. Prot.* **2017**, 1057-1074.

2. Friedrich, M. J., Air Pollution Is Greatest Environmental Threat to Health. *JAMA* **2018,** *319* (11).

3. Criteria Air Pollutants. https://www.epa.gov/criteria-air-pollutants (accessed August 11).

4. Mielke, H. W.; Gonzales, C. R.; Powell, E. T.; Laidlaw, M. A. S.; Berry, K. J.; Mielke, P. W.; Egendorf, S. P., The concurrent decline of soil lead and children's blood lead in New Orleans. *PNAS* **2019,** *116* (44), 22058-22064.

5. Sikarwar, P.; Gosu, V.; Subbaramaiah, V., An overview of conventional and alternative technologies for the production of ultra-low-sulfur fuels. *Rev. Chem. Eng.* **2019,** *35* (6), 669-705.

6. Gao, J.; Tian, G.; Sorniotti, A.; Karci, A. E.; Di Palo, R., Review of thermal management of catalytic converters to decrease engine emissions during cold start and warm up. *Appl. Therm. Eng.* **2019,** *147*, 177-187.

7. Krzyzanowski, M.; Apte, J. S.; Bonjour, S. P.; Mrauer, M.; Cohen, A. J.; Prüss-Ustun, A. M., Air Pollution in the Mega-cities. *Curr. Environ. Health Rep.* **2014,** *1*, 185-191.

8. Itano, Y.; Bandow, H.; Takenaka, N.; Saitoh, Y.; Asayama, A.; Fukuyama, J., Impact of NOx reduction on long-term ozone trends in an urban atmosphere. *Sci. Total Environ.* **2007,** *379* (1), 46-55.

9. Atkinson, R., Atmospheric chemistry of VOCs and NOx. *Atmos. Environ.* **2000,** *34* (12), 2063-2101.

10. Environmental Protection Agency *Nitrogen Oxides Emissions*; 2018.

11. World Helath Organization Ambient air pollution: Health impacts. https://www.who.int/airpollution/ambient/health-impacts/en/#:~:text=Ambient%20(outdoor%20air%20pollution)%20is,increased%20risk%20of%20premature%20death. (accessed June 2).

12. Clean Air Act Overview. https://www.epa.gov/clean-air-act-overview.

13. Paoletti, E.; De Marco, A.; Beddows, D. C. S.; Harrison, R. M.; Manning, W. J., Ozone levels in European and USA cities are increasing more than at rural sites, while peak values are decreasing. *Environ. Pollut.* **2014,** *192*, 295-299.

14. Sicard, P.; De Marco, A.; Troussier, F.; Renou, C.; Vas, N.; Paoletti, E., Decrease in surface ozone concentrations at Mediterranean remote sites and increase in the cities. *Atmos. Environ.* **2013,** *79*, 705-715.

15. Klumpp, A.; Ansel, W.; Klumpp, G.; Calatayud, V.; Garrec, J. P.; He, S.; Penuelas, J.; Ribas, A.; Ro-Poulsen, H.; Rasmussen, S.; Sanz, M. J.; Vergne, P., Ozone pollution and ozone biomonitoring in European cities. Part I: Ozone concentrations and cumulative exposure indices at urban and suburban sites. *Atmos. Environ.* **2006,** *40*, 7963–7974.

16. Rezaei, F.; Rownaghi, A. A.; Monjezi, S.; Lively, R. P.; Jones, C. W., SOx/NOx Removal from Flue Gas Streams by Solid Adsorbents: A Review of Current Challenges and Future Directions. *Energy Fuels* **2015,** *29*, 5467−5486.

17. Damma, D.; Ettireddy, P. R.; Reddy, B. M.; Smirniotis, P. G., A Review of Low Temperature NH3-SCR for Removal of NOx. *Catalysts* **2019,** *9* (4).

18. Walker, A. P., Controlling Particulate Emissions from Diesel Vehicles. *Top. Catal.* **2004,** *28* (1), 165-170.

19. Richter, J. M.; Klingmann, R.; Spiess, S.; Wong, K.-F., Application of Catalyzed Gasoline Particulate Filters to GDI Vehicles. *SAE Int. J. Engines* **2012,** *5* (3), 1361-1370.

20. Hoffmann, M. R.; Martin, S. T.; Choi, W.; Bahnemann, D. W., Environmental Applications of Semiconductor Photocatalysis. *Chem. Rev.* **1995,** *95* (1), 69-96.

21. Ibhadon, A. O.; Fitzpatrick, P., Heterogeneous Photocatalysis: Recent Advances and Applications. *Catalysis* **2013,** *3* (1), 189-218.

22. Fujishima, A.; Honda, K., Electrochemical Photolysis of Water at a Semiconductor Electrode. *Nature* **1972,** *238* (5358), 37-38.

23. Hoffmann, M. R.; Martin, S. T.; Choi, W.; Bahnemann, D. W., Environmental Applications of Semiconductor Photocatalysis. *Chemical Reviews* **1995**, 69-96.

24. Cowan, A. J.; Tang, J.; Leng, W.; Durrant, J. R.; Klug, D. R., Water Splitting by Nanocrystalline TiO2 in a Complete Photoelectrochemical Cell Exhibits Efficiencies Limited by Charge Recombination. *J. Phys. Chem. C* **2010,** *114* (9), 4208-4214.

25. Ibhadon, A. O.; Fitzpatrick, P., Heterogeneous Photocatalysis: Recent Advances and Applications. *Catalysts* **2013,** *3*, 189-218.

26. Kondarides, D. I., Photocatalysis. *Catalysis* **2010**.

27. Kazemi, M.; Mohammadizadeh, M. R., Superhydrophilicity and photocatalytic activity of sol–gel deposited nanosized titania thin films. *Thin Solid Films* **2011,** *519* (19), 6432-6437.

28. Biskupski, D.; Herbig, B.; Schottner, G.; Moos, R., Nanosized titania derived from a novel sol–gel process for ammonia gas sensor applications. *Sens. Actuators B Chem.* **2011,** *153* (2), 329-334.

29. Moan, J., Visible Light and UV radiation. In *Radiation at Home, Outdoors and in the Workplace*, Oslo: Scandinavian Science Publisher: 2001; pp 69-85.

30. Asahi, R.; Morikawa, T.; Ohwaki, T.; Aoki, K.; Taga, Y., Visible-Light Photocatalysis in Nitrogen-Doped Titanium Oxides. *Science* **2001,** *293* (5528), 269-271.

31. Wang, Y.; Wang, Y.; Meng, Y.; Ding, H.; Shan, Y.; Zhao, X.; Tang, X., A Highly Efficient Visible-Light-Activated Photocatalyst Based on Bismuth- and Sulfur-Codoped TiO2. *J. Phys. Chem. C* **2008,** *112* (17), 6620-6626.

32. Gai, Y.; Li, J.; Li, S.-S.; Xia, J.-B.; Wei, S.-H., Design of Narrow-Gap TiO2: A Passivated Codoping Approach for Enhanced Photoelectrochemical Activity. *Phys. Rev. Lett.* **2009,** *102* (3), 036402.

33. Vijayan, B. K.; Dimitrijevic, N. M.; Finkelstein-Shapiro, D.; Wu, J.; Gray, K. A., Coupling Titania Nanotubes and Carbon Nanotubes To Create Photocatalytic Nanocomposites. *ACS Catal.* **2012,** *2*, 223-229.

34. Woan, K.; Pyrgiotakis, G.; Sigmund, W., Photocatalytic Carbon-Nanotube-TiO2 Composites. *Adv. Mater.* **2009,** *21* (21), 2233-2239.

35. An, G.; Ma, W.; Sun, Z.; Liu, Z.; Han, B.; Miao, S.; Miao, Z.; Ding, K., Preparation of Titania/Carbon Nanotube Composites Using Supercritical Ethanol and Their Photocatalytic Activity for Phenol Degradation under Visible Light Irradiation. *Carbon* **2007,** *45*, 1795-1801.

36. Silva, C. G.; Faria, J. L., Photocatalytic Oxidation of Benzene Derivatives in Aqueous Suspensions: Synergic Effect Induced by the Introduction of Carbon Nanotubes in a TiO_2 Matrix. *Appl. Catal. B: Environ.* **2010,** *101*, 81-89.

37. Li, N.; Ma, Y.; Wang, B.; Huang, Y.; Wu, Y.; Yang, X.; Chen, Y., Synthesis of Semiconducting SWNTs by Arc Discharge and Their Enhancement of Water Splitting Performance with TiO_2 Photocatalyst. *Carbon* **2011,** *49*, 5132-5141.

38. Iijima, S., Helical microtubules of graphitic carbon. *Nature* **1991,** *354* (6348), 56-58.

39. Popov, V. N., Carbon nanotubes: properties and application. *Mater. Sci. Eng.: R: Rep* **2004,** *43* (3), 61-102.

40. Berber, S.; Kwon, Y.-K.; Tománek, D., Unusually High Thermal Conductivity of Carbon Nanotubes. *Phys. Rev. Lett.* **2000,** *84* (20), 4613-4616.

41. Baughman, R. H.; Zakhidov, A. A.; de Heer, W. A., Carbon Nanotubes--the Route Toward Applications. *Science* **2002,** *297* (5582), 787-792.

42. Landi, B. J.; Ganter, M. J.; Cress, C. D.; DiLeo, R. A.; Raffaelle, R. P., Carbon nanotubes for lithium ion batteries. *Energy Environ. Sci.* **2009,** *2* (6), 638-654.

43. Pop, E.; Mann, D.; Wang, Q.; Goodson, K.; Dai, H., Thermal Conductance of an Individual Single-Wall Carbon Nanotube above Room Temperature. *Nano Lett.* **2005,** *6* (1), 96-100.

44. Tans, S. J.; Devoret, M. H.; Dai, H.; Thess, A.; Smalley, R. E.; Geerligs, L. J.; Dekker, C., Individual single-wall carbon nanotubes as quantum wires. *Nature* **1997,** *386* (6624), 474-477.

45. Cao, Q.; Kim, H.-s.; Pimparkar, N.; Kulkarni, J. P.; Wang, C.; Shim, M.; Roy, K.; Alam, M. A.; Rogers, J. A., Medium-scale carbon nanotube thin-film integrated circuits on flexible plastic substrates. *Nature* **2008,** *454* (7203), 495-500.

46. Park, S.; Vosguerichian, M.; Bao, Z., A review of fabrication and applications of carbon nanotube film-based flexible electronics. *Nanoscale* **2013,** *5* (5), 1727-1752.

47. Lefebvre, J.; Ding, J.; Li, Z.; Finnie, P.; Lopinski, G.; Malenfant, P. R. L., High-Purity Semiconducting Single-Walled Carbon Nanotubes: A Key Enabling Material in Emerging Electronics. *Acc. Chem. Res.* **2017,** *50* (10), 2479-2486.

48. Cao, Q.; Han, S.-j.; Tulevski, G. S.; Zhu, Y.; Lu, D. D.; Haensch, W., Arrays of single-walled carbon nanotubes with full surface coverage for high-performance electronics. *Nat. Nanotechnol.* **2013,** *8* (3), 180-186.

49. Norizan, M. N.; Moklis, M. H.; Ngah Demon, S. Z.; Halim, N. A.; Samsuri, A.; Mohamad, I. S.; Knight, V. F.; Abdullah, N., Carbon nanotubes: functionalisation and their application in chemical sensors. *RSC Adv.* **2020,** *10* (71), 43704-43732.

50. Camilli, L.; Passacantando, M., Advances on Sensors Based on Carbon Nanotubes. *Chemosensors* **2018,** *6* (4).

51. Mohsen, M. O.; Alansari, M.; Taha, R.; Senouci, A.; Abutaqa, A., Impact of CNTs' treatment, length and weight fraction on ordinary concrete mechanical properties. *Constr. Build. Mater.* **2020,** *264*, 120698.

52. Dai, H., Carbon Nanotubes: Synthesis, Integration, and Properties. *Acc. Chem. Res* **2002,** *35*, 1035-1044.

53. Bachilo, S. M.; Balzano, L.; Herrera, J. E.; Pompeo, F.; Resasco, D. E.; Weisman, R. B., Narrow (n,m)-Distribution of Single-Walled Carbon Nanotubes Grown Using a Solid Supported Catalyst. *J. Am. Chem. Soc.* **2003,** *125* (37), 11186-11187.

54. Odom, T. W.; Huang, J.-L.; Lieber, C. M., STM studies of single-walled carbon nanotubes. *J. Condens. Matter Phys.* **2002,** *14* (6), R145-R167.

55. Tan, L. L.; Ong, W. J.; Chai, S. P.; Mohamed, A., Reduced Graphene Oxide-TiO2 Nanocomposite as a Promising Visible-Light-Active Photocatalyst for the Conversion of Carbon Dioxide. *Nanoscale Res. Lett.* **2013,** *8*, 1-9.

56. Zhang, W. D.; Xu, B.; Jiang, L. C., Functional Hybrid Materials Based on Carbon Nanotubes and Metal Oxides. *J. Mater. Chem.* **2010,** *20*, 6383-6391.

57. Pyrgiotakis, G.; Lee, S. H.; Sigmund, W., Advanced Photocatalysis with Anatase Nanocoated Multi-walled Carbon Nanotubes. *Mater. Res. Soc. Symp. Proc.* **2005,** *876*, 1-6.

58. Linsebigler, A. L.; Lu, G.; Yates, J., J.T., Photocatalysis on TiO_2 Surfaces: Principles, Mechanisms, and Selected Results. *Chem. Rev.* **1995,** *95* (3), 735-758.

59. Yu, H.; Quan, X.; Chen, S.; Zhao, H., TiO_2-Multiwalled Carbon Nanotube Heterojuntion Arrays and their Charge Separation Capability. *J. Phys. Chem. C* **2007,** *111* (35), 12987-12991.

Chapter 2 - Efficient Growth of Carbon Nanotube Carpets Enabled by In-Situ Generation of Water

Chapter 2 is reprinted with permission from:

Everhart, B. M.;[1] Almkhelfe, H.;[1] Li, X.; Wales, M.; Nikolaev, P.; Rao, R.; Maruyama, B.; Amama, P. B., Efficient Growth of Carbon Nanotube Carpets Enabled by In Situ Generation of Water. *Industrial & Engineering Chemistry Research* **2020,** *59* (19), 9095-9104.

[1]*Equal contribution*

2.1 Introduction

Emergence of carbon nanotube (CNT) carpets, consisting of self-aligned nanotubes produced via catalytic chemical vapor deposition (CVD) from densely packed catalyst nanoparticles on a substrate, has inspired application opportunities in many important areas.[1-9] Scale-up of the process is often plagued by complicated optimization procedures due to the high sensitivity of the growth process to variations in feedstock composition, flow characteristics, and reactor geometry.[10-12] Single-walled CNT (SWCNT) carpet growth experienced a major boost with the discovery of 'supergrowth,' a process that leads to dramatic enhancement in catalytic activity upon the addition of a small amount of water.[8, 13, 14] Other oxygen-containing feedstocks or additives such as ethanol,[15, 16] acetone,[17] CO[17-19] and CO_2[19-22] have also shown the ability to promote SWCNT carpet growth. However, as shown by a number of studies, determining the optimum amount of oxidant required for efficient growth remains a challenge. Xie et al.[23] revealed that growth rate and catalyst lifetime during 'supergrowth' have high sensitivity to water concentration. At optimum water concentration (~200 ppm), high lifetime (>1065 s) and growth

rate (~0.13 g_{CNTs} g^{-1}_{cat} s^{-1}) can be achieved, whereas operating below or above this level of water results in a decrease in CNT yield. Szabo et al.[24] observed the presence of water vapor in the feed yielded CNT carpets of higher quality, but at the expense of carpet height; the effects were attributed to the oxidizing property of water. In light of increasing global demand for CNTs,[7] there is a need to develop approaches that maximize yield, minimize production cost, and have process conditions relatively easier to optimize.

Catalytic CVD, utilizing the gaseous product mixture of Fischer-Tropsch synthesis (FTS), offers the possibility of scaling-up synthesis of CNTs due to its high growth efficiency.[25, 26] FTS is a gas-to-liquid polymerization process that transforms syngas (mixture of CO and H_2) into liquid hydrocarbons. Based on the Anderson-Schulz-Flory model that predicts the distribution of products from FTS, even at optimum probability of chain growth, substantial yield of low-molecular-weight gaseous products is unavoidable.[27] The gaseous product mixture from FTS (referred to as FTS-GP) usually consists of a variety of C1-C4 hydrocarbons and unreacted CO and H_2. As demonstrated in prior studies, FTS-GP is a promising feedstock for efficient CVD growth of SWCNT[26] and multi-walled CNT (MWCNT) carpets under a broad range of conditions.[25] A comparison of growth profiles (carpet height as a function of growth time) of SWCNT carpets from FTS-GP CVD, using Fe catalysts and other conventional CVD processes with different feedstocks, reveals a relatively high growth rate (~50 μm/min) and a catalyst lifetime (> 90 min) superior to other CVD approaches.[26,28] Use of FTS-GP as a feedstock has multiple benefits. First, it does not require stringent optimization of process conditions as it appears to have a broad window for growth of SWCNT carpets. Second, it has an uncommon feature of not only supplying a high flux of carbon species to the catalyst particles, but also protecting them from early loss of activity. Third, in light of increasing global demand for CNTs, use of FTS-GP as a

feedstock in industrial-scale production is expected to minimize gaseous waste in FTS plants. Further improvement, control, and scale-up of FTS-GP CVD will require a good understanding of the role of FTS-GP in CNT growth enhancement.

Here, we hypothesize water formed by a reaction between H_2 and the low-volume fraction of CO in FTS-GP is responsible for enhanced growth efficiency characteristic of FTS-GP CVD. The water, formed in the vicinity of the catalyst during the process as illustrated in Figure 2.1, is expected to play a similar role as reported for 'supergrowth': oxidizing carbon contaminants deposited on the catalyst surface[8, 29] and inhibiting mass loss (Ostwald ripening and subsurface diffusion) during SWCNT growth, thus extending catalyst lifetime.[30-35] We study the role of FTS-GP in CNT growth using a combination of experimental and theoretical methodologies. Thermodynamic analysis investigates feasibility of the reaction between water and CO at different growth temperatures and estimates the amount of water generated under our CVD conditions.

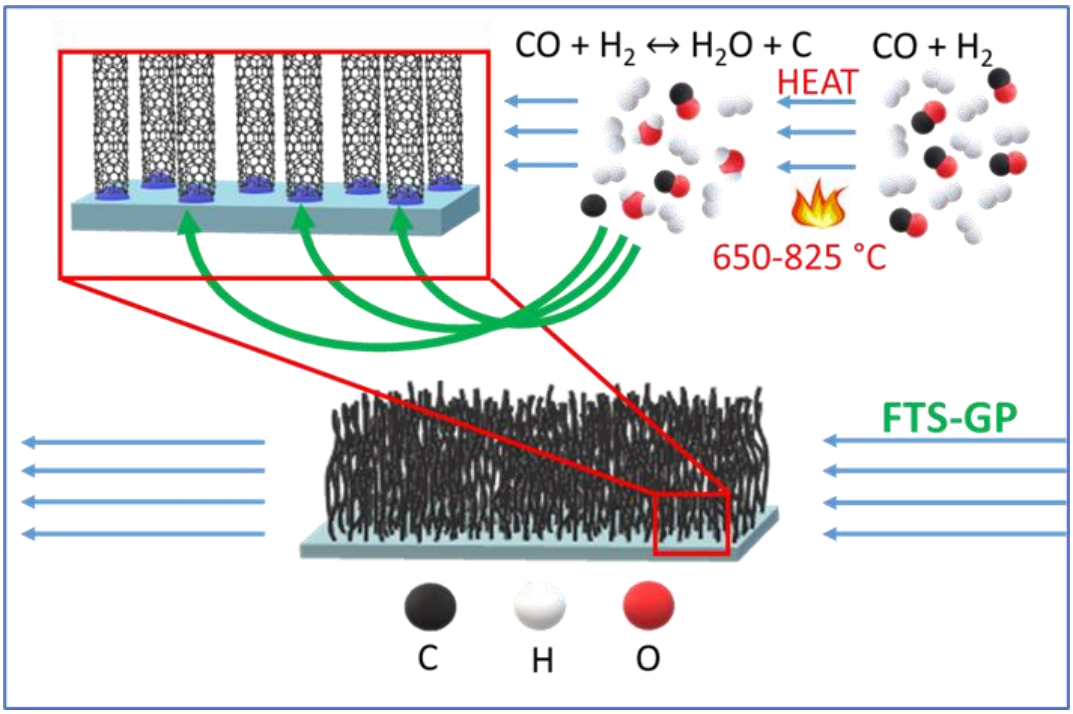

Figure 2.1. Schematic illustration of onsite generation of water during CNT carpet growth via FTS-GP CVD.

The first experimental approach involves direct analysis of gas-phase products from thermal decomposition of FTS-GP in a batch reactor (without the catalyst) at different reaction temperatures (650, 700, 750, and 800°C). Second, due to the breadth of parameters that affect CVD growth of SWCNTs, rapid experimentation is necessary for effective optimization of growth conditions and understanding of the role of feedstock in growth. Here, we employ an Autonomous Research System (ARES)[36, 37] — an automated, high-throughput, laser-induced CVD system with in-situ Raman spectral feedback — to measure SWCNT growth kinetics and compare the differences in growth with FTS-GP and a conventional feedstock (C_2H_4) in the presence and absence of water. Illumination of the complex interdependence of growth parameters and the role of FTS-GP in growth enhancement is expected to provide a rational framework for potential optimization and scale-up of CNT growth via FTS-GP CVD.

2.2 Experimental Section

2.2.1 SWCNT Growth by FTS-GP CVD

A thin Fe film supported on an amorphous alumina film (Al_xO_y/Fe) was used as the catalyst for SWCNT carpet growth. The films were deposited by an ion beam sputter deposition and etching system (IBS/e, South Bay Technology) on Si (100) substrates with a native oxide layer (P type and B-doped) at 10^{-4} Torr chamber pressure without exposing the films to air between depositions. Nominal thicknesses of Fe and Al_xO_y films were 1.3 and 30 nm, respectively. Thicknesses of the films deposited were measured by a quartz crystal thickness monitor and corroborated by height profile measurements using an atomic force microscope. The feedstock used was FTS-GP (supplied by Matheson Inc.) with the following composition: CO (5%), C_2H_6 (8%), C_2H_4 (6%), CH_4 (30%), N_2 (4%), C_3H_8 (5%), H_2 (40%), and C_3H_6 (2%),[38-40] which is similar

to the typical composition of a gaseous product mixture for FTS and hydrocracking processes in the presence of Fe catalysts.[41]

SWCNT growth was carried out at atmospheric pressure using the EasyTube 101 CVD system (CVD Equipment Corporation) equipped with several features for improved process control including a LabView-based process control software, static mixer for optimum gas mixing, and control system for precise temperature control. A typical growth experiment involved heating the Al_xO_y/Fe catalyst to the desired temperature (650, 700, 750, or 800 °C) at a rate of 45 °C/min in flowing Ar. Once at the growth temperature, the catalyst was reduced for 10 min by introducing hydrogen; the respective flow rates were 250 standard cubic centimeters per minute (sccm) H_2 and 250 sccm Ar. Thereafter, SWCNT growth was initiated at the respective temperatures by introducing FTS-GP in combination with Ar as the diluent (100 sccm FTS-GP and 1000 sccm Ar) for different durations. At the end of each growth experiment, samples were rapidly cooled in H_2 followed by slow cooling to room temperature in 700 sccm Ar.

2.2.2 Characterization

Morphologies and quality of the grown SWCNT carpets were characterized by field emission scanning electron microscopy (SEM, FEI-Versa 3D DualBeam) and Raman spectroscopy. Raman spectroscopic characterization was carried out in a Renishaw in Via Raman microscope using a laser excitation wavelength of 633 nm. Heights of tall carpets (> 0.5 μm) were measured using an optical microscope.

Products formed during FTS-GP CVD in a batch reactor were analyzed by a Hewlett-Packard 6890 series gas chromatograph (GC) with a thermal conductivity detector (TCD). The injector port was held constant at 170 ºC, and was operated in slip mode with a 150:1 split ratio

using a split linear with deactivated wool (Agilent 5183-4711). Samples were separated using a non-polar column connected in series with a polar column HP-5 (Agilent 19091J-413) and DB-Wax (Agilent 122-7032), respectively. Columns were connected using a press-fit connector (Agilent 5190-6979) and operated in constant flow (1.2 mL/min) with He as a carrier gas. The GC temperature was initially at 50 ºC and held at this temperature for 1 min, followed by a ramp of 20 ℃ per minute to a final temperature of 200 ℃; total run time was 8.5 min. The detector was maintained at 150 ºC with He as the reference gas.

2.2.3 SWCNT Growth Investigations in ARES

Growth experiments in ARES were performed at a pressure of 20 Torr and a temperature of 825°C. ARES growth substrates contain silicon micropillars fabricated by reactive ion etching. Each substrate contains a 12×12 array of patches, each consisting of a 5×5 array of 10 μm-diameter, 10-μm-high silicon pillars (on an SiO_2 underlayer) coated with a 10-nm-thick Al_xO_y support layer and a 1-nm-thick Fe catalyst film. The support and catalyst layers were also deposited by IBS/e following steps described earlier for catalysts used in conventional CVD. A high power (6W, Verdi) laser (532 nm) serves as both the heat and Raman excitation source. The Si micropillars were heated to growth temperatures by regulating the laser power, and temperatures were estimated from the redshift of the Raman peak frequency of the Si micropillar. During each growth experiment, Raman spectra were collected every 5 seconds and experiments were allowed to proceed until SWCNT growth appeared to cease, as determined by a plateauing of the intensity of the SWCNT Raman peak (G band).

Growth profiles were obtained by measuring the G-band areas and each profile was fit to a radioactive decay model (explained in detail in the following section) to extract initial growth

rates and catalyst lifetimes. Water concentration in the system was measured by a dewpoint sensor (Shaw) placed at the inlet of the growth chamber. For each experiment, water concentration represents the amount of water added to the system relative to the baseline concentration (2.0 - 4.5 ppm). Gas lines were purged until baseline water concentrations fell below 4.5 ppm before beginning experiments. Experiments were conducted with the different feedstocks (FTS-GP and C_2H_4) without a diluent gas.

2.3 Results and Discussion

2.3.1 Catalytic Performance at Different Temperatures

Figure 2.2 summarizes CNT carpet growth data at 650, 700, 750, and 800°C using FTS-GP as a feedstock. Dense nanotube carpets with uniform coverage across the substrates were grown at these temperatures as shown by the SEM images. SWCNT selectivity is highest at 750°C for Fe catalysts with the lowest amounts of MWCNTs.[26]

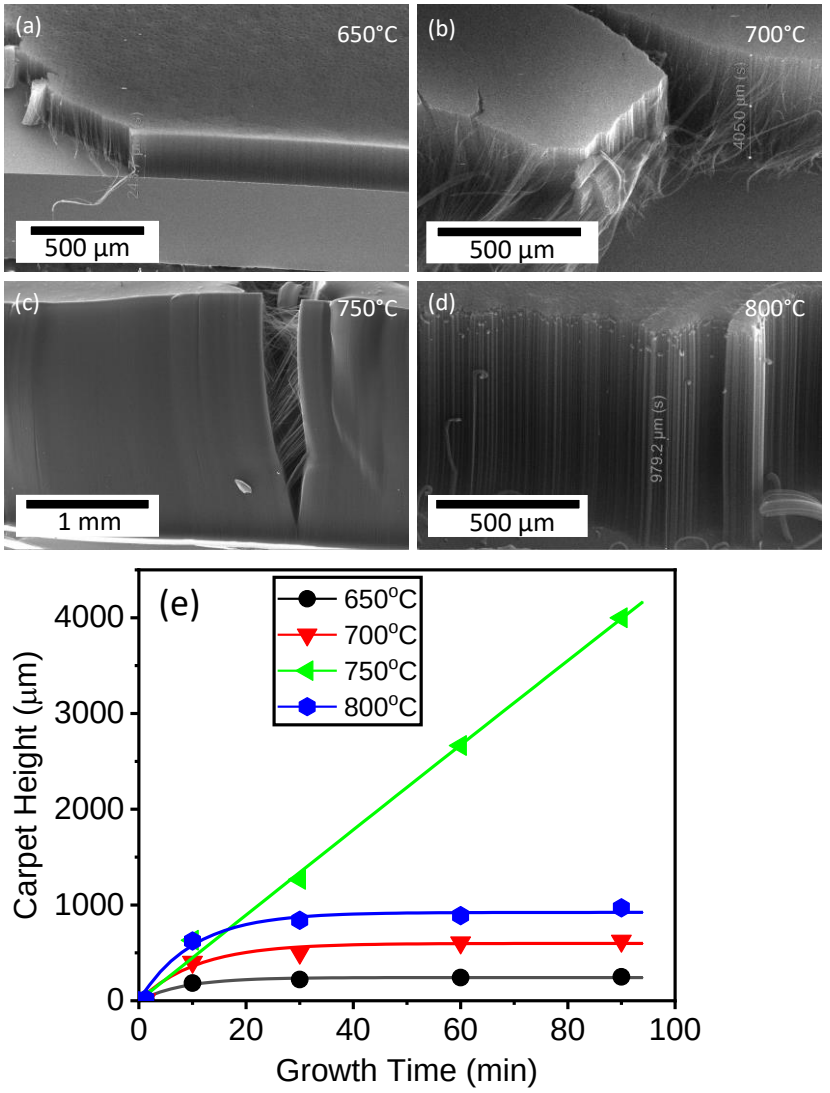

Figure 2.2. SEM images of SWCNT carpets grown on Al_2O_3/Fe substrates at different temperatures after 90 min: (a) 650°C; (b) 700°C; (c) 750°C; and (d) 800°C. (e) Plots of SWCNT carpet height as a function of growth time for different growth temperatures; solid lines represent curve fitting of the radioactive decay model (Equation 1) to the experimental data shown in symbols.

After performing growth for 90 min at the different temperatures, SWCNT carpets of strikingly different heights were obtained. From the SEM data in Figures. 2.2a-d, measured heights of the resulting SWCNT carpets after 90 min of growth at 650, 700, 750, and 800°C were 250, 625, 4000, and 970 µm, respectively. Analysis of the growth profiles in Figure 2.2e provides a better understanding of the catalytic performance (activity and lifetime) at the different

temperatures. The evolution of nanotube carpet height with time is generally characterized by a high growth rate at the onset that subsequently decreases gradually until complete growth termination occurs.[13, 26, 42-44] Futaba et al.[13] showed the growth profile of SWCNT carpets during 'supergrowth' to be analogous to the radioactive decay process whereby catalysts lose their activity over time. Therefore, SWCNT carpet growth can be modeled by the radioactive decay model (Equation 2.1):

$$H(t) = \beta\tau_o(1 - e^{-\frac{t}{\tau_o}}) \qquad (2.1)$$

where H is the carpet height at various times, t, while fitting parameters β and τ_o represent the initial growth rate and characteristic catalyst lifetime, respectively. Based on the goodness of fit ($R^2 > 0.971$), the curve fitting of the model to the growth data at different temperatures, shown in Figure 2.2e, is quite good.

Table 2.1. Summary of fitting parameters (β and τ) and goodness of fit, modeled by the radioactive decay model (Equation 1), for different growth temperatures.

Growth temperature (°C)	**Growth rate (β) (μm/min)**	**Lifetime (τ_o) (min)**	**R^2**
650	28.9	8.4	0.979
700	55.3	10.8	0.971
750	44.9	3975.0	0.997
800	91.4	10.1	0.985

Fitting parameters for the different temperatures and goodness of fit are summarized in Table 2.1. Activity and lifetime of catalysts in FTS-GP CVD are highly sensitive to growth temperature. Even though signs of deactivation are not apparent after 90 min for growth at 750 °C, fitting parameters are also extracted for comparison; we note, in all likelihood, unlike the value of β, the value of τ_o has a large uncertainty due to absence of any sign of deactivation within 90 min. As a result, even though the fitting parameters for growth at 750°C are shown, the experimental value of $\tau_o$is considered as the lower bound and used for comparisons.

A long catalyst lifetime, with not many parallels in the literature for conventional CVD with a monometallic catalyst, is observed at 750°C as the catalyst stays active after 90 min of growth and experiences no sign of deactivation during growth. On the other hand, growth at a lower (700°C) or higher temperature (800°C) resulted in a significant drop in catalyst lifetime. Growth at low temperature (650°C) exhibits a low growth rate accompanied by a short catalyst lifetime. At higher temperatures (> 650°C), growth rate generally increases while lifetime remains roughly the same for all temperatures (~10 min), except at our optimum growth temperature (750°C). Maximum fitted carpet heights predicted from the product of the two fitting parameters in the model (β and τ_o) are 243 μm at 650°C, 599 μm at 700°C, 179 mm at 750°C, and 923 μm at 800 °C. We assume that catalyst lifetime for growth at 750°C is longer than 90 min because growth termination during FTS-GP CVD does not appear to be instantaneous.[25, 26, 44] Therefore, except for growth at 750°C, maximum fitted carpet heights are within the same range as experimental carpet heights for the growth temperatures. In other words, maximum carpet heights are most likely attained for growth at 650, 700, and 800°C, and are significantly lower than the theoretical carpet height at 750°C, as well as the experimental height of ~ 4 mm after 90 min of growth.

The Raman spectra of SWCNT carpets grown at different temperatures are shown in Figure 2.3. In addition to the omnipresent D and G bands associated with SWCNTs, radial breathing mode peaks (RBMs) in the low-frequency region, characteristic of SWCNTs, are observed in all spectra. G-band peak corresponds to in-plane C-C vibrations while D band is attributed to carbon impurities and defects present in the CNTs. The presence of RBMs (Figure 2.3) suggests the presence of SWCNTs in the carpet samples. From the intensity ratios of the G band (I_G) and D band (I_D) in Figure 2.3 and TEM analysis,[26] carpets grown at 750°C, a temperature that supports the longest catalyst lifetime, have the highest quality as evidenced by the highest I_G/I_D of 9.1 and SWCNT selectivity.

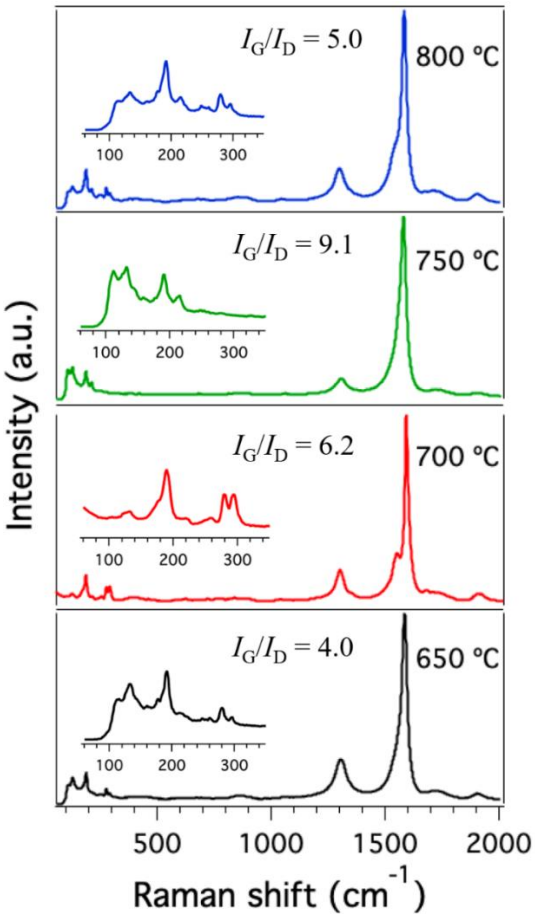

Figure 2.3. Representative Raman spectra of SWCNT carpet samples (excitation at 633 nm) with their respective I_G/I_D ratios.

To facilitate comparisons between SWCNT growth efficiency of FTS-GP CVD and conventional growth processes, we use representative studies involving monometallic catalysts in the literature to generate a catalyst lifetime versus growth rate map (Figure 2.4).[10, 13, 22, 29, 30, 43, 45-52] As reported by Chen et al.[53] achieving a high growth rate and long catalyst lifetime simultaneously during SWCNT carpet growth is difficult due to the inverse relationship between the two, a behavior that may intrinsically be connected to growth mechanisms. The growth map showing fitting parameters (β and τ_o), adapted from Yasuda et al.,[52] exhibits three main regions. The first, on the left side of the map (A), is characterized by long catalyst lifetimes, but low growth rates. Conversely, the second region, on the right side of the map (B), is characterized by rapid growth rates, but short catalyst lifetimes. Increased growth rates of catalysts in region (B) are attributed to the presence of an oxidizer that serves as a growth enhancer to improve resistance to catalyst deactivation during rapid growth, and control of the gas-flow direction in some of the studies. Data in (C) represent an improvement of 'supergrowth' studies in (B), whereby control of the dwell time of the carbon feedstock and the carbon flux to the catalyst are used to overcome the inverse relationship between lifetime and growth rate.[52] The corresponding performance of FTS-GP CVD from fitting with Equation 1 shows an estimated lifetime (F) that is quite long, albeit with high uncertainty. For meaningful comparison, the experimental value (E) is also included in the map. The lifetimes are shown with an arrow pointing from E to F—points we have assumed to be the lower and upper bounds, respectively, because growth cessation does not appear to be instantaneous. FTS-GP CVD, without any modification in the gas-flow direction or control of dwell time, exhibits a catalyst performance (based on experimental data) superior to studies in region (A) and lower bound that is at par with (B). In the following sections, a combined

thermodynamic and experimental study is carried out to probe the role of FTS-GP in observed growth enhancement.

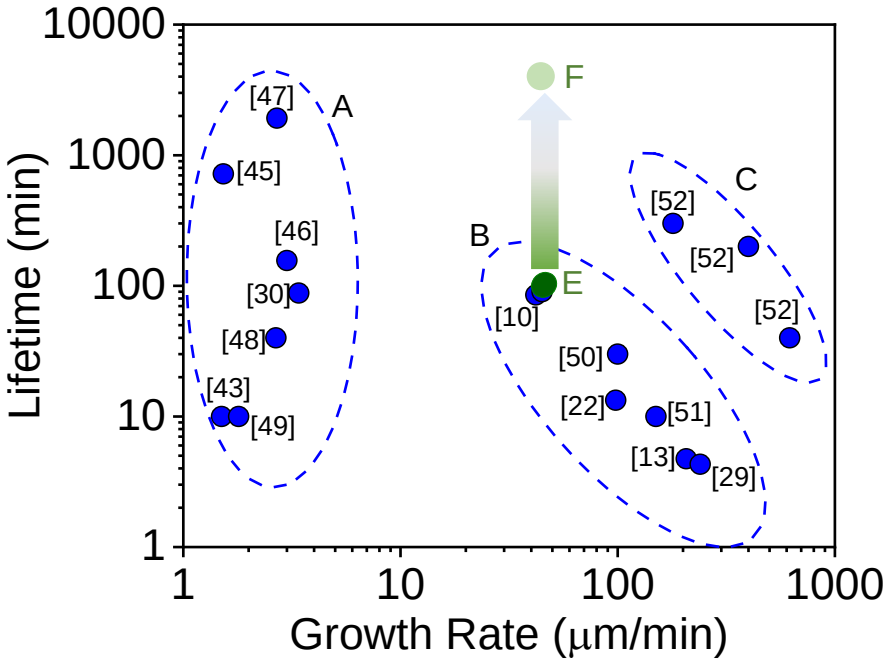

Figure 2.4. Growth rate-catalyst lifetime map of SWCNT carpets using supported monometallic catalyst showing a comparison of representative studies (in blue) including our results from FTS-GP CVD using an Fe catalyst (in green). E and F show the experimental and fitted lifetimes for FTS-GP CVD growth at 750°C, respectively; E and F and are assumed to be the limits of $\boldsymbol{\tau_o}$. The number indicates the reference for each datum.

2.3.2 Thermodynamic Prediction of In-situ Generation of Water

The high growth efficiency of FTS-GP CVD is attributed to the simultaneous high flux of carbon species to the catalyst and oxidative removal of excess amorphous carbon from the catalyst surface by water generated in situ.[25] The generation of water is hypothesized to occur via a reaction between CO and hydrogen:

$$CO_{(g)} + H_{2(g)} \leftrightarrow H_2O_{(g)} + C_{(s)} \tag{2.1}$$

The reaction involving CO has two distinct pathways depending on its partial pressure: at higher partial pressure of CO, the Boudouard reaction is favored, whereas a reaction between hydrogen and CO (Reaction 2.1) is favored at a lower partial pressure of CO and temperatures higher than 400°C (ΔG = -90 kJ/mole).[18, 54, 55] The conditions for Reaction 1 are quite similar to our SWCNT growth conditions in FTS-GP CVD, evidenced by the low-volume fraction of CO in the feedstock (5 vol% in FTS-GP) and growth temperatures greater than 400°C. Our objectives in this section are to (1) carry out a thermodynamic analysis to determine the feasibility of Reaction 2.1 and (2) estimate the amount of water generated under FTS-GP CVD conditions. Using data for free energy of formation (ΔG) with respect to temperature presented on FactWeb,[56] ΔG^0 (T) for CO, H_2, H_2O and C at standard conditions (1 atm of pressure) were obtained.

ΔG^0 for the reaction (ΔG^0_{rxn}) is calculated using Equation 2.2:

$$\Delta G^0_{rxn} = \sum n\Delta G^0_f \text{ (products)} - \sum n\Delta G^0_f \text{ (reactants)} \tag{2.2}$$

The free energy of formation ΔG^0 as a function of temperature for CO, H_2, H_2O, and C is given as

$$\Delta G^0_{rxn} = \Delta G^0 (H_2O) + \Delta G^0 (C) - \Delta G^0 (H_2) - \Delta G^0 (CO) \tag{2.3}$$

To calculate the ΔG under non-standard conditions, ΔG is expressed as

$$\Delta G = \Delta G^0 + RT\, lnQ \tag{2.4}$$

where Q is the reaction quotient and given as

$$Q = \frac{P_{H2O}}{P_{H2}\, P_{CO}} \tag{2.5}$$

Since the partial pressure of water is unknown, ΔG cannot be determined. However, at thermodynamic equilibrium, ΔG = 0, the equilibrium partial pressure of water (P_{H2O}) can be calculated as follows:

$$P_{(H2O)} = P_{(CO)} * \ P_{(H2)} \exp\left(-\frac{\Delta G^0}{RT}\right) \quad (6)$$

Partial pressures of CO and H_2 were determined for different feed compositions (0.05, 0.1 and 0.3 fractions) assuming 5% CO and 40% H_2. An important assumption in this analysis is that Reaction 2.1 proceeds on a small-enough scale that it does not significantly alter the partial pressures of H_2 and CO. Using the calculated ΔG^0 as a function of temperature, equilibrium water pressures ($P_{(H2O)}$) for the respective temperatures were obtained from Equation 2.6.

Profiles of the predicted equilibrium partial pressure as a function of temperature for different feed compositions (5, 10, 20, and 30% FTS-GP) are shown in Figure 2.5a; water concentrations in parts per million (ppm) in the temperatures that correspond to the SWCNT growth data are adapted from Figure 2.4a and shown in Figure 2.5b. Along the plot lines in Figure 2.5b, ΔG of Reaction 1 is zero (i.e., in equilibrium). Therefore, if the partial pressure of water for a particular temperature is below these lines, ΔG of Reaction 2.1 is negative, and therefore the forward reaction is favored. Conversely, if the partial pressure of water for a particular temperature is above these lines, ΔG of Reaction 2.1 is positive, and the reverse reaction will be favored. In other words, these plot lines are essentially the maximum partial pressure of water that can be generated at a particular temperature via Reaction 2.1. An inverse relationship between the concentration of water generated and temperature is observed for all FTS-GP compositions studied (Figure 2.5 and Table A2.1). We therefore conclude the equilibrium partial pressure of water is strongly dependent on temperature.

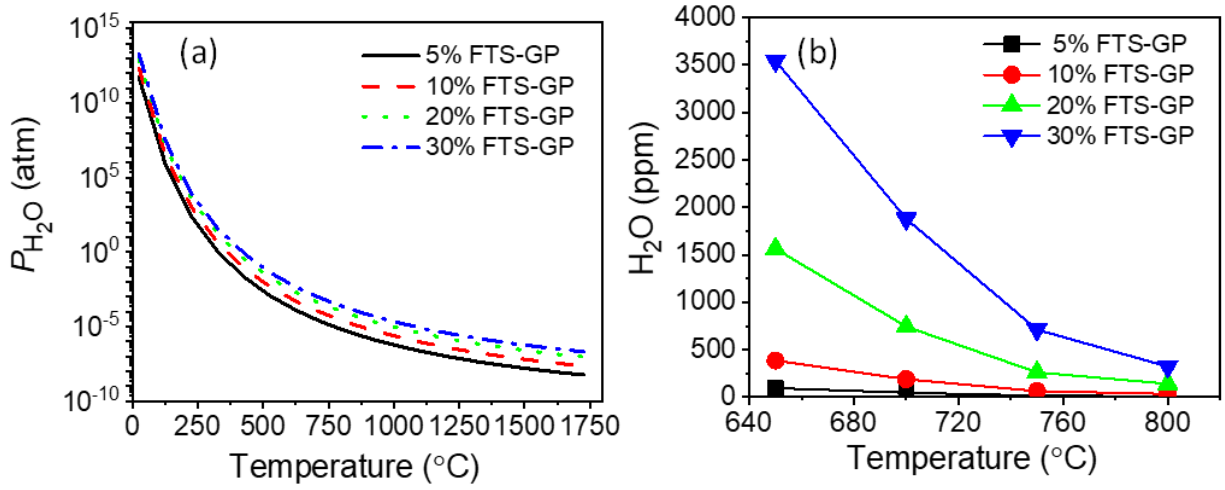

Figure 2.5. Thermodynamic prediction of the concentration of water generated during FTS-GP CVD. (a) Profiles of partial pressures of water as functions of growth temperatures for different feed compositions of FTS-GP (5, 10, 20, and 30%) with Ar as balance over a broad temperature range (0 – 1750°C). Along these lines, ΔG of Reaction 1 is zero, i.e., it is in equilibrium. (b) Profiles of water concentrations (ppm) as functions of temperatures with data points corresponding to growth temperatures used during FTS-GP CVD [adapted from (a)].

We note that if Reaction 2.1 is incomplete, the actual water concentration produced may be less and if it goes to completion, the predicted concentration of water generated is expected to be far lower than that of CO, which is 2500, 5000, and 15000 ppm for 5, 10, and 30% FTS-GP, respectively. Water concentrations obtained from this thermodynamic calculation are upper limits for the various growth conditions. Predicted concentrations of water generated for the FTS-GP fraction used in this study (10% FTS-GP) at 650, 700, 750, and 800°C are 386.5, 190.7, 64.6, and 34.6 ppm, respectively. Interestingly, the concentration of water generated for reactions with a low FTS-GP fraction is rather low (~3 ppm for 0.05 fraction, 850°C temperature) while for high FTS-GP fraction is fairly large (~3200 ppm for 0.3 fraction, 650°C temperature). Small amounts of water are generally beneficial to growth while excess amounts tend to be detrimental.[23] Assuming Reaction 1 goes to completion, it is important to understand whether relatively high levels of water generated during FTS-GP CVD are beneficial for SWCNT carpet growth.

2.3.3 Experimental Verification of Water Generation

The concentration of water generated during the gas-phase reaction of FTS-GP in a batch reactor was investigated as a function of temperature in the absence of a catalyst (Figure 2.6), and the data are presented along with the experimental carpet height attained after 90 min for the respective temperatures. The absence of the catalyst invalidates the argument that water is generated via the reduction of Fe_2O_3.

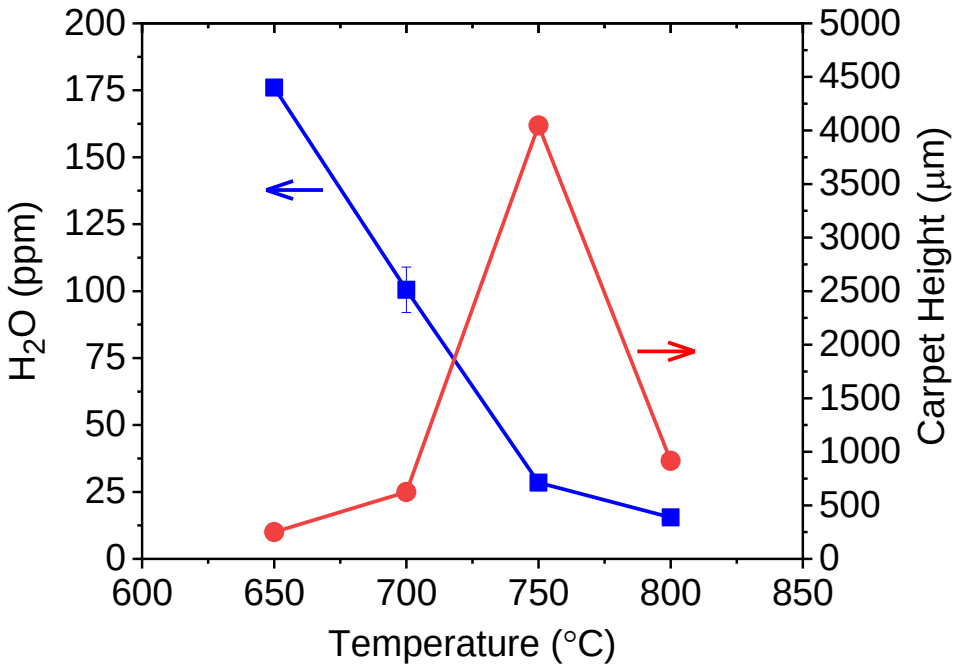

Figure 2.6. Concentration of water produced via gas-phase reaction of FTS-GP in a batch reactor as a function of temperature. Plot of carpet height after 90 min of growth versus temperature is included for comparison. The green shade shows the sweet spot for efficient carpet growth under the conditions used.

In agreement with the thermodynamic prediction, the concentration of water generated during decomposition of FTS-GP decreases with increasing temperature. Even though the concentration of water measured experimentally is lower than the concentration predicted by a factor of ~2, the trends are consistent with decreasing slope at higher temperatures. In light of the

dependence of SWCNT growth steps (such as feedstock decomposition, catalyst stability, and CNT nucleation) on temperature, the generation of different concentrations of water at different temperatures convolutes the role of water. It is possible using growth conditions optimized at 750°C for growth at other temperatures may be partly responsible for the stark difference in growth kinetics.

2.3.4 Using ARES to Probe the Effect of Water Concentration

To further understand the role of water in FTS-GP CVD, growth experiments were performed in ARES [36, 37] with C_2H_4 or FTS-GP as a feedstock at a constant temperature (825°C) in the presence of different concentrations of water. The presence of water, depending on the amount, can lead to growth enhancement, catalyst oxidation (high water level), or catalyst deactivation via coking or mass loss (low water level). An additional amount of water (up to 24 ppm) was added in our study to probe the water tolerance of SWCNT growth with the feedstocks. As described in detail in the Experimental Section, growth experiments in ARES are performed in a cold-wall CVD chamber where a high-power laser is the heat source and Raman excitation source, and Raman spectra are collected continuously during growth in order to monitor growth kinetics. Even though ARES utilizes a cold-wall reactor for growth, the effect of temperature on SWCNT growth followed the same trend as observed in a conventional hot-wall CVD (Figure A2.1). Here we used the maximum G-band intensity at the end of the growth experiment as a proxy for yield. SWCNT yield and quality (I_G/I_D) increased with temperature, reached a maximum at 825°C (higher than the optimum temperature of 750°C for FTS-GP CVD), and then decreased continuously. The difference in the optimum temperature between conventional CVD and ARES could be attributed to limited or possible absence of gas-phase decomposition of the feedstock in the latter.

SWCNT growth curves obtained from ARES at 825°C using different feedstocks in the presence of 0, 11.8, and 23.6 ppm of water were fitted with the radioactive decay model (Equation 2.1). Representative curves of SWCNT yield (G-band integrated area) versus growth time with the fits are shown in Figure 2.7, while extracted initial growth rates and lifetimes are shown in Figure 2.8. Growth rates of SWCNTs (Figure 2.8a) were significantly higher with C_2H_4 as the feedstock compared to FTS-GP. For both feedstocks, the growth rate decreased with increasing concentrations of water in the reactor; however, FTS-GP appears to exhibit a higher tolerance for the added water than C_2H_4. On the other hand, as shown in Figure 2.8b, growth performed with FTS-GP exhibited a substantial increase in lifetime with the addition of water, whereas growth with C_2H_4 exhibited a constant or even shortened catalyst lifetime with increasing concentrations of water. The remarkably high catalyst lifetimes observed for growth with FTS-GP compared to a standard feedstock indicates the high tolerance it has for relatively high levels of water near the catalysts, demonstrating a lifetime in the presence of 23.6 ppm water that is 11 times longer than that of C_2H_4.

Disparity in growth rates for experiments performed with FTS-GP and C_2H_4 may be due to factors such as a possible water-gas shift reaction and poor utilization of methane in ARES. During SWCNT growth in a hot-wall CVD reactor, decomposition of the feedstock occurs in the gas phase and on the catalyst surface. On the other hand, ARES relies on heating from the laser, suggesting that gas phase reactions are extremely low or nonexistent; this feature is expected to not only limit the carbon flux to the catalyst but also the in-situ water generation via Reaction 2.1. In spite of these differences, SWCNTs produced by ARES using C_2H_4 and FTS-GP were of similar diameters compared to those grown in conventional CVD. Post-growth Raman analysis of the SWCNTs revealed multiple RBMs between 100 and 300 cm^{-1} (Figure A2.2), similar to RBMs

observed in conventional CVD growth experiments (Figure 2.3). High growth efficiency observed with FTS-GP in conventional CVD has been associated with the ability of the unsaturated hydrocarbon to dissociate in the gas phase, generating free radicals that attack the more stable hydrocarbons such as CH_4.[25] The process enhances the flux of carbon species to the surface while simultaneously inhibiting the catalyst deactivation pathways via Reaction 2.1. Unfortunately, due to the absence of (or limited) gas-phase reactions in ARES, dissociation of CH_4 (40 vol% of FTS-GP) hardly occurs. This hypothesis is supported by the similarity in growth between FTS-GP, and the C_2H_4 and hydrogen mixture with no additional water (Figure A2.3). Significantly higher lifetimes measured with FTS-GP in comparison with C_2H_4 highlight the high tolerance of water with FTS.

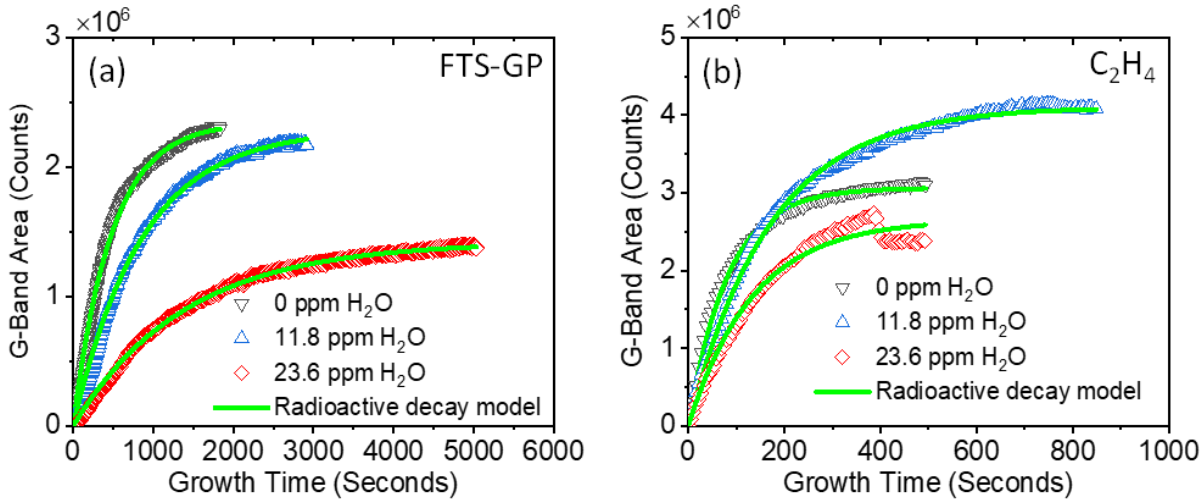

Figure 2.7. Plots of CNT yield as a function of growth time during CVD growth for different levels of water in ARES using FTS-GP (a) and ethylene (b) as feedstocks. The green solid lines represent curve fitting of the radioactive decay model (Equation 1) to the experimental data shown in symbols.

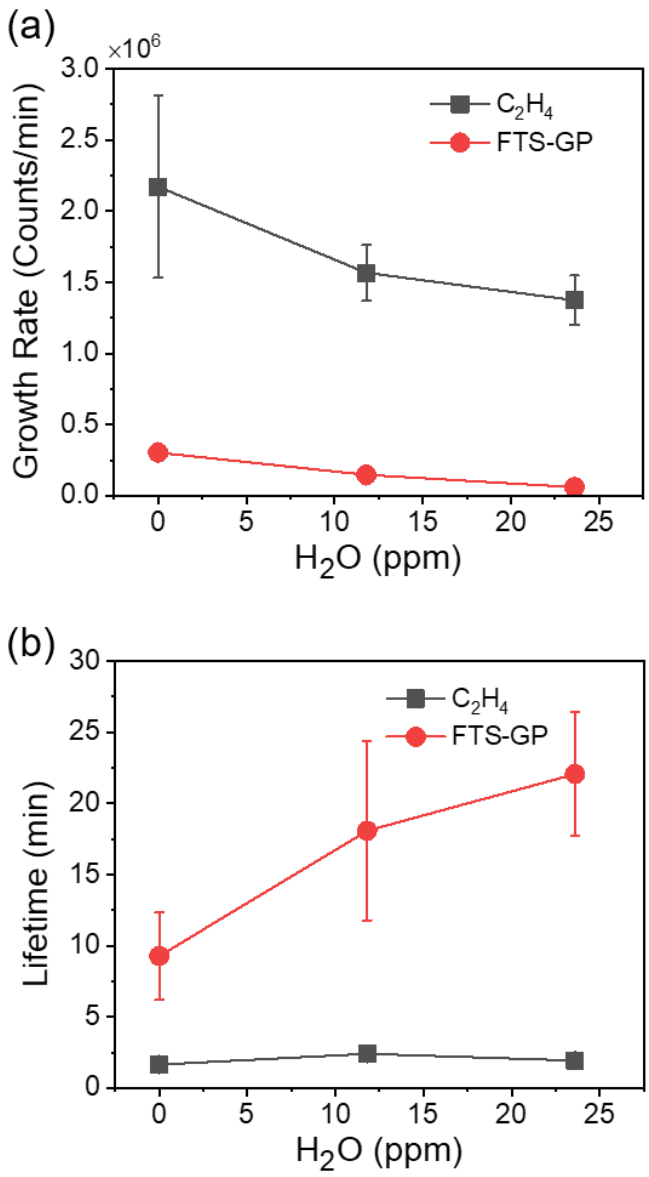

Figure 2.8. Growth kinetics parameters obtained by fitting the ARES growth curves with the radioactive decay model (Equation 1). (a) Plots of initial growth rate of SWCNTs as a function of water concentrations for FTS-GP and ethylene. (b) Plots of catalyst lifetime as a function of water concentrations for FTS-GP and ethylene.

The optimum concentration of water for 'supergrowth' is still debatable with most studies reporting values anywhere from 20 to 900 ppm.[8, 10, 12, 57, 58] However, a water concentration as low as 12 ppm has been reported by In et al.[59] to extend catalyst lifetime; in fact, the study concludes

even a very small amount of water (~1 ppm) in a feed of high purity can dramatically affect the kinetics of SWCNT growth. Therefore, it is reasonable to assume the estimated water amounts produced by FTS-GP at 750°C (64.6 ppm) in the vicinity of the catalyst are enough to protect the catalyst from deactivation. We speculate the optimum concentration of water in 'supergrowth' is starkly different for different studies because of a variety of factors, including type of feedstock, feed composition, and reactor geometry. As an example, Yasuda et al.[10] showed the optimum concentration of water during 'supergrowth' changes with gas-flow direction, with top-flow growth showing relatively the highest sensitivity to water as opposed to lateral-flow growth. In addition, growth data from ARES reveal the poor water tolerance of C_2H_4, in agreement with the work of Xie et al.[23] that revealed a narrow range of water concentrations that support efficient growth. We hypothesize that water generated during FTS-GP CVD as depicted in Figure 2.1 will experience significantly fewer diffusion limitations and water level can be better controlled in comparison to water introduced with the feed as in 'supergrowth' — making FTS-GP CVD more adaptable for scalable and controlled SWCNT growth.

Considering the complex composition of the feedstock and impact of gas-phase chemistry on CNT growth, the observed in situ generation of water may not be the only mechanism at play in the growth enhancement in FTS-GP CVD. Studies have revealed the formation of a broad population of specific hydrocarbon intermediates (volatile organic compounds and polycyclic aromatic compounds) in gas phase for a conventional feedstock (C_2H_4), suggesting the existence of competing reaction pathways that may inhibit or enhance CNT carpet growth.[42, 60, 61] Under SWCNT growth conditions, it is also possible that the small Fe nanoparticles with high free energies may become highly reactive even for reactions that are not favorable under equilibrium conditions. However, in light of the critical role water plays in extending catalyst lifetime during

SWCNT growth as demonstrated by 'supergrowth,' we believe this study provides an important foundation for mechanistic development of this new process and will complement future mechanistic studies on cracking pattern of the hydrocarbons and interactions of the different species.

2.4 Conclusions

In this study, the role of FTS-GP in growth enhancement of FTS-GP CVD was studied using a combination of experimental and theoretical approaches. The results reveal in-situ formation of water during FTS-GP CVD via a reaction between H_2 and the low-volume fraction of CO. The water formed is expected to play a similar role as reported for 'supergrowth.' Catalytic performance (activity and lifetime) and the concentration of water formed during FTS-GP CVD experiments (or equilibrium partial pressure of water determined from thermodynamic calculations) are sensitive to the decomposition temperature of FTS-GP. Maximum carpet heights are achieved for growth at 650, 700, and 800°C, and are significantly lower than the experimental carpet height of ~ 4 mm for growth at 750°C that is still active after 90 min and experiences no sign of deactivation. Experiments conducted in ARES, in the presence of different amounts of water, revealed a higher overall yield of SWCNTs with C_2H_4 as the feedstock compared to FTS-GP. On the other hand, the catalyst lifetime for growth performed with FTS-GP exhibited a substantial increase with the addition of water, while growth with C_2H_4 exhibited a constant or even shortened catalyst lifetime with increasing concentrations of water. The ARES data support our mechanistic rationale for the observed growth enhancement with FTS-GP CVD. FTS-GP CVD has the combined advantage of supporting on-site generation of water and having a high tolerance for high concentrations of water, making process optimization and scale-up promising.

2.5 References

1. Almkhelfe, H.; Li, X.; Thapa, P.; Hohn, K. L.; Amama, P. B., Carbon nanotube-supported catalysts prepared by a modified photo-Fenton process for Fischer–Tropsch synthesis. *J. Catal.* **2018,** *361*, 278-289.

2. Serp, P.; Machado, B., *Nanostructured carbon materials for catalysis*. Royal Society of Chemistry: Cambridge, UK, 2015; p xiv, 555 pages.

3. De las Casas, C.; Li, W., A review of application of carbon nanotubes for lithium ion battery anode material. *J. Power Sources* **2012,** *208* (0), 74-85.

4. Carter, R.; Oakes, L.; Cohn, A. P.; Holzgrafe, J.; Zarick, H. F.; Chatterjee, S.; Bardhan, R.; Pint, C. L., Solution Assembled Single-Walled Carbon Nanotube Foams: Superior Performance in Supercapacitors, Lithium-Ion, and Lithium–Air Batteries. *J. Phys. Chem. C* **2014,** *118* (35), 20137-20151.

5. Cola, B. A.; Xu, X.; Fisher, T. S.; Capano, M. A.; Amama, P. B., Carbon nanotube array thermal interfaces for high-temperature silicon carbide devices. *Nanosc. Microsc. Therm.* **2008,** *12* (3), 228-237.

6. Cola, B. A.; Xu, X.; Fisher, T. S., Increased Real Contact in Thermal Interfaces: A Carbon Nanotube/Foil Material. *Appl. Phys. Lett.* **2007,** *90* (9), 093513.

7. De Volder, M. F. L.; Tawfick, S. H.; Baughman, R. H.; Hart, A. J., Carbon Nanotubes: Present and Future Commercial Applications. *Science* **2013,** *339* (6119), 535-539.

8. Hata, K.; Futaba, D. N.; Mizuno, K.; Namai, T.; Yumura, M.; Iijima, S., Water-Assisted Highly Efficient Synthesis of Impurity-Free Single-Walled Carbon Nanotubes. *Science* **2004,** *306* (5700), 1362-1364.

9. Cohn, A. P.; Oakes, L.; Carter, R.; Chatterjee, S.; Westover, A. S.; Share, K.; Pint, C. L., Assessing the improved performance of freestanding, flexible graphene and carbon nanotube hybrid foams for lithium ion battery anodes. *Nanoscale* **2014,** *6* (9), 4669-4675.

10. Yasuda, S.; Futaba, D. N.; Yamada, T.; Satou, J.; Shibuya, A.; Takai, H.; Arakawa, K.; Yumura, M.; Hata, K., Improved and Large Area Single-Walled Carbon Nanotube Forest Growth by Controlling the Gas Flow Direction. *ACS Nano* **2009,** *3* (12), 4164-4170.

11. Lee, J.; Oh, E.; Kim, T.; Sa, J.-H.; Lee, S.-H.; Park, J.; Moon, D.; Kang, I. S.; Kim, M. J.; Kim, S. M.; Lee, K.-H., The influence of boundary layer on the growth kinetics of carbon nanotube forests. *Carbon* **2015,** *93*, 217-225.

12. Rao, R.; Pint, C. L.; Islam, A. E.; Weatherup, R. S.; Hofmann, S.; Meshot, E. R.; Wu, F.; Zhou, C.; Dee, N.; Amama, P. B.; Carpena-Nuñez, J.; Shi, W.; Plata, D. L.; Penev, E. S.;

Yakobson, B. I.; Balbuena, P. B.; Bichara, C.; Futaba, D. N.; Noda, S.; Shin, H.; Kim, K. S.; Simard, B.; Mirri, F.; Pasquali, M.; Fornasiero, F.; Kauppinen, E. I.; Arnold, M.; Cola, B. A.; Nikolaev, P.; Arepalli, S.; Cheng, H.-M.; Zakharov, D. N.; Stach, E. A.; Zhang, J.; Wei, F.; Terrones, M.; Geohegan, D. B.; Maruyama, B.; Maruyama, S.; Li, Y.; Adams, W. W.; Hart, A. J., Carbon Nanotubes and Related Nanomaterials: Critical Advances and Challenges for Synthesis toward Mainstream Commercial Applications. *ACS Nano* **2018,** *12* (12), 11756-11784.

13. Futaba, D. N.; Hata, K.; Yamada, T.; Mizuno, K.; Yumura, M.; Iijima, S., Kinetics of water-assisted single-walled carbon nanotube synthesis revealed by a time-evolution analysis. *Phys. Rev. Lett.* **2005,** *95* (5), 056104.

14. Meshot, E. R.; Park, S. J.; Buchsbaum, S. F.; Jue, M. L.; Kuykendall, T. R.; Schaible, E.; Bayu Aji, L. B.; Kucheyev, S. O.; Wu, K. J. J.; Fornasiero, F., High-yield growth kinetics and spatial mapping of single-walled carbon nanotube forests at wafer scale. *Carbon* **2020,** *159*, 236-246.

15. Zhang, Y.; Gregoire, J. M.; van Dover, R. B.; Hart, A. J., Ethanol-Promoted High-Yield Growth of Few-Walled Carbon Nanotubes. *J. Phys. Chem. C* **2010,** *114* (14), 6389-6395.

16. Sugime, H.; Noda, S., Millimeter-tall single-walled carbon nanotube forests grown from ethanol. *Carbon* **2010,** *48* (8), 2203-2211.

17. Dai, H.; Rinzler, A. G.; Nikolaev, P.; Thess, A.; Colbert, D. T.; Smalley, R. E., Single-wall nanotubes produced by metal-catalyzed disproportionation of carbon monoxide. *Chem. Phys. Lett.* **1996,** *260* (3), 471-475.

18. Zheng, B.; Lu, C.; Gu, G.; Makarovski, A.; Finkelstein, G.; Liu, J., Efficient CVD Growth of Single-Walled Carbon Nanotubes on Surfaces Using Carbon Monoxide Precursor. *Nano Lett.* **2002,** *2* (8), 895-898.

19. Futaba, D. N.; Goto, J.; Yasuda, S.; Yamada, T.; Yumura, M.; Hata, K., General Rules Governing the Highly Efficient Growth of Carbon Nanotubes. *Adv. Mater.* **2009,** *21* (47), 4811-4815.

20. Magrez, A.; Seo, J. W.; Kuznetsov, V. L.; Forró, L., Evidence of an Equimolar C2H2–CO2 Reaction in the Synthesis of Carbon Nanotubes. *Angew. Chem. Int. Edit.* **2007,** *46* (3), 441-444.

21. Wen, Q.; Qian, W.; Wei, F.; Liu, Y.; Ning, G.; Zhang, Q., CO2-Assisted SWNT Growth on Porous Catalysts. *Chem. Mater.* **2007,** *19* (6), 1226-1230.

22. Sato, T.; Sugime, H.; Noda, S., CO2-assisted growth of millimeter-tall single-wall carbon nanotube arrays and its advantage against H2O for large-scale and uniform synthesis. *Carbon* **2018,** *136*, 143-149.

23. Xie, K.; Muhler, M.; Xia, W., Influence of Water on the Initial Growth Rate of Carbon Nanotubes from Ethylene over a Cobalt-Based Catalyst. *Ind. Eng. Chem. Res.* **2013,** *52* (39), 14081-14088.

24. Szabó, A.; Kecsenovity, E.; Pápa, Z.; Gyulavári, T.; Németh, K.; Horvath, E.; Hernadi, K., Influence of synthesis parameters on CCVD growth of vertically aligned carbon nanotubes over aluminum substrate. *Sci. Rep.* **2017,** *7* (1), 9557.

25. Almkhelfe, H.; Carpena-Nunez, J.; Back, T. C.; Amama, P. B., Gaseous product mixture from Fischer-Tropsch synthesis as an efficient carbon feedstock for low temperature CVD growth of carbon nanotube carpets. *Nanoscale* **2016,** *8* (27), 13476-13487.

26. Almkhelfe, H.; Li, X.; Rao, R.; Amama, P. B., Catalytic CVD growth of millimeter-tall single-wall carbon nanotube carpets using industrial gaseous waste as a feedstock. *Carbon* **2017,** *116*, 181-190.

27. Jahangiri, H.; Bennett, J.; Mahjoubi, P.; Wilson, K.; Gu, S., A review of advanced catalyst development for Fischer–Tropsch synthesis of hydrocarbons from biomass derived syn-gas. *Catal. Sci. Technol.* **2014,** *4* (8), 2210-2229.

28. Almkhelfe, H. Scalable Carbon Nanotube Growth and Design of Efficient Catalysts for Fischer-Tropsch Synthesis. Doctoral Dissertation, Kansas State University, 2017.

29. Yamada, T.; Maigne, A.; Yudasaka, M.; Mizuno, K.; Futaba, D. N.; Yumura, M.; Iijima, S.; Hata, K., Revealing the Secret of Water-Assisted Carbon Nanotube Synthesis by Microscopic Observation of the Interaction of Water on the Catalysts. *Nano Lett.* **2008,** *8* (12), 4288-4292.

30. Amama, P. B.; Pint, C. L.; McJilton, L.; Kim, S. M.; Stach, E. A.; Murray, P. T.; Hauge, R. H.; Maruyama, B., Role of Water in Super Growth of Single-Walled Carbon Nanotube Carpets. *Nano Lett.* **2009,** *9* (1), 44-49.

31. Kim, S.; Pint, C.; Amama, P.; Zakharov, D.; Hauge, R.; Maruyama, B.; Stach, E., Understanding Growth Termination of Single-Walled Carbon Nanotube Carpets by Documenting the Evolution of Catalyst Morphology with the Transmission Electron Microscope. *Microsc. Microanal.* **2009,** *15* (2), 1176.

32. Kim, S. M.; Pint, C. L.; Amama, P. B.; Hauge, R. H.; Maruyama, B.; Stach, E. A., Catalyst and catalyst support morphology evolution in single-walled carbon nanotube supergrowth: Growth deceleration and termination. *J. Mater. Res.* **2010,** *25* (10), 1875-1885.

33. Kim, S. M.; Pint, C. L.; Amama, P. B.; Zakharov, D. N.; Hauge, R. H.; Maruyama, B.; Stach, E. A., Evolution in catalyst morphology leads to carbon nanotube growth termination. *J. Phys. Chem. Lett.* **2010,** *1* (6), 918-922.

34. Amama, P. B.; Pint, C. L.; Kim, S. M.; McJilton, L.; Eyink, K. G.; Stach, E. A.; Hauge, R. H.; Maruyama, B., Influence of Alumina Type on the Evolution and Activity of Alumina-Supported Fe Catalysts in Single-Walled Carbon Nanotube Carpet Growth. *ACS Nano* **2010,** *4* (2), 895-904.

35. Amama, P. B.; Pint, C. L.; Mirri, F.; Pasquali, M.; Hauge, R. H.; Maruyama, B., Catalyst–support interactions and their influence in water-assisted carbon nanotube carpet growth. *Carbon* **2012,** *50* (7), 2396-2406.

36. Nikolaev, P.; Hooper, D.; Webber, F.; Rao, R.; Decker, K.; Krein, M.; Poleski, J.; Barto, R.; Maruyama, B., Autonomy in materials research: a case study in carbon nanotube growth. *npj Comput. Mater.* **2016,** *2*, 1-6.

37. Nikolaev, P.; Hooper, D.; Perea-Lopez, N.; Terrones, M.; Maruyama, B., Discovery of Wall-Selective Carbon Nanotube Growth Conditions via Automated Experimentation. *ACS Nano* **2014,** *8*, 10214-10222.

38. Hall, W. K.; Kokes, R. J.; Emmett, P. H., Mechanism Studies of the Fischer-Tropsch Synthesis. The Addition of Radioactive Methanol, Carbon Dioxide and Gaseous Formaldehyde. *J. Am. Chem. Soc.* **1957,** *79* (12), 2983-2989.

39. Kibby, C.; Jothimurugesan, K.; Das, T.; Lacheen, H. S.; Rea, T.; Saxton, R. J., Chevron's gas conversion catalysis-hybrid catalysts for wax-free Fischer–Tropsch synthesis. *Catal. Today* **2013,** *215*, 131-141.

40. Tavasoli, A.; Sadagiani, K.; Khorashe, F.; Seifkordi, A. A.; Rohani, A. A.; Nakhaeipour, A., Cobalt supported on carbon nanotubes — A promising novel Fischer–Tropsch synthesis catalyst. *Fuel Process. Technol.* **2008,** *89* (5), 491-498.

41. Zgolicz, P. D.; Stassi, J. P.; Yañez, M. J.; Scelza, O. A.; de Miguel, S. R., Influence of the support and the preparation methods on the performance in citral hydrogenation of Pt-based catalysts supported on carbon nanotubes. *J. Catal.* **2012,** *290*, 37-54.

42. Meshot, E. R.; Plata, D. L.; Tawfick, S.; Zhang, Y.; Verploegen, E. A.; Hart, A. J., Engineering Vertically Aligned Carbon Nanotube Growth by Decoupled Thermal Treatment of Precursor and Catalyst. *ACS Nano* **2009,** *3* (9), 2477-2486.

43. Einarsson, E.; Murakami, Y.; Kadowaki, M.; Maruyama, S., Growth dynamics of vertically aligned single-walled carbon nanotubes from in situ measurements. *Carbon* **2008,** *46* (6), 923-930.

44. Li, X.; Gray, E. R.; Islam, A. E.; Sargent, G. A.; Maruyama, B.; Amama, P. B., Magnesia and Magnesium Aluminate Catalyst Substrates for Carbon Nanotube Carpet Growth. *ACS Appl. Nano Mater.* **2020,** *3* (2), 1830-1840.

45. Miura, S.; Yoshihara, Y.; Asaka, M.; Hasegawa, K.; Sugime, H.; Ota, A.; Oshima, H.; Noda, S., Millimeter-tall carbon nanotube arrays grown on aluminum substrates. *Carbon* **2018,** *130*, 834-842.

46. Eres, G.; Kinkhabwala, A. A.; Cui, H.; Geohegan, D. B.; Puretzky, A. A.; Lowndes, D. H., Molecular Beam-Controlled Nucleation and Growth of Vertically Aligned Single-Wall Carbon Nanotube Arrays. *J. Phys. Chem. B* **2005,** *109* (35), 16684-16694.

47. Zhong; Iwasaki, T.; Robertson, J.; Kawarada, H., Growth Kinetics of 0.5 cm Vertically Aligned Single-Walled Carbon Nanotubes. *J. Phys. Chem. B* **2007,** *111* (8), 1907-1910.

48. Xu, Y.-Q.; Flor, E.; Kim, M. J.; Hamadani, B.; Schmidt, H.; Smalley, R. E.; Hauge, R. H., Vertical Array Growth of Small Diameter Single-Walled Carbon Nanotubes. *J. Am. Chem. Soc.* **2006,** *128* (20), 6560-6561.

49. Xiang, R.; Einarsson, E.; Okawa, J.; Miyauchi, Y.; Maruyama, S., Acetylene-Accelerated Alcohol Catalytic Chemical Vapor Deposition Growth of Vertically Aligned Single-Walled Carbon Nanotubes. *J. Phys. Chem. C* **2009,** *113* (18), 7511-7515.

50. Suguru, N.; Kei, H.; Hisashi, S.; Kazunori, K.; Zhengyi, Z.; Shigeo, M.; Yukio, Y., Millimeter-Thick Single-Walled Carbon Nanotube Forests: Hidden Role of Catalyst Support. *Jpn. J. Appl. Phys.* **2007,** *46* (5L), L399.

51. Hasegawa, K.; Noda, S., Real-Time Monitoring of Millimeter-Tall Vertically Aligned Single-Walled Carbon Nanotube Growth on Combinatorial Catalyst Library. *Jpn. J. Appl. Phys.* **2010,** *49* (8), 085104.

52. Yasuda, S.; Futaba, D. N.; Yamada, T.; Yumura, M.; Hata, K., Gas dwell time control for rapid and long lifetime growth of single-walled carbon nanotube forests. *Nano Lett.* **2011,** *11* (9), 3617-23.

53. Chen, G.; Davis, R. C.; Kimura, H.; Sakurai, S.; Yumura, M.; Futaba, D. N.; Hata, K., The relationship between the growth rate and the lifetime in carbon nanotube synthesis. *Nanoscale* **2015,** *7* (19), 8873-8878.

54. Anna, M.; Albert, G. N.; Esko, I. K., The role of metal nanoparticles in the catalytic production of single-walled carbon nanotubes—a review. *J. Phys. - Condens. Mat.* **2003,** *15* (42), S3011.

55. Nasibulin, A. G.; Moisala, A.; Brown, D. P.; Kauppinen, E. I., Carbon nanotubes and onions from carbon monoxide using Ni(acac)2 and Cu(acac)2 as catalyst precursors. *Carbon* **2003,** *41* (14), 2711-2724.

56. C. W. Bale, E. B., P. Chartrand, S. A. Decterov, G. Eriksson, K. Hack, I. H. Jung, Y. B. Kang, J. Melançon, A. D. Pelton, C. Robelin and S. Petersen, FactSage Thermochemical Software and Databases - Recent Developments. 2009; Vol. 33, pp 295-311.

57. Yamada, T.; Namai, T.; Hata, K.; Futaba, D. N.; Mizuno, K.; Fan, J.; Yudasaka, M.; Yumura, M.; Iijima, S., Size-selective growth of double-walled carbon nanotube forests from engineered iron catalysts. *Nat. Nanotechnol.* **2006,** *1* (2), 131-136.

58. Cho, W.; Schulz, M.; Shanov, V., Kinetics of Growing Centimeter Long Carbon Nanotube Arrays. In *Syntheses and Applications of Carbon Nanotubes and Their Composites*, 2013.

59. In, J. B.; Grigoropoulos, C. P.; Chernov, A. A.; Noy, A., Hidden role of trace gas impurities in chemical vapor deposition growth of vertically-aligned carbon nanotube arrays. *Appl. Phys. Lett.* **2011,** *98* (15), 153102.

60. Plata, D. L.; Meshot, E. R.; Reddy, C. M.; Hart, A. J.; Gschwend, P. M., Multiple Alkynes React with Ethylene To Enhance Carbon Nanotube Synthesis, Suggesting a Polymerization-like Formation Mechanism. *ACS Nano* **2010,** *4* (12), 7185-7192.

61. Nessim, G. D.; Seita, M.; Plata, D. L.; O'Brien, K. P.; John Hart, A.; Meshot, E. R.; Reddy, C. M.; Gschwend, P. M.; Thompson, C. V., Precursor gas chemistry determines the crystallinity of carbon nanotubes synthesized at low temperature. *Carbon* **2011,** *49* (3), 804-810.

Chapter 3 - High-Throughput Experimentation for Selective Growth of Small-Diameter Single-Wall Carbon Nanotubes using Ru-Promoted Co Catalysts

Chapter 3 is reprinted with permission from:

Everhart, B. M.; Rao, R.; Nikolaev, P.; Liu, T.-W.; Gómez-Gualdrón, D. A.; Maruyama, B.; Amama, P. B., High-Throughput Experimentation for Selective Growth of Small-Diameter Single-Wall Carbon Nanotubes Using Ru-Promoted Co Catalysts. *Chemistry of Materials* **2022,** *34* (10), 4548-4559.

3.1 Introduction

Owing to their high carrier mobility, semiconducting single-wall carbon nanotubes (SWCNTs) are well-suited as building blocks in a wide range of electronic applications from nanoscale transistors,[1-4] flexible electronics,[5-11] and chemical and biological sensors to clean energy harvesting and storage devices.[12-17] These applications require SWCNTs with band gaps larger than 1 eV. However, due to the inverse relationship between nanotube diameter and band gap, nominally semiconducting SWCNTs with large diameters feature small band gaps that in practice make them semi-metallic.[18] Indeed, based on theoretical calculations,[19] to obtain the desired larger than 1 eV band gap requires the SWCNT diameter to be less than 1 nm. The challenge is that SWCNT synthesis, using scalable methods such chemical vapor deposition (CVD) aided by conventional catalysts (Fe or Co supported on Al_2O_3), usually results in wide diameter distributions, with nanotubes ranging from 0.7 nm to 3 nm.[20, 21] Moreover, approaches such as the growth of self-supporting vertically aligned SWCNTs (i.e., SWCNT carpets or forests)

using conventional catalysts is particularly prone to producing SWCNTs that tend toward larger diameters. (> 1.5 nm).[22-25]

Although numerous post-processing techniques such as DNA wrapping,[26] density-gradient ultracentrifugation,[27] gel chromatography,[28] and aqueous two-phase extraction[29] have been proposed to effectively sort SWCNTs by diameter, these methods are low throughput and ultimately induce defects that degrade the nanotubes electronic properties. Therefore, to unleash the full potential of SWCNTs as components of electronic devices, a critical challenge that needs to be addressed is the development of reliable approaches for scalable selective synthesis of small-diameter, semiconducting SWCNTs (< 1 nm), as this would reduce the need for throughput-limiting postprocessing altogether.[30] The central strategy for reducing nanotube diameter during CVD synthesis is to minimize the catalyst particle size. The hypothesis that drives this strategy is the intimate relationship between the catalyst particle and SWCNT structure growing from it. For instance, molecular simulations modeling SWCNT growth make visually apparent the correlation between nanoparticle and nanotube diameter.[31] Furthermore, the correlation between size of the catalyst particle and SWCNT diameter is also supported by several experimental studies.[21, 32, 33]

One method of controlling catalyst size in general involves incorporating high-melting-point transition metals into the catalyst, either as a promoter or co-catalyst (bimetallic catalyst), to enhance catalyst stability by suppressing sintering. The efficacy of this strategy has been demonstrated in several heterogeneous catalytic reactions such as methane oxidation and Fischer Tropsch Synthesis (FTS).[34-41] Cui et al.[40] showed that a Mo promoter reduced sintering of Fe catalyst in FTS, resulting in high catalytic activity, while Cao et al.[34] found that the addition of Rh promoter enhanced the thermal stability of Pt nanoparticles. In other studies, the introduction of a Ru promoter has been demonstrated to reduce catalyst sintering in numerous catalytic processes.[35,

[37, 38, 41] The unique ability of high-melting-point transition metals to reduce catalyst sintering has been applied to CVD synthesis of small-diameter SWCNTs. The first work utilizing high-melting-point transition metal for growth of SWCNTs was the CoMoCAT process, which utilized Mo to reduce sintering of Co catalyst during gas-phase growth of SWCNTs via CO disproportionation.[33, 42] The CoMoCAT catalyst reduced the average SWCNT diameter by ~0.1 nm compared to SWCNTs produced from other well-established approaches such as the HiPCO process (0.81 nm vs. 0.93 nm). For alcohol CVD, Maruyama and coworkers demonstrated the use of the anchoring effect of Cu in Co-Cu bimetallic catalyst.[43] Despite successes in SWCNT synthesis, the wide parameter space of growth conditions has largely been unexplored to date. As a result, the complex relationship between catalyst promotion, type of feedstock, SWCNT diameter, and growth temperature is still poorly understood.

In light of the breadth of parameters that affect CVD growth, rapid experimentation is a powerful tool for investigating favorable conditions that promote selective growth of small-diameter SWCNTs. Here we utilize an Autonomous Research System (ARES)—an automated, high throughput, laser-induced CVD system with in situ Raman spectral feedback—to probe the combined role of Ru as a catalyst promoter and type of feedstock in the growth of small-diameter SWCNTs using conventional feedstocks (ethylene and acetylene) and a gaseous product mixture from Fischer-Tropsch synthesis (FTS-GP),[25, 44-46] our new feedstock that offers potential for scale-up. We demonstrate through over 200 growth experiments that the deposition of 0.1-nm-thick Ru on a Co catalyst film (1nm total thickness) nearly doubles the selectivity of SWCNTs with diameters below 1nm as determined by multi-excitation Raman spectroscopy. Furthermore, Ru stabilizes Co catalyst particles at elevated temperatures, increasing the selectivity of small-diameter SWCNTs by almost a factor of three at temperatures between 800°C and 850°C in

comparison to Co. A mechanistic understanding of the observed phenomenon has been developed with support from density functional theory (DFT), which attributes the reduced diameters to the increased cohesive energy of catalyst particles. Higher Ru amounts (20% and 100%) are also probed to develop a deeper understanding of the role of Ru in SWCNT growth. These findings clearly highlight the importance of Ru promotion of Co for small-diameter SWCNT growth, which opens the door for future applications requiring small diameter SWCNTs.

3.2 Experimental Section

3.2.1 Preparation of catalyst substrates

The substrates used for growth in ARES contain silicon micropillars fabricated by reactive ion etching. A substrate contains a 12×12 array of patches, each of which consists of a 5×5 array of 10-μm-diameter, 10-μm-high silicon pillars on an SiO_2 underlayer. The pillars were coated with an alumina layer (10 nm thick) by atomic layer deposition. Additional experiments were also performed using alumina deposited by ion beam sputtering (IBS/e) and the results are summarized in the Supporting Information. Substrates with the different catalysts (Co, Co-Ru and Ru) were deposited using IBS/e. For Co or Ru, a 1-nm-thick Co or Ru film was deposited on the alumina-coated layer, while for Co-Ru, a 0.9-nm-thick Co film was deposited followed by a 0.1-nm-thick Ru film (the thicknesses were adjusted accordingly for Co-Ru with 20 wt% Ru). A unique feature of ARES is that each pillar behaves as a microreactor and can be rapidly heated to the growth temperature within a fraction of a second due to the poor thermal conductivity of SiO_2 and the small thermal mass of the pillars. Further description of the ARES system is presented elsewhere.[47]

3.2.2 SWCNT growth in ARES

The ARES system (Figure 3.1) utilizes a high power (6 W, Verdi) laser (532 nm) that serves as the heat and Raman excitation sources. Each substrate contains several silicon micropillars (fabricated by reactive ion etching) that are thermally isolated by a silicon dioxide underlayer. During each growth experiment, a micropillar was heated to the growth temperature by regulating the laser power. The laser enables instantaneous heating of the micropillar and de-wetting of the catalyst film without requiring an annealing step. The temperature resolution is ±10-15 °C. Conventional carbon feedstocks (ethylene and 1% acetylene in helium) and our recently developed feedstock (FTS-GP) were used for this investigation. FTS-GP has the ability to support high growth rate and exceptionally long catalyst lifetime.[25, 44-46] Over the duration of an experiment, growth rate, yield, and temperature can be monitored via in-situ Raman spectroscopy using the same laser for heating. Raman spectra were acquired every 5 s and experiments were allowed to progress until SWCNT growth seemed to terminate, which was evidenced by a plateauing of the intensity of the SWCNT Raman peak (G band). The red shift of the Raman peak frequency was used to estimate the growth temperatures. When the growth appears to have terminated, the temperature can be reduced before moving to the next micropillar on the substrate. Raman spectra were collected before and after growth on each micropillar, enabling baseline subtraction for examination of radial breathing modes (RBMs), G-band, and D-band.

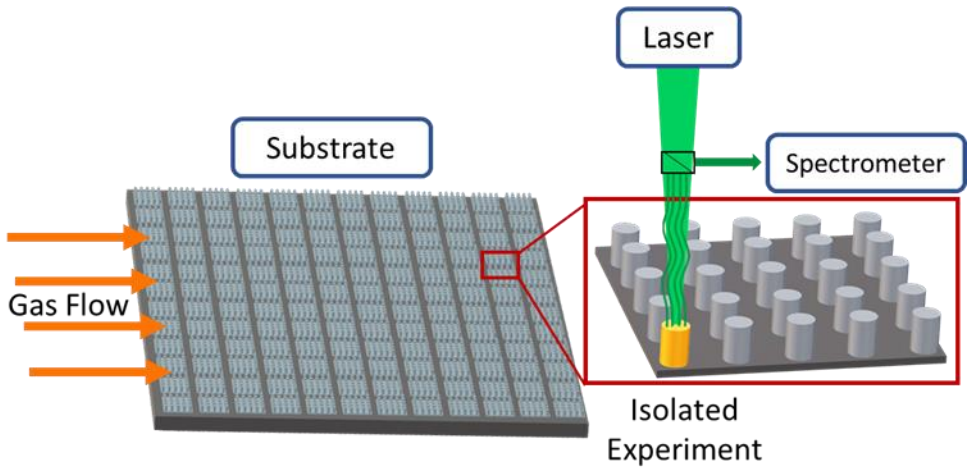

Figure 3.1. Schematic illustration of ARES, a high throughput laser-induced CVD system capable of in-situ Raman spectroscopy.

SWCNT growth is generally modeled by a self-exhausting exponential decay model (Equation 3.1) as the growth is characterized by a high growth rate at the beginning that subsequently diminishes until complete growth cessation occurs.[48] This model has been used in previous studies for the analysis of SWCNT growth kinetics in ARES.[47, 49-53] The model used is given as:

$$G(t) = v\tau\left(1 - e^{-\frac{t}{\tau}}\right) \tag{3.1}$$

where G represents area under the G-band at various times, t, while fitting parameters v and τ represent the initial growth rate and catalyst lifetime, respectively.

Ex-situ Raman characterization of growth products was performed with a Renishaw InVia Raman microscope with a 633 nm excitation source for all pillars. In addition, multi-excitation Raman characterization was performed on selected pillars using 514, 633, 785, and 1064 nm excitation lasers. These additional laser excitations allow the measurement of the majority of the chiralities grown by CVD. The ex-situ Raman spectra also allowed for improved analysis of the RBMs due to the smaller spot size when compared to those obtained in ARES (1 μm vs. 10 μm).

Each pillar was analyzed via a 10×10 array of spectra collected over the entire surface of the pillar. The 100 spectra collected were averaged and the resulting spectrum was analyzed, providing representative RBM data on the surface of each pillar. The combined use of Raman data collected from the 532 nm laser (ARES) and 633 nm laser (Renishaw) in our analysis increased our data integrity and reliability of our findings. The morphology and density of SWCNTs grown on the pillars were further characterized with a Hitachi S5200 field-emission scanning electron microscope (SEM) operated at 5 kV.

Statistical analysis was performed on the Raman data to demonstrate the difference in selectivity toward small-diameter SWCNTs for growth on Co and Co-Ru catalysts. Variables considered include excitation wavelength (532 nm vs. 633 nm excitation), catalyst type (Co vs. Co-Ru), and growth temperature range (650 – 699°C, 700 – 749°C, 750 – 799°C, and 800 –850°C). Weighted average RBM values were calculated by summing the products of the integrated peak area for each RBM and the peak location, and dividing by the sum of the peak areas. Error bars have been included to show standard deviation. The average selectivity towards small-diameter SWCNTS for each experiment performed at each temperature range was calculated for each catalyst and Raman excitation wavelength. The average selectivity values at Raman excitation wavelengths of 532 nm and 633 nm were subsequently averaged to be more representative of the small-diameter SWCNT selectivity at each temperature range for the respective catalysts. In total, over 300 unique data points were analyzed. Comparison of the selectivity of Co and Co-Ru was performed by averaging the previously calculated values across all temperature ranges. Analysis of SWCNT diameter selectivity for the different feedstocks was also calculated and included in the Supporting Information.

3.2.3 Computational analysis methods

Spin-polarized, plane-wave density functional theory (DFT) cluster optimizations were performed using the Vienna ab initio simulation package (VASP 5.4.1).[54-56] The plane wave basis set to construct the solution to the Kohn-Sham equations was built using an energy cutoff of 400 eV. Electronic and atomic structure were solved using an iterative procedure, with the electronic structure for a given geometry was considered solved when the energy difference for the electronic structures of two consecutive iterations was lower than 10^{-4} eV. The geometry was considered optimized once the energy difference for the geometries of two consecutive iterations is lower than 10^{-3} eV. The generalized-gradient approximation (GGA) functional, Perdew-Burke-Ernzerhof (PBE)[57] was used to model electron exchange and correlation. Dispersion forces were modeled explicitly using the D2 correction by Grimme.[58] The core electrons were modeled using the projected-augmented wave method (PAW).[59, 60] During the optimizations, 13-atom or 55-atom clusters were placed at the center of an orthorhombic 30 Å × 31 Å × 32 Å supercell, and calculations were made at the gamma point, with Gaussian smearing using a 0.03 smearing parameter.[61] The cluster sizes for this study were selected for their highly symmetric and stable structures, and diameter within the range of interest for the experimental work.[62]

3.3 Results

3.3.1 SWCNT growth in ARES using different feedstocks

Raman spectra collected in situ during SWCNT growth in ARES were used to probe the diameter distributions. The RBM regions, between 100 and 360 cm^{-1}, were deconvoluted with several peak components (Lorentzian) to obtain peak frequencies. Representative Raman spectra and peak fitting of the RBM peaks for SWCNTs grown on Co and Co-Ru are shown in Figure

B3.1. Figures 3.2a-c show the weighted average RBM values as a function of temperature for Co and Co-Ru using 532 nm and 633 nm laser excitations as well as the combined average of the two datasets.

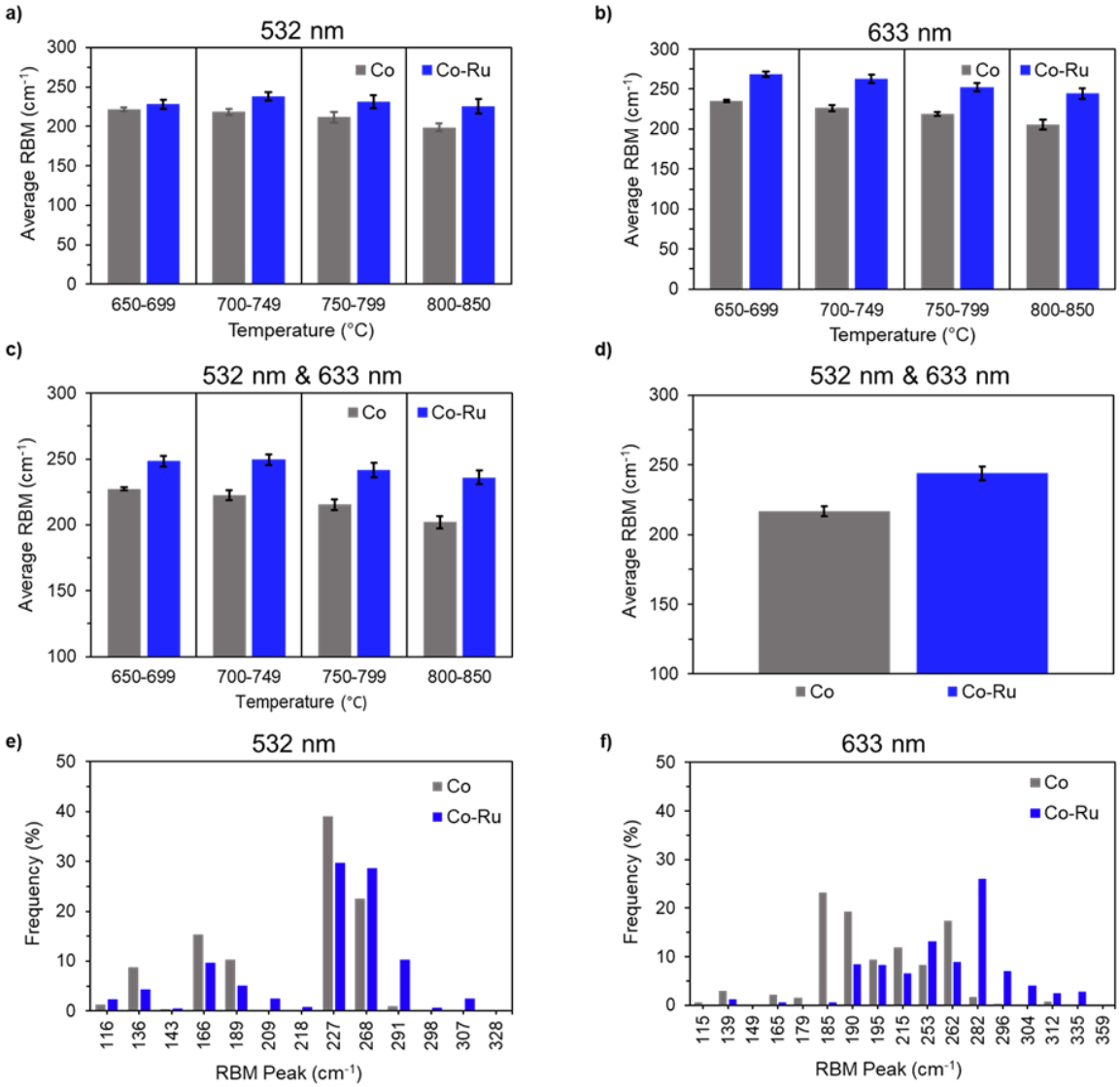

Figure 3.2. Weighted average RBM frequency data acquired with 532 nm (a) and 633 nm (b) laser excitations at different growth temperature. (c) Approximation of the true RBM frequency distribution in each temperature bracket by averaging data in (a) and (b). (d) Mean of weighted average RBM frequency data in (c) for Co and Co-Ru. Histograms of relative frequency of RBM peaks as a function of peak location for Co and Co-Ru using 532 nm (e) and 633 nm (f) laser excitations; the relative frequency is the percentage of each RBM peak area to the total RBM peak area.

Analysis of the Raman spectra acquired with 532 nm and 633 nm excitations (summarized in Figure 3.2) indicates growth on Co-Ru results in RBM peaks with significantly higher frequencies (corresponding to smaller SWCNT diameters) relative to growth on Co at all growth temperature ranges evaluated. While average RBM frequencies decrease with increasing temperature, Co-Ru is much less temperature dependent than Co (Figures 3.1a -c). The average RBM frequency for Co in the temperature range of 650-699 °C is 227 cm^{-1}, but decreases to 202 cm^{-1} at a higher temperature range (800-850 °C). On the other hand, growth on Co-Ru results in average RBM frequencies of 249 cm^{-1} and 236 cm^{-1} in the lowest and highest temperature ranges, respectively. Figure 3.2d shows the average RBM frequency for Co and Co-Ru obtained by averaging data in Figure 3.2c. Co-Ru exhibits a higher average RBM frequency (244 cm-1) than Co (217 cm^{-1}). Figures 3.2e and f show the average RBM components for all experiments performed on Co and Co-Ru using both laser excitations. It is clear from the histograms that spectra associated with Co-Ru have much higher relative frequency of RBM peaks corresponding to small SWCNT diameters, including a significant increase in RBMs > 290 cm^{-1}, which are almost non-existent for growth on Co. It should be noted that these RBM peak positions fluctuate +/- 3 cm^{-1} from spectra to spectra and likely represent several RBMs each. Additional analysis of RBM frequencies, including their analysis as a function of growth temperature and type of feedstock is summarized in Figures B3.2-4.

It has been well established that RBM frequencies of SWCNTs are diameter dependent.[63-72] The following equation can be used to approximate SWCNT diameters from RBM peaks:

$$\omega_{RBM} = \frac{C_1}{d} + C_2 \qquad (3.2)$$

where C_1 and C_2 are constants. Based on SEM evidence of the formation small tube bundles in our work, SWCNT diameters were calculated using $C_1 = 234$ and $C_2 = 10$.[66, 69] Detailed analysis of Equation 3.2 is included in the Supporting Information including the effects of SWCNT diameter, bundling interactions, and bundle size on appropriate C_2 values.

Selectivity of the catalysts toward growth of small-diameter SWCNTs was calculated from the fraction of the integrated intensities of all peak components below a diameter of 1 nm to the total integrated intensity of all fitted peak components in the RBM region between 100 and 360 cm^{-1} (Equation 3.3):

$$Selectivity = \frac{\text{Integrated area of RBM peaks corresponding to} < 1\text{nm}}{\text{Total integrated area of all RBM peaks}} \qquad (3.3)$$

Representative SEM images of SWCNT bundles grown on pillars coated with Co and Co-Ru catalysts using ethylene as a feedstock reveal uniform growth across the entire catalyst surface with a higher density of SWCNTs grown on pillars coated with Co catalyst (Figure 3.3a) than pillars with Co-Ru catalyst (Figure 3.3b).

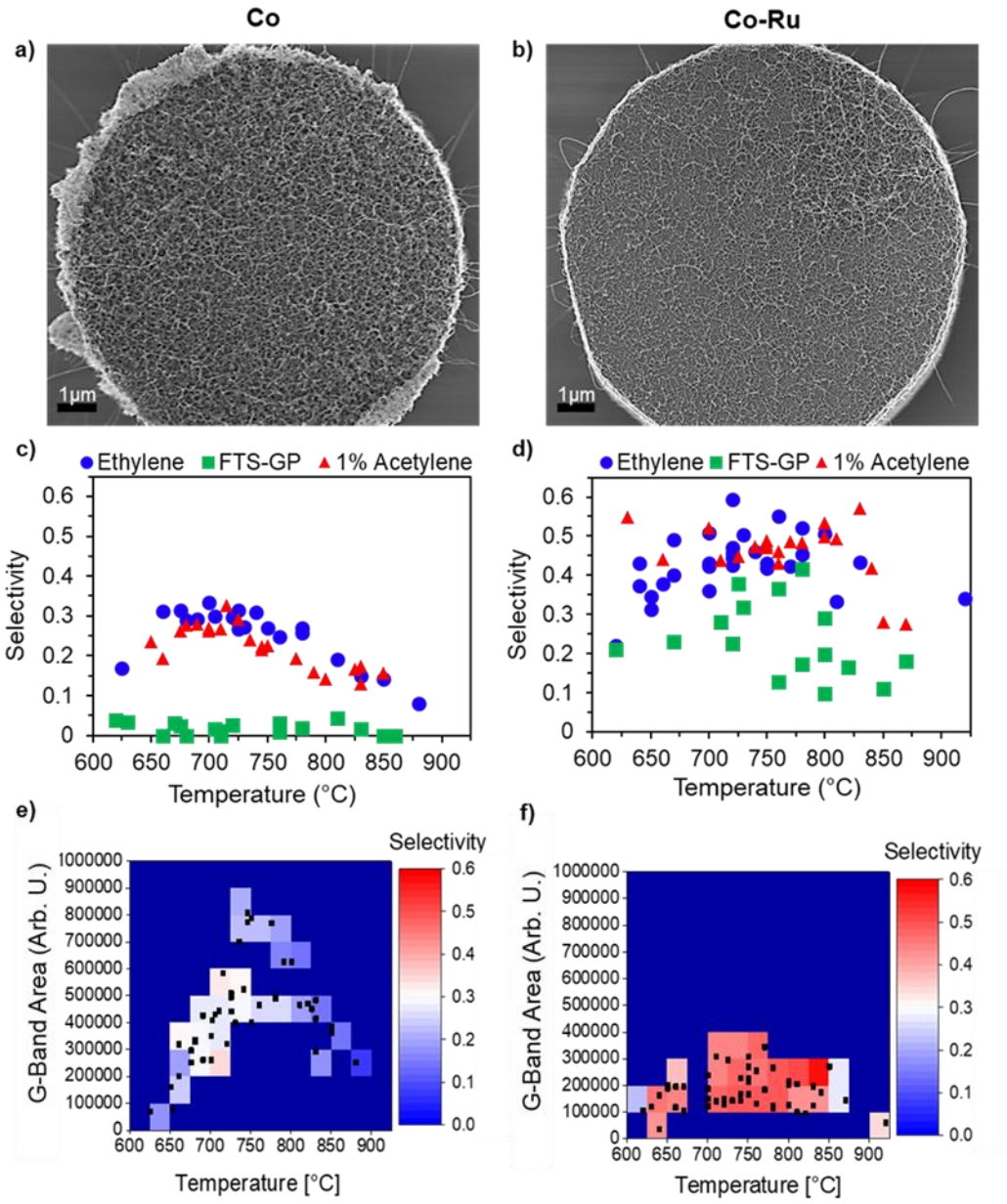

Figure 3.3. SEM images showing density of SWCNTs grown on Co (a) and Co-Ru (b) catalysts. Plots of selectivity toward small-diameter SWCNTs as a function of growth temperature using different feedstocks on Co (c) and Co-Ru (d) catalysts (calculated from Raman spectra acquired with 532 nm laser excitation). Heat/contour plots illustrating selectivity (in c and d) and G-band area (proxy for abundance of SWCNT growth) versus growth temperature for Co (e) and Co-Ru (f) catalysts using growth results for ethylene and acetylene.

Figure 3.3 (c-d) shows calculated selectivity toward small-diameter SWCNTs grown on Co and Co-Ru as a function of growth temperature for the different feedstocks (ethylene, FTS-GP, and acetylene) obtained using an excitation wavelength of 532 nm; the selectivity calculated from spectra obtained with 633 nm laser excitation are shown in Figure B3.5. SWCNTs grown on Co catalyst using ethylene or acetylene as a feedstock exhibited a maximum selectivity of 0.35 at ~700°C, whereas growth on the same catalyst using FTS-GP showed substantially lower selectivity (≤ 0.05) at all temperatures. On the other hand, SWCNTs grown on Co-Ru reached a maximum selectivity of 0.6 for ethylene, 0.57 for acetylene, and 0.42 for FTS-GP. It is evident from these results there is improved selectivity toward growth of small-diameter SWCNTs on Co-Ru catalyst even with FTS-GP as the feedstock. A clear trend of the scatterplots emerges for pure Co (using either acetylene or ethylene) with selectivity initially increasing with growth temperature from 600°C and peaking around 725°C and then decreasing with further increase in temperature. Using Ru as a catalyst promoter resulted in scattered selectivity data at the different temperatures; unlike acetylene, the trend that emerges for ethylene and FTS-GP is somewhat similar to that observed when Co catalyst is used. The spread in the data when Ru is present may be attributed to several factors including reduced density of tube nucleation and non-uniformity in the distribution of Ru in individual catalyst nanoparticles. The latter may lead to a slightly wider distribution of catalyst sizes that are comparatively smaller in size than those formed on Co. It is clear from these results that selectivity towards small-diameter SWCNTs decreases in the following order: ethylene > acetylene > FTS-GP. The effects of different values of C_1 and C_2 on the selectivity are summarized in Figure B3.6. Further analysis of selectivity using ethylene and acetylene (Figure B3.7) shows the higher small-diameter selectivity of ethylene over acetylene and Co-Ru over Co.

To compare the catalyst activity (in terms of SWCNT yield) and SWCNT diameter selectivity of Co and Co-Ru catalysts, heat plots showing selectivity to small-diameter SWCNTs (adapted from Figure 3.3 (c) and (d)) and SWCNT yield (or density) as functions of growth temperature as shown in Figure 3.3e and f. The analysis focuses on experiments utilizing ethylene and acetylene as feedstocks due to their overall high selectivity toward small-diameter SWCNTs. The integrated intensity of the G-band from the Raman spectrum collected at the end of each growth is used as a proxy for the yield of SWCNTs deposited on the catalyst-coated pillars. The SWCNT yield obtained from the G-band signal in ARES was verified by SEM and is consistent with previous studies.[44, 49, 50] The SWCNT structures were not characterized by TEM due to the challenge associated with removing SWCNTs from individual micropillars without destroying the pillars and contaminating the SWCNT samples. Growth conditions favorable for high yield of small-diameter SWCNTs can be discerned from the heat plots. Growth on Co catalyst yielded SWCNTs with a maximum G-band area of ~8.0×10^5, but with a selectivity ~0.2; whereas growth on Co-Ru resulted in a lower maximum G-band area of ~3.5×10^5, but with a much higher selectivity ~0.4. The maximum yield on Co catalyst occurs at temperatures between 725 and 775°C, which is higher than the temperature range that supports the highest selectivity toward small-diameter SWCNTs (675 – 725°C, Figure 3.3c). In contrast, for Co-Ru catalyst, both SWCNT yield and selectivity were maximized at a temperature range of 725 – 775°C. We note that the maximum selectivity achieved for growth on Co-Ru is nearly twice that achieved on Co alone, whereas SWCNT yield on Co was two times higher than that on Co-Ru catalyst; this increased selectivity supports the hypothesis that the presence of Ru increases sintering resistance of catalysts and decreases the formation of large particles, and thus the yield of large-diameter SWCNTs. We conclude that using ethylene or acetylene as a feedstock under a temperature range

of 700-750°C favors the growth of small-diameter SWCNTs with Co-Ru being more selective and Co more active in terms of SWCNT yield.

To further understand the effect of Ru on catalytic activity during SWCNT growth, we fitted the growth curves at different growth temperatures for the various feedstock-catalyst combinations (Figures 3.4 a-d) to Equation 1: (a) ethylene and Co, (b) ethylene and Co-Ru, (c) acetylene and Co, and (d) acetylene and Co-Ru. The goodness of fit (R^2) for the analysis involving data from 20 experiments had an average value of 0.98. Figures 3.4e and f along with the average values of the fitting parameters (v and τ), summarized in Table B3.1, suggest that the presence of Ru increases the growth rate of SWCNTs, but with a decreased catalyst lifetime. Conversely, for pure Co a longer catalyst lifetime and lower growth rate are observed. The optimum temperature whereby catalyst lifetime and growth rate are maximized for both Co and Co-Ru is ~750°C.

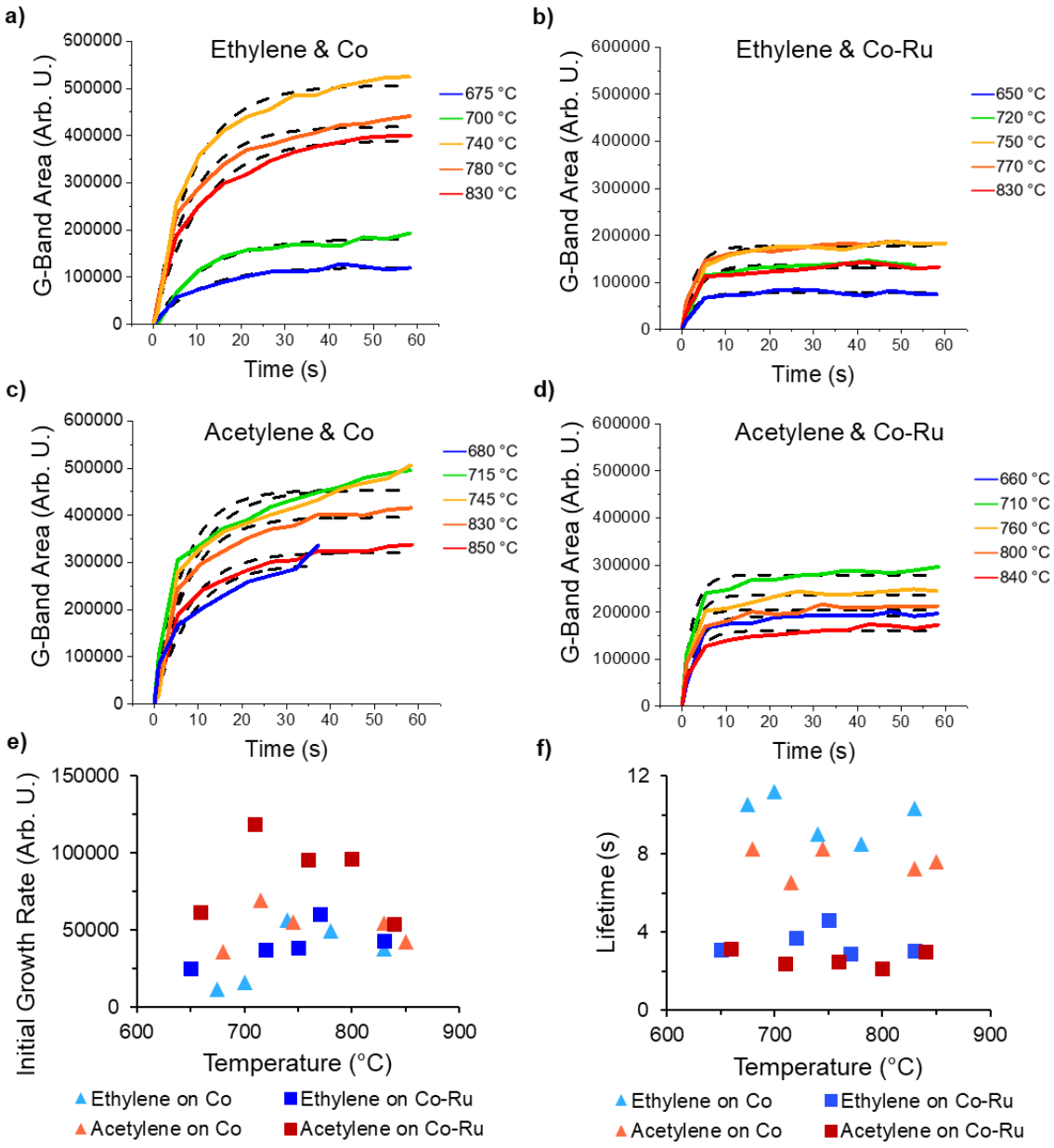

Figure 3.4. Plots of SWCNT yield as a function of growth time using different feedstock-catalyst combinations: (a) ethylene and Co, (b) ethylene and Co-Ru, (c) acetylene and Co, and (d) acetylene and Co-Ru. The solid lines represent curve fitting of the radioactive decay model (Equation 1). Scatter plots of initial growth rate (e) and catalyst lifetime (f), obtained by fitting plots a-d to Equation 1, as a function of growth temperature.

3.3.2 Multi-excitation Raman spectroscopic characterization of SWCNTs grown with ethylene

Due to the high selectivity towards small-diameter SWCNTs shown by ethylene, it was used in subsequent experiments to probe the diameter distributions of SWCNTs grown on Co and Co-Ru. SWCNT samples obtained using ethylene as a feedstock were further characterized ex situ by multi-excitation Raman spectroscopy (Figure 3.5). Green shades are added to the spectra to indicate the RBM frequencies corresponding to small diameter (< 1nm) SWCNTs. Figures 3.5a and 5b highlight the difference in RBM frequencies and intensities for SWCNTs grown on Co and Co-Ru with ethylene precursor. Interestingly, for each pair of SWCNT spectra on Co and Co-Ru acquired with the same excitation energy, there is an increase in the number of RBM peaks observed at higher frequencies for SWCNTs grown on Co-Ru catalyst. In addition, RBM peaks with the same frequency in the shaded region with diameters < 1 nm for the same excitation wavelength are characterized by different intensities, with SWCNTs grown on Co-Ru exhibiting a higher intensity. For instance, in Figure 3.5a, there is a weak intensity peak at ~300 cm^{-1} in the spectrum collected with 785 nm excitation, however in Figure 3.5b, the peak becomes prominent—an observation that occurs simultaneously with the disappearance of the peak at ~150 cm^{-1}. In the spectra acquired with the 633 nm laser, there is substantial increase in the intensities of peaks at ~255 cm^{-1} and ~285 cm^{-1}, relative to the peaks below 250 cm^{-1}. A similar trend is observed for spectra acquired with the 514 nm laser. Although there were no observable RBMs below 250 cm^{-1} for spectra acquired with the 1064 nm laser, peaks that appear above 300 cm^{-1} exhibit substantial increase in intensity. Multi-excitation Raman spectra for growth experiments using acetylene are shown in Figure B3.8. Ru appears to increase the selectivity of small-diameter SWCNTs by decreasing the relative amount of large-diameter SWCNTs and increasing the relative

amount of small-diameter SWCNTs, evidenced by the reduced intensities of RBM peaks associated with large-diameter SWCNTs and increased intensities of those associated with small-diameter SWCNTs (Figures 3.5 and B3.8).

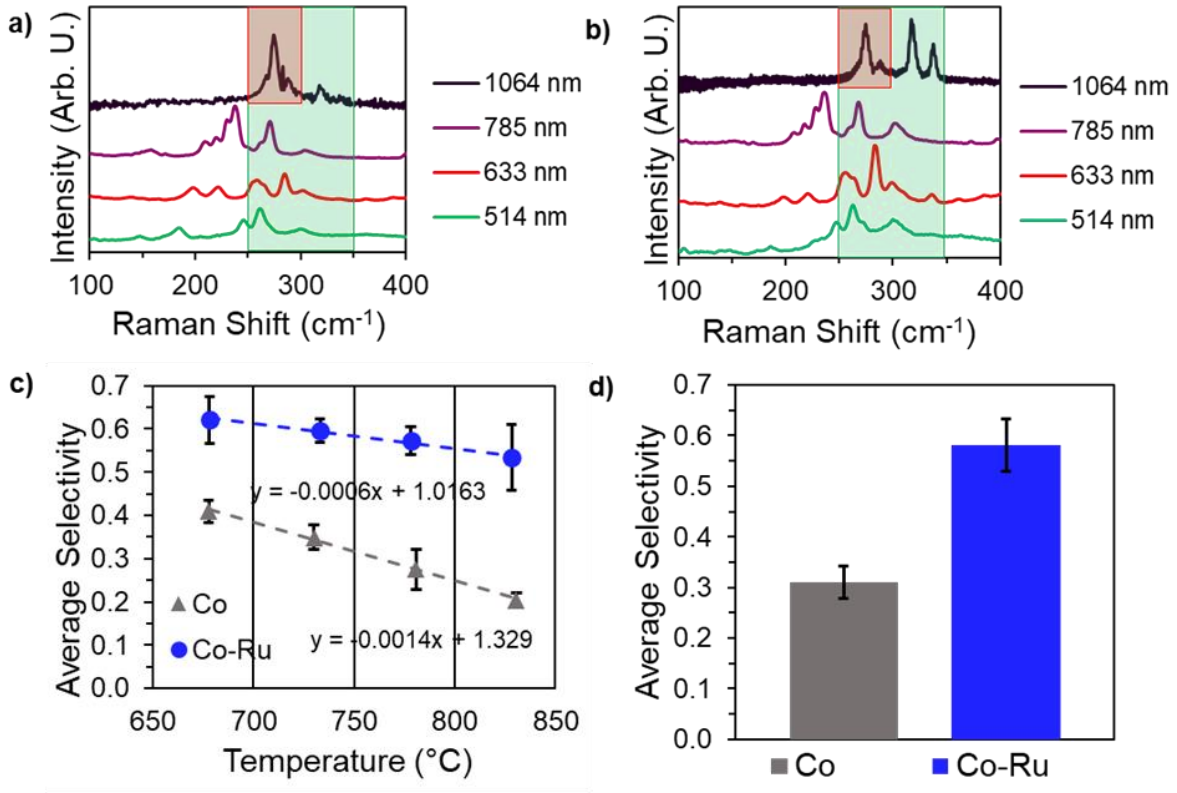

Figure 3.5. Multi-excitation Raman spectra of SWCNTs grown on Co (a) and Co-Ru (b) catalysts; green shade highlights the small-diameter region (<1 nm). (c) Plots of selectivity averages for small-diameter SWCNTs on Co and Co-Ru catalysts. Data used for analysis were acquired with 532 nm and 633 nm laser excitations over four temperature ranges (650-699 °C, 700-749 °C, 750-799 °C, 800-849°C). (d) Histogram of average selectivity across temperature ranges for Co and Co-Ru catalysts. Error bars show standard deviations for the calculated average values.

The plots in Figure 3.5 (c) clearly show the difference in selectivity toward small SWCNT diameters for Co and Co-Ru catalysts as a function of growth temperature, calculated by averaging selectivity data from Raman spectra acquired with 532 nm and 633 nm laser excitations. The separated statistical analysis and trends for data obtained using the two laser excitations are shown in Figure B3.9. An important takeaway from the analysis is not only that the Co-Ru catalyst leads

to higher selectivity for small-diameter SWCNTs at all growth temperatures investigated, but it is also less dependent on temperature. In fact, Co-Ru catalyst experiences minimal decrease in selectivity even in the highest temperature range (800 - 850°C). In contrast, Co catalyst experiences substantial drop-off in selectivity as temperature increases. The average selectivity values combined over all the growth temperatures are plotted in Figure 3.5 (d) and show that Ru as a catalyst promoter nearly doubles the selectivity of small-diameter SWCNTs. Our previous work revealed that catalyst activity during SWCNT growth is sensitive to the porosity or type of alumina (based on the deposition technique).[73] To understand the effect of alumina substrate porosity on catalyst behavior, we conducted additional experiments using Co and Co-Fe catalysts supported on IBS/e-deposited alumina films (with higher porosity) of the same thickness (10 nm) and the results (summarized in Figures B3.11-14) are consistent with those discussed so far for catalysts supported on ALD-deposited alumina films.

3.3.3 DFT calculations

To understand the promotion role of Ru in increasing selectivity toward growth of small-diameter SWCNTs, we investigated the stability of Co and bimetallic Co_XRu_Y clusters using DFT calculations. These calculations focused on 13- and 55-atom clusters due to the high stability and symmetry of their structures, with sizes relevant to our experiments ((less than 1 nm). The Ru content of these clusters is similar to those used in the ARES experiments (which is 10%), with content ranging between 8% and 11% from the 13- and 55-atom cases, respectively ($Co_{12}Ru$ and $Co_{49}Ru_6$). However, to elucidate trends, calculations on pure Co clusters (Co_{13} and Co_{55}), as well as on clusters with higher Ru content ($Co_{43}Ru_{12}$) were also performed. To obtain the cohesive energy, E_C, we used:

$$E_C = \frac{E_{cluster} - N_{Co}E_{Co} - N_{Ru}E_{Ru}}{N_{Co} + N_{Ru}} \quad (3)$$

The set of calculations on the 13-atom clusters are shown in Figure 3.6a, which shows the strengthening of cluster cohesive energy upon the addition of Ru. Specifically, the cohesive energy of the $Co_{12}Ru$ (8% Ru content) is 0.1 eV stronger than for Co_{13} (-3.4 eV for $Co_{12}Ru$ vs -3.3 eV for Co_{13}), which is expected to engender an increase in melting temperature and a reduction in atom mobility. While the stability of the $Co_{12}Ru$ cluster is slightly sensitive to the positioning of the Ru atom in the cluster, notice that the abovementioned strengthening of the cohesive energy occurs irrespective of whether the Ru atom is on the surface of the cluster ($Co_{12}Ru|_A$) or in the bulk ($Co_{12}Ru|_B$).

The set of calculations on the 55-atom clusters is shown in Figure 3.6b, which also shows the strengthening of cluster cohesive energy upon the addition of Ru. Specifically, the cohesive energy of $Co_{49}Ru_6$ (roughly 11% Ru) is around 0.2 eV stronger than for Co_{55}. Similar to the 13-atom cluster case, the stability of the 55-atom cluster is slightly sensitive to the exact arrangement of Ru atoms within the cluster. Yet, upon evaluation of six different configurations, the strengthening of the cohesive energy was similar, suggesting the robustness of the effect. To further confirm the trend of cohesive energy strengthening with Ru addition, we optimized a $Co_{43}Ru_{12}$ cluster (~22% Ru content). The cohesive energy was found to strengthen a further 0.2 eV upon the addition of six more Ru atoms.

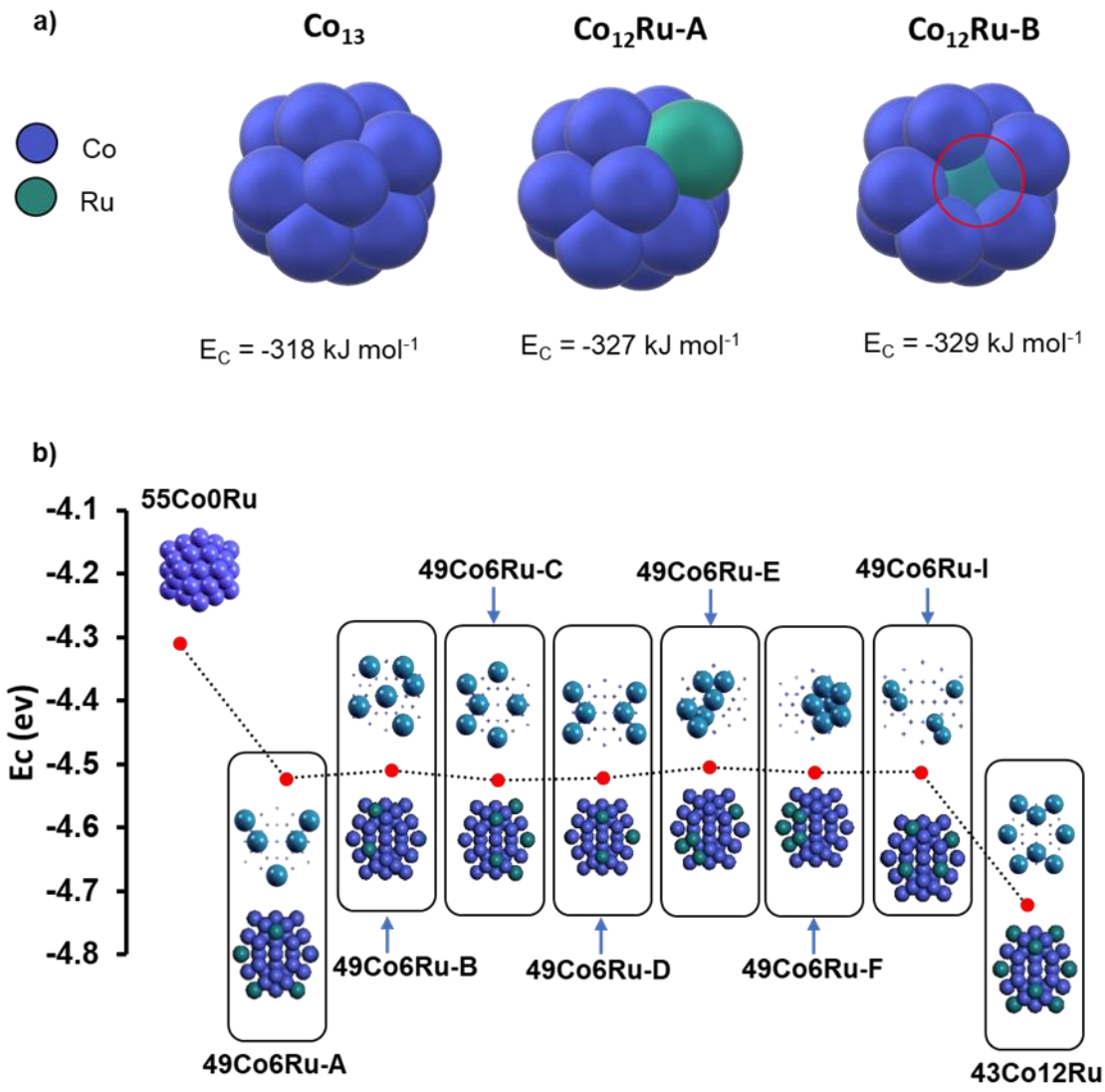

Figure 3.6. (a) DFT optimization and calculation of cohesive energy, E_C, for13- and 55-atom clusters of Co and Co-Ru. a) Co13, Co12Ru (A) with adsorbed Ru atom, and Co12Ru (B) with Ru atom in the bulk region of the cluster. (b) Co55, Co49Ru6 (A-F), Co43Ru12, which contain 0, 6, and 12 Ru atoms, respectively. Configurations A through I were generated randomly and represent different arrangement scenarios for Ru on the cluster surface. Notably A represents the arrangement with the Ru atoms most separated from each other, D represents the arrangement with most symmetric Ru atom placement, and F represents the most segregated arrangement (notice all Ru atoms clustering together).

Based on the above calculations, it appears Ru addition consistently increases the cohesive energy of the cluster—at least within the ranges experimentally tested—and that strengthening occurs by about the same magnitude regardless of the exact Ru distribution within the cluster. The

results from these calculations are thus supportive of an increase in melting point and reduction in atom mobility, which should increase the resistance to catalyst sintering. We hypothesize the latter results in enhanced stability of small nanoparticles, which leads to higher selectivity of small-diameter SWCNTs.

3.3.4 SWCNT growth in ARES using pure Ru or Co-Ru with a higher Ru amount

To develop a deeper understanding of the catalytic properties of Ru, we conducted further experiments with pure Ru as a catalyst and a higher amount of Ru in Co-Ru catalysts and the results are summarized in Figure 3.7. We note that growth on pillars with a 1-nm-thick catalyst containing 20% Ru under conditions identical to those used for Co and Co-Ru (10% Ru) did not appear to yield SWCNTs, due to the absence of RBMs in their Raman spectra (Figure 3.7a). The results are likely related to the catalytic activity of the particles and not their stability, suggesting there might be an optimal amount of Ru in Co catalyst that supports good SWCNT growth, above which SWCNT growth might be inhibited. It is also possible SWCNT growth did not occur on Co-Ru (20% Ru) because the standard conditions used were optimum for pure Co and Co-Ru (10% Ru), not Co-Ru with higher Ru amount (20% Ru). To test this conjecture, we implemented the 'supergrowth' approach,[48, 74] well known for dramatically enhancing catalyst activity and lifetime[73, 75, 76] during CVD growth. Interestingly, upon introduction of ~11ppm H_2O, Co-Ru (20% Ru) that was inactive for SWCNT growth under standard conditions as shown in Figure 3.7a, exhibited exceptional SWCNT growth (Figure 3.7b); however, the selectivity towards small-diameter SWCNTs was comparable to that observed with Co catalyst.

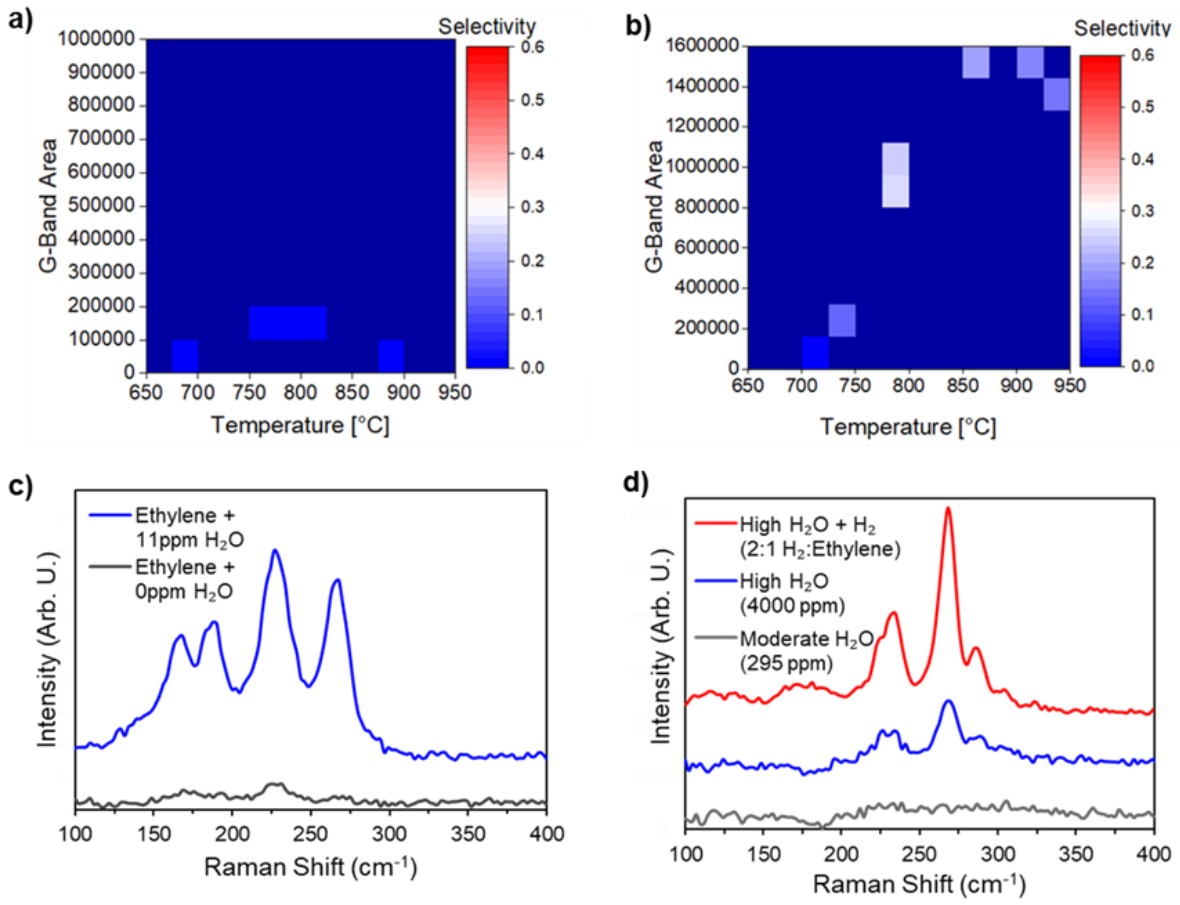

Figure 3.7. Heat plots of G-band intensity and small diameter SWCNT selectivity of growth experiments performed on a Co-Ru catalyst (20% Ru) with ethylene and the addition of 0 ppm (a) and 11ppm H_2O (b). (c) Representative Raman spectra of SWCNTs grown on pure Ru catalyst with ethylene in the absence and presence of water (11 ppm). (d) Representative Raman spectra of SWCNTs grown on pure Ru catalysts under conditions that maximize small-diameter SWCNT selectivity.

For comparison, we also conducted growth on pure Ru and the results are presented in Figures 3.7c and d. Little to no growth was observed even at a moderate water concentration (295 ppm). At extremely high-water concentrations (4000 ppm), growth of small-diameter SWCNTs occurred, although the total yield was extremely low (integrated G-band area < 7.0×10^4). Further optimization revealed that introducing a hydrogen-to-ethylene ratio of 2:1 yielded small-diameter SWCNTs at ratios comparable to that obtained on Co-Ru (10% Ru). It should be noted, however,

that growth on pure Ru required higher temperatures (900 - 950°C). Our results indicate that a high-melting-point metal like Ru in its pure form or as a promoter can generate small-diameter SWCNTs under optimum temperature and feedstock conditions.

3.4 Discussion

The Co-Ru catalyst nanoparticles formed by annealing the deposited films (a Ru layer on top of a Co layer) show higher selectivity toward small-diameter SWCNTs. Based on the DFT results, we hypothesize the presence of Ru in Co catalysts stabilizes small catalyst nanoparticles or suppresses sintering, resulting in a higher number density of small catalyst nanoparticles and a lower average catalyst size. To understand the role of Ru in catalyst evolution, similar as-deposited and annealed Co (1 nm) and Co-Ru (0.9 nm Co, 0.1 nm Ru) films on silicon substrates with alumina underlayers were studied; annealing was performed at 850°C in Ar/H_2 for 3, 10, and 30 min using a conventional CVD. AFM topographic profiles of the catalysts (Figure B3.10) reveal the average RMS roughness (proxy for feature height)[77, 78] formed on Co-Ru is slightly lower than that of Co. The Co-Ru nanoparticles with smaller sizes nucleate SWCNTs with a much higher selectivity toward small-diameters and exhibit diminished overall SWCNT yield in comparison to pure Co. Even though FTS-GP exhibits relatively lower selectivity towards small-diameter SWCNTs, the promotion of Co with Ru leads to growth of small-diameter SWCNTs, affirming the key role Ru plays in the nucleation of small-diameter SWCNTs. We speculate the low yield observed for growth with FTS-GP on Co catalyst may be due to a number of reasons including on-site generation of water[25, 44] and the high-volume fraction of methane in FTS-GP. The water generated in situ via a reaction between H_2 and CO may etch some small-diameter SWCNTs during nucleation or growth.[79-82] Gas phase reactions in ARES are extremely low or nonexistent

because it relies on heating from the laser. We therefore expect the utilization of methane, a stable hydrocarbon and a major component (30 vol%) of FTS-GP, to be poor, thus limiting the carbon flux to the catalyst and contributing to growth inhibition. In consistent with this observation, we observed lower growth rate with FTS-GP in ARES.[44] When Ru is added to Co as a promoter, nucleation of small-diameter SWCNTs occurs with FTS-GP as a feedstock, despite the oxidizing environment that is created by water generation, for two reasons: (1) There is an increased number of small nanoparticles available for nucleation; and (2) Ru acts as an electron donor, which may protect SWCNTs from oxidation during nucleation.

The high variability observed in selectivity of small-diameter SWCNTs for Co-Ru may be due to the resulting catalyst nanoparticles not having equal amounts of Ru. It is unlikely the intended one-atom thick layer of Ru obtained via ion beam sputtering was uniform across the entire substrate. Possible clustering of Ru during deposition is expected to yield Co-Ru particles with slightly different Ru amounts in the nanoparticles after dewetting and particle formation, a phenomenon that has also been observed in Mo-on-Fe type catalysts.[83] The nonuniform amounts of Ru in the resulting Co-Ru catalyst particles may cause a variation in their catalytic activity, possibly due to the difference in their carbon solubility. Based on the DFT calculations, AFM characterization of annealed catalyst films, and growth in ARES, a mechanistic understanding of the role of Ru as a promoter of Co catalyst for SWCNT growth begins to take shape. As discussed earlier, DFT calculations indicate the inclusion of Ru atoms in a Co cluster increases cohesive energy, suggesting that smaller catalyst particles may be more resistant to sintering on a support. AFM analysis of annealed catalyst films reveals dewetted catalyst particles are smaller in the case of Co-Ru compared to pure Co, even at shorter time scales (3 min). The results support the idea that Ru stabilizes Co nanoparticles, resulting in growth of small-diameter SWCNTs. In general,

catalyst sintering is strongly dependent on temperature. Interestingly SWCNT size in the case of the Co-Ru catalyst is much less dependent on temperature as opposed to SWCNTs grown on pure Co. Our results indicate that the high melting point of Ru may be responsible for the increased cohesive energy and subsequent catalyst stability observed under SWCNT growth conditions.

3.5 Conclusions

In this work, rapid experimentation was used to probe favorable conditions that promote selective growth of small-diameter SWCNTs via catalytic CVD. To minimize Co catalyst size and enhance resistance to sintering, a high-melting-point metal (Ru) was used as a promoter of Co catalyst. The addition of 10% Ru to a 1-nm thick Co (Co-Ru) catalyst increases the selectivity of small-diameter SWCNTs, as calculated from Raman spectra collected using 532-nm and 633-nm laser excitations. In addition, Ru appears to stabilize catalyst particle size at elevated temperatures, as selectivity towards small-diameter SWCNTs is less temperature dependent for growth on Co-Ru compared to Co. The results are supported by AFM data on annealed catalyst films, which show slightly lower catalyst particle height on Co-Ru compared to Co for time-scales representative of SWCNT growth in ARES. The reduction in catalyst particle sintering has been attributed to an increase in cohesive energy in Co particles when Ru atoms are included in the cluster, as calculated by DFT for 13-atom and 55-atom clusters. Growth on Co-Ru resulted in lower overall SWCNT nucleation density compared to Co, whereas growth rates on Co-Ru were higher than growth on Co, with lifetimes roughly three times shorter than those for growth on Co. Furthermore, our results reveal that pure Ru or Co-Ru with a higher Ru amount can support growth of small-diameter SWCNTs under optimum temperature and water concentration. The study reveals important relationships between catalyst promotion using Ru, type of feedstock, SWCNT

diameter, and growth temperature. These findings highlight the role of Ru as a promoter of Co and as a catalyst in the growth of small-diameter SWCNTs, which opens the door for future applications requiring small-diameter SWCNTs.

3.6 References

1. Franklin, A. D.; Luisier, M.; Han, S.-J.; Tulevski, G.; Breslin, C. M.; Gignac, L.; Lundstrom, M. S.; Haensch, W., Sub-10 nm Carbon Nanotube Transistor. *Nano Lett.* **2012,** *12* (2), 758-762.

2. Qiu, C.; Zhang, Z.; Xiao, M.; Yang, Y.; Zhong, D.; Peng, L.-M., Scaling carbon nanotube complementary transistors to 5-nm gate lengths. *Science* **2017,** *355* (6322), 271.

3. Yan, H.; Choe, H. S.; Nam, S.; Hu, Y.; Das, S.; Klemic, J. F.; Ellenbogen, J. C.; Lieber, C. M., Programmable nanowire circuits for nanoprocessors. *Nature* **2011,** *470* (7333), 240-244.

4. Zhang, L.; Zaric, S.; Tu, X.; Wang, X.; Zhao, W.; Dai, H., Assessment of Chemically Separated Carbon Nanotubes for Nanoelectronics. *J. Am. Chem. Soc.* **2008,** *130* (8), 2686-2691.

5. Miyata, Y.; Shiozawa, K.; Asada, Y.; Ohno, Y.; Kitaura, R.; Mizutani, T.; Shinohara, H., Length-sorted semiconducting carbon nanotubes for high-mobility thin film transistors. *Nano Res.* **2011,** *4* (10), 963-970.

6. Cao, Q.; Kim, H.-s.; Pimparkar, N.; Kulkarni, J. P.; Wang, C.; Shim, M.; Roy, K.; Alam, M. A.; Rogers, J. A., Medium-scale carbon nanotube thin-film integrated circuits on flexible plastic substrates. *Nature* **2008,** *454* (7203), 495-500.

7. Park, S.; Vosguerichian, M.; Bao, Z., A review of fabrication and applications of carbon nanotube film-based flexible electronics. *Nanoscale* **2013,** *5* (5), 1727-1752.

8. Lefebvre, J.; Ding, J.; Li, Z.; Finnie, P.; Lopinski, G.; Malenfant, P. R. L., High-Purity Semiconducting Single-Walled Carbon Nanotubes: A Key Enabling Material in Emerging Electronics. *Acc. Chem. Res.* **2017,** *50* (10), 2479-2486.

9. Jiang, S.; Hou, P.-X.; Chen, M.-L.; Wang, B.-W.; Sun, D.-M.; Tang, D.-M.; Jin, Q.; Guo, Q.-X.; Zhang, D.-D.; Du, J.-H.; Tai, K.-P.; Tan, J.; Kauppinen, E. I.; Liu, C.; Cheng, H.-M., Ultrahigh-performance transparent conductive films of carbon-welded isolated single-wall carbon nanotubes. *Sci. Adv.* **2018,** *4* (5), eaap9264.

10. Asada, Y.; Nihey, F.; Ohmori, S.; Shinohara, H.; Saito, T., Diameter-Dependent Performance of Single-Walled Carbon Nanotube Thin-Film Transistors. *Adv. Mater.* **2011,** *23* (40), 4631-4635.

11. Cao, Q.; Han, S.-j.; Tulevski, G. S.; Zhu, Y.; Lu, D. D.; Haensch, W., Arrays of single-walled carbon nanotubes with full surface coverage for high-performance electronics. *Nat. Nanotechnol.* **2013,** *8* (3), 180-186.

12. Landi, B. J.; Ganter, M. J.; Cress, C. D.; DiLeo, R. A.; Raffaelle, R. P., Carbon nanotubes for lithium ion batteries. *Energy Environ. Sci.* **2009,** *2* (6), 638-654.

13. Kaempgen, M.; Chan, C. K.; Ma, J.; Cui, Y.; Gruner, G., Printable Thin Film Supercapacitors Using Single-Walled Carbon Nanotubes. *Nano Lett.* **2009,** *9* (5), 1872-1876.

14. Kim, B.; Chung, H.; Kim, W., High-performance supercapacitors based on vertically aligned carbon nanotubes and nonaqueous electrolytes. *Nanotechnology* **2012,** *23* (15), 155401.

15. Li, M.; Carter, R.; Douglas, A.; Oakes, L.; Pint, C. L., Sulfur Vapor-Infiltrated 3D Carbon Nanotube Foam for Binder-Free High Areal Capacity Lithium–Sulfur Battery Composite Cathodes. *ACS Nano* **2017,** *11* (5), 4877-4884.

16. Blackburn, J. L., Semiconducting Single-Walled Carbon Nanotubes in Solar Energy Harvesting. *ACS Energy Lett.* **2017,** *2* (7), 1598-1613.

17. Habisreutinger, S. N.; Leijtens, T.; Eperon, G. E.; Stranks, S. D.; Nicholas, R. J.; Snaith, H. J., Enhanced Hole Extraction in Perovskite Solar Cells Through Carbon Nanotubes. *J. Phys. Chem. Lett.* **2014,** *5* (23), 4207-4212.

18. Odom, T. W.; Huang, J.-L.; Lieber, C. M., STM studies of single-walled carbon nanotubes. *J. Condens. Matter Phys.* **2002,** *14* (6), R145-R167.

19. Matsuda, Y.; Tahir-Kheli, J.; Goddard, W. A., Definitive Band Gaps for Single-Wall Carbon Nanotubes. *J. Phys. Chem. Lett.* **2010,** *1* (19), 2946-2950.

20. Cheung, C. L.; Kurtz, A.; Park, H.; Lieber, C. M., Diameter-controlled synthesis of carbon nanotubes. *Journal of Physical Chemistry B* **2002,** *106* (10), 2429-2433.

21. Li, Y.; Kim, W.; Zhang, Y.; Rolandi, M.; Wang, D.; Dai, H., Growth of single-walled carbon nanotubes from discrete catalytic nanoparticles of various sizes. *J. Phys. Chem. B* **2001,** *105* (46), 11424-11431.

22. Chen, Z.; Kim, D. Y.; Hasegawa, K.; Noda, S., Methane-Assisted Chemical Vapor Deposition Yielding Millimeter-Tall Single-Wall Carbon Nanotubes of Smaller Diameter. *ACS Nano* **2013,** *7* (8), 6719-6728.

23. Hata, K.; Futaba, D. N.; Mizuno, K.; Namai, T.; Yumura, M.; Iijima, S., Water-Assisted Highly Efficient Synthesis of Impurity-Free Single-Walled Carbon Nanotubes. *Science* **2004,** *306* (5700), 1362-1364.

24. Sakurai, S.; Inaguma, M.; Futaba, D. N.; Yumura, M.; Hata, K., A Fundamental Limitation of Small Diameter Single-Walled Carbon Nanotube Synthesis—A Scaling Rule of the Carbon Nanotube Yield with Catalyst Volume. *Materials* **2013,** *6* (7), 2633-2641.

25. Almkhelfe, H.; Li, X.; Rao, R.; Amama, P. B., Catalytic CVD growth of millimeter-tall single-wall carbon nanotube carpets using industrial gaseous waste as a feedstock. *Carbon* **2017,** *116*, 181-190.

26. Zheng, M.; Jagota, A.; Strano, M. S.; Santos, A. P.; Barone, P.; Chou, S. G.; Diner, B. A.; Dresselhaus, M. S.; McLean, R. S.; Onoa, G. B.; Samsonidze, G. G.; Semke, E. D.; Usrey,

M.; Walls, D. J., Structure-Based Carbon Nanotube Sorting by Sequence-Dependent DNA Assembly. *Science* **2003,** *302* (5650), 1545.

27. Arnold, M. S.; Green, A. A.; Hulvat, J. F.; Stupp, S. I.; Hersam, M. C., Sorting carbon nanotubes by electronic structure using density differentiation. *Nat. Nanotechnol.* **2006,** *1* (1), 60-65.

28. Liu, H.; Nishide, D.; Tanaka, T.; Kataura, H., Large-scale single-chirality separation of single-wall carbon nanotubes by simple gel chromatography. *Nat. Commun.* **2011,** *2* (1), 309.

29. Fagan, J. A.; Khripin, C. Y.; Silvera Batista, C. A.; Simpson, J. R.; Hároz, E. H.; Hight Walker, A. R.; Zheng, M., Isolation of Specific Small-Diameter Single-Wall Carbon Nanotube Species via Aqueous Two-Phase Extraction. *Adv. Mater.* **2014,** *26* (18), 2800-2804.

30. Rao, R.; Pint, C. L.; Islam, A. E.; Weatherup, R. S.; Hofmann, S.; Meshot, E. R.; Wu, F.; Zhou, C.; Dee, N.; Amama, P. B.; Carpena-Nuñez, J.; Shi, W.; Plata, D. L.; Penev, E. S.; Yakobson, B. I.; Balbuena, P. B.; Bichara, C.; Futaba, D. N.; Noda, S.; Shin, H.; Kim, K. S.; Simard, B.; Mirri, F.; Pasquali, M.; Fornasiero, F.; Kauppinen, E. I.; Arnold, M.; Cola, B. A.; Nikolaev, P.; Arepalli, S.; Cheng, H.-M.; Zakharov, D. N.; Stach, E. A.; Zhang, J.; Wei, F.; Terrones, M.; Geohegan, D. B.; Maruyama, B.; Maruyama, S.; Li, Y.; Adams, W. W.; Hart, A. J., Carbon Nanotubes and Related Nanomaterials: Critical Advances and Challenges for Synthesis toward Mainstream Commercial Applications. *ACS Nano* **2018,** *12* (12), 11756-11784.

31. Gómez-Gualdrón, D. A.; Balbuena, P. B., Characterization of carbon atomistic pathways during single-walled carbon nanotube growth on supported metal nanoparticles. *Carbon* **2013,** *57*, 298-309.

32. Fiawoo, M. F. C.; Bonnot, A. M.; Amara, H.; Bichara, C.; Thibault-Pénisson, J.; Loiseau, A., Evidence of Correlation between Catalyst Particles and the Single-Wall Carbon Nanotube Diameter: A First Step towards Chirality Control. *Phys. Rev. Lett.* **2012,** *108* (19), 195503.

33. Bachilo, S. M.; Balzano, L.; Herrera, J. E.; Pompeo, F.; Resasco, D. E.; Weisman, R. B., Narrow (n,m)-Distribution of Single-Walled Carbon Nanotubes Grown Using a Solid Supported Catalyst. *J. Am. Chem. Soc.* **2003,** *125* (37), 11186-11187.

34. Cao, A.; Veser, G., Exceptional high-temperature stability through distillation-like self-stabilization in bimetallic nanoparticles. *Nat. Mater.* **2010,** *9* (1), 75-81.

35. Romanenko, A. V.; Tyschishin, E. A.; Moroz, E. M.; Likholobov, V. A.; Zaikovskii, V. I.; Jhung, S. H.; Park, Y. S., Influence of ruthenium addition on sintering of carbon-supported palladium. *Appl. Catal. A: Gen.* **2002,** *227* (1), 117-123.

36. Budiman, A. W.; Song, S. H.; Chang, T. S.; Choi, M. J., Preparation of a high performance cobalt catalyst for CO2 reforming of methane. *Adv. Powder Technol.* **2016,** *27* (2), 584-590.

37. Wang, X.; Fu, X.-P.; Yu, W.-Z.; Ma, C.; Jia, C.-J.; Si, R., Synthesis of a ceria-supported iron–ruthenium oxide catalyst and its structural transformation from subnanometer clusters to

single atoms during the Fischer–Tropsch synthesis reaction. *Inorg. Chem. Front.* **2017,** *4* (12), 2059-2067.

38. Liu, X.; Zeng, J.; Shi, W.; Wang, J.; Zhu, T.; Chen, Y., Catalytic oxidation of benzene over ruthenium–cobalt bimetallic catalysts and study of its mechanism. *Catal. Sci. Technol.* **2017,** *7* (1), 213-221.

39. Tanabe, K., Catalytic application of niobium compounds. *Catal. Today* **2003,** *78* (1), 65-77.

40. Cui, X.; Xu, J.; Zhang, C.; Yang, Y.; Gao, P.; Wu, B.; Li, Y., Effect of pretreatment on precipitated Fe–Mo Fischer–Tropsch catalysts: Morphology, carburization, and catalytic performance. *J. Catal.* **2011,** *282* (1), 35-46.

41. Phaahlamohlaka, T. N.; Dlamini, M. W.; Mogodi, M. W.; Kumi, D. O.; Jewell, L. L.; Billing, D. G.; Coville, N. J., A sinter resistant Co Fischer-Tropsch catalyst promoted with Ru and supported on titania encapsulated by mesoporous silica. *Appl. Catal. A: Gen.* **2018,** *552*, 129-137.

42. Resasco, D. E.; Alvarez, W. E.; Pompeo, F.; Balzano, L.; Herrera, J. E.; Kitiyanan, B.; Borgna, A., A Scalable Process for Production of Single-walled Carbon Nanotubes (SWNTs) by Catalytic Disproportionation of CO on a Solid Catalyst. *J. Nanoparticle Res.* **2002,** *4* (1), 131-136.

43. Cui, K.; Kumamoto, A.; Xiang, R.; An, H.; Wang, B.; Inoue, T.; Chiashi, S.; Ikuhara, Y.; Maruyama, S., Synthesis of subnanometer-diameter vertically aligned single-walled carbon nanotubes with copper-anchored cobalt catalysts. *Nanoscale* **2016,** *8* (3), 1608-1617.

44. Everhart, B. M.; Almkhelfe, H.; Li, X.; Wales, M.; Nikolaev, P.; Rao, R.; Maruyama, B.; Amama, P. B., Efficient Growth of Carbon Nanotube Carpets Enabled by In Situ Generation of Water. *Ind. Eng. Chem. Res.* **2020,** *59* (19), 9095-9104.

45. Almkhelfe, H.; Carpena-Nunez, J.; Back, T. C.; Amama, P. B., Gaseous product mixture from Fischer-Tropsch synthesis as an efficient carbon feedstock for low temperature CVD growth of carbon nanotube carpets. *Nanoscale* **2016,** *8* (27), 13476-13487.

46. Li, X.; Gray, E. R.; Islam, A. E.; Sargent, G. A.; Maruyama, B.; Amama, P. B., Magnesia and Magnesium Aluminate Catalyst Substrates for Carbon Nanotube Carpet Growth. *ACS Appl. Nano Mater.* **2020,** *3* (2), 1830-1840.

47. Nikolaev, P.; Hooper, D.; Perea-López, N.; Terrones, M.; Maruyama, B., Discovery of Wall-Selective Carbon Nanotube Growth Conditions via Automated Experimentation. *ACS Nano* **2014,** *8* (10), 10214-10222.

48. Futaba, D. N.; Hata, K.; Yamada, T.; Mizuno, K.; Yumura, M.; Iijima, S., Kinetics of Water-Assisted Single-Walled Carbon Nanotube Synthesis Revealed by a Time-Evolution Analysis. *Physical Review Letters* **2005,** *95* (5), 056104.

49. Rao, R.; Liptak, D.; Cherukuri, T.; Yakobson, B. I.; Maruyama, B., In situ evidence for chirality-dependent growth rates of individual carbon nanotubes. *Nat. Mater.* **2012,** *11* (3), 213-216.

50. Nikolaev, P.; Hooper, D.; Webber, F.; Rao, R.; Decker, K.; Krein, M.; Poleski, J.; Barto, R.; Maruyama, B., Autonomy in materials research: a case study in carbon nanotube growth. *npj Computational Materials* **2016,** *2* (1), 16031.

51. Kluender, E. J.; Hedrick, J. L.; Brown, K. A.; Rao, R.; Meckes, B.; Du, J. S.; Moreau, L. M.; Maruyama, B.; Mirkin, C. A., Catalyst discovery through megalibraries of nanomaterials. *PNAS* **2019,** *116* (1), 40-45.

52. Rao, R.; Pierce, N.; Liptak, D.; Hooper, D.; Sargent, G.; Semiatin, S. L.; Curtarolo, S.; Harutyunyan, A. R.; Maruyama, B., Revealing the Impact of Catalyst Phase Transition on Carbon Nanotube Growth by in Situ Raman Spectroscopy. *ACS Nano* **2013,** *7* (2), 1100-1107.

53. Meshot, E. R.; Plata, D. L.; Tawfick, S.; Zhang, Y.; Verploegen, E. A.; Hart, A. J., Engineering Vertically Aligned Carbon Nanotube Growth by Decoupled Thermal Treatment of Precursor and Catalyst. *ACS Nano* **2009,** *3* (9), 2477-2486.

54. Kresse, G.; Hafner, J., Ab initio molecular dynamics for liquid metals. *Phys. Rev. B* **1993,** *47* (1), 558-561.

55. Kresse, G.; Furthmüller, J., Efficiency of ab-initio total energy calculations for metals and semiconductors using a plane-wave basis set. *Comput. Mater. Sci.* **1996,** *6* (1), 15-50.

56. Kresse, G.; Furthmüller, J., Efficient iterative schemes for ab initio total-energy calculations using a plane-wave basis set. *Phys. Rev. B* **1996,** *54* (16), 11169-11186.

57. Perdew, J. P.; Burke, K.; Ernzerhof, M., Generalized Gradient Approximation Made Simple. *Phys. Rev. Lett.* **1996,** *77* (18), 3865-3868.

58. Grimme, S., Semiempirical GGA-type density functional constructed with a long-range dispersion correction. *J. Comput. Chem.* **2006,** *27* (15), 1787-1799.

59. Blöchl, P. E., Projector augmented-wave method. *Phys. Rev. B* **1994,** *50* (24), 17953-17979.

60. Kresse, G.; Joubert, D., From ultrasoft pseudopotentials to the projector augmented-wave method. *Phys. Rev. B* **1999,** *59* (3), 1758-1775.

61. Ho, K. M.; Fu, C. L.; Harmon, B. N.; Weber, W.; Hamann, D. R., Vibrational Frequencies and Structural Properties of Transition Metals via Total-Energy Calculations. *Phys. Rev. Lett.* **1982,** *49* (9), 673-676.

62. Rodríguez-López, J. L.; Aguilera-Granja, F.; Michaelian, K.; Vega, A., Structure and magnetism of cobalt clusters. *Phys. Rev. B* **2003,** *67* (17), 174413.

63. Rao, A. M.; Richter, E.; Bandow, S.; Chase, B.; Eklund, P. C.; Williams, K. A.; Fang, S.; Subbaswamy, K. R.; Menon, M.; Thess, A.; Smalley, R. E.; Dresselhaus, G.; Dresselhaus, M. S., Diameter-Selective Raman Scattering from Vibrational Modes in Carbon Nanotubes. *Science* **1997,** *275* (5297), 187-191.

64. Dresselhaus, M. S.; Dresselhaus, G.; Saito, R.; Jorio, A., Raman spectroscopy of carbon nanotubes. *Phys. Rep.* **2005,** *409* (2), 47-99.

65. Jorio, A.; Saito, R.; Hafner, J. H.; Lieber, C. M.; Hunter, M.; McClure, T.; Dresselhaus, G.; Dresselhaus, M. S., Structural (n, m) determination of isolated single-wall carbon nanotubes by resonant Raman scattering. *Phys. Rev. Lett.* **2001,** *86* (6), 1118-21.

66. Henrard, L.; Hernández, E.; Bernier, P.; Rubio, A., van der Waals interaction in nanotube bundles: Consequences on vibrational modes. *Phys. Rev. B* **1999,** *60* (12), R8521-R8524.

67. Strano, M. S., Probing Chiral Selective Reactions Using a Revised Kataura Plot for the Interpretation of Single-Walled Carbon Nanotube Spectroscopy. *J. Am. Chem. Soc.* **2003,** *125* (51), 16148-16153.

68. Milnera, M.; Kürti, J.; Hulman, M.; Kuzmany, H., Periodic Resonance Excitation and Intertube Interaction from Quasicontinuous Distributed Helicities in Single-Wall Carbon Nanotubes. *Phys. Rev. Lett.* **2000,** *84* (6), 1324-1327.

69. Kuzmany, H.; Plank, W.; Hulman, M.; Kramberger, C.; Grüneis, A.; Pichler, T.; Peterlik, H.; Kataura, H.; Achiba, Y., Determination of SWCNT diameters from the Raman response of the radial breathing mode. *Eur. Phys. J. B* **2001,** *22* (3), 307-320.

70. O'Connell, M. J.; Sivaram, S.; Doorn, S. K., Near-infrared resonance Raman excitation profile studies of single-walled carbon nanotube intertube interactions: A direct comparison of bundled and individually dispersed HiPco nanotubes. *Phys. Rev. B* **2004,** *69* (23), 235415.

71. Telg, H.; Maultzsch, J.; Reich, S.; Hennrich, F.; Thomsen, C., Chirality Distribution and Transition Energies of Carbon Nanotubes. *Phys. Rev. Lett.* **2004,** *93* (17), 177401.

72. Maultzsch, J.; Telg, H.; Reich, S.; Thomsen, C., Radial breathing mode of single-walled carbon nanotubes: Optical transition energies and chiral-index assignment. *Phys. Rev. B* **2005,** *72* (20), 205438.

73. Amama, P. B.; Pint, C. L.; Kim, S. M.; McJilton, L.; Eyink, K. G.; Stach, E. A.; Hauge, R. H.; Maruyama, B., Influence of Alumina Type on the Evolution and Activity of Alumina-Supported Fe Catalysts in Single-Walled Carbon Nanotube Carpet Growth. *ACS Nano* **2010,** *4* (2), 895-904.

74. Hata, K.; Futaba, D. N.; Mizuno, K.; Namai, T.; Yumura, M.; Iijima, S., Water-assisted highly efficient synthesis of impurity-free single-walled carbon nanotubes. *Science* **2004,** *306* (5700), 1362-4.

75. Amama, P. B.; Pint, C. L.; McJilton, L.; Kim, S. M.; Stach, E. A.; Murray, P. T.; Hauge, R. H.; Maruyama, B., Role of Water in Super Growth of Single-Walled Carbon Nanotube Carpets. *Nano Lett.* **2009,** *9* (1), 44-49.

76. Kim, S. M.; Pint, C. L.; Amama, P. B.; Zakharov, D. N.; Hauge, R. H.; Maruyama, B.; Stach, E. A., Evolution in catalyst morphology leads to carbon nanotube growth termination. *J. Phys. Chem. Lett.* **2010,** *1* (6), 918-922.

77. Zaitsev, B. N.; Baklanova, N. I.; Zima, T. M., Atomic force microscopy study of surface-modified carbon fibers. *Inorg. Mater.* **2008,** *44* (6), 592-597.

78. Paik, P.; Kar, K. K., Surface roughness and morphology of polypropylene nanospheres: effects of particles size. *Surf. Eng.* **2008,** *24* (5), 341-349.

79. Zhang, M.; Yudasaka, M.; Iijima, S., Diameter Enlargement of Single-Wall Carbon Nanotubes by Oxidation. *J. Phys. Chem. B* **2004,** *108* (1), 149-153.

80. Borowiak-Palen, E.; Pichler, T.; Liu, X.; Knupfer, M.; Graff, A.; Jost, O.; Pompe, W.; Kalenczuk, R. J.; Fink, J., Reduced diameter distribution of single-wall carbon nanotubes by selective oxidation. *Chem. Phys. Lett.* **2002,** *363* (5), 567-572.

81. Dementev, N.; Osswald, S.; Gogotsi, Y.; Borguet, E., Purification of carbon nanotubes by dynamic oxidation in air. *J. Mater. Chem.* **2009,** *19* (42), 7904-7908.

82. Liao, Y.; Hussain, A.; Laiho, P.; Zhang, Q.; Tian, Y.; Wei, N.; Ding, E.-X.; Khan, S. A.; Nguyen, N. N.; Ahmad, S.; Kauppinen, E. I., Tuning Geometry of SWCNTs by CO2 in Floating Catalyst CVD for High-Performance Transparent Conductive Films. *Adv. Mater. Interfaces* **2018,** *5* (23), 1801209.

83. Youn, S. K.; Park, H. G., Morphological Evolution of Fe–Mo Bimetallic Catalysts for Diameter and Density Modulation of Vertically Aligned Carbon Nanotubes. *J. Phys. Chem. C* **2013,** *117* (36), 18657-18665.

Chapter 4 - Hydrothermal Synthesis of Carbon Nanotube-Titania Composites for Enhanced Photocatalytic Performance

Chapter 4 is reprinted with permission from:

Everhart, B. M.; Baker-Fales, M.; McAuley, B.; Banning, E.; Almkhelfe, H.; Back, T. C.; Amama, P. B., Hydrothermal synthesis of carbon nanotube–titania composites for enhanced photocatalytic performance. *Journal of Materials Research* **2020,** *35* (11), 1451-1460.

4.1 Introduction

Photocatalytic oxidation (PCO) using semiconductors as catalysts has become an appealing approach as a green technology for environmental remediation since the discovery of UV-assisted splitting of water on TiO_2 by Fujishima and Honda.[1] Air contaminants such as SO_x, NO_x, halogenated organics, and volatile organic compounds (VOCs) are suitable candidates for PCO.[2-10] TiO_2 has been identified as the most promising photocatalytic material based on its strong oxidizing power, chemical stability, relatively low price, and biological benignity.[11, 12] However, photocatalytic performance of conventional TiO_2 is limited by its wide band gap (3.2 eV for the anatase crystal phase)[13] and fast electron-hole recombination. These properties restrict the photon absorption range to ultraviolet wavelengths (only 8.3% of total solar irradiance [14]) and limit the quantum efficiency.[15, 16]

In an effort to overcome these problems and increase the photocatalytic activity of TiO_2, researchers have explored a number of modification approaches[17-20] and recently turned to carbon nanotubes (CNTs) and other carbon nanomaterials.[21-24] CNTs, which are either single-walled (SWCNTs) or multi-walled (MWCNTs), possess unique properties that make them the ideal supports for catalysts such as large surface area (>200 m^2/g), high thermal and chemical stability,

as well as excellent electrical and mechanical properties. In particular, CNTs have a large electron-storage capacity (one electron for every 32 carbon atoms) and thus can serve as an electron sink; additionally, the highly conductive nature of CNTs promotes charge separation via the creation of heterojunctions at the CNT-TiO_2 interface.[25] A number of studies[21-31] have shown the unique electronic properties of CNTs can be exploited to induce beneficial charge transfer properties and synergistic effects between carbon phases and TiO_2, thus coupling CNTs to TiO_2 can improve photocatalytic performance of TiO_2. However, the exact role of CNTs in TiO_2/CNT composites is still poorly understood especially as it can be convoluted by factors such as synthesis methods, CNT morphologies, and weight ratio of CNTs to TiO_2. Further insight into their syntheses and mechanisms is clearly required.

The conventional method for synthesizing TiO_2/CNT is either a sol-gel or hydrothermal process.[32] Sol-gel synthesis utilizes inorganic metal salts or metal organic compounds to produce a sol, which transitions from a liquid to a gel upon polymerization of the precursor and loss of solvent. The hydrothermal method[33] used in this study involves heating a solution containing the titanium precursor to temperatures above the boiling point of the solvent, resulting in significantly increased pressures within the autoclave reactor. Synthesis parameters such as heating time in the autoclave, temperature, and pH affect the properties of resulting TiO_2 and offer a reliable path for improved control of the composite properties. Low temperature and relatively short reaction time proved best for synthesis of small TiO_2 particles, while mild acidity led to control of the crystal phase and yielded pure anatase.[33, 34] The hydrothermal method described above has been used by Zhang et al.[35] for creating TiO_2/CNT composites, whereas Jitianu et al.[36] showed TiO_2 decorations on MWCNTs were possible. Silva et al.[37] also showed that microwave-assisted hydrothermal process can be used for high mass loading of metal oxide and CNT composites. Hydrothermal

synthesis of TiO_2/MWCNT composites was explored in this work due to the possibility of controlling the TiO_2 phase by controlling pH during the TiO_2 nucleation step in the hydrothermal aging process. To the best of our knowledge, no studies have been reported on the degradation of acetaldehyde, a common indoor pollutant,[38, 39] using a hydrothermally prepared mesoporous CNT/TiO_2 photocatalyst. Moreover, while many studies involving TiO_2/CNT composites have focused on liquid-phase degradation of dyes, few have investigated gas-phase VOC degradation.[40, 41]

In this work, a hydrothermal synthesis method has been used to synthesize TiO_2/MWCNT catalyst composites for efficient degradation of acetaldehyde under UV illumination. The hydrothermal method shows promise in controlling the anatase/rutile ratio, as well as producing diameter-controlled crystalline TiO_2 particles on a large scale.[42] Catalysts were synthesized with nominal mass ratios of 1:100 (TiO_2/MWCNT-1%), 1:20 (TiO_2/MWCNT-5%), and pure TiO_2 (100% TiO_2) as a reference. Performance of the composites was tested in the photocatalytic degradation of acetaldehyde in a batch reactor.

4.2 Experimental

4.2.1 Chemicals

MWCNTs (purity >95%, outer diameter 20-30 nm, length 10-30 μm) were obtained from Chengdu Organic Chemicals Co., Ltd. Hydrogen peroxide (30%) was obtained from Fisher Scientific. Titanium tetrachloride ($TiCl_4$, purity >99.0 %) was obtained from Strem Chemicals. Sodium hydroxide (NaOH, purity >99%) and acetaldehyde (C_2H_4O, purity >99%) were obtained from Sigma-Aldrich. Dry air was obtained from Matheson.

4.2.2 CNT oxidation

MWCNTs were photo-oxidized in 30 wt% H_2O_2 via UV illumination (White-Rodger Comfort Plus UV200, 2 Philips TUV PL-L 60 W bulbs). UV-assisted H_2O_2 oxidation of MWCNTs has been shown to be effective and less aggressive in comparison to conventional acid oxidation using HNO_3.[43, 44] In a typical batch, 0.5 g of MWCNTs were added to 200 mL of H_2O_2, which was maintained at 60 °C under UV illumination and vigorous stirring. The MWCNTs were oxidized for 72 hours, with 50 mL of H_2O_2 being added at 24 and 48 hours to sustain the process. After 72 hours, the oxidized MWCNTs were removed from solution via vacuum filtration and rinsed with distilled water. Oxidized MWCNTs were obtained after the samples were vacuum-dried overnight at 60 °C.

4.2.3 Catalyst synthesis

Oxidized MWCNTs were dispersed in 50 mL H_2O via sonication at room temperature for 3 hours. Following sonication, $TiCl_4$ amounts corresponding to TiO_2:MWCNT ratios of 99:1 and 95:5 were added dropwise at a rate of 1 ml/min, to the dispersed MWCNTs at ~5 °C under moderate stirring (0.88 mol/L Ti). After addition of the $TiCl_4$ and resulting exothermic reaction, the solution was allowed to cool from ~25 to 10 °C under continuous stirring. Once the solution reached 10 °C, 35 ml of 5M NaOH were added to the solution to obtain a pH of 3-5. The addition of the strong base led to the formation of abundant NaCl, causing the solution to become highly viscous. The stir rate was increased gradually from 300 to 800 RPM as the viscosity increased. When the solution reached a pH range of 3 – 5, water was added under constant stirring to produce a solution of 0.44 mol/L Ti. The solution was then put in a steel autoclave and heated in the oven for 3 hours at 150 °C, removed and allowed to cool for 3 hours. The TiO_2/MWCNT composite

was dried by air continuously flowing over it for 24 hours followed by 3 hours in the oven at 80 °C. Once dried, TiO_2/MWCNT was crushed into a fine powder and baked at 250 °C for 3 hours. To remove the NaCl, the composite was rinsed via vacuum filtration with 250 ml of deionized water and allowed to dry for 12 hours. Finally, the composite was calcined at 450 °C for 3 hours (a temperature low enough to prevent TiO_2 sintering),[45] cooled, and stored as a powder. Prior to evaluation of the catalyst performance, the powders were sieved to <125μm to reduce particle agglomeration and grain size distribution. Photocatalysts were synthesized with nominal mass ratios of 1:100 (TiO_2/MWCNT-1%), 1:20 (TiO_2/MWCNT-5%), and pure TiO_2 (100% TiO_2) as a reference.

4.2.4 Characterization

XRD patterns were obtained using a Rigaku MiniFlex II diffractometer with a Cu Kα radiation source. Two theta scanning angles from 10° to 80° degrees were taken with a step size of 0.02° and scan speed of 2.0°/min for all photocatalysts. Surface area and pore volume were derived from N_2 adsorption-desorption measurements at -196°C. The Brunauer-Emmet-Teller (BET) method[46] was applied to the adsorption isotherm in the relative pressure range of 0.02 to 0.35 to calculate the specific surface area of the synthesized photocatalysts. Pore-size distribution was obtained from the desorption branch at a relative pressure of 0.99 of the isotherm using the Barrett-Joyner-Halenda (BJH) model.[47] Scanning electron micrographs (SEM) were obtained using a Hitachi S5200, operated at 10 kV and equipped with energy-dispersive X-ray spectroscopy (EDX). Transmission electron microscopic (TEM) images were obtained with an FEI Tecnai F20 XT equipped with EDX at 120kV. A small amount of photocatalyst powder was dispersed in ethanol by sonication for 10 minutes and a drop of the solution was deposited onto a carbon TEM

grid. Raman spectroscopy was obtained from a Renishaw Raman spectrometer using a CW laser with a wavelength of 514 nm. Raman spectra were collected at different locations of the sample. The TiO_2 and TiO_2/MWCNT samples were analyzed by UV-visible diffuse reflectance spectroscopy (UV-vis DRS) using a Shimadzu UV-2600 spectrometer with $BaSO_4$ as the background material. X-ray photoelectron spectroscopic (XPS) measurements were conducted on a Kratos Ultra XPS system with a standard Mg Kα source (hv =1253.6 eV). A charge neutralizer was employed to minimize the effect of charging. High-resolution spectra were acquired at 20 eV pass energy with 0.1 eV steps. XPS spectra were analyzed using CasaXPS software. Peak components in the high-resolution spectra were fit with a combination of Gaussian and Lorentzian peak shapes.

4.2.5 Photocatalytic performance

In a standard catalyst evaluation, 0.100 ± 0.001 g of sieved photocatalyst powder was loaded into a borosilicate sample dish, which was then placed in a 750-mL borosilicate batch reactor. The reactor was purged using UHP air (low CO_2 and H_2O content) at 6 liters per minute (LPM) for 5 minutes. Thereafter, acetaldehyde vapor corresponding to 1000 ppmv was injected into the reactor and allowed to equilibrate in darkness for 90 minutes. The ultraviolet illumination system – consisting of two 25 W Sylvania 21703 (356 nm) bulbs and two 13 W ReptiSun 10.0 UV/B bulbs (emission spectrum displayed in Figure C4.1) – was switched on to initiate the reaction for a duration of 120 minutes. One-mL gas samples were taken from the reactor at ~10 minute intervals for analysis. The decrease in acetaldehyde concentration and increase in CO_2 concentration were monitored using an SRI 310C gas chromatograph equipped with a Restek silica gel column (8046-895, 6 ft length, 2 mm ID), flame ionization detector (FID), and on-column

injection. Detected peaks were integrated using PeakSimple Chromatography Integration software. The relative concentration is expressed as C/C_o, where C is the concentration of acetaldehyde at time *t* and C_o is the initial acetaldehyde concentration. The photocatalytic experiment was conducted at room temperature (~25°C) with an indoor relative humidity of ~50%. The photocatalytic performance of three separate 0.100 g samples from each composite ratio were tested to ensure statistical significance of the results. Average catalyst performance was calculated using the average concentration of three degradation experiments for each catalyst. First-order rate assumptions were applied in analysis of the degradation data.

4.3 Results and Discussion

4.3.1 Characterization of photocatalysts

XRD was used to characterize the phase composition of TiO_2 and TiO_2/MWCNT composites and their diffraction patterns are presented in Figure 4.1. The anatase peaks at 2θ values of 25.40°, 37.9°, 48.0°, 53.9°, and 55.1° can be indexed to (101), (004), (200), (105), and (211) crystal planes, respectively. Diffraction peaks for rutile at 27.4° 36.2°, 41.3°, 54.4°, and 56.7° are present, which are indexed to (110), (101), (111), (211), and (220) crystal planes. The primary diffraction peak for brookite at 30.9°, indexed to (121), is also present. These peak assignments are also in agreement with prior studies.[48-51] Comparing the reflection peaks observed in TiO_2 to the TiO_2/MWCNT composites, it can be concluded the dominant phase in all photocatalysts is anatase, although the TiO_2/MWCNT-5% composite appears to have a substantial fraction of rutile. A summary of the complete phase composition of the photocatalysts is presented in Table C4.1. The height ratio of the dominant anatase peak at 25.2° to the dominant rutile peak at 27.4° (I_{Ana}/I_{Rut}) can be used to determine the weight fraction of anatase and rutile crystalline phases of TiO_2 from

Equation 1 as demonstrated by Spurr and Myers;[52] the calculated mass ratios of anatase to rutile in TiO_2, TiO_2/MWCNT-1%, and TiO_2/MWCNT-5% are 66:34, 98:2, and 92:8, respectively. It is worth mentioning the characteristic peak of MWCNTs (002) located at $2\theta = 25°$, is not observed for the TiO_2/MWCNT samples. This is most likely due to the overlap with the strong anatase (101) reflections.

$$\boldsymbol{f} = \frac{\mathbf{1}}{\mathbf{1+1.26}\left(\frac{\boldsymbol{I_R}}{\boldsymbol{I_A}}\right)} \tag{4.1}$$

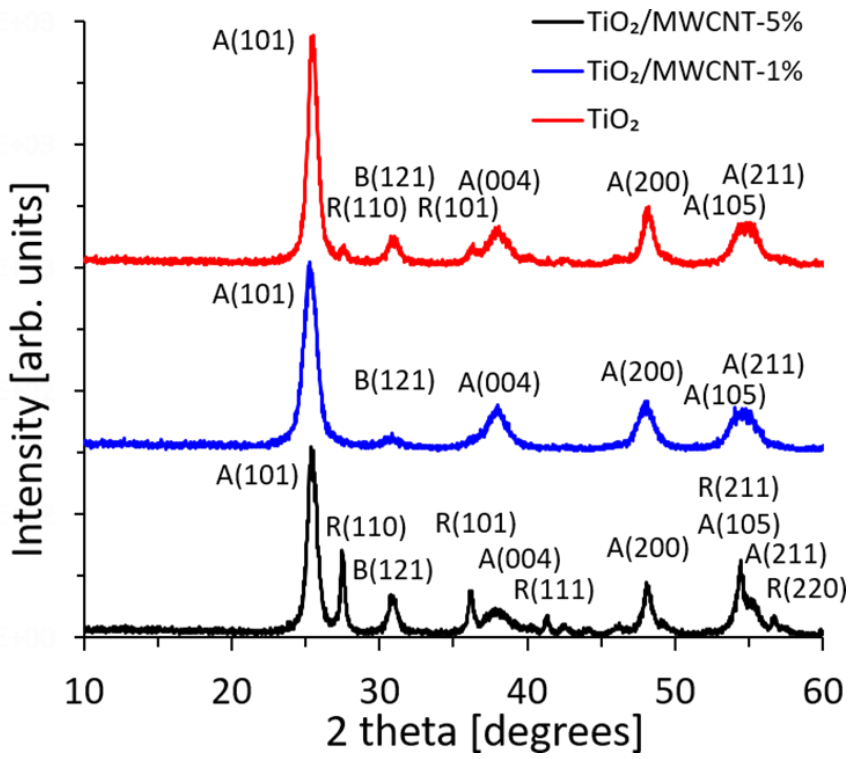

Figure 4.1. XRD patterns of TiO_2 and TiO_2-MWCNT nanocomposites. Peak labels have been included to correlate peaks to crystal phase (Anatase [A], Rutile [R], or Brookite [B]).

Table 4.1. Summary of catalyst properties.

Catalyst characterization			
	TiO_2	TiO_2/MWCNT-1%	TiO_2/MWCNT-5%
Surface area (m^2/g)[a]	74.6	141.6	68.2
Total pore volume (cm^3/g)[a]	0.14	0.30	0.16
Average pore diameter (nm)[a]	7.60	8.36	9.42
TiO_2 average diameter (nm)[b]	6.1	5.8	7.2
Anatase content (wt%)[b]	92	100	67
Carbon content (wt%)[c]	N/A	1.4	6.6

[a]Nitrogen physisorption.
[b]XRD.
[c]EDX.

Average TiO_2 particle size for the samples (Table 4.1) was calculated from the full width at half maximum (FWHM) of the principal anatase (101) peak at 25.2° using the Williamson-Hall method. Average TiO_2 particle sizes for TiO_2, TiO_2/MWCNT-1%, and TiO_2/MWCNT-5% composites are 6.1, 5.8, and 7.2 nm, respectively. The high uniformity in TiO_2 particle sizes for the catalyst composites indicates the addition of MWCNTs during synthesis did not affect the size. Analysis of the E_g band (≈142cm^{-1}) in the Raman spectra (Figure C4.1) confirms the insignificant differences in particle size, as size discrepancies would manifest as an increase in peak frequency.[53] SEM images of the synthesized photocatalysts presented in Figure 4.2 further illustrate the similarity of the bulk powder morphologies. Using EDX, carbon amounts were estimated at 1.4 and 6.6 wt% for TiO_2/MWCNT-1% and TiO_2/MWCNT-5% catalysts, respectively; these values indicate good agreement with the nominal values of 99 and 95 wt% TiO_2 in the samples. EDX data shown in Figure 4.3 reveal TiO_2/MWCNT-5% contains pockets of carbon in different regions exceeding 10 wt%, which may indicate CNT clustering during the TiO_2 nucleation phase. Intimate contact between MWCNTs and TiO_2 is apparent in the TEM images for TiO_2/MWCNT-5% in Figure 4.4, even after 10 minutes of sonication during the sample preparation process for TEM

characterization; this provides evidence of strong interactions between MWCNTs and TiO_2 nanoparticles, and high dispersion, especially for TiO_2/MWCNT-1%. Particle sizes estimated from the TEM images for the samples are in the range of 3 – 8 nm. The slight discrepancy in particle size obtained from TEM and XRD is consistent with overestimation of the size of crystallite particles by the Scherrer equation.[54, 55]

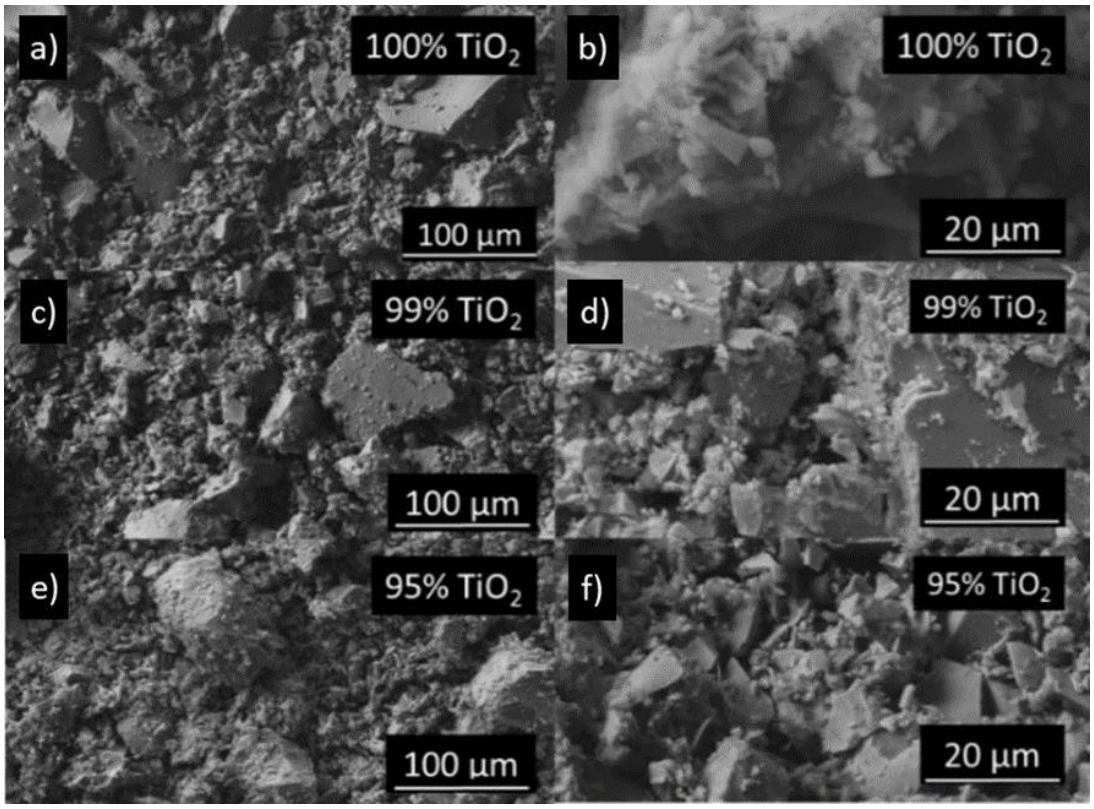

Figure 4.2. Low- and high-magnification SEM images of photocatalysts: TiO_2 (a, b), TiO_2/MWCNT-1% (c, d), TiO_2/MWCNT-5% (e, f).

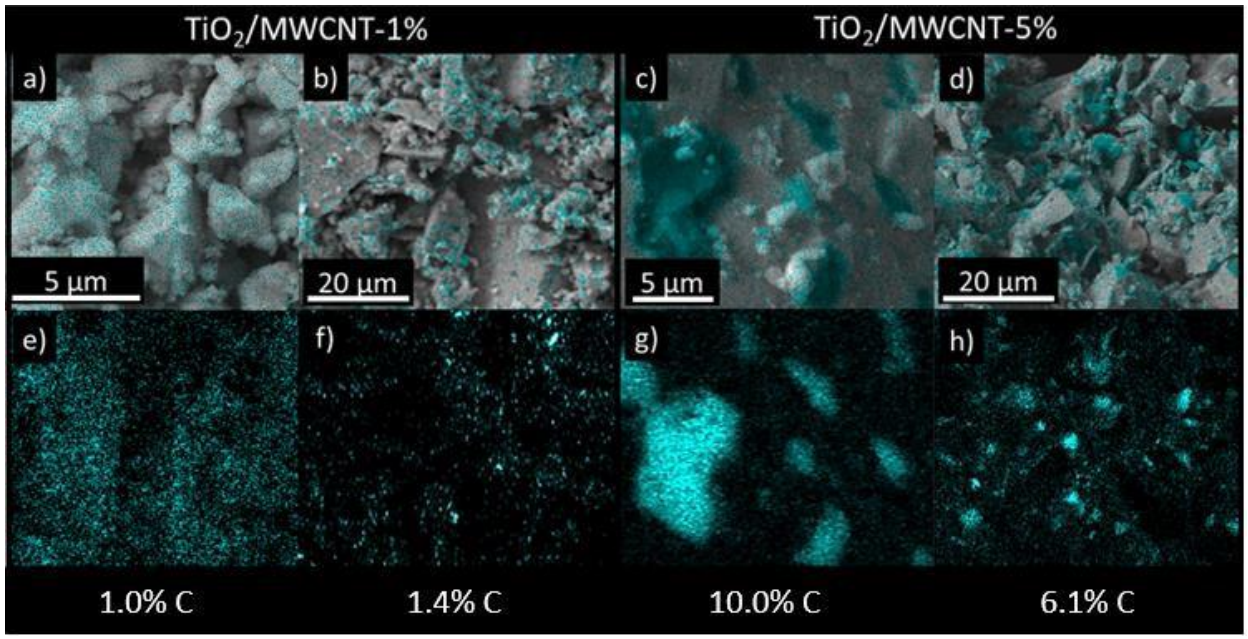

Figure 4.3. Carbon dispersion within photocatalysts. SEM images with EDS mapping of elemental carbon overlayed (a – d). EDS mapping of elemental carbon illustrating carbon dispersion (e – h).

BET surface areas of pure TiO_2, TiO_2/MWCNT-1%, and TiO_2/MWCNT-5% were determined to be 74.6, 141.6, and 68.2 m^2/g, respectively. The adsorption-desorption isotherms are presented in Figure C4.2. The dramatic difference in surface area clearly indicates an effect of MWCNTs on the morphology of the photocatalysts, which could stem from the presence of MWCNTs during the nucleation of TiO_2 nanoparticles as part of the hydrothermal process. A small amount of MWCNTs (~1 wt%) effectively increased the surface area of resulting composites while a further increase in the amount of MWCNTs (~5wt%) resulted in particle agglomeration, reducing overall surface area of the catalyst composite. Total pore volumes and average pore sizes determined by the BJH method for pure TiO_2, TiO_2/MWCNT-1%, and TiO_2/MWCNT-5% are summarized in Table 4.1. The existence of mesopores in the catalyst composites is evidenced by pore sizes in the order 7.6, 8.4, and 9.4 nm for TiO_2, TiO_2/MWCNT-1%, and TiO_2/MWCNT-5%, respectively. Significant increase in porosity is observed in the TiO_2/MWCNT-1% composite,

evidenced by substantially greater pore volume despite comparable pore size. Use of a hydrothermal method with a low weight fraction of MWCNTs yields TiO_2/MWCNT composites characterized by a combination of large specific surface area and pore size distributions in the mesopore range — features beneficial in catalysis.

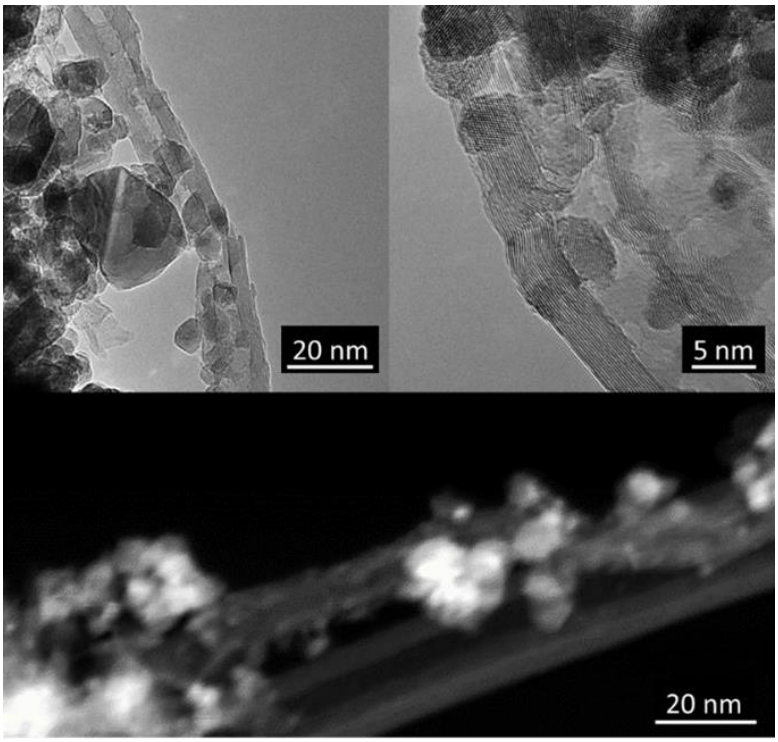

Figure 4.4. TEM images of TiO_2 particles on MWCNTs in the TiO_2/MWCNT-5% sample.

XPS characterization was performed to elucidate the surface composition of the photocatalysts. Figure 4.5 shows high-resolution XPS spectra for the 1s region of photocatalysts fitted using two asymmetric peak components. The peak component at binding energy of ~531 eV is attributed to the oxygen bonded to Ti (Ti-O) in TiO_2, while the component at ~532 eV is related to the hydroxyl group.[56] Results of deconvolution of O 1s peak for the photocatalysts are summarized in Table 4.2. Percentage concentrations of the two oxygen species identified changes with the amount of MWCNTs used during synthesis. Hydroxyl content in the photocatalysts decreases in the following order: TiO_2/MWCNT-1% > TiO_2/MWCNT-5% > TiO_2. This result

suggests presence of small amounts of MWCNTs (~1 wt%) enhances chemisorption of water on the surface of TiO_2 — a feature hardly observed for composites with 5 wt%. Prior studies have shown chemisorption of water on TiO_2 composites is enhanced with the addition of CNTs.[56, 57] Since XPS analysis occurs under ultra-high vacuum, the observed hydroxyl species is a result of chemisorption, not physisorption. XPS analysis of the catalyst composites reveals a substantially higher percentage of chemisorbed hydroxyl groups on the surface of the TiO_2/MWCNT-1%. Hydroxyl enrichment on the surface of TiO_2 promotes photocatalytic activity due to an increase in the generation of *OH radicals from the reaction between photogenerated holes and chemisorbed hydroxyl ions (or moisture) on the surface of photocatalyst. Therefore, synthesis approaches that yield high amounts of hydroxyl groups on the surface benefit photocatalytic reactions.

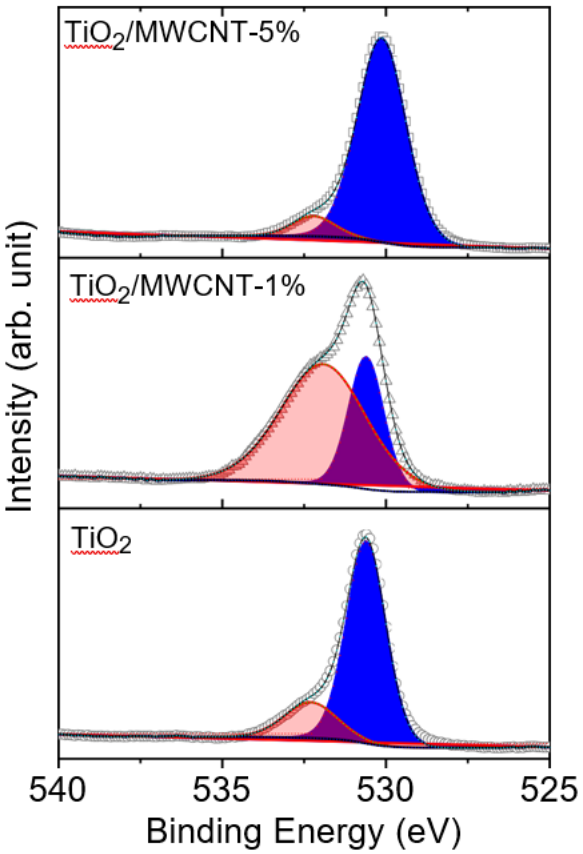

Figure 4.5. XPS high-resolution O 1s spectra of photocatalysts fitted using two asymmetric peak components.

Table 4.2. Summary of results of deconvolution of high-resolution XPS O 1s spectrum of TiO_2 and TiO_2/MWCNT composites using peak components with asymmetric line shapes.

Materials	O 1*s* (Ti–O)	O 1*s* (OH)
TiO_2		
Binding energy (eV)	530.1	532.2
Peak area	38941.7	3402.4
% Concentration	91.97	8.03
TiO_2/CNT-1%		
Binding energy (eV)	530.6	531.9
Peak area	10104.5	22672.0
% Concentration	30.84	69.16
TiO_2/CNT-5%		
Binding energy (eV)	530.6	532.3
Peak area	32081.9	7597.3
% Concentration	80.86	19.14

4.3.2 Photocatalytic activity

Activity of photocatalysts was measured by evaluating the rate of acetaldehyde degradation in the gas phase under UV light illumination. Figure 4.6 shows data for degradation of acetaldehyde over pure TiO_2, TiO_2/MWCNT-1% and TiO_2/MWCNT-5%. It is clear from the results that TiO_2/MWCNT-1% shows the highest photocatalytic performance because the rate of decrease of relative concentration (C/Co) is the fastest among the photocatalysts (Figure 4.6a). Photocatalytic degradation of acetaldehyde is assumed to be a pseudo-first-order reaction[58] with the following simplified Langmuir-Hinshelwood kinetic model when initial concentration (C_o) is negligible:

$$\ln\left(\frac{C}{Co}\right) = -k_o t \qquad (4.2)$$

where k_o is the apparent first-order rate constant. From the kinetic plots in Figure 4.6b, the TiO_2/MWCNT-1% shows the highest slope and consequently, the highest average rate constant (Figure 4.6c). In contrast, composites prepared without MWCNTs (pure TiO_2), or with relatively

high amounts of MWCNTs (TiO_2/MWCNT-5%), exhibit inferior photocatalytic performance. The respective shades around the plots in Figure 4.6 show the range within one standard deviation for all data collected at each time interval. Projection lines intercept the y-axis after time zero due to desorption of acetaldehyde when the UV lights were switched on.

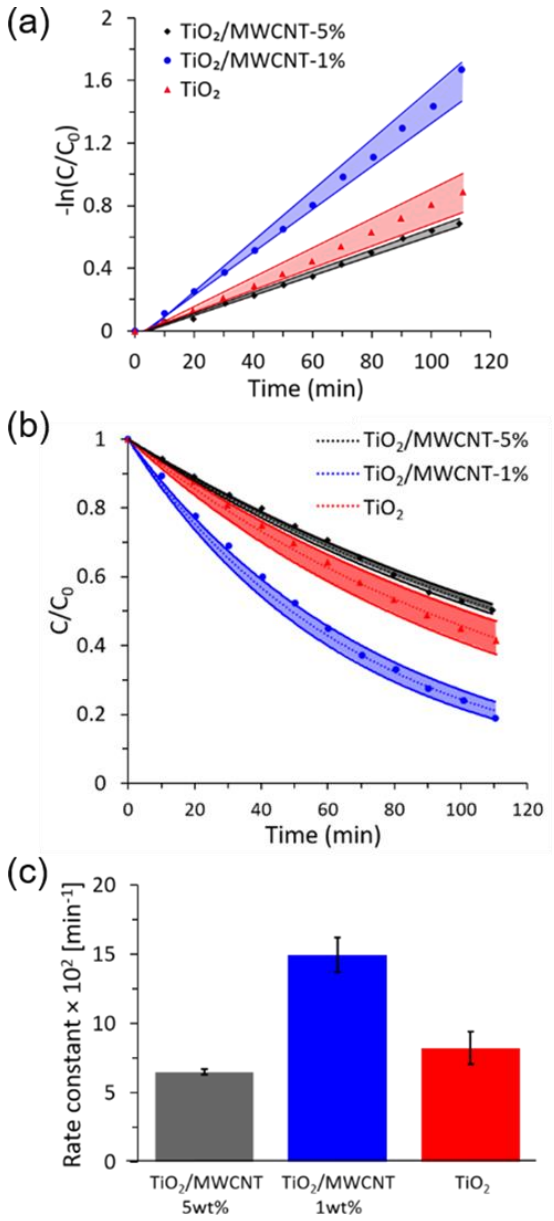

Figure 4.6. (a) Degradation curves of photocatalyst performance projection. Center lines indicate the first order rate equation derived from the average degradation data for each catalyst. (b) Photocatalytic degradation of acetaldehyde as a function of UV illumination time. (c) Comparison of the average rate constants for the photocatalytic degradation of acetaldehyde using TiO_2, TiO_2/MWCNT-1%, and TiO_2/MWCNT-5%.

The average rate constant for acetaldehyde degradation with TiO_2 is 8.23×10^{-2} min^{-1}. In particular, degradation reactions with TiO_2/MWCNT-1% resulted in a photocatalytic rate constant of 15.0×10^{-2} min^{-1}, which is higher than that of a pure TiO_2 photocatalyst by almost a factor of two. By comparison, Sano et al.[59] saw a 60% increase in acetaldehyde degradation rate using a platinum-doped TiO_2 catalyst as compared to P25 in humid air, while Vijayan et al.[60] achieved a 40% increase in reaction rate for acetaldehyde photocatalytic oxidation under UV illumination with a TiNT/SWCNT composite. It is apparent introducing a small amount of MWCNTs into a TiO_2 matrix enhances photocatalytic activity of the resulting TiO_2-based composites. Conversely, the rate constant obtained for the degradation reaction with TiO_2/MWCNT-5% is 6.50×10^{-2} min^{-1}, which is surprisingly lower than that of pure TiO_2; this indicates a further addition of MWCNTs, beyond the optimum loading ratio of 1:100 (MWCNTS:TiO_2), diminishes the effectiveness of the photocatalyst.

As mentioned earlier, the TiO_2/MWCNT-5% catalyst is characterized by a lower percentage of anatase (~67 wt%). The observed difference in photocatalytic performance is not attributed to the composition of the crystal phases because the ideal ratio of anatase to rutile for maximal PCO rates has been shown to be between 40 and 80% anatase,[61] and ratios for all synthesized photocatalysts were within this range. Electronic structure calculations for mixed rutile-anatase systems have revealed band alignment of rutile lies higher than that of anatase, resulting in hole accumulation in the valence band of rutile.[62] This conclusion supports the idea that higher rutile amounts than that in P25 may be beneficial to photocatalytic reactions that utilize holes generated in the valence band.

The TiO_2/MWCNT-1% composite is able to achieve 80% degradation of acetaldehyde after 110 min while pristine TiO_2 achieves less than 60% degradation for the same illumination

time. The primary mechanism for photocatalytic activity enhancement in TiO_2/MWCNT-1% is thought to be the result of structural effects from the addition of small amounts of MWCNTs. When higher amounts of MWCNTs are present, CNT agglomeration within the bulk catalyst occurs, resulting in TiO_2 nucleation around CNT bundles. This phenomenon is illustrated in Figure 4.7. While the average TiO_2 particle sizes are comparable, stark differences in surface area and pore volume suggest dispersion is affected by the presence of CNTs during TiO_2 particle nucleation. Without the presence of CNTs, TiO_2 particles experience some agglomeration during nucleation. Adding a small amount of MWCNTs (~1%) increased dispersion while providing nucleation sites for TiO_2 particle formation. Further addition of MWCNTs results in CNT clustering in the aqueous solution, due to their high hydrophobicity despite the oxidation of the MWCNTs. MWCNT clustering can be observed in both EDX (Figure 4.3) and Raman spectroscopic results (Figure C4.1). Raman spectra for the TiO_2/MWCNT-5% sample show substantial differences in intensity of the characteristic peaks of MWCNTs (i.e., the D-band ~1350 cm^{-1} and G-band ~1590 cm^{-1}) between the two spectra obtained from two different spots. The spectrum with carbon peaks of higher intensity exemplifies the agglomeration of CNTs in the scanned region.

MWCNT clustering results in agglomeration of TiO_2 particles around the MWCNT bundles in addition to the typical nucleation and aggregation experienced in pristine TiO_2 solution. As a consequence, surface area and total pore volume of the photocatalyst decreases, resulting in a lower photocatalytic performance. In addition, CNT light absorption may begin to hinder the effectiveness of TiO_2 as the active photocatalytic material.[63] UV-vis DRS data provided in Figure C4.3 confirms the photocatalytic activity enhancement in the TiO_2/MWCNT-1% catalyst is not due to band-gap reduction as it appears to have blue-shifted subtly compared to the TiO_2 catalyst.

These results support the hypothesis of photocatalytic enhancement from MWCNT addition due to physical effects.

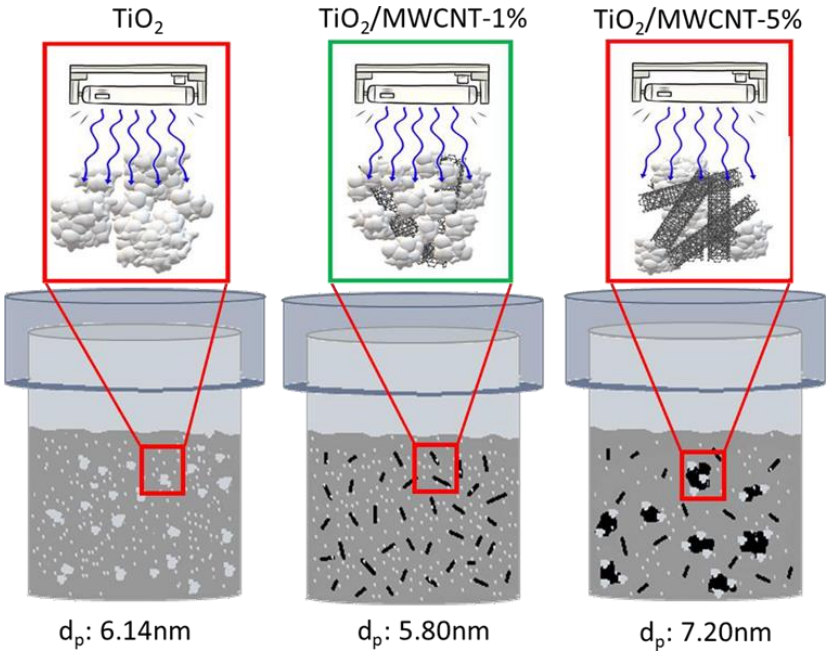

Figure 4.7. Proposed mechanism for the role of CNTs in TiO_2 nucleation and dispersion during hydrothermal synthesis of TiO_2/MWCNTs.

4.4 Conclusions

CNT/TiO_2 catalysts of different CNT:TiO_2 ratios were synthesized using a hydrothermal method. The addition of only 1wt% MWCNTs resulted in nearly double the degradation rate of acetaldehyde vapor. The observed catalytic enhancement is attributed to morphological differences caused by the presence of MWCNTs during TiO_2 particle nucleation and change in surface chemistry of the photocatalysts. The presence of small amounts of MWCNTs (~1 wt%) enhances chemisorption of water on the surface of TiO_2. Further addition of MWCNTs corresponding to 5 wt% resulted in lower photocatalytic performance, which is attributed to the agglomeration of CNTs during the hydrothermal process and possible reduction, as well as interference in the absorption of light by TiO_2.

4.5 References

1. Fujishima, A.; Honda, K., Electrochemical Photolysis of Water at a Semiconductor Electrode. *Nature* **1972,** *238* (5358), 37-38.

2. Hoffmann, M. R.; Martin, S. T.; Choi, W.; Bahnemann, D. W., Environmental Applications of Semiconductor Photocatalysis. *Chem. Rev.* **1995,** *95* (1), 69-96.

3. Kjellstrom, T.; Lodh, M.; McMichael, T.; Ranmuthugala, G.; Shrestha, R.; Kingsland, S., Air and Water Pollution: Burden and Strategies for Control. In *Disease Control Priorities in Developing Countries*, 2nd ed.; Jamison, D. T.; Breman, J. G.; Measham, A. R.; Alleyne, G.; Claeson, M.; Evans, D. B.; Jha, P.; Mills, A.; Musgrove, P., Eds. Washington (DC), 2006.

4. Amama, P. B.; Itoh, K.; Murabayashi, M., Photocatalytic oxidation of trichloroethylene in humidified atmosphere. *J. Mol. Catal. A: Chem.* **2001,** *176* (1), 165-172.

5. Amama, P. B.; Itoh, K.; Murabayashi, M., Gas-phase photocatalytic degradation of trichloroethylene on pretreated TiO2. *Appl. Catal. B: Environ.* **2002,** *37* (4), 321-330.

6. Amama, P. B.; Itoh, K.; Murabayashi, M., Photocatalytic degradation of trichloroethylene in dry and humid atmospheres: role of gas-phase reactions. *J. Mol. Catal. A: Chem.* **2004,** *217* (1), 109-115.

7. Amama, P. B.; Itoh, K.; Murabayashi, M., Effect of RuO2 deposition on the activity of TiO2: Photocatalytic oxidation of trichloroethylene in aqueous phase. *J. Mater. Sci.* **2004,** *39* (13), 4349-4351.

8. Huang, D.; Liao, S.; Quan, S.; Liu, L.; He, Z.; Wan, J.; Zhou, W., Preparation and characterization of anatase N–F-codoped TiO2 sol and its photocatalytic degradation for formaldehyde. *J. Mater. Res.* **2007,** *22* (9), 2389-2397.

9. Chan, A. H. C.; Porter, J. F.; Barford, J. P.; Chan, C. K., Effect of Thermal Treatment on the Photocatalytic Activity of TiO2 Coatings for Photocatalytic Oxidation of Benzoic Acid. *J. Mater. Res.* **2002,** *17* (7), 1758-1765.

10. Wen, J.; Li, X.; Liu, W.; Fang, Y.; Xie, J.; Xu, Y., Photocatalysis fundamentals and surface modification of TiO2 nanomaterials. *Chinese J. Catal.* **2015,** *36* (12), 2049-2070.

11. Fujishima, A.; Rao, T. N.; Tryk, D. A., Titanium dioxide photocatalysis. *J. Photoch. Photobio. C* **2000,** *1* (1), 1-21.

12. Trépanier, M.; Dalai, A. K.; Abatzoglou, N., Synthesis of CNT-supported cobalt nanoparticle catalysts using a microemulsion technique: Role of nanoparticle size on reducibility, activity and selectivity in Fischer–Tropsch reactions. *Appl. Catal. A: Gen.* **2010,** *374* (1–2), 79-86.

13. Prasai, B.; Cai, B.; Underwood, M. K.; Lewis, J. P.; Drabold, D. A., Properties of amorphous and crystalline titanium dioxide from first principles. *J. Mater. Sci.* **2012,** *47* (21), 7515-7521.

14. Frederick, J. E.; Snell, H. E.; Haywood, E. K., SOLAR ULTRAVIOLET RADIATION AT THE EARTH'S SURFACE. *Photochem. Photobiol.* **1989,** *50* (4), 443-450.

15. Heller, A., Conversion of sunlight into electrical power and photoassisted electrolysis of water in photoelectrochemical cells. *Acc. Chem. Res.* **1981,** *14* (5), 154-162.

16. Cowan, A. J.; Tang, J.; Leng, W.; Durrant, J. R.; Klug, D. R., Water Splitting by Nanocrystalline TiO2 in a Complete Photoelectrochemical Cell Exhibits Efficiencies Limited by Charge Recombination. *J. Phys. Chem. C* **2010,** *114* (9), 4208-4214.

17. Asahi, R.; Morikawa, T.; Ohwaki, T.; Aoki, K.; Taga, Y., Visible-Light Photocatalysis in Nitrogen-Doped Titanium Oxides. *Science* **2001,** *293* (5528), 269-271.

18. Wang, Y.; Wang, Y.; Meng, Y.; Ding, H.; Shan, Y.; Zhao, X.; Tang, X., A Highly Efficient Visible-Light-Activated Photocatalyst Based on Bismuth- and Sulfur-Codoped TiO2. *J. Phys. Chem. C* **2008,** *112* (17), 6620-6626.

19. Gai, Y.; Li, J.; Li, S.-S.; Xia, J.-B.; Wei, S.-H., Design of Narrow-Gap TiO2: A Passivated Codoping Approach for Enhanced Photoelectrochemical Activity. *Phys. Rev. Lett.* **2009,** *102* (3), 036402.

20. Vijayan, B. K.; Dimitrijevic, N. M.; Finkelstein-Shapiro, D.; Wu, J.; Gray, K. A., Coupling Titania Nanotubes and Carbon Nanotubes To Create Photocatalytic Nanocomposites. *ACS Catal.* **2012,** *2*, 223-229.

21. Woan, K.; Pyrgiotakis, G.; Sigmund, W., Photocatalytic Carbon-Nanotube–TiO2 Composites. *Adv. Mater.* **2009,** *21* (21), 2233-2239.

22. An, G.; Ma, W.; Sun, Z.; Liu, Z.; Han, B.; Miao, S.; Miao, Z.; Ding, K., Preparation of titania/carbon nanotube composites using supercritical ethanol and their photocatalytic activity for phenol degradation under visible light irradiation. *Carbon* **2007,** *45* (9), 1795-1801.

23. Silva, C. G.; Faria, J. L., Photocatalytic oxidation of benzene derivatives in aqueous suspensions: Synergic effect induced by the introduction of carbon nanotubes in a TiO2 matrix. *Appl. Catal. B: Environ.* **2010,** *101* (1–2), 81-89.

24. Li, N.; Ma, Y.; Wang, B.; Huang, Y.; Wu, Y.; Yang, X.; Chen, Y., Synthesis of semiconducting SWNTs by arc discharge and their enhancement of water splitting performance with TiO2 photocatalyst. *Carbon* **2011,** *49* (15), 5132-5141.

25. Zhang, W.-D.; Xu, B.; Jiang, L.-C., Functional hybrid materials based on carbon nanotubes and metal oxides. *J. Mater. Chem.* **2010,** *20* (31), 6383-6391.

26. Tan, L.-L.; Ong, W.-J.; Chai, S.-P.; Mohamed, A., Reduced graphene oxide-TiO2 nanocomposite as a promising visible-light-active photocatalyst for the conversion of carbon dioxide. *Nanoscale Res. Lett.* **2013,** *8* (1), 1-9.

27. Long, Y.; Lu, Y.; Huang, Y.; Peng, Y.; Lu, Y.; Kang, S.-Z.; Mu, J., Effect of C60 on the Photocatalytic Activity of TiO2 Nanorods. *J. Phys. Chem. C* **2009,** *113* (31), 13899-13905.

28. Yu, J.; Ma, T.; Liu, G.; Cheng, B., Enhanced photocatalytic activity of bimodal mesoporous titania powders by C60 modification. *Dalton Trans.* **2011,** *40* (25), 6635-6644.

29. Jiang, G.; Lin, Z.; Chen, C.; Zhu, L.; Chang, Q.; Wang, N.; Wei, W.; Tang, H., TiO2 nanoparticles assembled on graphene oxide nanosheets with high photocatalytic activity for removal of pollutants. *Carbon* **2011,** *49* (8), 2693-2701.

30. Xiang, Q.; Yu, J.; Jaroniec, M., Preparation and Enhanced Visible-Light Photocatalytic H2-Production Activity of Graphene/C3N4 Composites. *J. Phys. Chem. C* **2011,** *115* (15), 7355-7363.

31. Fan, W.; Lai, Q.; Zhang, Q.; Wang, Y., Nanocomposites of TiO2 and Reduced Graphene Oxide as Efficient Photocatalysts for Hydrogen Evolution. *J. Phys. Chem. C* **2011,** *115* (21), 10694-10701.

32. Wang, C.-C.; Ying, J. Y., Sol−Gel Synthesis and Hydrothermal Processing of Anatase and Rutile Titania Nanocrystals. *Chem. Mater.* **1999,** *11*, 3113-3120.

33. Cheng, H.; Ma, J.; Zhao, Z.; Qi, L., Hydrothermal Preparation of Uniform Nanosize Rutile and Anatase Particles. *Chem. Mater.* **1995,** *7*, 663-671.

34. Kotsyubynsky, V. O.; Myronyuk, I. F.; Myronyuk, L. I.; Chelyadyn, V. L.; Mizilevska, M. H.; Hrubiak, A. B.; Tadeush, O. K.; Nizamutdinov, F. M., The effect of pH on the nucleation of titania by hydrolysis of TiCl4. *Materialwiss. Werkstofftech.* **2016,** *47* (2-3), 288-294.

35. Zhang, B.; Shi, R.; Zhang, Y.; Pan, C., CNTs/TiO_2 composites and its electrochemical properties after UV light irradiation. *Prog. Nat. Sci.: Mater. Int.* **2013,** *23* (2), 164-169.

36. Jitianu, A.; Cacciaguerra, T.; Benoit, R.; Delpeux, S.; Béguin, F.; Bonnamy, S., Synthesis and characterization of carbon nanotubes–TiO2 nanocomposites. *Carbon* **2004,** *42* (5-6), 1147-1151.

37. Silva, R. M.; Noremberg, B. S.; Marins, N. H.; Milne, J.; Zhitomirsky, I.; Carreño, N. L. V., Microwave-assisted hydrothermal synthesis and electrochemical characterization of niobium pentoxide/carbon nanotubes composites. *J. Mater. Res.* **2019,** *34* (4), 592-599.

38. Hulin, M.; Caillaud, D.; Annesi-Maesano, I., Indoor air pollution and childhood asthma: variations between urban and rural areas. *Indoor Air* **2010,** *20* (6), 502-514.

39. Marchand, C.; Bulliot, B.; Le Calvé, S.; Mirabel, P., Aldehyde measurements in indoor environments in Strasbourg (France). *Atmos. Environ.* **2006,** *40* (7), 1336-1345.

40. An, T.; Chen, J.; Nie, X.; Li, G.; Zhang, H.; Liu, X.; Zhao, H., Synthesis of Carbon Nanotube–Anatase TiO2 Sub-micrometer-sized Sphere Composite Photocatalyst for Synergistic Degradation of Gaseous Styrene. *ACS Appl. Mater. Inter.* **2012,** *4* (11), 5988-5996.

41. Chen, J.; Li, G.; Huang, Y.; Zhang, H.; Zhao, H.; An, T., Optimization synthesis of carbon nanotubes-anatase TiO2 composite photocatalyst by response surface methodology for photocatalytic degradation of gaseous styrene. *Appl. Catal. B: Environ.* **2012,** *123-124*, 69-77.

42. Suchanek, W. L.; Riman, R. E., Hydrothermal Synthesis of Advanced Ceramic Powders. *Adv. Sci. Technol.* **2006,** *45*, 184-193.

43. Czecha, B.; Oleszczuka, P.; Wiącek, A., Advanced oxidation (H2O2 and/or UV) of functionalized carbon nanotubes (CNT-OH and CNT-COOH) and its influence on the stabilization of CNTs in water and tannic acid solution. *Environ. Pollut.* **2015,** *200*, 161-167.

44. Almkhelfe, H.; Li, X.; Thapa, P.; Hohn, K. L.; Amama, P. B., Carbon nanotube-supported catalysts prepared by a modified photo-Fenton process for Fischer–Tropsch synthesis. *Journal of Catalysis* **2018,** *361*, 278-289.

45. Hahn, H.; Logas, J.; Averback, R. S., Sintering characteristics of nanocrystalline TiO2. *J. Mater. Res.* **1990,** *5* (3), 609-614.

46. Brunauer, S.; Emmett, P. H.; Teller, E., Adsorption of Gases in Multimolecular Layers. *J. Am. Chem. Soc.* **1938,** *60* (2), 309-319.

47. Barrett, E. P.; Joyner, L. G.; Halenda, P. P., The Determination of Pore Volume and Area Distributions in Porous Substances. I. Computations from Nitrogen Isotherms. *J. Am. Chem. Soc.* **1951,** *73* (1), 373-380.

48. Mutuma, B. K.; Shao, G. N.; Kim, W. D.; Kim, H. T., Sol–gel synthesis of mesoporous anatase–brookite and anatase–brookite–rutile TiO2 nanoparticles and their photocatalytic properties. *J. Colloid Interf. Sci.* **2015,** *442*, 1-7.

49. Zhang, Y.; Tang, Z.-R.; Fu, X.; Xu, Y.-J., TiO2−Graphene Nanocomposites for Gas-Phase Photocatalytic Degradation of Volatile Aromatic Pollutant: Is TiO2−Graphene Truly Different from Other TiO2−Carbon Composite Materials? *ACS Nano* **2010,** *4* (12), 7303-7314.

50. Xia, X.-H.; Jia, Z.-J.; Yu, Y.; Liang, Y.; Wang, Z.; Ma, L.-L., Preparation of multi-walled carbon nanotube supported TiO2 and its photocatalytic activity in the reduction of CO2 with H2O. *Carbon* **2007,** *45* (4), 717-721.

51. Zhu, Y.; Liu, T.; Ding, C., Structural characterization of TiO2 ultrafine particles. *J. Mater. Res.* **1999,** *14* (2), 442-446.

52. Spurr, R. A.; Myers, H., Quantitative Analysis of Anatase-Rutile Mixtures with an X-Ray Diffractometer *Anal. Chem.* **1957,** *29* (5), 760-762.

53. Papo, C.; Tetana, Z.; Franklyn, P.; Mhlanga, S., Synthesis and study of carbon/TiO2 and carbon/TiO2 core–shell micro-/nanospheres with increased density. *J. Mater. Res.* **2013,** *28* (3), 440-448.

54. Khodakov, A. Y.; Chu, W.; Fongarland, P., Advances in the Development of Novel Cobalt Fischer−Tropsch Catalysts for Synthesis of Long-Chain Hydrocarbons and Clean Fuels. *Chem. Rev.* **2007,** *107* (5), 1692-1744.

55. Li, J.; Xu, Y.; Wu, D.; Sun, Y., Hollow mesoporous silica sphere supported cobalt catalysts for F–T synthesis. *Catal. Today* **2009,** *148* (1), 148-152.

56. Yu, Y.; Yu, J. C.; Chan, C.-Y.; Che, Y.-K.; Zhao, J.-C.; Ding, L.; Ge, W.-K.; Wong, P.-K., Enhancement of adsorption and photocatalytic activity of TiO_2 by using carbon nanotubes for the treatment of azo dye. *Appl. Catal. B: Environ.* **2005,** *61*, 1-11.

57. Yu, J.; Yu, J. C.; Ho, W.; Jiang, Z., Effects of calcination temperature on the photocatalytic activity and photo-induced super-hydrophilicity of mesoporous TiO2 thin films. *New J. Chem.* **2002,** *26* (5), 607-613.

58. Sopyan, I.; Watanabe, M.; Murasawa, S.; Hashimoto, K.; Fujishima, A., An efficient TiO2 thin-film photocatalyst: photocatalytic properties in gas-phase acetaldehyde degradation. *J. Photochem. Photobiol. A: Chem.* **1996,** *98* (1), 79-86.

59. Sano, T.; Negishi, N.; Uchino, K.; Tanaka, J.; Matsuzawa, S.; Takeuchi, K., Photocatalytic degradation of gaseous acetaldehyde on TiO_2 with photodeposited metals and metal oxides. *J. Photochem. Photobiol. A: Chem.* **2003,** *160*, 93-98.

60. Vijayan, B. K.; Dimitrijevic, N. M.; Finkelstein-Shapiro, D.; Wu, J.; Gray, K. A., Coupling Titania Nanotubes and Carbon Nanotubes To Create Photocatalytic Nanocomposites. *ACS Catalysis* **2012,** *2* (2), 223-229.

61. Su, R.; Bechstein, R.; So, L.; Vang, R. T.; Sillassen, M.; Esbjornsson, B.; Palmqvist, A.; Besenbacher, F., How the Anatase-to-Rutile Ratio Influences the Photoreactivity of TiO_2. *J. Phys. Chem. C* **2011,** *115*, 24287-24292.

62. Deak, P.; Aradi, B.; Frauenheim, T., Band Lineup and Charge Carrier Separation in Mixed Rutile-Anatase Systems. *J. Phys. Chem. C* **2011,** *115*, 3443-3446.

63. Yu, Y.; Yu, J. C.; Yu, J.-G.; Kwok, Y.-C.; Che, Y.-K.; Zhao, J.-C.; Ding, L.; Ge, W.-K.; Wong, P.-K., Enhancement of photocatalytic activity of mesoporous TiO2 by using carbon nanotubes. *Appl. Catal. A Gen.* **2005,** *289* (2).

Chapter 5 - Photocatalytic NO_x Mitigation Under Relevant Conditions Using Carbon Nanotube-Modified Titania

Chapter 5 is reprinted with permission from:

Everhart, B. M.; McAuley, B.; Al Mayyahi, A.; Tonyali, B.; Yucel, U.; Amama, P. B., Photocatalytic NOx mitigation under relevant conditions using carbon nanotube-modified titania. *Chemical Engineering Journal* **2022,** *446*, 136984

5.1 Introduction

Nitrogen oxides (NO_x), classified as criteria air pollutants by the Environmental Pollution Agency (EPA), are not only harmful at concentrations as low as 21ppb (40ug/m^3),[1] but also react in atmosphere to generate tropospheric ozone, resulting in smog[2-4] and even contribute to particulate matter ($PM_{2.5}$) pollution concentrations via formation of nitrate aerosols.[5] NO_x is a generic term that refers to a mixture of nitrogen monoxide (NO) and dioxide (NO_2). Each of these pollutants is monitored by the EPA and World Health Organization (WHO) as they lead to respiratory issues including infection and irritation due to their ability to act as free radicals and induce high oxidative stress.[6] Over 90% of all atmospheric NO_x originates from anthropogenic sources, including energy production and distribution, and energy use in industry.[4] At combustion temperatures, the equilibrium constant for the following reaction increases exponentially, leading to substantial NO_x formation.

$$N_2 + O_2 \leftrightarrow 2NO \tag{5.1}$$

The conventional approach for reducing ambient NO_x concentrations requires elimination at the source via selective catalytic reduction (SCR) of flue gas or vehicle exhaust.[7-10] SCR introduces a reductant, such as ammonia or urea, to reduce NO_x to N_2, therefore reducing emissions

at the source.[9, 10] Because flue gas can contain hundreds of ppb of NO_x, even efficient conversion of NO_x by SCR results in emission with concentrations nearly 1000× greater than the WHO permissible exposure limits.[5, 7] Once NO_x disperses into the atmosphere, passive air purification techniques that are effective at sub-ppb level concentrations are required to convert the dilute NO_x concentrations to innocuous compounds.

Heterogeneous photocatalysis using semiconductors has been studied as an effective method to eliminate atmospheric pollutants, including NO_x.[11-27] Photocatalytic oxidation of NO to nitrates first requires the generation of reactive oxygen species (ROS) via reactions with photogenerated excited electrons and holes. Once ROS are generated, NO oxidizes to NO_2 before converting to HNO_3 via the following reactions:[28]

$$TiO_2 + hv \rightarrow e_{CB}^- + h_{VB}^+ \quad (5.2)$$

$$h_{VB}^+ + H_2O_{ads} \rightarrow HO_{ads}^\bullet + H^+ \quad (5.3)$$

$$h_{VB}^+ + HO_{ads}^- \rightarrow HO_{ads}^\bullet \quad (5.4)$$

$$e_{CB}^- + O_{2_{ads}} \rightarrow O_{2_{ads}}^{\bullet -} \quad (5.5)$$

The use of the gold standard TiO_2 (or P25) in photocatalysis suffers from two major limitations which severely limits its ability to efficiently remove atmospheric NO_x: rapid recombination rate of electrons and holes that diminish its efficiency, and a wide band gap (E_g = 3.2 eV for anatase) that confines its photoactivity to the UV range.[19, 29] To address the former, studies have mostly focused on coupling with a noble metal/narrow band-gap semiconductor to form Schottky barriers or heterojunctions.[13, 30-32] With the advent of nanocarbons, recent efforts have focused on exploiting their exceptional properties in designing efficient TiO_2-nanocarbon hybrid photocatalysts. Composites such as graphene-TiO_2[19, 21, 29] and TiO_2-graphene-carbon nitride (g-C_3N_4)[21, 33, 34] have been used in photocatalytic oxidation of NO_x and have shown enhanced performance. While carbon nanotube-titania (CNT-TiO_2) photocatalysts have been

applied in aqueous phase and gas phase studies involving other VOCs, there is surprisingly little research presented on their ability to degrade NO_x.[35-37] Liu et al. investigated Cu-doped TiO_2 supported on CNTs for SO_2 and NO removal, but did not monitor NO_2 or NO_x concentrations.[35] Li et al.[36] introduced CNTs to a traditional V_2O_5/TiO_2 catalyst for SCR of high NO concentrations (200ppm) while Yen et al.[37] synthesized CNT-TiO_2 composites and tested their photocatalytic performance in 1000 ppb NO, obtaining modest conversion (32% NO_x conversion).

As shown in Equations 3 and 4, the generation of ROS requires adsorbed moisture. While a humid environment is favorable for generation of hydroxyl radicals due to increased adsorption of water molecules, elevated relative humidity can have an adverse effect on the conversion of NO_x. A few studies have shown the increase of NO conversion as humidity increases due to the increased generation of hydroxyl radicals[38, 39] Others, however, have reported humidity reduces NO conversion due to the competitive adsorption of water and the target pollutant molecule[14, 40-44]. For oxidation of NO_x, there is therefore strong evidence that elevated humidity levels will lead to reduced NO_x conversion with traditional photocatalysts at low concentrations (< 1ppb). This may be attributed in part to competitive adsorption of water and NO_x, where water molecules outnumber NO_x molecules by several orders of magnitude. On the other hand, high NO concentrations may benefit from elevated humidity, as a larger quantity of hydroxyl radicals would be required for oxidation reactions. While some of these studies concluded that NO conversion to NO_2 decreased with increasing humidity,[14, 41, 44] others suggested that impaired NO_x oxidation is due to increased NO_2 generation despite relatively constant NO conversion.[16, 45] Flue gas contains the products of combustion that includes a large amount of moisture even when mixed with outdoor air. For successful coupling with existing remediation technology, it is important to understand the role of humidity in NO_x removal. Unfortunately, thus far, there is no conclusive

understanding of the role of humidity in complete oxidation of NO_x to nitrates. In particular, there have been no reports on performance of CNT-TiO_2 photocatalysts at different humidity levels or their $DeNO_x$ ability under any set of conditions.

In this study, CNT-TiO_2 hybrid photocatalyst films with optimum amount of CNTs were systematically investigated in NO_x oxidation under conditions that will enable their implementation as part of flue gas treatment system, downstream of SCR and prior to emission to the atmosphere. The desired photocatalyst is required to maintain effective De-NO_x ability under variable humidity, concentrations, catalyst conditions (fresh vs. used), and NO_x ratios. To determine the ability of a photocatalyst to eliminate the hazards associated with NO_x pollution, we have calculated the "De-NO_x index," a measure of photonic efficiency during NO_x abatement, for CNT-TiO_2 and a reference (P25) under the different oxidation conditions. Utilizing the De-NO_x index, an objective figure of merit for photocatalytic NO_x abatement, in tandem with relative NO_x oxidation has provided a better understanding of the photocatalyst performance. We have examined, for the first time, the effect of the reactor headspace distance thereby probing the role of mass transfer limitations in the photocatalytic process. Evaluation of the performance of recycled and fresh photocatalysts has provided valuable insight into their stability. Furthermore, the study provides valuable insight into the mechanism of NO_x oxidation, specifically as it pertains to NO_x storage selectivity and De-NO_x index using electron paramagnetic resonance spectroscopy (EPR) to determine the relative formation of hydroxyl and superoxide radicals for P25 and CNT-TiO_2 photocatalysts.

5.2 Experimental

5.2.1 Oxidation of CNTs

Multi-walled CNTs (MWCNTs) obtained from Times Nano (diameter 20-30 nm, purity >95%) were photo-oxidized using H_2O_2 (Fisher Scientific, 30 wt%) via UV irradiation (White-Rodger Comfort plus UV200 2 Phillips TUV PL-L 60 W Bulbs) as described elsewhere.[46, 47] In a typical batch, 1 g of CNTs were added to 400 ml of H_2O_2 in a round bottom flask. The mixture was sonicated for 15 minutes to uniformly disperse the CNTs. The CNTs were then heated to 60°C under constant stirring and UV irradiation for 72 hours; 50 ml of H_2O_2 was added every 24 hours to make up for evaporation. The CNTs were vacuum filtered, rinsed with deionized water, and dried at 50°C for 20 hours to yield CNT powders with oxygen-containing functional groups on the surface.

5.2.2 Synthesis of CNT-TiO_2 hybrid photocatalyst

Synthesis of CNT-TiO_2 composite was performed via a modified sol-gel process, adapted from the method developed by Yu et al.[48] The optimum amount of CNTs, as determined previously,[47] was used in the synthesis of CNT-TiO_2 hybrids. First, functionalized CNTs were dispersed in ethanol for 30 minutes via sonication. Second, the titanium precursor, titanium (IV) isopropoxide (Sigma Aldrich, > 97%), was added dropwise to the ethanol/CNT solution and the resulting solution sonicated for 30 minutes to disperse the precursor. Addition of 80 mL nitric acid (0.001M) to the solution, resulted in the formation of a viscous, grey sol. The sols were sonicated for 30 minutes to ensure completion of the reaction before aging at 25°C for 20 hours. The product was vacuum filtered, rinsed with DI water and dried for 12 hours at 80°C. The resulting powders were crushed and calcined at 400°C for 3 hours. A total of 12 batches of photocatalyst were

synthesized and were uniformly mixed into a large reserve to allow for use of identical fresh catalyst for each NO_x degradation experiment.

5.2.3 Coating of photocatalysts

The calcined CNT-TiO_2 photocatalysts were sieved to <125μm to increase powder uniformity and dispersion in solution. The photocatalyst powder was then dispersed in ethanol at a ratio of 0.15g/ml and sonicated for 15 minutes following established steps by Weon and Choi.[49] The solution was drop cast onto glass slides (50 mm × 100 mm) via a pipet. A doctor blade set to a height of 250 μm above the slide was pulled across the surface to ensure a uniform coating thickness. Approximately, 0.25g of photocatalyst was deposited on each slide. The slides were then allowed to dry before being stored until testing.

5.2.4 Characterization of photocatalysts

X-ray diffraction (XRD) patterns of P-25 and the synthesized CNT-TiO_2 photocatalysts were obtained from a Rigaku MiniFlex II diffractometer utilizing a Cu Ka radiation source. Two-theta scanning angles from 10° to 80° degrees were taken with a step size of 0.02° and a scan speed of 2.0°/min. Scanning electron microscopy (SEM) with energy dispersive X-ray spectroscopy (EDX) was used to study the morphology and composition of photocatalysts. SEM images and EDX profiles were obtained using a Hitachi S5200, operated at 10 kV. The samples were characterized by UV-visible diffuse reflectance spectroscopy (UV-vis DRS) using a Shimadzu UV-2600 spectrometer with $BaSO_4$ as the background material. Photoluminescence (PL) spectroscopy was performed using a spectraMax i3x multi-mode microplate reader with an excitation wavelength of 360 nm. Thermogravimetric analysis (TGA) of photocatalysts was

performed on a Shimadzu TGA-50 Analyzer. Roughly 8 mg of each sample was heated under a stream of air flow (10 mL/min) from room temperature to 600 °C at a rate of 5 °C/ min. X-ray photoelectron spectroscopy (XPS) data were collected using a PHI 5000 VersaProbe II (Physical Electronics Inc.) spectrometer with a monochromated Alk_{α} X-ray source, at ultrahigh vacuum ($1x10^{-9}$ bar) using an X-ray beam size of 100 μm. Survey spectra were recorded with pass energy (PE) of 117 eV, step size 1 eV and dwell time 20 ms, whereas high-energy resolution spectra were recorded with PE of 47eV, step size 0.1 eV and dwell time 20ms. Surface area and pore volume were derived from N_2 adsorption–desorption measurements at -196 °C. The BET method was applied to the adsorption isotherm (relative pressure range of 0.02–0.35) to calculate specific surface areas.[50] Pore-size distribution was obtained from the desorption isotherm at a relative pressure of 0.99 using the BJH model.[51]

Electron paramagnetic resonance (EPR) spectroscopy measurements were performed using a stable nitroxide spin trap, 5,5-dimethyl-1-pyrroline-N-oxide (DMPO, Enzo Life Sciences, Plymouth Meeting, MI, USA) following the method described in Brezova et al.[52] The catalysts (0.2 mg/mL) were dispersed in water with sodium dodecyl sulfate (SDS, 0.2 mg/mL) as a surfactant to inhibit catalyst particle aggregation in an ultrasonic bath for 15 minutes. Then, an aliquot of freshly-prepared DMPO solution (0.2 M) was added into the catalyst solution (10 mM DMPO final concentration), which was immediately irradiated with UV light under continuous stirring. After 5 minutes, an aliquot of solution (100 μL) was transferred to a borosilicate capillary tube, and sealed with vinyl plastic putty (Leica Microsystems, Wetzlar, Germany). The samples were inserted to the center of EPR cavity (SpinscanX, ADANI, Minsk, Belarus) analyzed using the following parameters: microwave frequency 93 kHz, microwave power 10 mW, center field 336.4 mT, sweep width 10 mT, and modulation amplitude 200 uT. The formation of DMPO-ROS

spin adducts was quantified by calculating the total area under the curve via double-integration of the characteristic EPR peaks using GRAMS/AI™ Spectroscopy Software (Thermo Scientific™, Version 9).

The formation of superoxide radicals was investigated as follows. The photocatalysts were dispersed in water (10 mL) containing ethanol (1%, v/v) to final concentrations of 0.2 mg/mL and 1 mg/mL for P25 and CNT-TiO_2, respectively, using an ultrasonic bath for 15 minutes. An aliquot of freshly prepared DMPO solution (0.2 M) was added into the photocatalyst solution (50 mM final DMPO concentration), which was immediately irradiated with UV light under continuous stirring. After 5 minutes, 100 µL of solution was transferred to a capillary tube, and sealed with vinyl plastic putty. The samples were immediately inserted to the center of EPR cavity and analyzed using the parameters described above. In EPR experiments, dispersion of the catalyst in solution is imperative for accurate analysis of a catalyst's ability to generate hydroxyl radicals upon illumination. EPR experiments revealed the importance of catalyst dispersion for determining accurate OH radical generation.

5.2.5 Photocatalytic performance evaluation

Photocatalytic oxidation experiments were conducted at room temperature in a laminar-flow reactor constructed in accordance to ISO standards.[53] Two gas lines were connected to the reactor: the first contained 100 ppm NO in nitrogen while the second contained breathable air. Gases flowed through their respective mass flow controllers into a bubbler/bypass apparatus, enabling both humidity control and improved mixing of the gases upstream of the reactor. The relative humidity was monitored using a SensorPush HT1 humidity sensor. The reactor chamber was constructed from steel with a quartz glass window enabling UV light penetration to the photocatalyst surface. The sample holder within the reactor, constructed from PLA (polylactic acid

polymer), held photocatalyst samples directly underneath the lighting apparatus. Photocatalysts were illuminated with four UVA/UVB AgroMax Pure UV fluorescent lights (2 ft F24T5HO Pure UV, 75% UV-B / 25% UV-A) producing a UVA/UVB intensity reading of approximately 2 mW/cm^2. A Chemiluminescent 42C Low Source analyzer from Thermo Fisher Scientific was used to continuously measure the concentration of NO and NO_x. Figures 5.1a and b provide a schematic illustration of the reactor apparatus.

Prior to conducting each experiment, a different catalyst substrate was inserted into the sample holder and irradiated with UV light for ≥ 1 hour with continuous airflow to remove any adsorbed contaminants. The lights were then turned off and NO_x was flowed with the air for 30 minutes to allow for adequate adsorption onto the photocatalyst surface. The UV lights were then turned on for 2 hours under a constant flow of NO_x before the lights were turned off and NO_x levels allowed to re-equilibrate. Once each photocatalytic oxidation experiment was completed, concentrations of NO, NO_2, and NO_x were saved at one-minute intervals. Relative concentrations were determined by dividing the concentration at time t (C_t) by initial values (C_0). Average conversion percentages were determined after replicating each experiment (2-4 experiments per datum point). De-NO_x index values were calculated from these averaged relative concentration values.

Figure 5.1c provides a graphic of the experimental conditions investigated. The effect of humidity was determined before investigating other conditions. Experiments were performed at 1000 ppb initial NO_x concentration and a total airflow of 3000 sccm at different RH levels (10-70% RH). Next, experiments were performed at different initial concentration levels (100-1000ppb NO_x) at low (10% RH) and high (50% RH) humidity. After these experiments, the effect of headspace on the photocatalytic process (or the possibility of mass transfer limitations convoluting

the DeNO$_x$ index) was explored. These experiments were performed by changing the height of the sample holder (headspace distance), which involved directly changing the headspace in the reactor between 2 and 8mm.

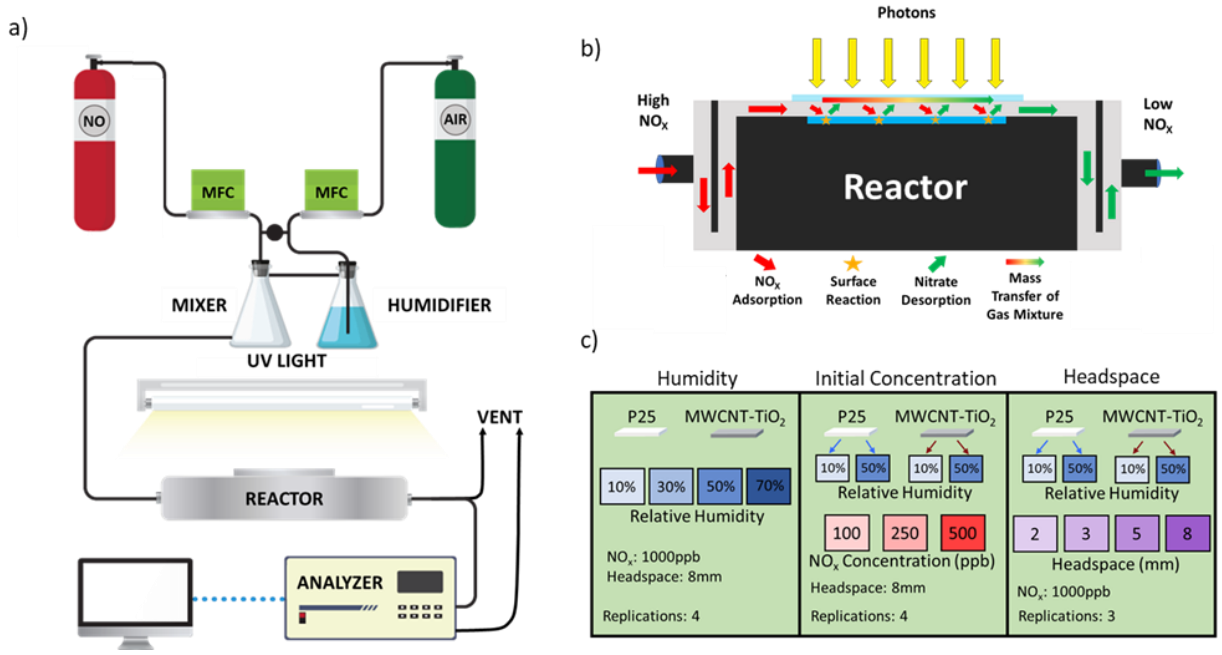

Figure 5.1. (a) Schematic illustration of the photocatalytic reactor setup. (b) Schematic illustration of the laminar-flow reactor configuration constructed according to ISO standards showing NO$_x$ flow and oxidation on photocatalyst surface. (c) Overview of experiments conducted.

5.3 Results and Discussion

5.3.1 Characterization of photocatalysts

XRD was used to determine the crystal structure of the photocatalysts. Figure 5.2a shows XRD patterns of P25 and CNT-TiO$_2$ and their corresponding peak assignments. Patterns for each individual CNT-TiO$_2$ batch prior to mixing are presented in Figure D5.1a; they confirm the batch-to-batch uniformity of the synthesized CNT-TiO$_2$. Clear differences between CNT-TiO$_2$ and P25 can be gleaned from the XRD patterns. Table 5.1 provides crystallographic (XRD) and surface area (BET) data. First, CNT-TiO$_2$ predominantly contains anatase (78%) with the remaining

fraction is comprised of brookite (121). As expected, P25 contains a notable fraction of the rutile (110) crystal phase (18%), while containing no brookite (121). The presence of anatase and rutile in P25, and anatase and brookite in CNT-TiO_2 was confirmed with Raman spectroscopy (Figure D5.1c).

Another apparent difference is crystal size, as the peak width of CNT-TiO_2 is broader than that of P25. The crystallite size calculated from the Scherrer equation for CNT-TiO_2 and P25 is 8.1nm and 21.4nm, respectively. These results indicate a relatively smaller anatase crystal size in CNT-TiO_2 as compared to P25. The small anatase crystal size for the CNT-TiO_2 sample was in part due to the use of dilute (0.001M) nitric acid during synthesis in place of deionized water. The use of nitric acid lowers the pH of the solution and has been shown to reduce crystallite size of TiO_2 powders.[54] Smaller crystallite size, along with the presence of CNTs, results in a higher surface area relative to P25. Figure D5.2 provides nitrogen adsorption-desorption isotherms, as well as optical microscopic images of catalyst films deposited on glass substrates. Tauc plots of the photocatalysts (inset of Figure 5.2b) generated from their UV-vis spectra (Figure 5.2b) were used to determine their band gaps assuming a direct allowed transition ($\gamma = 0.5$) and following the steps outlined in the literature [55]. The band gaps obtained for P25 and CNT-TiO_2 were ~3.3 eV and ~3.2 eV, respectively.

Figure 5.2 (c-e) shows SEM and EDS images of CNT-TiO_2 (c and d) and P25 (e and f). The images in panels (c) and (e) show the comparable macrostructure of both photocatalysts, and the small crystallite size of CNT-TiO_2 is verified by the SEM image of the microstructure (Figure D5.1). EDS results showing the elemental compositions are presented as insets in panels (d) and (f). P25 and CNT-TiO_2 contain 2.1 wt% and 4.2 wt % of carbon, respectively. We attribute the carbon present in P25 to background contamination; thus, the estimate of the actual carbon

concentration in CNT-TiO_2 is approximately 2 wt%, slightly higher than the nominal concentration of 1 wt%. A carbon concentration of 2 wt% in CNT-TiO_2 may indicate the reduced yield of TiO_2 during the synthesis process. Additional characterization of the catalyst films are summarized in the supplementary section (Tables D5.1-2).

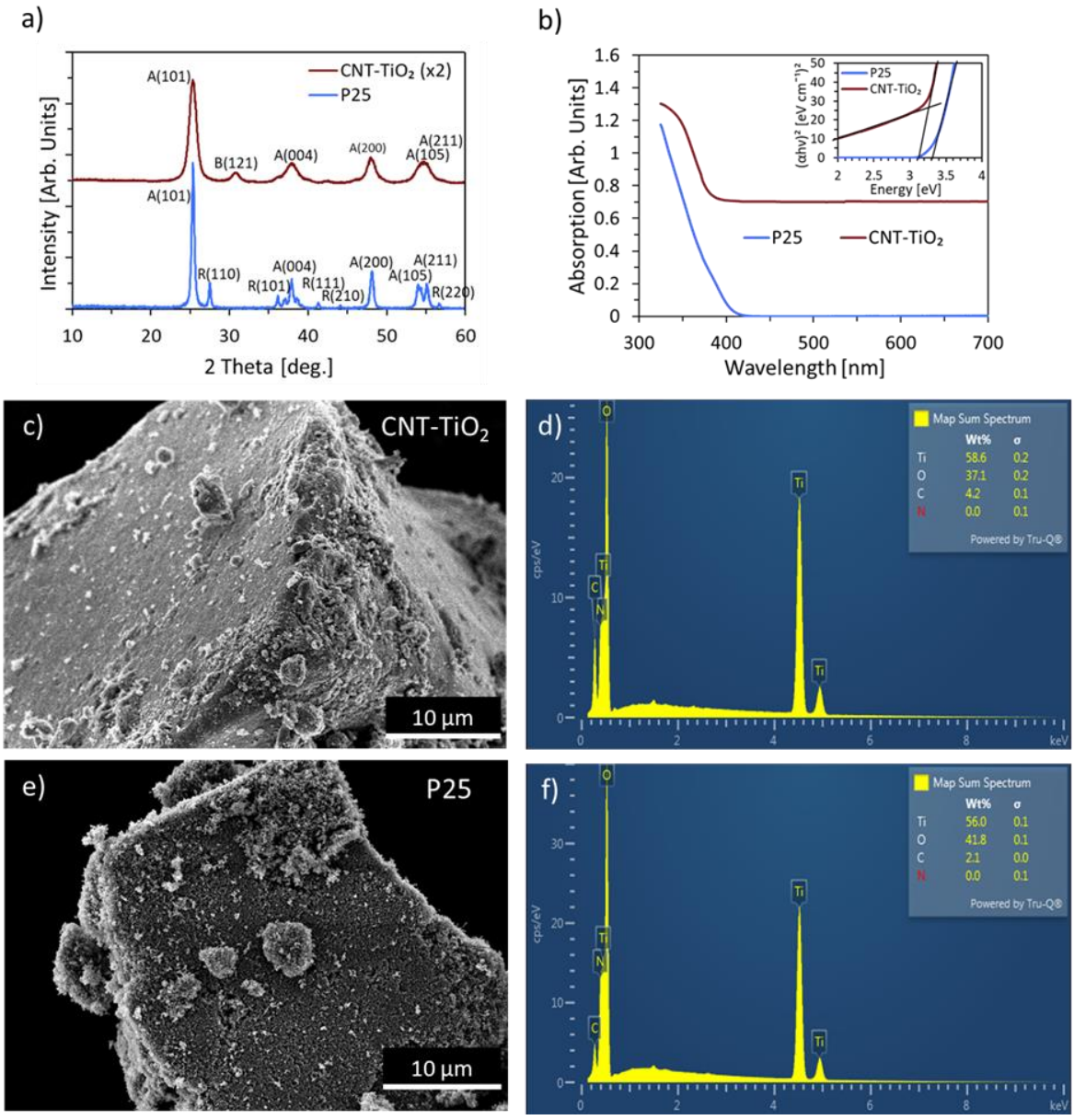

Figure 5.2. (a) XRD patterns for CNT-TiO_2 (red) and P25 (blue) photocatalysts. (b) UV-Vis spectra of CNT-TiO_2 (red) and P25 (blue) photocatalysts (inset: Tauc plots of the photocatalysts). SEM images of CNT-TiO_2 (c) and P25 (e), and corresponding EDS spectra and chemical composition including weight percentage of carbon for CNT-TiO_2 (d) and P25 (f).

Table 5.1. Catalyst powder characterization

	P25	CNT-TiO_2
Surface Area (m^2/g)[a]	51.6	131.0
Average Pore Diameter (nm)[a]	24.2	7.2
Total Pore Volume (cm^3/g)[a]	0.31	0.24
Anatase Content (wt%)[b]	81.9	77.8
Rutile Content (wt%)[b]	18.1	0.0
Brookite Content (wt%)[b]	0.0	22.2
Anatase Crystal Size (nm)[b]	21.4	8.1

[a] Nitrogen physisorption
[b] XRD

5.3.2 Effect of humidity

Representative photocatalytic oxidation profiles in Figure 5.3 show typical degradation of NO, NO_2 and NO_x on CNT-TiO_2 and P25 at low (10% RH) and high humidity (50% RH). Oxidation profiles in each figure has four distinct regions labelled 1– 4: (1) initiation of NO_x flow indicated by the steep rise in relative concentration (~10 min), (2) NO_x equilibration with the lights off (~30 min), (3) oxidation under illumination (~120 min), and (4) NO_x re-equilibration after lights are shut off (~160 min). When NO_x flow is initiated, a slightly higher concentration flows through the reactor to increase adsorption before the flow decreases to the desired concentration. At low RH (Figures 5.3a-c), when the lights are turned on, profiles for NO, NO_2, and NO_x all immediately decrease to roughly half of the initial concentrations for both CNT-TiO_2 and P25. However, at 50% RH (Figures 5.3d-f) the NO_2 degradation profiles for the photocatalysts show stark contrast in their relative concentrations, leading to notable differences in the overall NO_x profiles. While the NO_2 profile for the CNT-TiO_2 photocatalyst exhibits substantial reduction in concentration under illumination, the NO_2 profile for P25 actually increases to values even higher than the initial concentration. Despite differences in the concentration profiles under illumination, concentrations of NO, NO_2, and NO_x, all quickly re-equilibrate back to a concentration of 1000

ppb after the lights are turned off before NO_x flow is shut off and the concentrations decrease sharply as air purges the system.

To further investigate the photocatalytic performance under different conditions, the widely used and objective figure of merit for photocatalytic NO_x abatement, the $DeNO_x$ index, was used. The index provides a measurement of the overall photocatalyst performance in NO_x removal, as it considers NO conversion as well as NO storage selectivity, defined as the percentage of NO completely oxidized to nitrates versus the total amount of NO oxidized to NO_2. To calculate $DeNO_x$ index, the photonic efficiency for NO, NO_2, and NO_x must first be calculated using the following equation:[17]

$$\xi = \frac{(c_d - c_i)\dot{V}p}{\varphi ART} \tag{5.6}$$

where ξ represents the photonic efficiency of a given species; c_d and c_i the species concentrations in the dark and under illumination, respectively; $\dot{V}$ the volumetric flow rate; p the pressure in the system (1 atm for this work); and φ the photon flux at the photocatalyst surface, which is dependent on the wavelength of light (320 nm) and intensity (20 W/m^2). A, R, and T, are the catalyst irradiated area (5cm × 10cm), gas constant, and temperature (K), respectively. Once the photonic efficiency was calculated for each species, $DeNO_x$ and NO_x storage selectivity (S) were calculated via the following equations:

$$\xi_{DeNO_x} = \xi_{NO_x}\left(3 - \frac{2}{S}\right) \tag{5.7}$$

$$S = \frac{\xi_{NO_x}}{\xi_{NO}} \tag{5.8}$$

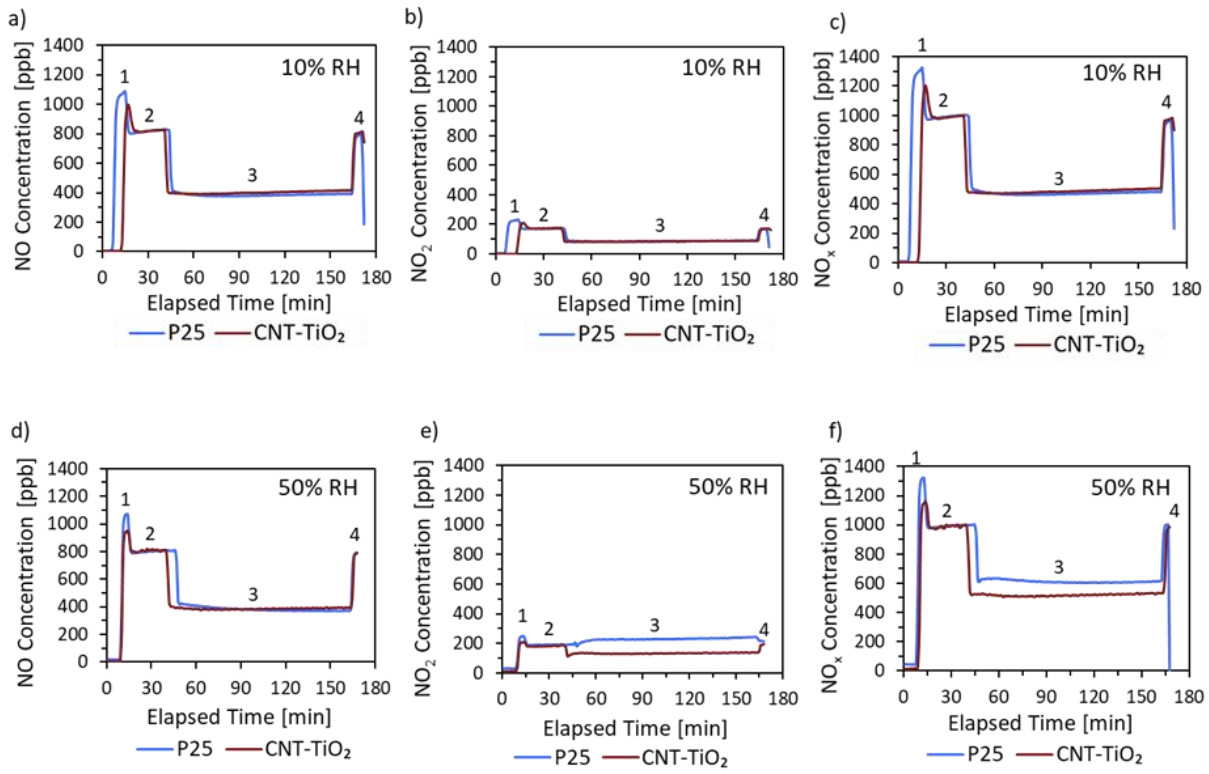

Figure 5.3. Representative NOx degradation profiles at over 2 hours using an initial NO_x concentration of 1000ppb at low humidity (10% RH) for NO (a), NO_2 (b), and NO_x (c); and at high humidity (50% RH) for NO (d), NO_2 (e), NO_x (f). Each degradation profile has four distinct regions: (1) initiation of NO_x flow indicated by the steep rise in relative concentration (~10 min), (2) NO_x equilibration with the lights off (~30 min), (3) degradation under illumination (~120 min), and (4) NO_x re-equilibration after lights are shut off (~10 min).

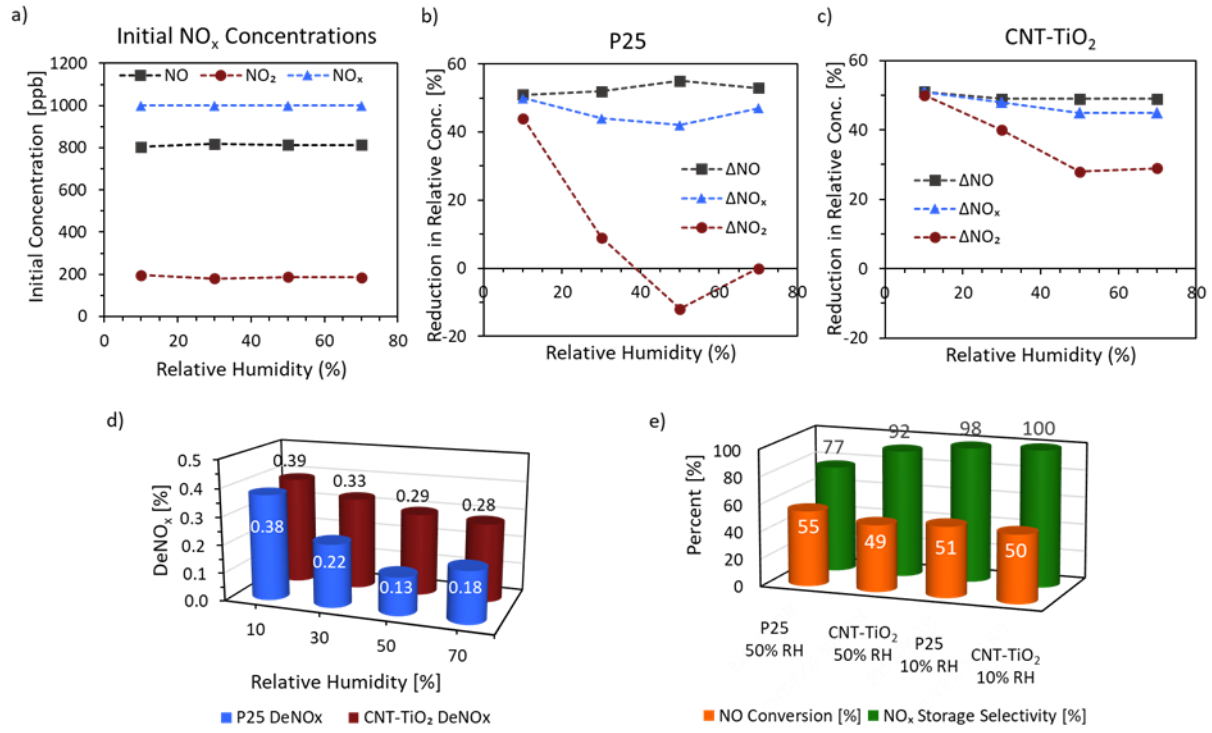

Figure 5.4. Profiles of NO, NO_2, and NO_x concentrations as a function of RH: (a) initial NOx concentrations, (b) reduction in relative concentrations for P25, and (c) reduction in relative concentrations for CNT-TiO_2. (d) $DeNO_x$ index for P25 and CNT-TiO_2 as a function of RH. (e) NO conversion and NO_x storage selectivity at low and high RH for each catalyst. Experiments were performed at 1000ppb initial NO_x concentration.

As discussed above, while the performance of the photocatalysts in NO oxidation are comparable irrespective of RH levels, there is a sharp contrast in performance in NO_2 conversion. Several studies[18, 19, 22, 34, 38, 56] involving TiO_2 and TiO_2-based hybrids also show high performance in the conversion of NO_x to NO_2 under elevated humidity levels; however, their performance in the subsequent oxidation of NO_2 to nitrates that is critical in NO_x abatement is either low or not reported. Figures 5.4a shows initial concentrations of NO and NO_2 at 1000ppb total NO_x while Figures 5.4b and c show reduction in relative concentration of NO, NO_2, and NO_x as a function of RH for P25 and CNT-TiO_2. The reduction in relative concentration for NO (ΔNO), NO_2 (ΔNO_2) and NO_x (ΔNO_x) were calculated according to the following equations:

$$\Delta NO = (NO_{in} - NO_{out})/NO_{in} \quad (5.9)$$

$$\Delta NO_2 = (NO_{2in} - NO_{2out})/NO_{2in} \quad (5.10)$$

$$\Delta NO_x = (NO_{xin} - NO_{xout})/NO_{xin} \quad (5.11)$$

The relative NO, NO_2, and NO_x degradation percentages are shown for NO, NO_2, and NO_x in Table D5.3. The calculated $DeNO_x$ values at different RH levels are shown in Figure 5.4d, while Figure 5.4e shows NO conversion and NO_x storage selectivity. It is clear from the results that at low RH levels, P25 and CNT-TiO_2 photocatalysts exhibit comparable $DeNO_x$ and selectivity, whereas at elevated RH levels, CNT-TiO_2 significantly outperforms P25 in terms of $DeNO_x$ despite comparable NO conversion due to higher NO_2 selectivity. Figure 5.4d clearly illustrates the inferior $DeNO_x$ index of P25 even at 30% RH and performs even worse at both 50% and 70% RH. Conversely, CNT-TiO_2 experiences only a small decrease in $DeNO_x$ at elevated humidity and maintains high NO_x storage selectivity. Therefore, CNT-TiO_2 outperforms P25 in terms of $DeNO_x$ despite converting slightly less NO overall.

$DeNO_x$ index is particularly important in evaluating the abatement of NO_x pollution, as conversion to nitrates is imperative, rather than partial conversion of NO to NO_2. Our extensive research on humidity levels around the world revealed few places experience humidity levels as low as 10% on a consistent basis.[57] Figure D5.3 provides humidity data of major cities, both in terms of relative humidity and absolute humidity (ppm). The humidity data indicate that realistic humidity conditions are at or above 50% RH, exceeding 5000 ppm water and reaching values as high as 15000 ppm or greater. Since air is used as diluent prior to the implementation of photocatalysis on treated flue gas waste stream, this necessitates the design of photocatalysts that exhibit high $DeNO_x$ index especially in humid environments.

5.3.3 Effect of initial concentration

The effect of initial concentration of NO_x on the oxidation of nitrogen oxides (NO, NO_2, and NO_x) and De-NO_x index for CNT-TiO_2 and P25 photocatalysts are shown in Figure 5.5. The experiments were performed at low (10% RH) and high (50% RH) humidity levels. At low RH, the oxidation profiles of the different nitrogen oxides for P25 and CNT-TiO_2 are quite similar, especially at low initial concentrations (< 500 ppb). However, at a NO_x concentration of 1000 ppb, it appears P25 starts to experience a decrease in NO_x storage selectivity, evidenced by the increase in the relative concentration of NO_2 compared to those of NO and NO_x. Corresponding plots of NO conversion and storage selectivity as functions of initial concentration can be found in Figure D5.4. These results show that NO conversion decreases with increasing initial concentration for both photocatalysts. Furthermore, P25 exhibits marginally higher NO conversion at all initial concentrations at low humidity; the trend becomes slightly more pronounced at high humidity. As observed in Figure 5.5, even though CNT-TiO_2 exhibits a lower NO conversion, its DeNO_x capability is superior especially at higher RH levels. CNT-TiO_2 shows a higher NO_x storage selectivity at all initial concentration at high humidity with the disparity becoming even more pronounced as initial concentration increases. The reduction in NO_2 conversion observed with P25 for an initial concentration of 1000 ppb (Figure 5.5a) corresponds to a slight decrease in NO_x storage selectivity as shown in Figure D5.4a. Values of relative NO, NO_2, and NO_x degradation percentages for P25 and CNT-TiO_2 catalysts at different initial concentration for a) 50% and 10% RH from Figure 5.5 are summarized in Table D5.4.

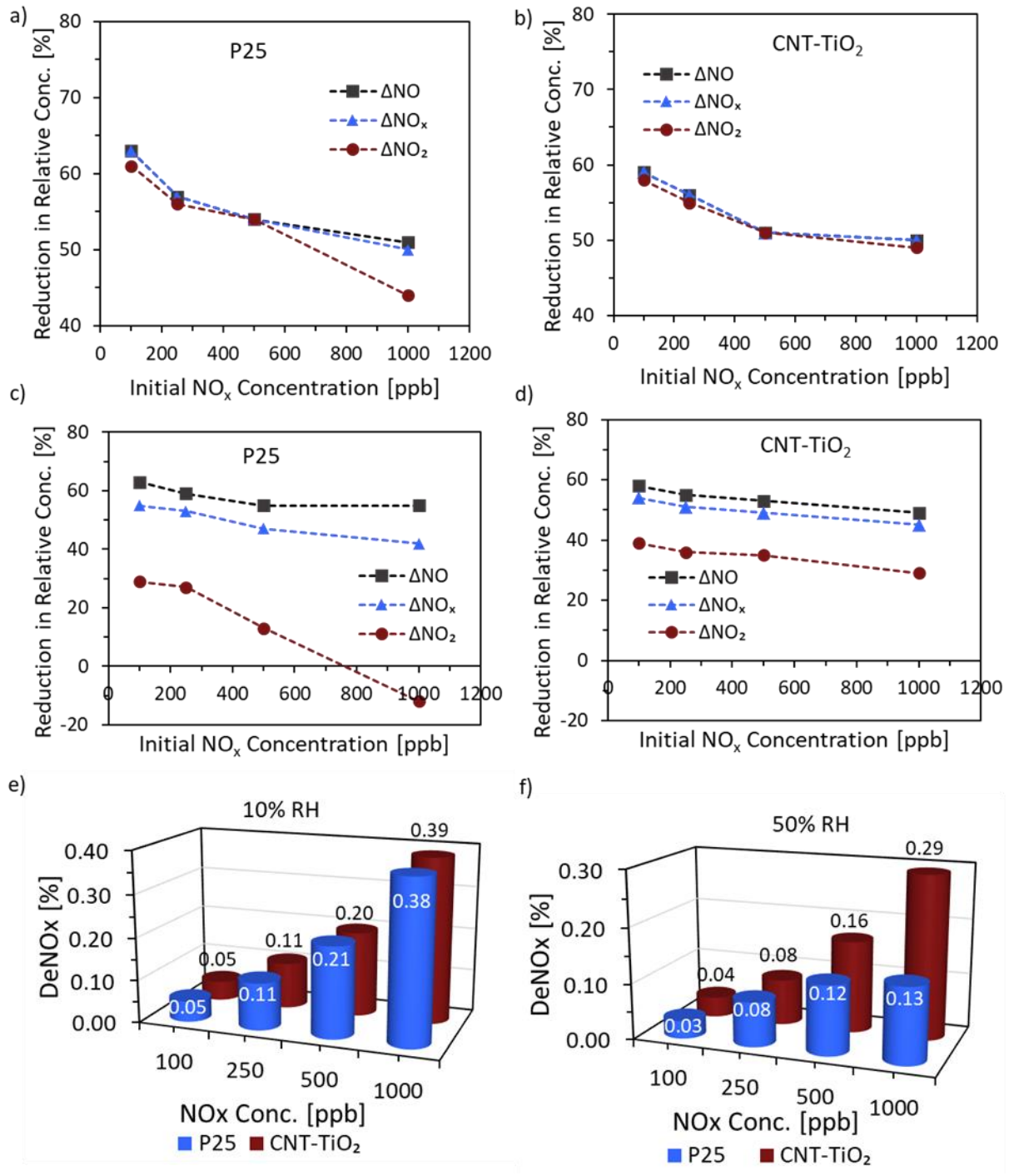

Figure 5.5. Reduction in relative concentration profiles of NO, NO_2, and NO_x versus initial NOx concentration at low RH (10%) for P25 (a) and CNT-TiO_2 (b) and high RH (50%) for P25 (c) and CNT-TiO_2 (d). (e) DeNOx index for P25 and CNT-TiO_2 as a function of initial concentration for 10% RH (e) and 50% RH (f).

5.3.4 Effect of headspace

The effect of mass transfer in the reactor on NO_x oxidation is poorly understood even though it could be a competing factor in reactions carried out under different RH levels and initial NO_x concentrations. To test for mass transfer, experiments were performed at headspace distances of 8, 5, 3, and 2 mm, corresponding to residence times of 0.95, 0.59, 0.36, and 0.24s, respectively (approximately 40-50% decrease in residence time at each interval). The effect of headspace on $DeNO_x$ for the photocatalysts is presented in Figures 5.6a-b. The results reveal that mass transfer limitations significantly impact results at a headspace distance of 8 mm and even 5 mm, as NO conversion and $DeNO_x$ index values are comparable at 3 mm, despite a significantly lower residence time. If conversion stays constant as a function of residence time, then apparent reaction rate is much lower than the actual surface reaction rate. Mass transfer from the bulk airflow therefore limits NO conversion when the reactor headspace is too large, due to limited diffusion of NO_x to the catalyst surface. To confirm these results, experiments were performed using P25 under low humidity at 3-mm headspace distance with different volumetric flowrates. Flowrate values were carefully selected to correspond to residence times used in the headspace experiments, allowing for comparison of NO conversion at identical residence times where mass transfer limitations were suspected. Figure 5.6d shows NO conversion data obtained at 10% RH using a constant headspace distance (0.3 cm), but different volumetric flow rates compared to those obtained at a constant volumetric flow rate, but different headspace distances (Figure 5.6c). If no mass transfer limitations were present at headspace distances of 5 and 8 mm, NO conversion in Figure 5.6c should correspond to the values obtained in Figure 5.6d for residence times of 0.60 and 0.96 s. As expected, increasing residence time by decreasing flow rate while maintaining a constant headspace distance improved NO conversion. The conversions at residence times of 0.6s

and 0.96s in Figure 5.6d are significantly higher than their corresponding values in Figure 5.6c at identical residence times, confirming the presence of mass transfer limitations at higher headspace values (> 3 mm).

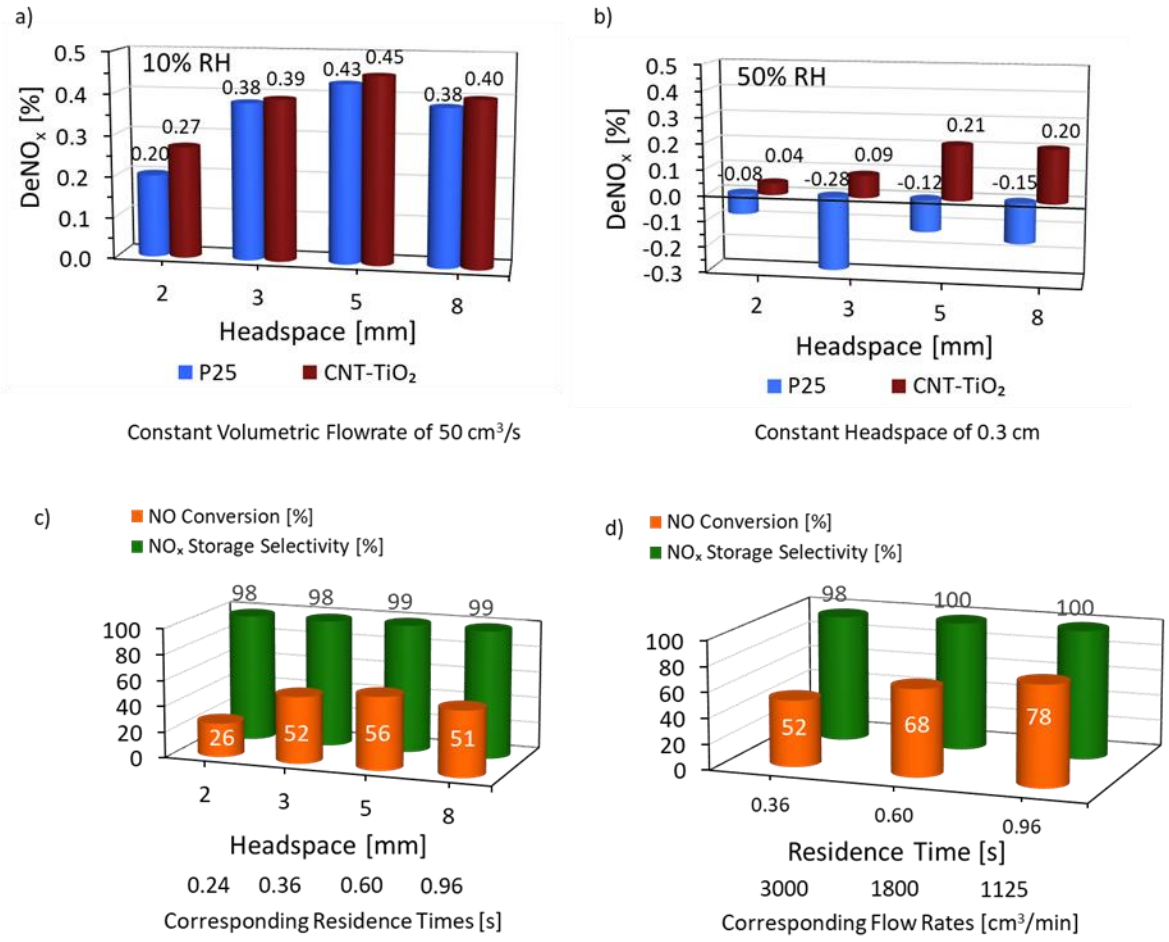

Figure 5.6. $DeNO_x$ index for P25 and CNT-TiO_2 as a function of reactor headspace distance for low RH (10%) (a) and high RH (50%) (b). (c) NO conversion and NOx storage selectivity corresponding to (a). (d) NO conversion and NOx storage selectivity for photocatalytic reactions performed at different flow rates using a headspace distance of 3mm at 10% RH. Flow rates in Figure (d) were chosen to equate residence times in Figure (c).

Under mass transfer limited conditions, transport of NO to the surface of the catalyst is limited, subsequently reducing the effective conversion rate of NO; this affects NO_2 generation and its conversion (or lack thereof) to nitrates. Furthermore, it allows extra time for the generated

NO_2 to react with generated radicals, improving the apparent $DeNO_x$. Under conditions where mass transfer does not appear to be limiting, NO (based on NO conversion) may rapidly diffuse from the bulk flow and adsorbs on the catalyst surface, while NO_2 diffuses more rapidly from the boundary layer to the bulk flow, reducing the NO_x storage selectivity, and thus decreasing the $DeNO_x$ index. Our results highlight the importance of headspace distance, a parameter that has mostly been overlooked in photocatalytic reactor design and kinetic studies involving NO_x oxidation. It is therefore necessary to test photocatalytic reactors for mass transfer limitations to ensure NO conversion, selectivity, and $DeNO_x$ values are accurate.

5.3.5 Effect of photocatalyst stability and recycling

To probe the stability and reusability of the photocatalysts, we compared the performance of fresh and used photocatalysts after aging. Photocatalysts used in experiments to probe the effect of humidity (1000 ppb of NO_x, 10% and 50% RH) were aged for 12 months and the photocatalytic performance of the samples were reevaluated under similar conditions. As shown in Figure 5.7, the humidity level has a significant impact on the performance of recycled catalysts. Both fresh and recycled P25 and CNT-TiO_2 show comparable performance at low humidity. At high humidity, however, P25 experiences substantially higher loss in catalytic performance than CNT-TiO_2. The reduced availability of active sites in P25 due to water adsorption at high humidity may be responsible for the poor activity. As discussed in Subsection 3.2, both photocatalysts experience a decrease in $DeNO_x$ at elevated humidity. P25 experiences a 66% reduction in $DeNO_x$ performance at high humidity compared to low humidity, but the CNT-TiO_2 catalyst only incurs a 27% reduction in $DeNO_x$ index. For recycled photocatalysts, this disparity becomes even more pronounced. CNT-TiO_2 experiences a 49% reduction in $DeNO_x$ at high humidity, whereas P25

experiences a 134% reduction. Several important observations can be made from Figure 5.7. First, the recycled CNT-TiO_2 catalyst has better $DeNO_x$ ability than pristine P25. The result is especially important when considering photocatalytic oxidation of NO_x using atmospheric air where RH values are generally 50% or greater (Figure D5.3). Second, recycled P25 experiences a significantly higher drop-off in $DeNO_x$ at high RH (68% reduction) compared to recycled CNT-TiO_2 (22% reduction). It is apparent from these results that as P25 and CNT-TiO_2 photocatalysts are used over time, the disparity in their performance becomes even larger, confirming CNT-TiO_2 as a reusable and robust catalyst for NO_x oxidation.

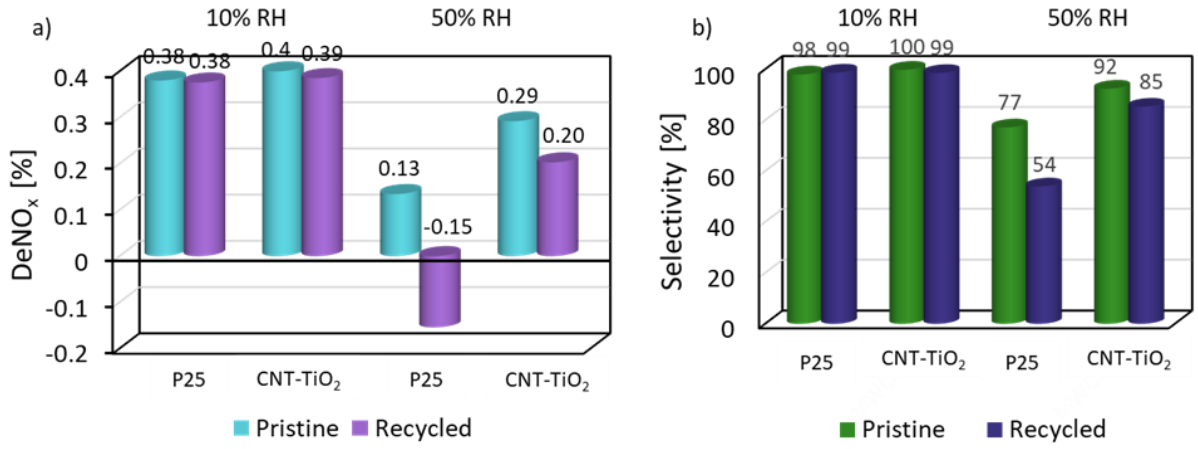

Figure 5.7. (a) $DeNO_x$ index for pristine and recycled P25 and CNT-TiO_2 catalysts at 10% RH and 50% RH levels. (b) NO_x storage selectivity for pristine and recycled P25 and CNT-TiO_2 catalysts at 10% RH and 50% RH levels.

5.3.6 Photocatalytic mechanism of NO_x oxidation

It is clear from our results that humidity negatively impacts $DeNO_x$, even though NO conversion stays constant or increases with humidity. The change in $DeNO_x$ was the direct result of inhibited NO_x storage selectivity. As noted earlier, a number of studies have reported increasing NO_2 concentrations with humidity, particularly for TiO_2 photocatalysts.[16, 41, 45] Adsorbed water contributes to generation of hydroxyl radicals via Equations 5.3 and 5.4 while also occupying

active sites, leading to counteracting phenomena during NO conversion. While reaction pathways for NO_x oxidation have been shown for both hydroxyl and oxygen radicals, most NO oxidation mechanisms focus on a multistep process dominated by hydroxyl radicals.[28, 58] As shown in Equations 5.12 – 5.14, the process requires oxidation of NO to HONO, which reacts with a secondary hydroxyl radical, generating NO_2, before reacting with a tertiary hydroxyl radical to generate HNO_3. For catalysts exhibiting equal NO conversion, their different $DeNO_x$ index values could be attributed to incomplete oxidation of NO and increased generation of NO_2.

$$NO + HO^{\bullet} \rightarrow HONO \quad (5.12)$$

$$HONO + HO^{\bullet} \rightarrow NO_2 + H_2O \quad (5.13)$$

$$NO_2 + HO^{\bullet} \rightarrow HNO_3 \quad (5.14)$$

While this conventional mechanism relies on OH radicals involved in a multistep oxidation of NO to nitrates, some studies have suggested that hydroxyl radicals are not the dominant mechanism for NO_x oxidation.[44, 59, 60] In this case, superoxide radicals ($O_2^{\bullet-}$), generated from the reaction of adsorbed oxygen with the excited electron (Equation 5.5), serve as a prominent reaction pathway for NO. Miyawaki et al.[16] also noted that NO_2 appeared to desorb more readily in a humid environment. These observations suggest the overall mechanism for NO_x oxidation to nitrates is more complicated than many of the current mechanisms suggest.

While no research has been performed on the effect of humidity on $DeNO_x$ using photocatalyst composites containing CNTs, a few studies have demonstrated that C_3N_4/TiO_2 photocatalysts can improve $DeNO_x$ in humid environments [20, 23, 33]. Generally, these composites improve the NO_x storage selectivity, leading to increased conversion of NO_2. Multiple studies[61-66] have highlighted the significant role of superoxide radicals, generated from reaction with the excited electron in the conduction band, in the photocatalytic oxidation of other pollutants. There

is compelling evidence from the above studies that the incorporation of graphitic carbon nanomaterials in photocatalysts can increase the dominance of the oxidation pathway involving superoxide radicals relative to that with hydroxyl radicals. Furthermore, Furman et al.[67] demonstrated that water-solid matrices actually increase the stability and reactivity of superoxide radicals, while Aristidou et al.[68] suggested that superoxide radicals are more reactive on perovskite solar cells in the presence of physisorbed water in a humid environment.

To rationalize the stark difference in photocatalytic performance between P25 and CNT-TiO_2 under the different conditions and provide a deeper understanding into the oxidation mechanism, the photocatalyst activity was further investigated using other analyses (Figure 5.8). EPR data in Figures 5.8a-b provides semi-quantitative insight into hydroxyl and superoxide radical concentrations generated from P25 and CNT-TiO_2. The spin-trapped hydroxyl radical (DMPO-OH) adduct presents as a quartet with an intensity ratio of 1:2:2:1.[69, 70] EPR results indicate the CNT-TIO_2 catalyst generates a lower hydroxyl radical concentration than P25, evidenced by the reduction of the signal intensity in the quartet (Figure 5.8a). This observation is consistent with the NO_x degradation data whereby NO to NO_2 conversion is slightly lower for CNT-TiO_2 than for P25. Despite the slightly lower generation of hydroxyl radicals, CNT-TiO_2 exhibits substantially higher NO_2 conversion particularly in a humid environment, highlighting the complex nature of the reaction.

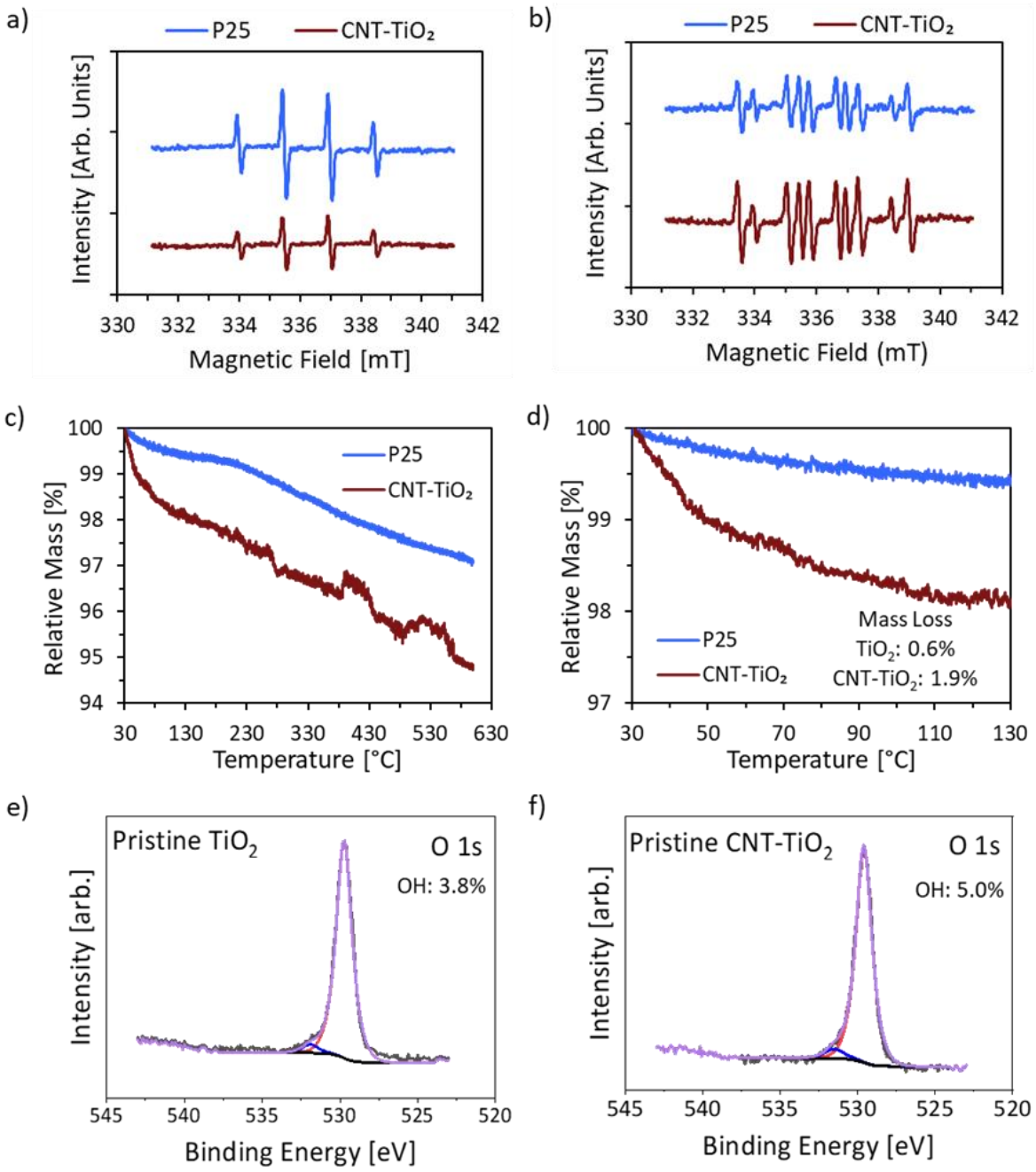

Figure 5.8. (a-b) EPR spectra of DMPO-hydroxyl radical spin adducts produced from P25 and CNT-TiO_2 catalysts in (a) aqueous dispersion (0.2 mg/mL) and (b) water containing ethanol (1%, v/v, 0.2 mg/mL) after 5 minutes of UV irradiation. (c) TGA profiles of P25 and CNT-TiO_2 catalysts obtained using a ramp rate of 5°C /min under air flow; (d) zoom-in version of (c) showing the temperature range of interest associated with desorption of physisorbed water. High-resolution XPS O 1s spectra of P25 (e) and CNT-TiO_2 (f) catalysts.

In an aqueous environment, singlet oxygen reacts with DMPO to produce DMPO-O_2^-, which immediately decomposes to hydroxyl radical adducts.[52, 71] Signal intensity in an aqueous environment is therefore correlated to formation of superoxide radicals; however, they are not observed directly because of their fast decomposition. EPR signals of superoxide radicals generated in presence of ethanol are shown in Figure 5.8b. The complex EPR spectra was formed by the signal of hydroxyl radicals (same peak location as in Figure 5.8a) and the larger peak signal of superoxide radicals next to the hydroxyl radicals. A similar EPR spectrum of DMPO-superoxide adducts was shown by Jackson et al.[72] This semi-quantitative analysis proposed that the signal intensity ratio of superoxide radicals to hydroxyl radicals is higher in CNT-TIO_2 than in P25, indicating that the CNT-TiO_2 photocatalyst can generate more superoxide radicals than P25.

Furthermore, TGA data in Figure 8c shows significant disparity in the mass loss experienced by the photocatalysts, particularly at low temperatures (<130°C). For emphasis, the temperature range in Figure 5.9c where physisorption occurs is shown in Figure 5.8d. The greater mass loss experienced by CNT-TiO_2 suggests the presence of high amounts of physisorbed water compared to P25. However, analysis of the high-resolution XPS O 1s peak (Figures 5.8e and 8f) reveals comparable OH fractions, indicating comparable amounts of chemisorbed water due to the absence of physisorbed water in the ultra-high-vacuum XPS analysis chamber. From the TGA and XPS data, it is clear the ratio of physisorbed-to-chemisorbed water is much higher on the surface of CNT-TiO_2 compared to P25. Yang et al.[73] demonstrated that improved $DeNO_x$ in humidity was directly correlated to this ratio of physisorbed-to-chemisorbed water. In agreement with our work, we observe significant improvement in $DeNO_x$ index for CNT-TiO_2 photocatalyst in humid environment due to improved NO_2 conversion. PL data (Figure D5.7) indicate that the CNT-TiO_2 photocatalyst has a significantly lower intensity, which may suggest slower charge

recombination.[74, 75] It is important to note, however, that the suppressed PL spectra could have other causes, such as increased non-radiative recombination.[74]

We therefore hypothesize that the CNT-TiO_2 catalyst generates a greater amount of superoxide radicals, which experience increased stability and reactivity due to the presence of physisorbed water. The $O_2^{\bullet-}$ radicals directly oxidize NO to NO_3^-, effectively bypassing the generation of NO_2.

$$NO + O_2^{\bullet-} \rightarrow NO_3^- \quad (15)$$

This reaction pathway would be present on the surface of P25 as well, but to a lesser extent as fewer superoxide radicals are generated; these radicals likely degrade more rapidly, partaking in limited oxidation of NO_x due to the significantly lower amount of physisorbed water. In contrast, P25 appears to rely more heavily on NO_x oxidation via hydroxyl radicals. A schematic representation of the role of CNTs in improving NO_2 conversion on CNT-TiO_2 surface in a humid environment is presented in Figure 5.9. Owing to the lower amounts of $OH^{\bullet}$ radicals generated by CNT-TiO_2, NO conversion is lower, particularly in a humid environment. NO_x storage electivity on the CNT-TiO_2 catalyst is higher, however, because a greater amount of NO is directly oxidized to nitrates via $O_2^{\bullet-}$ radicals. The increased reactivity of superoxide radicals may result from more efficient use of the radicals generated due to their longer lifetimes and greater reactivity in the physisorbed water micro-environment. In this environment, it is also possible other ROS species, such as perhydroxyl radicals ($HO_2^{\bullet}$) and hydrogen peroxide (H_2O_2) may play a part in secondary reactions bypassing the traditional hydroxyl radical-assisted pathway.

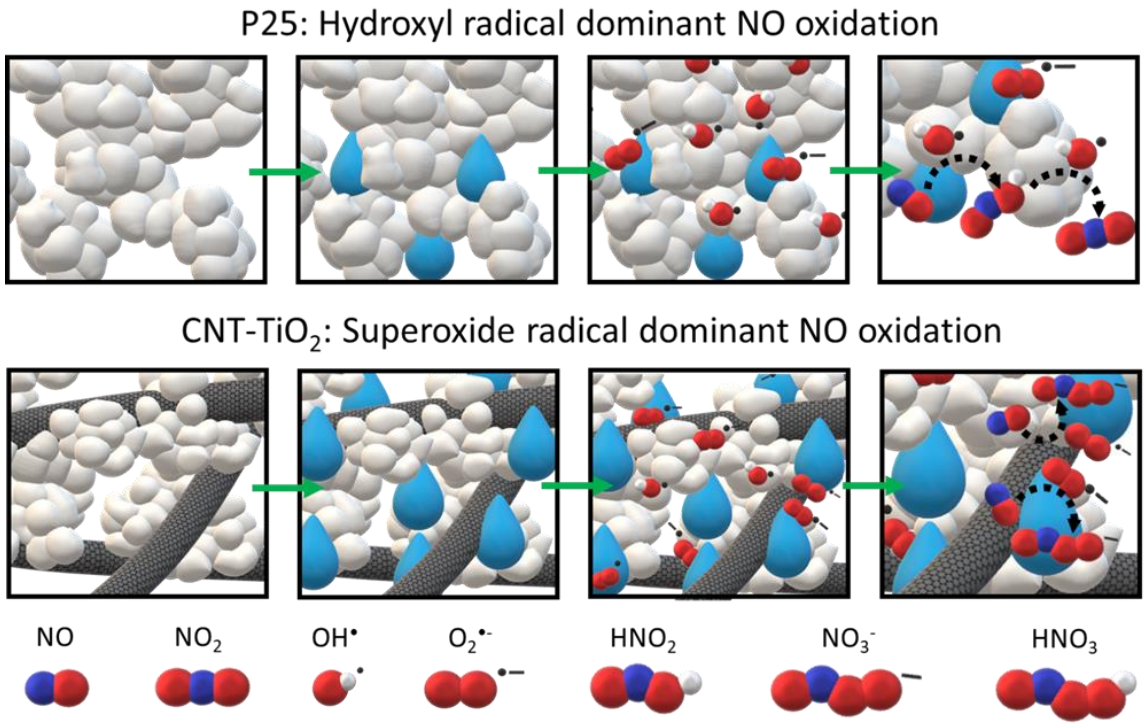

Figure 5.9. Schematic illustration of the role of CNT in improving NO_2 conversion on CNT-TiO_2 in a humid environment. The relatively higher adsorbed water content on CNT-TiO_2 compared to the predominantly OH radical dominant oxidation of NO_x on P25 is hypothesized to increase stability and activity of superoxide radicals.

The discussion of the mechanism would be incomplete without addressing the difference in surface area. We believe the effect of surface area is minor relative to the superoxide radical generation and reactivity discussed above. Yang et al.[73] demonstrated that two catalysts with very similar physisorbed-to-chemisorbed water ratios $\frac{H_2O}{OH+H_2O}$ had comparable NO, NO_2, and NO_x conversion efficiencies despite having significantly different surface areas (59.9 m^2/g vs. 321.1 m^2/g). We note that additional experiments with P25 indicated that there is a small effect of surface area on NO conversion, NO_x storage selectivity, and $DeNO_x$ when total catalyst weight is increased (Figure D5.8). However, since there are no significant differences in NO conversion or total catalyst weight (Table D5.2) for P25 and CNT-TiO_2, it is unlikely that surface area is playing a significant role in this case.

5.4 Conclusions

This work demonstrates the outstanding $DeNO_x$ and NO_x storage selectivity of CNT-TiO_2 photocatalysts under continuous flow under simulated conditions that will facilitate further removal of NOx from the waste stream of traditional flue gas treatment processes. While the CNT-TiO_2 catalyst significantly outperformed P25 at 50% RH and at higher initial NO_x concentrations (500 and 1000 ppb), the trend was less noticeable at initial concentrations of 250 ppb and 100 ppb. Headspace distance was determined to be an important factor in the evaluation of catalyst performance, as too large of a distance resulted in mass transfer limitations, preventing NO_x adsorption on the catalyst surface at a rate equivalent to the surface reaction. Further investigation of reactor headspace distance revealed that mass transfer limitations can convolute reaction results at a headspace distance greater than 3 mm, despite having significantly longer residence times. These results highlight the need to test for mass transfer limitations in photocatalytic reactor with different configurations including those designed to ISO standards. Comparison of fresh and recycled photocatalysts revealed CNT-TiO_2 maintains performance at elevated humidity after long periods of shelf life, whereas P25 performance drops substantially from an already poor starting point. The significantly higher ratio of physisorbed-to-chemisorbed water on the surface of CNT-TiO_2 in comparison to P25 is used to rationalize the remarkable DeNOx performance observed with the former. This study offers a pathway for the utilization of hybrid photocatalysts for efficient removal of NO_x downstream of industrial waste processing, which is expected to reduce the concentration of NO_x released to the atmosphere. The process has the potential of complementing current technologies used for NO_x reduction in flue gas and addressing industrial NO_x pollution at ground zero.

5.5 References

1. Friedrich, M. J., Air Pollution Is Greatest Environmental Threat to Health. *JAMA* **2018,** *319* (11).

2. Itano, Y.; Bandow, H.; Takenaka, N.; Saitoh, Y.; Asayama, A.; Fukuyama, J., Impact of NOx reduction on long-term ozone trends in an urban atmosphere. *Sci. Total Environ.* **2007,** *379* (1), 46-55.

3. Atkinson, R., Atmospheric chemistry of VOCs and NOx. *Atmos. Environ.* **2000,** *34* (12), 2063-2101.

4. Environmental Protection Agency *Nitrogen Oxides Emissions*; 2018.

5. Ambient (outdoor) air pollution. https://www.who.int/news-room/fact-sheets/detail/ambient-(outdoor)-air-quality-and-health (accessed February 18).

6. M. Kampa, E. C., Human health effects of air pollution. *Environ. Pollut.* **2008**, 362-367.

7. Liu, X.; Tan, H.; Wang, Y.; Yang, F.; Mikulcic, H.; Vujanovic, M.; Duic, N., Low NOx combustion and SCR flow field optimization in a low volatile coal fired boiler. *J. Environ. Manage.* **2018,** *220*, 30-35.

8. Fuse, R.; Kobayashi, H.; Ju, Y.; Maruta, K.; Niioka, T., NOx emission from high-temperature air/methane counterflow diffusion flame. *Int. J. Therm. Sci.* **2002,** *41* (7), 693-698.

9. Rezaei, F.; Rownaghi, A. A.; Monjezi, S.; Lively, R. P.; Jones, C. W., SOx/NOx Removal from Flue Gas Streams by Solid Adsorbents: A Review of Current Challenges and Future Directions. *Energy Fuels* **2015,** *29*, 5467−5486.

10. Koebel, M.; Elsener, M.; Kleemann, M., Urea-SCR: a promising technique to reduce NOx emissions from automotive diesel engines. *Catal. Today* **2000,** *59* (3), 335-345.

11. Dalton, J. S.; Janes, P. A.; Jones, N. G.; Nicholson, J. A.; Hallam, K. R.; Allen, G. C., Photocatalytic oxidation of NOx gases using TiO2: a surface spectroscopic approach. *Environ. Pollut.* **2002,** *120* (2), 415-422.

12. Wang, S.; Ang, H. M.; Tade, M. O., Volatile organic compounds in indoor environment and photocatalytic oxidation: State of the art. *Environ. Int.* **2007,** *33* (5), 694-705.

13. Woan, K.; Pyrgiotakis, G.; Sigmund, W., Photocatalytic Carbon-Nanotube–TiO2 Composites. *Adv. Mater.* **2009,** *21* (21), 2233-2239.

14. Maggos, T.; Bartzis, J. G.; Leva, P.; Kotzias, D., Application of photocatalytic technology for NOx removal. *Appl. Phys. A* **2007,** *89* (1), 81-84.

15. Yoon, S.-H.; Oh, S.-E.; Yang, J. E.; Lee, J. H.; Lee, M.; Yu, S.; Pak, D., TiO2 Photocatalytic Oxidation Mechanism of As(III). *Environ. Sci. Technol.* **2009,** *43* (3), 864-869.

16. Miyawaki, J.; Shimohara, T.; Shirahama, N.; Yasutake, A.; Yoshikawa, M.; Mochida, I.; Yoon, S.-H., Removal of NOx from air through cooperation of the TiO2 photocatalyst and urea on activated carbon fiber at room temperature. *Appl. Catal. B: Environ.* **2011,** *110*, 273-278.

17. Bloh, J. Z.; Folli, A.; Macphee, D. E., Photocatalytic NOx abatement: why the selectivity matters. *RSC Adv.* **2014,** *4* (86), 45726-45734.

18. Giannakopoulou, T.; Todorova, N.; Romanos, G.; Vaimakis, T.; Dillert, R.; Bahnemann, D.; Trapalis, C., Composite hydroxyapatite/TiO2 materials for photocatalytic oxidation of NOx. *Mater. Sci. Eng. B* **2012,** *177* (13), 1046-1052.

19. A. Trapalisa, N. T., T. Giannakopoulou, N. Boukos, T. Speliotis, D. Dimotikali, J. Yu, TiO2/graphene composite photocatalysts for NOx removal: A comparison of surfactant-stabilized graphene and reduced graphene oxide. *Appl. Catal. B: Environ.* **2016**, 634-647.

20. Papailias, I.; Todorova, N.; Giannakopoulou, T.; Yu, J.; Dimotikali, D.; Trapalis, C., Photocatalytic activity of modified g-C3N4/TiO2 nanocomposites for NOx removal. *Catal. Today* **2017,** *280*, 37-44.

21. Nikokavoura, A.; Trapalis, C., Graphene and g-C3N4 based photocatalysts for NOx removal: A review. *Appl. Surf. Sci.* **2018,** *430*, 18-52.

22. Papoulis, D.; Somalakidi, K.; Todorova, N.; Trapalis, C.; Panagiotaras, D.; Sygkridou, D.; Stathatos, E.; Gianni, E.; Mavrikos, A.; Komarneni, S., Sepiolite/TiO2 and metal ion modified sepiolite/TiO2 nanocomposites: synthesis, characterization and photocatalytic activity in abatement of NOx gases. *Appl. Clay Sci.* **2019,** *179*, 105156.

23. Irfan, M.; Sevim, M.; Koçak, Y.; Balci, M.; Metin, Ö.; Ozensoy, E., Enhanced photocatalytic NOx oxidation and storage under visible-light irradiation by anchoring Fe3O4 nanoparticles on mesoporous graphitic carbon nitride (mpg-C3N4). *Appl. Catal. B: Environ.* **2019,** *249*, 126-137.

24. Amama, P. B.; Itoh, K.; Murabayashi, M., Photocatalytic oxidation of trichloroethylene in humidified atmosphere. *J. Mol. Catal. A: Chem.* **2001,** *176* (1), 165-172.

25. Amama, P. B.; Itoh, K.; Murabayashi, M., Gas-phase photocatalytic degradation of trichloroethylene on pretreated TiO2. *Appl. Catal. B: Environ.* **2002,** *37* (4), 321-330.

26. Everhart, B. M.; Baker-Fales, M.; McAuley, B.; Banning, E.; Almkhelfe, H.; Back, T. C.; Amama, P. B., Hydrothermal synthesis of carbon nanotube–titania composites for enhanced photocatalytic performance. *J. Mater. Res.* **2020,** *35* (11), 1451-1460.

27. Al Mayyahi, A.; Everhart, B. M.; Shrestha, T. B.; Back, T. C.; Amama, P. B., Enhanced charge separation in TiO2/nanocarbon hybrid photocatalysts through coupling with short carbon nanotubes. *RSC Adv.* **2021,** *11* (19), 11702-11713.

28. Lasek, J.; Yu, Y.-H.; Wu, J. C. S., Removal of NOx by photocatalytic processes. *J. Photochem. Photobiol. C: Photochem. Rev.* **2013,** *14*, 29-52.

29. Chen, M.; Huang, Y.; Yao, J.; Cao, J.-j.; Liu, Y., Visible-light-driven N-(BiO)2CO3/Graphene oxide composites with improved photocatalytic activity and selectivity for NOx removal. *Appl. Surf. Sci.* **2018,** *430*, 137-144.

30. Zaleska, A., Doped-TiO2, a Review. *Recent Pat. Eng.* **2008**, 157-164.

31. Linsebigler, A. L.; Lu, G.; Yates, J. T., Photocatalysis on TiO2 Surfaces: Principles, Mechanisms, and Selected Results. *Chem. Rev.* **1995,** *95* (3), 735-758.

32. Chen, H.; Yang, R.; Zhu, K.; Zhou, W.; Jiang, M., Attenuating toluene mobility in loess soil modified with anion–cation surfactants. *J. Hazardous Mater.* **2002,** *94* (2), 191-201.

33. T. Giannakopoulou, I. P., N. Todorova, N. Boukos, Y. Liu, J. Yu, C. Trapalis, Tailoring the energy band gap and edges' potentials of g-C3N4/TiO2 composite photocatalysts for NOx Removal. *Chem. Eng. J.* **2017**, 571-581.

34. X. Song, Y. H., M. Zheng, C. Wei, Solvent-free in situ synthesis of g-C3N4/{0 0 1} TiO2 composite with enhanced UV- and visible-light photocatalytic activity for NO oxidation. *Appl. Catal. B: Environ.* **2016**, 587-597.

35. Liu, H.; Yu, X.; Yang, H., The integrated photocatalytic removal of SO2 and NO using Cu doped titanium dioxide supported by multi-walled carbon nanotubes. *Chem. Eng. J.* **2014,** *243*, 465-472.

36. Li, Q.; Yang, H.; Qiu, F.; Zhang, X., Promotional effects of carbon nanotubes on V2O5/TiO2 for NOX removal. *J. Hazard. Mater.* **2011,** *192* (2), 915-921.

37. Yen, C.-Y.; Lin, Y.-F.; Hung, C.-H.; Tseng, Y.-H.; Ma, C.-C. M.; Chang, M.-C.; Shao, H., The effects of synthesis procedures on the morphology and photocatalytic activity of multi-walled carbon nanotubes/TiO2nanocomposites. *Nanotechnology* **2008,** *19* (4), 045604.

38. Devahasdin, S.; Fan, C.; Li, K.; Chen, D. H., TiO2 photocatalytic oxidation of nitric oxide: transient behavior and reaction kinetics. *J. Photochem. Photobiol. A: Chem.* **2003,** *156* (1), 161-170.

39. Yu, Q. L.; Brouwers, H. J. H., Indoor air purification using heterogeneous photocatalytic oxidation. Part I: Experimental study. *Appl. Catal. B: Environ.* **2009,** *92* (3), 454-461.

40. Guo, G.; Hu, Y.; Jiang, S.; Wei, C., Photocatalytic oxidation of NOx over TiO2/HZSM-5 catalysts in the presence of water vapor: Effect of hydrophobicity of zeolites. *J. Hazard. Mater.* **2012,** *223-224*, 39-45.

41. Yang, L.; Hakki, A.; Zheng, L.; Jones, M. R.; Wang, F.; Macphee, D. E., Photocatalytic concrete for NOx abatement: Supported TiO2 efficiencies and impacts. *Cem. Concr. Res.* **2019,** *116*, 57-64.

42. Xie, X.; Hao, C.; Huang, Y.; Huang, Z., Influence of TiO2-based photocatalytic coating road on traffic-related NOx pollutants in urban street canyon by CFD modeling. *Sci. Total Environ.* **2020,** *724*, 138059.

43. Hüsken, G.; Hunger, M.; Brouwers, H. J. H., Experimental study of photocatalytic concrete products for air purification. *Building and Environment* **2009,** *44* (12), 2463-2474.

44. Laufs, S.; Burgeth, G.; Duttlinger, W.; Kurtenbach, R.; Maban, M.; Thomas, C.; Wiesen, P.; Kleffmann, J., Conversion of nitrogen oxides on commercial photocatalytic dispersion paints. *Atmos. Environ.* **2010,** *44* (19), 2341-2349.

45. Ao, C. H.; Lee, S. C., Enhancement effect of TiO2 immobilized on activated carbon filter for the photodegradation of pollutants at typical indoor air level. *Appl. Catal. B: Environ.* **2003,** *44* (3), 191-205.

46. Almkhelfe, H.; Li, X.; Thapa, P.; Hohn, K. L.; Amama, P. B., Carbon nanotube-supported catalysts prepared by a modified photo-Fenton process for Fischer–Tropsch synthesis. *J. Catal.* **2018,** *361*, 278-289.

47. Everhart, B. M.; Baker-Fales, M.; McAuley, B.; Banning, E.; Almkhelfe, H.; Back, T. C.; Amama, P. B., Hydrothermal synthesis of carbon nanotube–titania composites for enhanced photocatalytic performance. *Journal of Materials Research* **2020,** *35* (11), 1451-1460.

48. Yu, Y.; Yu, J. C.; Yu, J.-G.; Kwok, Y.-C.; Che, Y.-K.; Zhao, J.-C.; Ding, L.; Ge, W.-K.; Wong, P.-K., Enhancement of photocatalytic activity of mesoporous TiO2 by using carbon nanotubes. *Appl. Catal. A Gen.* **2005,** *289* (2).

49. Weon, S.; Choi, W., TiO2 Nanotubes with Open Channels as Deactivation-Resistant Photocatalyst for the Degradation of Volatile Organic Compounds. *Environ. Sci. Technol.* **2016,** *50* (5), 2556-2563.

50. Brunauer, S.; Emmett, P. H.; Teller, E., Adsorption of Gases in Multimolecular Layers. *Journal of the American Chemical Society* **1938,** *60* (2), 309-319.

51. Barrett, E. P.; Joyner, L. G.; Halenda, P. P., The Determination of Pore Volume and Area Distributions in Porous Substances. I. Computations from Nitrogen Isotherms. *Journal of the American Chemical Society* **1951,** *73* (1), 373-380.

52. Brezová, V.; Dvoranová, D.; Staško, A., Characterization of titanium dioxide photoactivity following the formation of radicals by EPR spectroscopy. *Res. Chem. Intermed.* **2007,** *33* (3), 251-268.

53. Standardization, I. O. f., Fine ceramics (advanced ceramics, advanced technical ceramics) — Test method for air-purification performance of semiconducting photocatalytic materials —. In *Removal of nitric oxide*, International Organization for Standardization: 2016; Vol. ISO 22197-1:2016(E).

54. Mahshid, S.; Askari, M.; Ghamsari, M. S., Synthesis of TiO2 nanoparticles by hydrolysis and peptization of titanium isopropoxide solution. *J. Mater. Process. Technol.* **2007,** *189* (1), 296-300.

55. Michalow, K. A.; Logvinovich, D.; Weidenkaff, A.; Amberg, M.; Fortunato, G.; Heel, A.; Graule, T.; Rekas, M., Synthesis, characterization and electronic structure of nitrogen-doped TiO2 nanopowder. *Catal. Today* **2009,** *144* (1), 7-12.

56. Wang, H.; Wu, Z.; Zhao, W.; Guan, B., Photocatalytic oxidation of nitrogen oxides using TiO2 loading on woven glass fabric. *Chemosphere* **2007,** *66* (1), 185-190.

57. Worldwide weather forecasts and climate information. https://weather-and-climate.com/ (accessed 5 November).

58. Nguyen, V.-H.; Nguyen, B.-S.; Huang, C.-W.; Le, T.-T.; Nguyen, C. C.; Nhi Le, T. T.; Heo, D.; Ly, Q. V.; Trinh, Q. T.; Shokouhimehr, M.; Xia, C.; Lam, S. S.; Vo, D.-V. N.; Kim, S. Y.; Le, Q. V., Photocatalytic NOx abatement: Recent advances and emerging trends in the development of photocatalysts. *J. Clean. Prod.* **2020,** *270*, 121912.

59. Martinez, T.; Bertron, A.; Ringot, E.; Escadeillas, G., Degradation of NO using photocatalytic coatings applied to different substrates. *Build. Environ.* **2011,** *46* (9), 1808-1816.

60. Hashimoto, K.; Wasada, K.; Toukai, N.; Kominami, H.; Kera, Y., Photocatalytic oxidation of nitrogen monoxide over titanium(IV) oxide nanocrystals large size areas. *J. Photochem. Photobiol. A: Chem.* **2000,** *136* (1), 103-109.

61. Ryu, J.; Choi, W., Effects of TiO2 Surface Modifications on Photocatalytic Oxidation of Arsenite: The Role of Superoxides. *Environ. Sci. Technol.* **2004,** *38* (10), 2928-2933.

62. Cermenati, L.; Pichat, P.; Guillard, C.; Albini, A., Probing the TiO2 Photocatalytic Mechanisms in Water Purification by Use of Quinoline, Photo-Fenton Generated OH• Radicals and Superoxide Dismutase. *J. Phys. Chem. B* **1997,** *101* (14), 2650-2658.

63. Moon, G.-h.; Kim, D.-h.; Kim, H.-i.; Bokare, A. D.; Choi, W., Platinum-like Behavior of Reduced Graphene Oxide as a Cocatalyst on TiO2 for the Efficient Photocatalytic Oxidation of Arsenite. *Environ. Sci. Technol. Lett.* **2014,** *1* (2), 185-190.

64. Monteagudo, J. M.; Durán, A.; Martínez, M. R.; San Martín, I., Effect of reduced graphene oxide load into TiO2 P25 on the generation of reactive oxygen species in a solar photocatalytic reactor. Application to antipyrine degradation. *Chem. Eng. J.* **2020,** *380*, 122410.

65. Zhong, J.; Jiang, H.; Wang, Z.; Yu, Z.; Wang, L.; Mueller, J. F.; Guo, J., Efficient photocatalytic destruction of recalcitrant micropollutants using graphitic carbon nitride under simulated sunlight irradiation. *Environ. Sci. Ecotechnol.* **2021,** *5*, 100079.

66. Waiskopf, N.; Ben-Shahar, Y.; Galchenko, M.; Carmel, I.; Moshitzky, G.; Soreq, H.; Banin, U., Photocatalytic Reactive Oxygen Species Formation by Semiconductor–Metal Hybrid

Nanoparticles. Toward Light-Induced Modulation of Biological Processes. *Nano Lett.* **2016,** *16* (7), 4266-4273.

67. Furman, O.; Laine, D. F.; Blumenfeld, A.; Teel, A. L.; Shimizu, K.; Cheng, I. F.; Watts, R. J., Enhanced Reactivity of Superoxide in Water−Solid Matrices. *Environ. Sci. Technol.* **2009,** *43* (5), 1528-1533.

68. Aristidou, N.; Eames, C.; Islam, M. S.; Haque, S. A., Insights into the increased degradation rate of CH3NH3PbI3 solar cells in combined water and O2 environments. *J. Mater. Chem. A* **2017,** *5* (48), 25469-25475.

69. Mrowetz, M.; Selli, E., Enhanced photocatalytic formation of hydroxyl radicals on fluorinated TiO2. *Phys. Chem. Chem. Phys.* **2005,** *7* (6), 1100-1102.

70. Pieper, G. M.; Felix, C. C.; Kalyanaraman, B.; Turk, M.; Roza, A. M., Detection by ESR of DMPO hydroxyl adduct formation from islets of langerhans. *Free Radic. Biol. Med.* **1995,** *19* (2), 219-225.

71. Ueda, J.-i.; Takeshita, K.; Matsumoto, S.; Yazaki, K.; Kawaguchi, M.; Ozawa, T., Singlet Oxygen–mediated Hydroxyl Radical Production in the Presence of Phenols: Whether DMPO–·OH Formation Really Indicates Production of ·OH? *Photochem. Photobiol.* **2003,** *77* (2), 165-170.

72. Jackson, S. K.; Thomas, M. P.; Smith, S.; Madhani, M.; Rogers, S. C.; James, P. E., In vivo EPR spectroscopy: biomedical and potential diagnostic applications. *Faraday Discuss.* **2004,** *126* (0), 103-117.

73. Yang, L.; Hakki, A.; Wang, F.; Macphee, D. E., Different Roles of Water in Photocatalytic DeNOx Mechanisms on TiO2: Basis for Engineering Nitrate Selectivity? *ACS Appl. Mater. Inter.* **2017,** *9* (20), 17034-17041.

74. Zhang, J.; Liu, X.; Suo, X.; Li, P.; Liu, B.; Shi, H., Facile synthesis of Ag/AgCl/TiO2 plasmonic photocatalyst with efficiently antibacterial activity. *Mater. Lett.* **2017,** *198*, 164-167.

75. Min, S.; Wang, F.; Lu, G., Graphene-induced spatial charge separation for selective water splitting over TiO2 photocatalyst. *Catal. Commun.* **2016,** *80*, 28-32.

Chapter 6 – Conclusions

In this dissertation, studies involving controlled SWCNT growth via catalytic CVD and synergistic effects of CNT-TiO_2 composites in photocatalytic oxidation of pollutants have been discussed. Insight into scalable growth of SWCNTs using FTS-GP as a precursor has been provided. Additional work was carried out to illuminate the role of Ru as a promoter of Co catalyst in the growth of small-diameter SWCNTs. Significant improvements in photocatalytic oxidation of VOCs in a batch reactor and NOx in a flow reactor system have been achieved using CNT-TiO_2 composites. Based on the results and discussions, the main conclusions are summarized below.

- During CVD growth of CNTs, FTS-GP generates water in situ via a reaction between H_2 and the low-volume fraction of CO. Catalytic performance and the concentration of water formed during FTS-GP CVD experiments are sensitive to the decomposition temperature of FTS-GP, and maximum carpet heights are achieved at 750°C. Additional experiments conducted in ARES support our mechanistic rationale for the observed growth enhancement with FTS-GP CVD, which has the combined advantage of supporting on-site generation of water and having a high tolerance for high concentrations of water, making process optimization and scale-up promising.
- The addition of 10% Ru to a 1-nm thick Co (Co-Ru) catalyst increases the selectivity of small-diameter SWCNTs, as calculated from Raman spectra collected using 532-nm and 633-nm laser excitations. In addition, Ru appears to stabilize catalyst particle size at elevated temperatures, as selectivity towards small-diameter SWCNTs is less temperature dependent for growth on Co-Ru compared to Co. The reduction in catalyst particle sintering has been attributed to an increase in cohesive energy in Co particles

when Ru atoms are included in the cluster, as calculated by DFT for 13-atom and 55-atom clusters. These findings open the door for growth of small-diameter SWCNTs in conventional CVD systems and future applications requiring small-diameter SWCNTs.

- The addition of only 1wt% MWCNTs to a TiO_2 photocatalyst composite result in nearly double the degradation rate of acetaldehyde vapor. The observed catalytic enhancement is attributed to morphological differences caused by the presence of MWCNTs during TiO_2 particle nucleation and change in surface chemistry of the photocatalysts. Further addition of MWCNTs results in lower photocatalytic performance, which is attributed to the agglomeration of CNTs during the hydrothermal process, as well as interference in the absorption of light by TiO_2.
- CNT-TiO_2 photocatalyst demonstrates outstanding $DeNO_x$ and NO_x storage selectivity under different conditions in a continuous flow reactor system when compared to P25, the standard photocatalytic material. CNT-TiO_2 generates a greater amount of superoxide radicals compared to P25, which results in direct oxidation of NO_x to nitrates. Headspace distance has also been highlighted to be an important factor in the evaluation of catalyst performance, as too large of a distance results in mass transfer limitations, preventing NO_x adsorption on the catalyst surface at a rate equivalent to the surface reaction.

This dissertation provides a deeper understanding into the growth of SWCNTs, both in terms of scalability and diameter control. It also provides insight into improved photocatalytic capabilities of CNT-TiO_2 composite materials in the oxidation of gas phase pollutants. This knowledge is expected to provide a foundation for development of composite materials which can remove a variety of gas phase pollutants under real world conditions.

Chapter 7 – Future Work

Recommendations for future work are as follow:

- Perform growth experiments using Ru-promoted Co catalysts in a conventional CVD system using different gas precursors.
- Investigate the role of Ru as a promotor on Fe catalysts for the high yield growth of small-diameter SWCNTs to establish the role of Ru as a promoter independent of chosen catalyst.
- Introduce different VOC pollutants to a standard NO_x experiment and monitor the simultaneous $DeNO_x$ performance with the oxidation of the VOCs, providing more realistic pollution conditions for photocatalysis as a remediation technique in the real world.
- Fabricate CNT-TiO_2 composite materials containing small diameter semiconducting SWCNTs and investigate the visible light photosensitization capability of the s-SWCNTs. Determine the ability of these composites to maintain high $DeNO_x$ performance while exposed to visible light, a necessary step for implementing photocatalytic coatings in the real world.
- Perform $DeNO_x$ experiments in the absence of oxygen and/or in the presence of a hole scavenger in order to provide greater insight into the complex mechanism of NO_x oxidation.
- Explore the use of time resolved photoluminescence for further insight into photogenerated charge lifetimes on photocatalyst composites. Time resolved PL, when performed alongside EPR characterization, would provide detailed insight into the ability of a photocatalyst composite to generate radicals from incident

photons. Current assumptions made in the literature using standard PL characterization may be inaccurate, as reduced PL signal can be attributed to several factors besides suppression of electron-hole recombination, such as decreased generation of charges or increased rate nonradiative recombination.

Appendix A – Supplementary Information for Chapter 2

Table A2.1. Predicted amount of water generated during FTS-GP CVD at different growth temperatures for different fractions of FTS-GP in the feed.

Temperature (°C)	**Water Generated (ppm)**			
	5% FTS-GP	**10% FTS-GP***	**20% FTS-GP**	**30% FTS-GP**
650	96.2	386.5	1563.8	3544.1
700	47.0	190.7	743.9	1878.8
750	16.6	64.6	261.5	711.7
800	9.1	34.6	141.2	322.6

*FTS-GP composition used in this study.

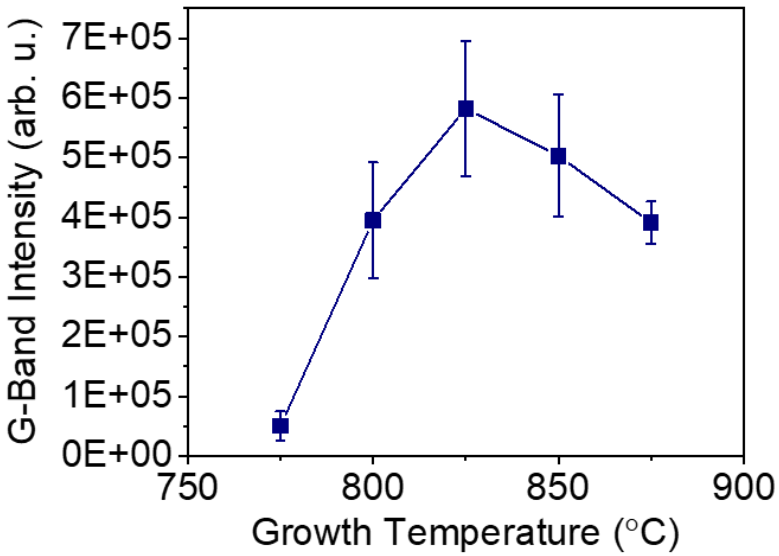

Figure A2.1. SWCNT yield as a function of growth temperature in ARES.

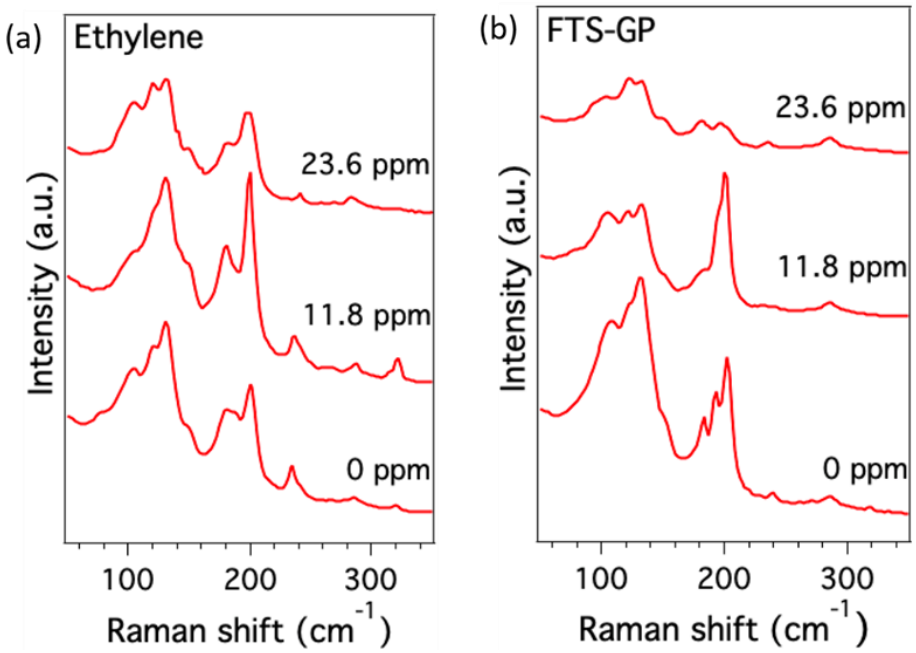

Figure A2.2. Post-growth Raman spectra (excitation wavelength 633 nm) collected from the ARES micropillars for SWCNT growth experiments performed using C_2H_4 (a) and FTS-GP (b) for varying amounts of H_2O.

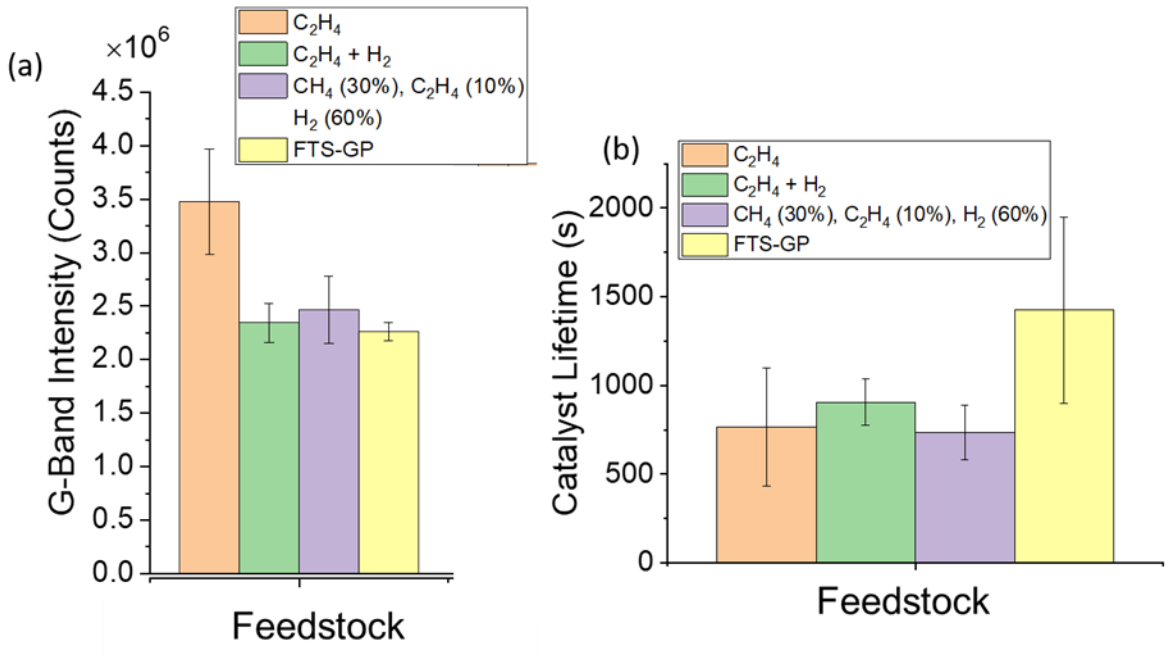

Figure A2.3. SWCNT yield and catalyst lifetime for different feedstocks and compositions in the absence of additional water at 825°C in ARES.

Appendix B – Supplementary Information for Chapter 3

Table B3.1. Average values of the fitting parameters (ν and τ) from Figure 4.

Feedstock-Catalyst Combination	Average ν (Arb. U.)	Average τ (s)	Average T (°C)
Ethylene & Co	34159	9.93	745
Acetylene & Co	51333	7.59	764
Ethylene & Co-Ru	40764	3.49	744
Acetylene & Co-Ru	84764	2.62	754

Table B3.2. G-band integrated area and small-diameter SWCNT selectivity as functions of temperature for growth on Co and Co-Ru as shown in Figure 3.3.

Co			Co-Ru		
Temperature (°C)	G-Band Area	Selectivity	Temperature (°C)	G-Band Area	Selectivity
625	71000	0.17	620	122000	0.22
650	162000	0.23	630	136000	0.55
660	320000	0.31	640	178000	0.37
660	203000	0.19	640	55000	0.43
675	298000	0.31	650	215000	0.35
675	253000	0.26	650	203000	0.31
680	330000	0.29	660	134000	0.38
680	336000	0.28	660	210000	0.44
690	263000	0.29	670	210000	0.40
690	427000	0.28	670	120000	0.49
700	263000	0.34	700	165000	0.51
700	352000	0.26	700	140000	0.43
701	409000	0.27	700	202000	0.36
705	431000	0.30	700	138000	0.42
710	445000	0.27	700	251000	0.52
715	585000	0.33	710	318000	0.44
720	322000	0.30	720	150000	0.42
725	495000	0.27	720	158000	0.45
725	442000	0.31	720	146000	0.59
725	510000	0.29	720	147000	0.47
730	400000	0.27	720	164000	0.44
735	701000	0.24	725	306000	0.45
740	525000	0.31	730	159000	0.50
745	809000	0.22	730	159000	0.50
745	774000	0.22	740	159000	0.46
750	402000	0.27	740	240000	0.47
750	788000	0.23	750	180000	0.43
760	467000	0.25	750	240000	0.42
775	770000	0.19	750	318000	0.48
780	495000	0.27	750	280000	0.49
780	490000	0.26	750	228000	0.47
790	626000	0.16	760	147000	0.55
800	626000	0.14	760	147000	0.55
810	467000	0.19	760	266000	0.46
825	452000	0.17	760	266000	0.43
830	416000	0.15	770	198000	0.42
830	485000	0.13	770	353000	0.49
830	293000	0.17	780	138000	0.52
850	386000	0.14	780	138000	0.52
850	362000	0.16	780	131000	0.45
880	254000	0.08	780	277000	0.48
			800	142000	0.51
			800	216000	0.50
			800	228000	0.53
			810	117000	0.33
			810	218000	0.49
			830	140000	0.43
			830	210000	0.57
			840	189000	0.42
			850	282000	0.28
			870	159000	0.28
			920	77000	0.34

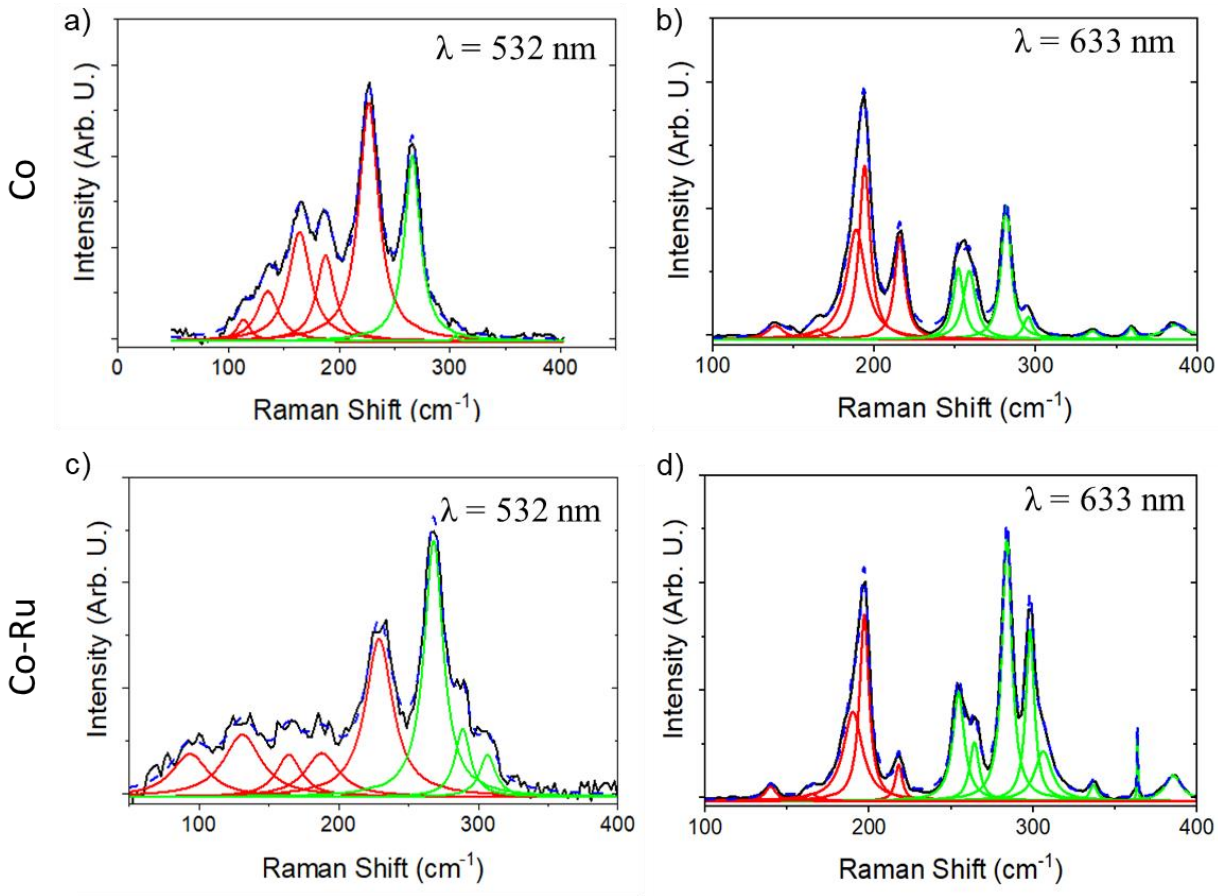

Figure B3.1. Representative Raman spectra and peak fitting for SWCNTs grown on Co (a) – (b) and Co-Ru (c) – (d) using acetylene as the feedstock. For spectra acquired with 532 nm (a and c) excitation, the small-diameter SWCNT selectivity of Co in (a) is 0.293 (T = 750°), while the selectivity of Co-Ru in (c) is 0.485 (T = 770°). For spectra acquired with 633 nm laser (b and d), the small-diameter SWCNT selectivity of Co in (c) is 0.364 (T = 750°), while the selectivity of Co-Ru in (d) is 0.646 (T = 770°).

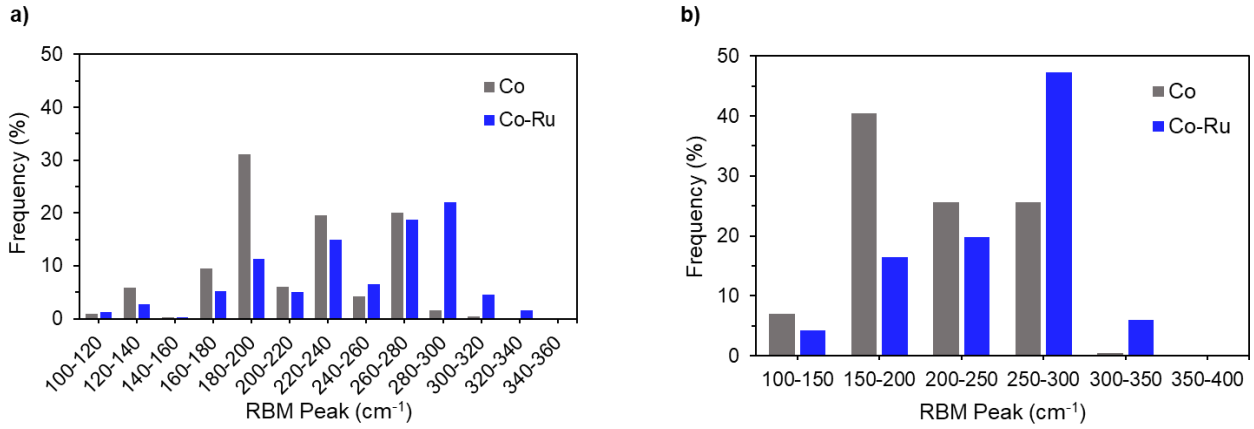

Figure B3.2. Relative frequency of RBM peaks obtained by averaging Raman data from 532 nm and 633 nm laser excitations shown in Figures 2(e) – (f) versus peak position using 20 cm^{-1} (a) and 50 cm^{-1} (b) brackets.

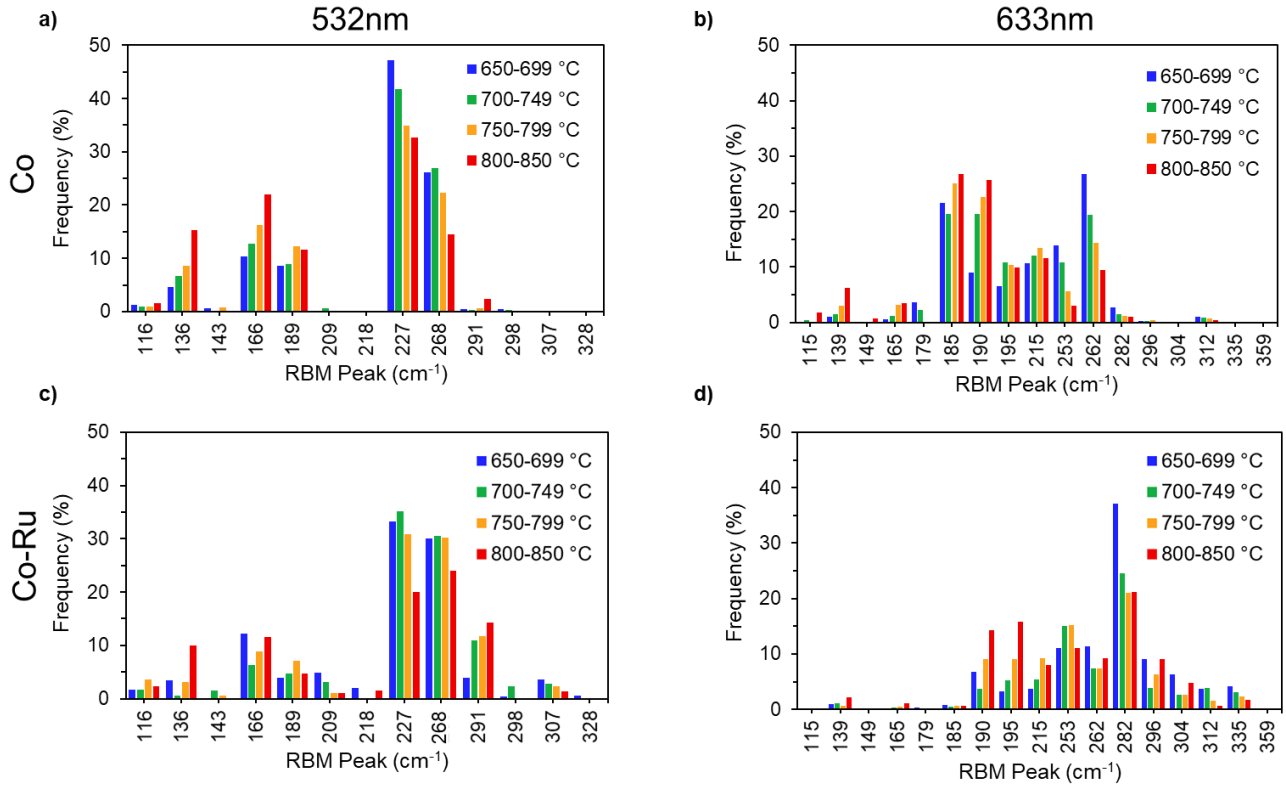

Figure B3.3. Relative frequency of RBM peaks for Co (a-b) and Co-Ru (c-d) versus peak position using Raman data from 532 nm and 633 nm laser excitations at different growth temperature ranges.

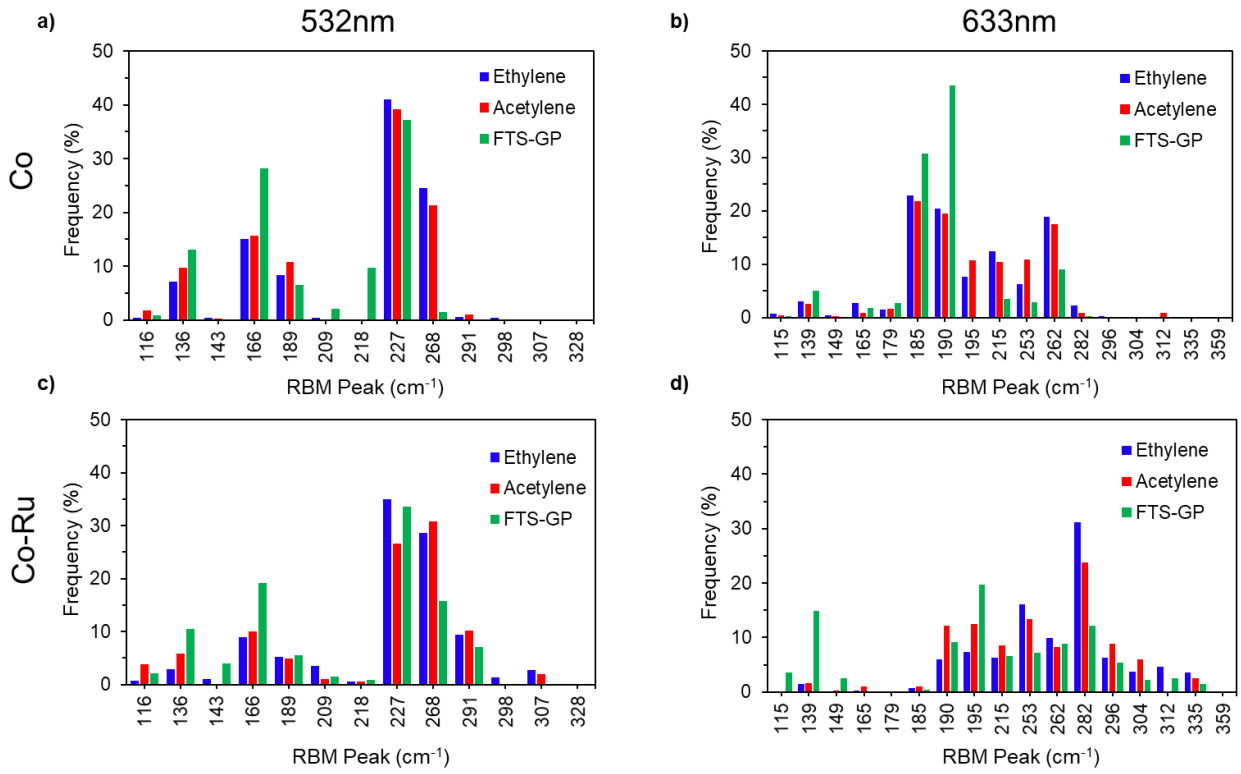

Figure B3.4. Relative frequency of RBM peaks for growth on Co (a-b) and Co-Ru (c-d) versus peak position using ethylene, acetylene, and FTS-GP precursors. Data are shown for 532 nm and 633 nm laser excitations.

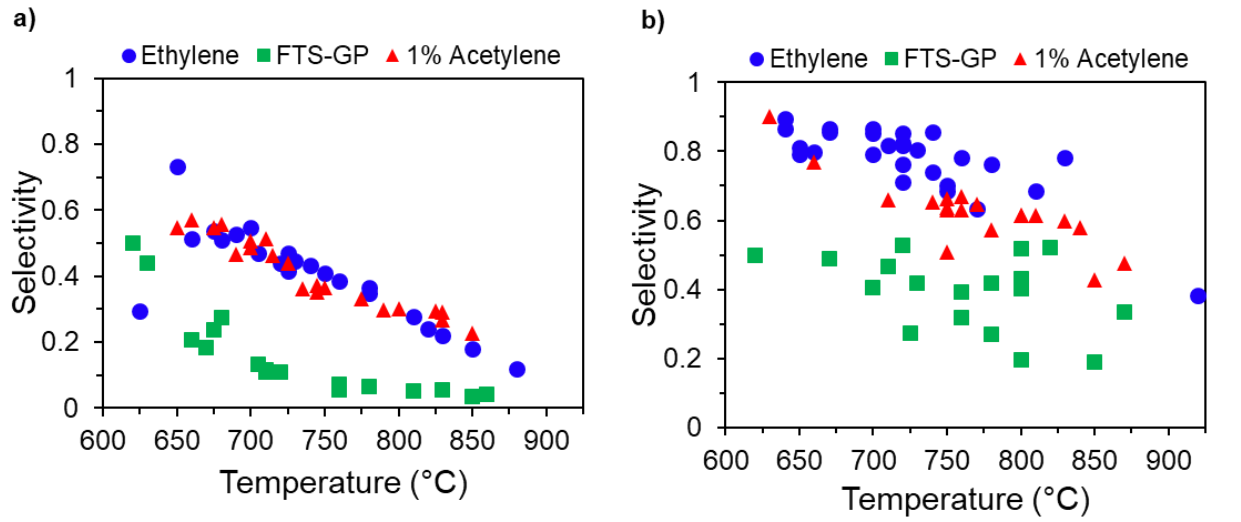

Figure B3.5. (a) – (b) Difference in selectivity towards small-diameter SWCNTs for the different feedstocks on Co and Co-Ru; data were calculated from Raman spectra acquired with 633 nm laser excitation.

B.1 Analysis of C1 and C2 values in Equation (1)

$$\omega_{RBM} = \frac{c_1}{d} + c_2 \quad (1)$$

Values for C_1 and C_2 in Equation 1 have been reported in the ranges of 210 - 260 for C_1 and 0 - 20 for C_2.[1-6] Generally, larger C_2 values correspond to larger interaction effects, such as interaction with dispersion fluid in the case of isolated tubes or tube-tube interactions in bundles.[4, 5, 7] In the case of tube bundling, RBMs can shift as much as 8-12% relative to the RBM frequency of the isolated tube.[6, 8] Kuzmany et al.[6] presented a function for C_2 (using $C_1 = 234$) that is dependent on both SWCNT diameter and size of SWCNT bundle:

$$C_2 = \frac{c(10.3d-2.3)2.56}{d}\left(1 - \frac{1}{N^{0.46}}\right) \quad (2)$$

where c is a scaling factor for tube-tube interaction (listed as 1) and *N* is the number of tubes in the bundle. Considering a SWCNT diameter of 1 nm and for bundles of relatively few tubes, $C_2 \approx 10$, whereas for infinitely large tube bundles, $C_2 = 20.5$. In this work, we have assumed small tube bundles based on the SEM images as evidenced by SEM data; therefore, the average small-diameter SWCNT selectivity has been calculated using $C_1 = 234$ and $C_2 = 10$ (values discussed by Dresselhaus et al.[5]).

Further analysis was carried out to investigate the impact of different values of C_1 and C_2 on the small-diameter SWCNT selectivity for Co and Co-Ru and the results are summarized in Figure S6. Using $C_1 = 214.4$ and $C_2 = 18.7$, as reported for isolated tubes by Telg et al.[2], result in the same selectivity as $C_1 = 234$ and $C_2 = 10$. Assuming very large tube bundles whereby $C_1 = 234$ and $C_2 = 20.5$, the small-diameter SWCNT selectivity decreases slightly; notice that the RBM peak at ~253 cm^{-1} in the spectra obtained with the 633 nm excitation no longer contributes to the selectivity. Small-diameter SWCNT selectivity calculations using $C_1 = 255$ and $C_2 = 20$ are also included in Figure S6 to set a minimum bound, using values at the top end of the ranges presented by Maultzsch et al.[4] Using these values ($C_1 = 255$ and $C_2 = 20$) removes the peak at 262 cm^{-1} in the spectra collected with 633 nm

excitation and the peak at 268 cm^{-1} in the spectra collected with 532 nm excitation from the small-diameter SWCNT selectivity.

Results in Figure S6 indicate that the small-diameter SWCNT selectivity on Co-Ru is significantly higher than on Co regardless of the values of C_1 and C_2 chosen. In addition, selectivity is less temperature dependent on Co-Ru compared to Co at all values of C_1 and C_2 examined. Furthermore, as more conservative values for C_1 and C_2 are chosen, the disparity in selectivity increases. For the values $C_1 = 234$ and $C_2 = 10$, the average selectivity of Co-Ru is nearly higher than that of Co by a factor of two. When $C_1 = 255$ and $C_2 = 20$, growth using Co-Ru results in selectivity three times that of Co. It is important to note that while no difference in selectivity is observed between the first and second values of C_1 and C_2, it is likely due to the use of 532 nm and 633 nm laser excitations, which are not in resonance with any RBMs between 233cm^{-1} and 244cm^{-1}.[9] The use of additional laser excitation wavelengths (such as 785nm and 1064nm) would likely result in a small decrease in selectivity between results in the first ($C_1 = 214.4$ and $C_2 = 18.7$) and second ($C_1 = 234$ and $C_2 = 10$) panels.

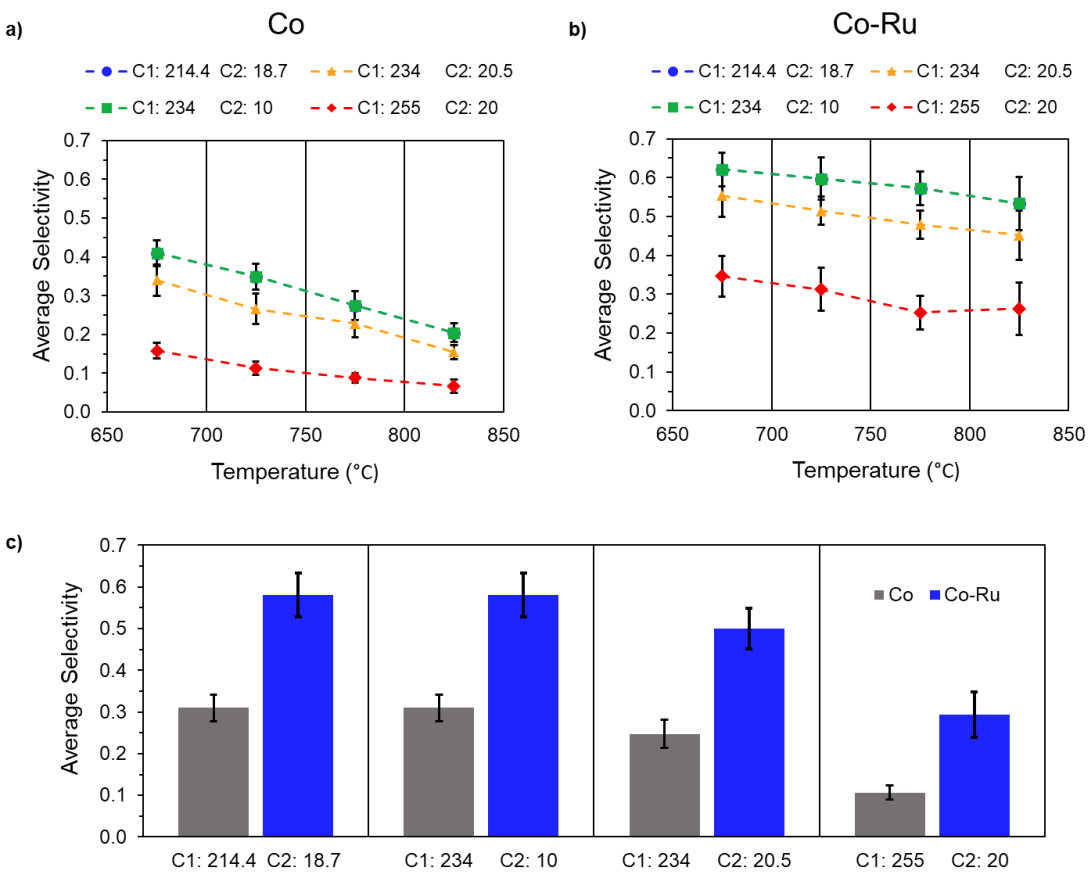

Figure B3.6. The effect of different C_1 and C_2 values on the average small-diameter selectivity at different growth temperatures for Co (a) and Co-Ru (b). (c) Average selectivity using the four sets of C_1 and C_2 values for Co and Co-Ru.

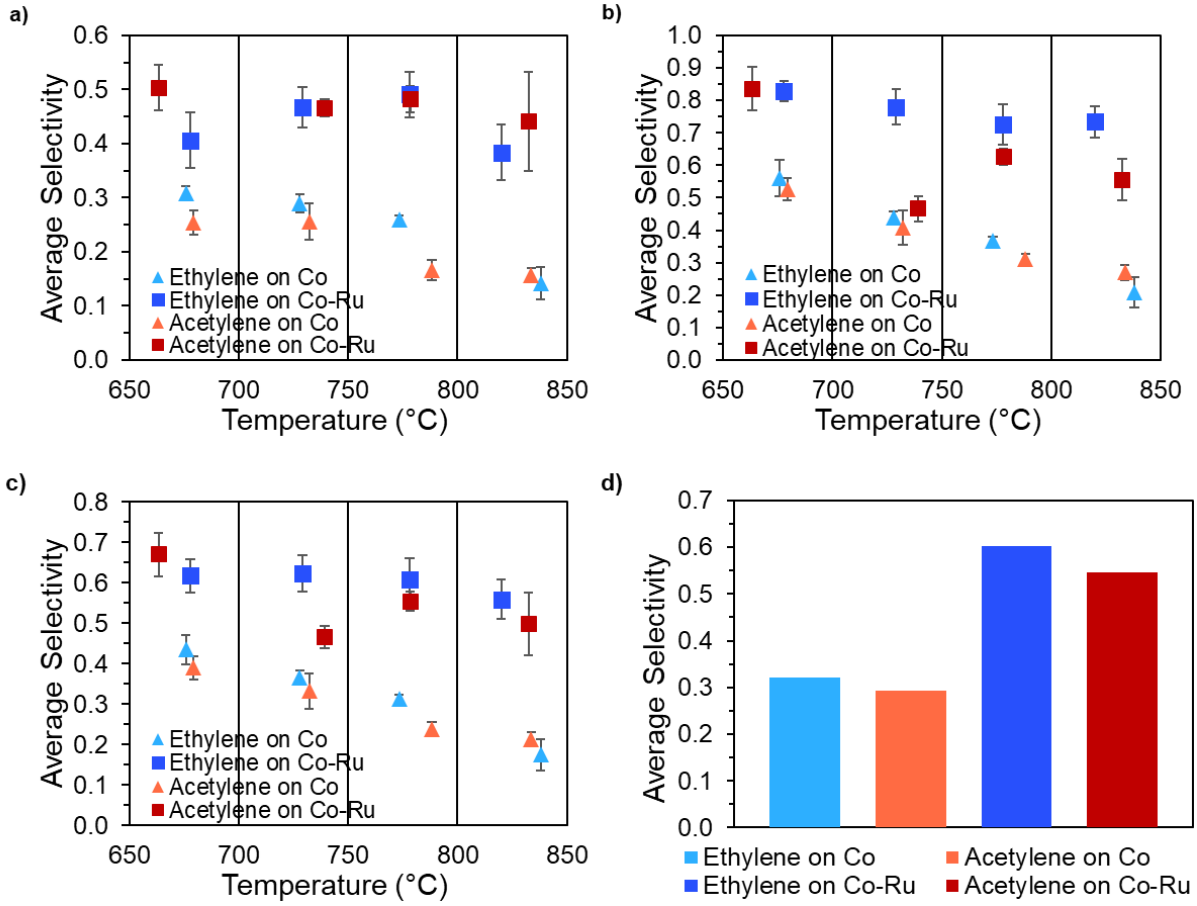

Figure B3.7. Data used in Figure 3 (c) separated to show small-diameter selectivity for growth performed with ethylene and acetylene as feedstocks: (a) data from 532nm Raman excitation; (b) data from 633nm Raman excitation. (c) Averaged data from spectra acquired using 532nm and 633nm excitation. (d) Histogram of average selectivity across temperature ranges for Co and Co-Ru catalysts. Error bars show standard deviations for the calculated average values.

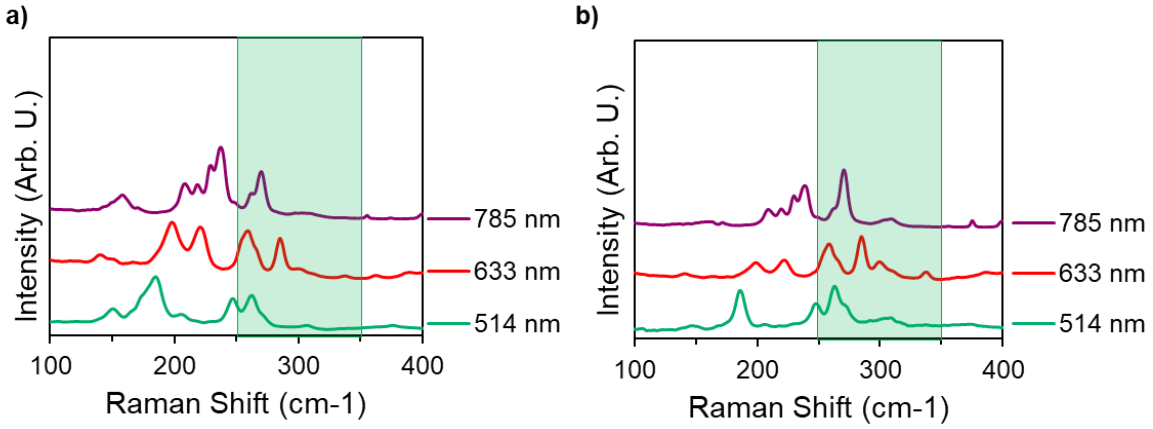

Figure B3.8. Multi-excitation Raman spectra of SWCNTs grown on Co (a) and Co-Ru (b) catalysts using acetylene as the feedstock; the green shade highlights the small-diameter region (<1 nm).

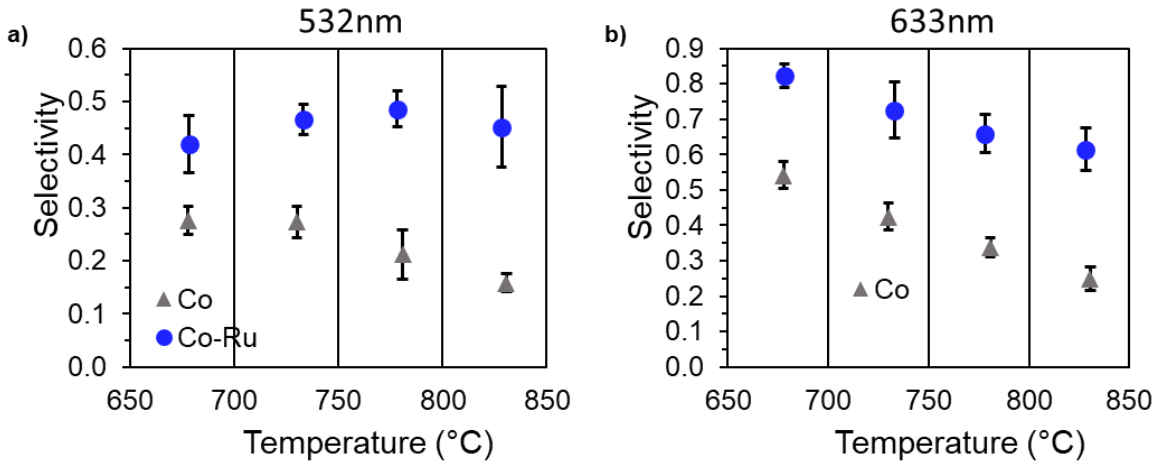

Figure B3.9. Selectivity data used in Figure 3 (c) separated based on their excitation wavelength: (a) 532 nm, and (b) 633 nm.

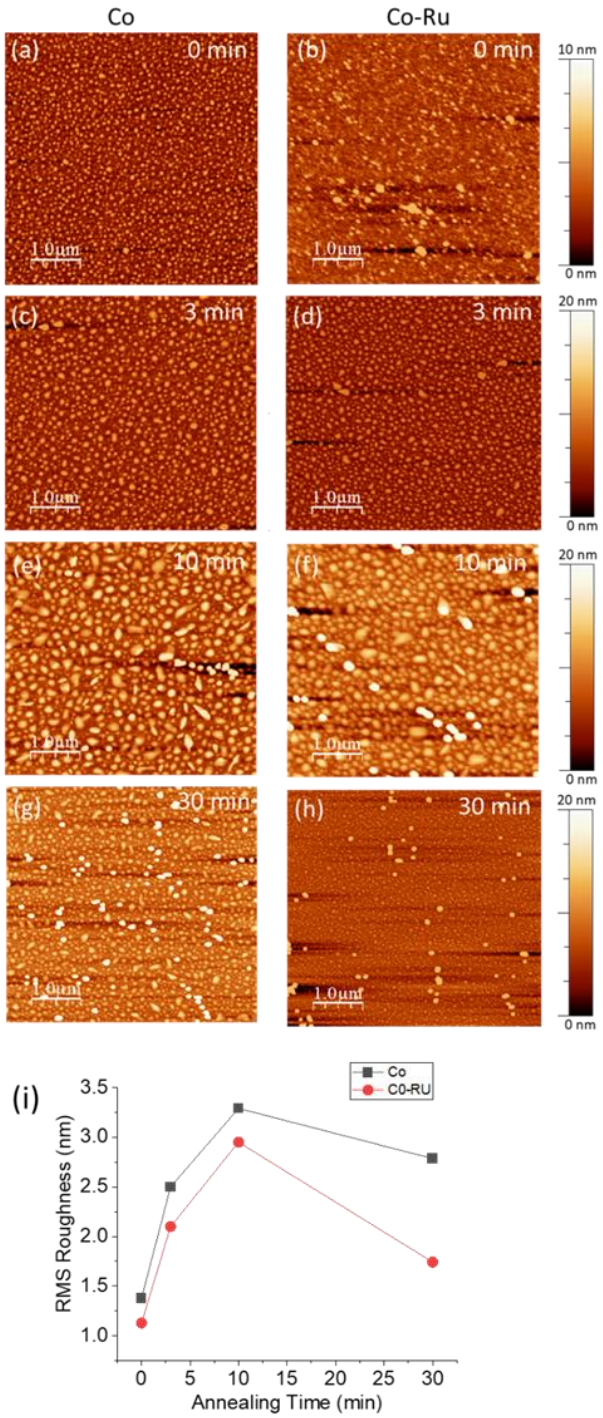

Figure B3.10. AFM images of as-deposited catalyst films and annealed in H_2/Ar for 0 min (a and b), 3 min (c and d), 10 min (e and f), and 30 min (g and h) for Co (left panel) and Co-Ru (right panel). A plot of RMS roughness obtained from the images as a function of annealing time (i). Films were deposited on Si substrates and annealed in a regular hot-wall CVD.

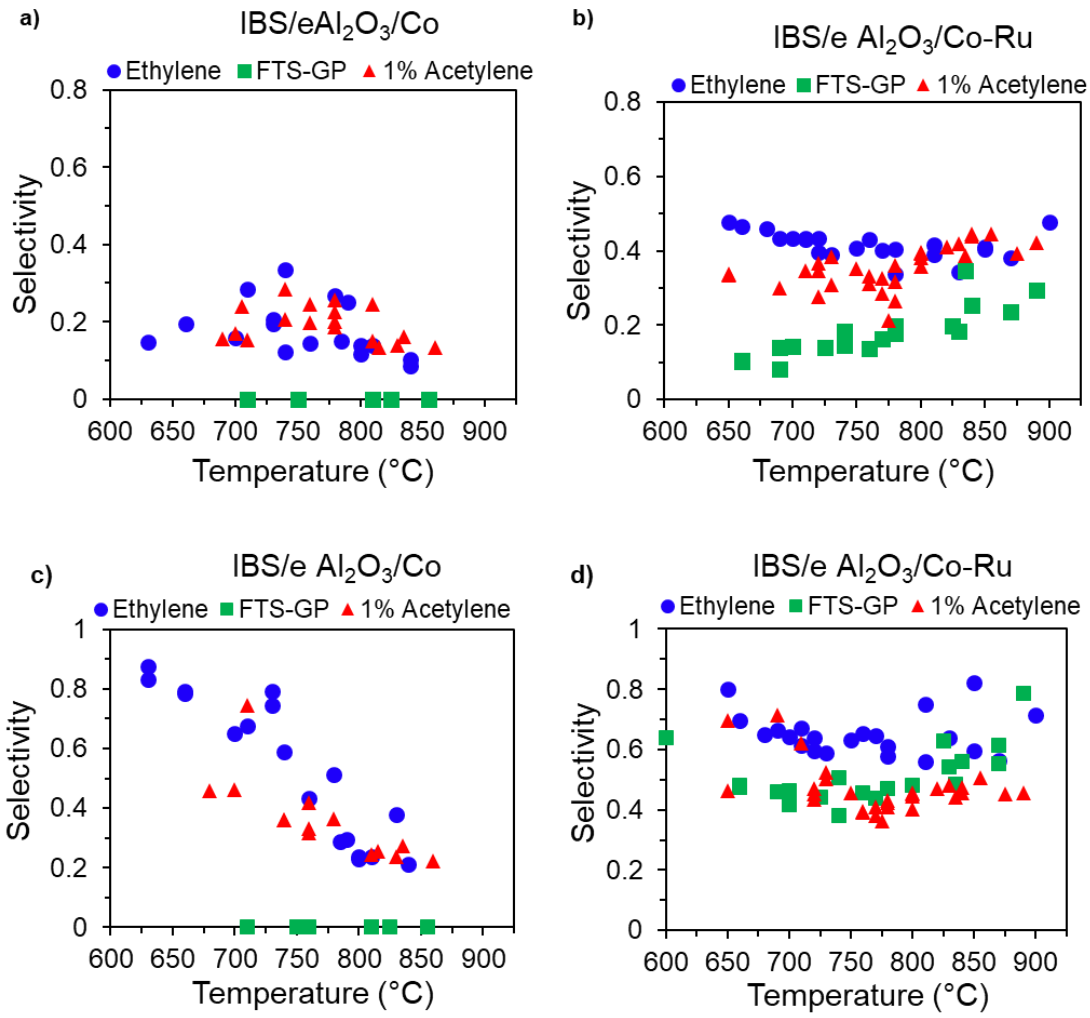

Figure B3.11. Small-diameter selectivity of SWCNTs grown on IBS/e alumina-supported Co and Co-Ru catalysts for the different feedstocks as a function of temperature. (a) – (b) Selectivity calculated from Raman spectra acquired with 532 nm excitation. (c) – (d) Selectivity calculated from Raman spectra acquired with 633 nm excitation.

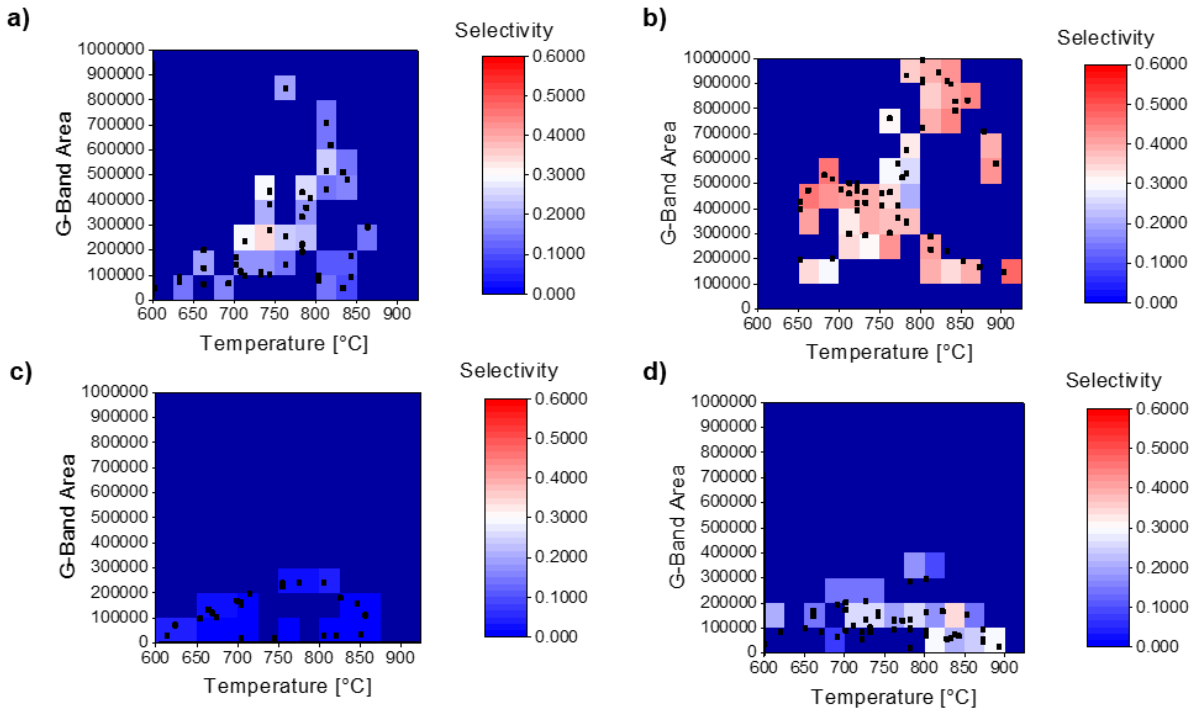

Figure B3.12. Heat plots illustrating the small-diameter SWCNT selectivity and G-band area (representing abundance of growth) versus temperature for growth on IBS/e alumina-supported Co and Co-Ru catalysts. Plots for growth using ethylene and acetylene on Co (a) and Co-Ru (b). Plots for growth using FTS-GP on Co (c) and Co-Ru (d).

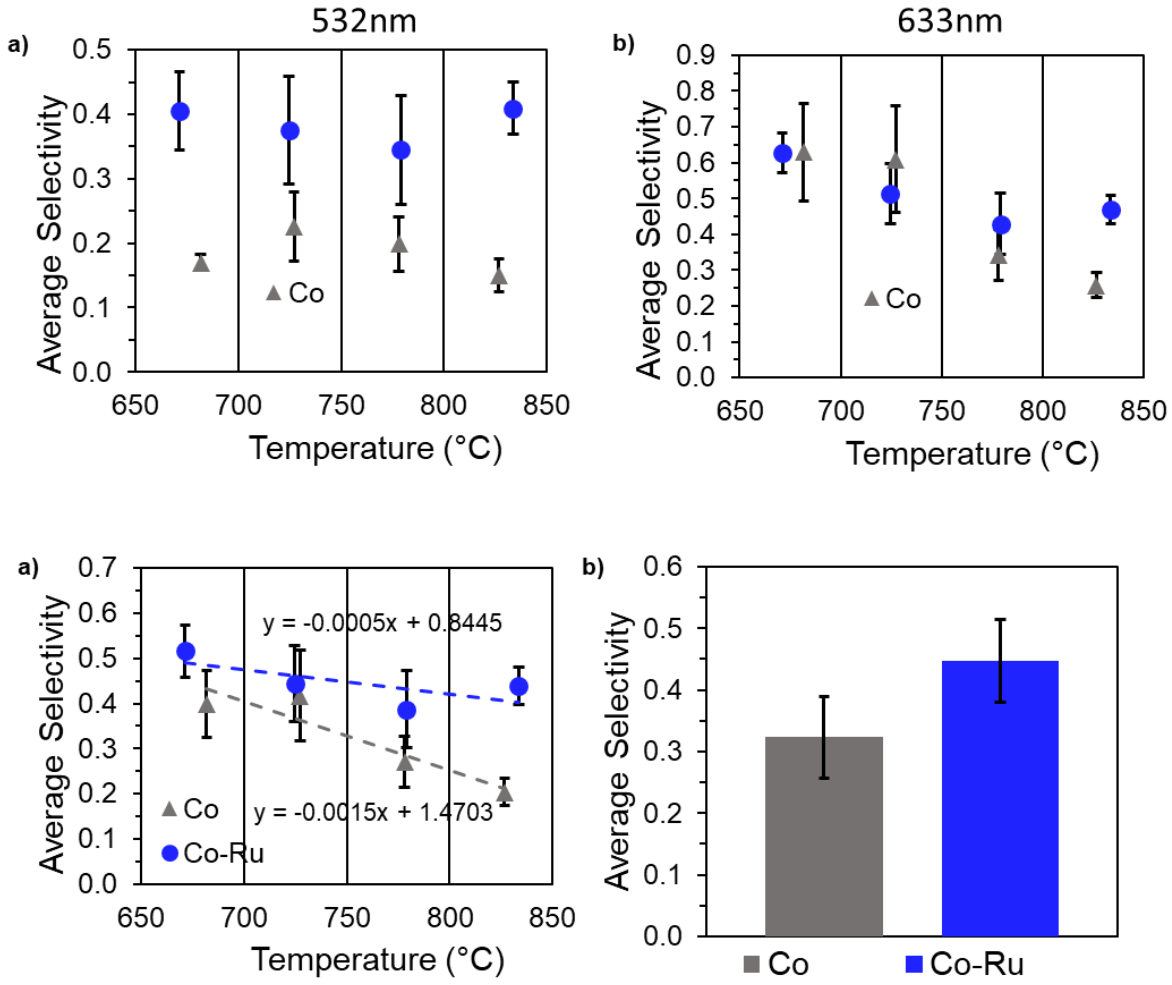

Figure B3.13. (a) Plots of average selectivity towards small-diameter SWCNTs on IBS/e alumina-supported Co and Co-Ru catalysts versus growth temperature: (a) data acquired with 532nm excitation; (b) data acquired with 633 nm excitation. (c) Average selectivity for combined data acquired with 532 nm and 633 nm excitations. (d) Histogram of average selectivity across temperature ranges for Co and Co-Ru catalysts. Error bars show standard deviations for the calculated average values.

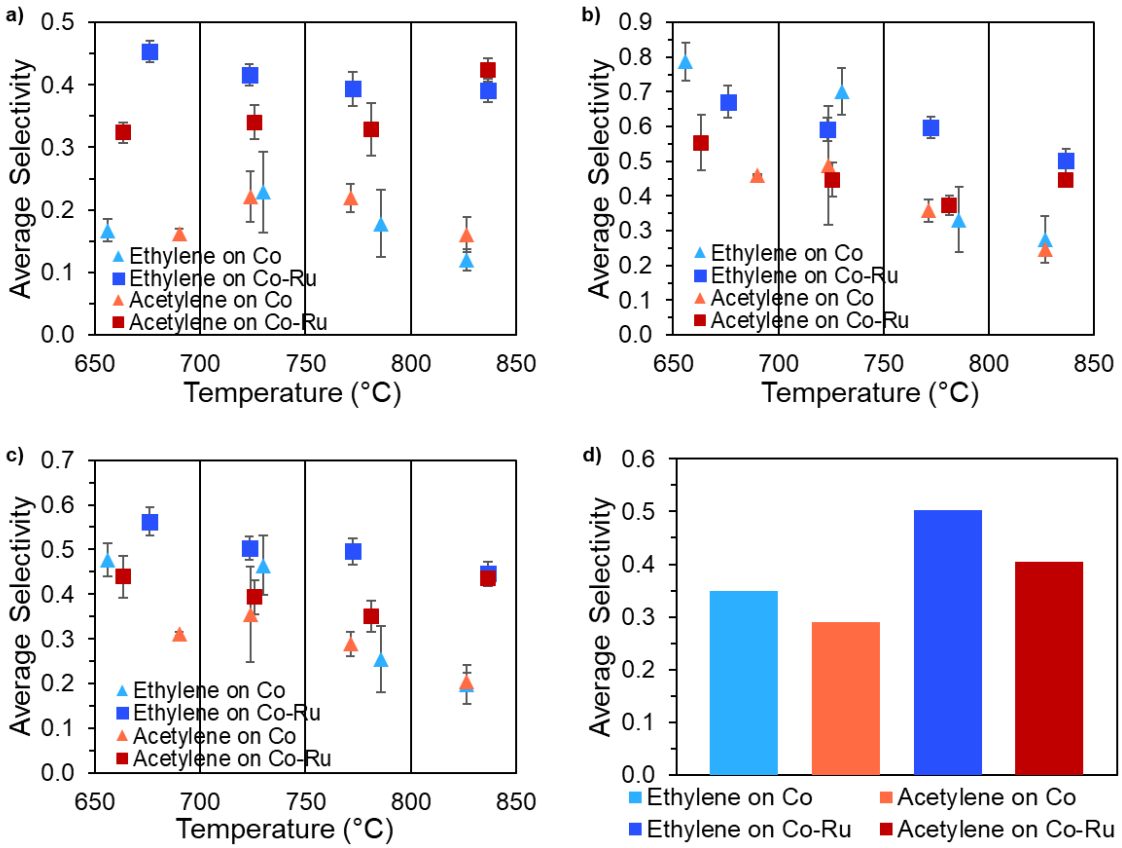

Figure B3.14. Data adapted from Figure S8 to compare average small-diameter SWCNT selectivity for growth with ethylene and acetylene on Co and Co-Ru catalysts supported on IBS/e alumina: (a) data acquired with 532 nm excitation; (b) data acquired with 633 nm excitation. (c) Average selectivity for combined data acquired with 532 nm and 633 nm excitations. (d) Histogram of average selectivity across temperature ranges for Co and Co-Ru catalysts. Error bars show standard deviations for the calculated average values.

B.2 References

REFERENCES

1. Jorio, A.; Saito, R.; Hafner, J. H.; Lieber, C. M.; Hunter, M.; McClure, T.; Dresselhaus, G.; Dresselhaus, M. S., Structural (n, m) determination of isolated single-wall carbon nanotubes by resonant Raman scattering. *Phys. Rev. Lett.* **2001,** *86* (6), 1118-21.

2. Telg, H.; Maultzsch, J.; Reich, S.; Hennrich, F.; Thomsen, C., Chirality Distribution and Transition Energies of Carbon Nanotubes. *Phys. Rev. Lett.* **2004,** *93* (17), 177401.

3. O'Connell, M. J.; Sivaram, S.; Doorn, S. K., Near-infrared resonance Raman excitation profile studies of single-walled carbon nanotube intertube interactions: A direct comparison of bundled and individually dispersed HiPco nanotubes. *Phys. Rev. B* **2004,** *69* (23), 235415.

4. Maultzsch, J.; Telg, H.; Reich, S.; Thomsen, C., Radial breathing mode of single-walled carbon nanotubes: Optical transition energies and chiral-index assignment. *Phys. Rev. B* **2005,** *72* (20), 205438.

5. Dresselhaus, M. S.; Dresselhaus, G.; Saito, R.; Jorio, A., Raman spectroscopy of carbon nanotubes. *Phys. Rep.* **2005,** *409* (2), 47-99.

6. Kuzmany, H.; Plank, W.; Hulman, M.; Kramberger, C.; Grüneis, A.; Pichler, T.; Peterlik, H.; Kataura, H.; Achiba, Y., Determination of SWCNT diameters from the Raman response of the radial breathing mode. *Eur. Phys. J. B* **2001,** *22* (3), 307-320.

7. Milnera, M.; Kürti, J.; Hulman, M.; Kuzmany, H., Periodic Resonance Excitation and Intertube Interaction from Quasicontinuous Distributed Helicities in Single-Wall Carbon Nanotubes. *Phys. Rev. Lett.* **2000,** *84* (6), 1324-1327.

8. Henrard, L.; Hernández, E.; Bernier, P.; Rubio, A., van der Waals interaction in nanotube bundles: Consequences on vibrational modes. *Phys. Rev. B* **1999,** *60* (12), R8521-R8524.

9. Kataura, H.; Kumazawa, Y.; Maniwa, Y.; Umezu, I.; Suzuki, S.; Ohtsuka, Y.; Achiba, Y., Optical properties of single-wall carbon nanotubes. *Synth. Met.* **1999,** *103* (1), 2555-2558.

Appendix C – Supplementary Information for Chapter 4

Table C4.1. Summary of phase composition of photocatalysts: calculated ratio of anatase and rutile determined from Equation 1 and the phase composition determined via RIR method.

	Calculated Ratio (%)		RIR Method (wt%)		
	Anatase	Rutile	Anatase	Rutile	Brookite
TiO_2	92	8	82.5	9.6	7.9
TiO_2/MWCNT-1%	98	2	87.6	9.7	2.7
TiO_2/MWCNT-5%	66	34	58.6	15.5	25.9

"The Reference Intensity Ratio (RIR) is a general, instrument-independent constant for use in quantitative phase analysis by the X-ray powder diffraction internal standard method."[1]

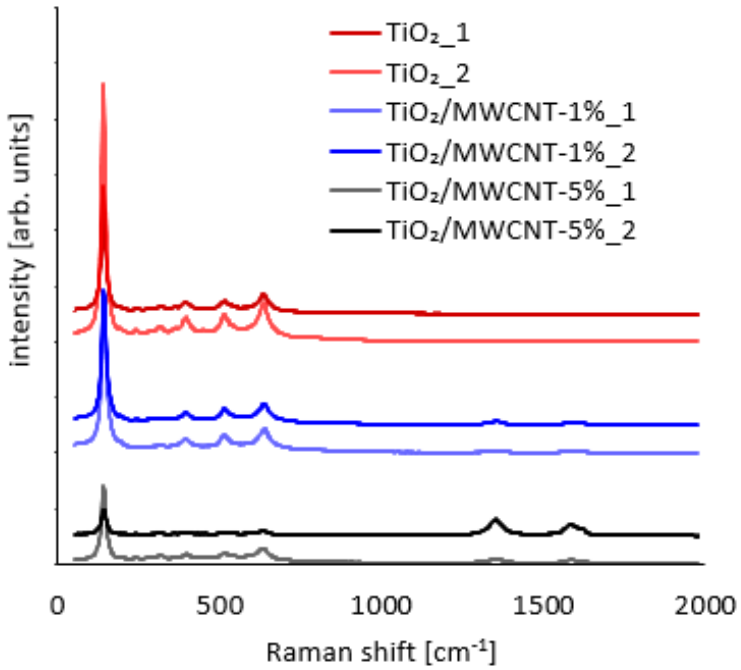

Figure C4.1. Raman spectra of TiO_2, TiO_2/MWCNT-1%, and TiO_2/MWCNT-5% using 514 nm laser excitation.

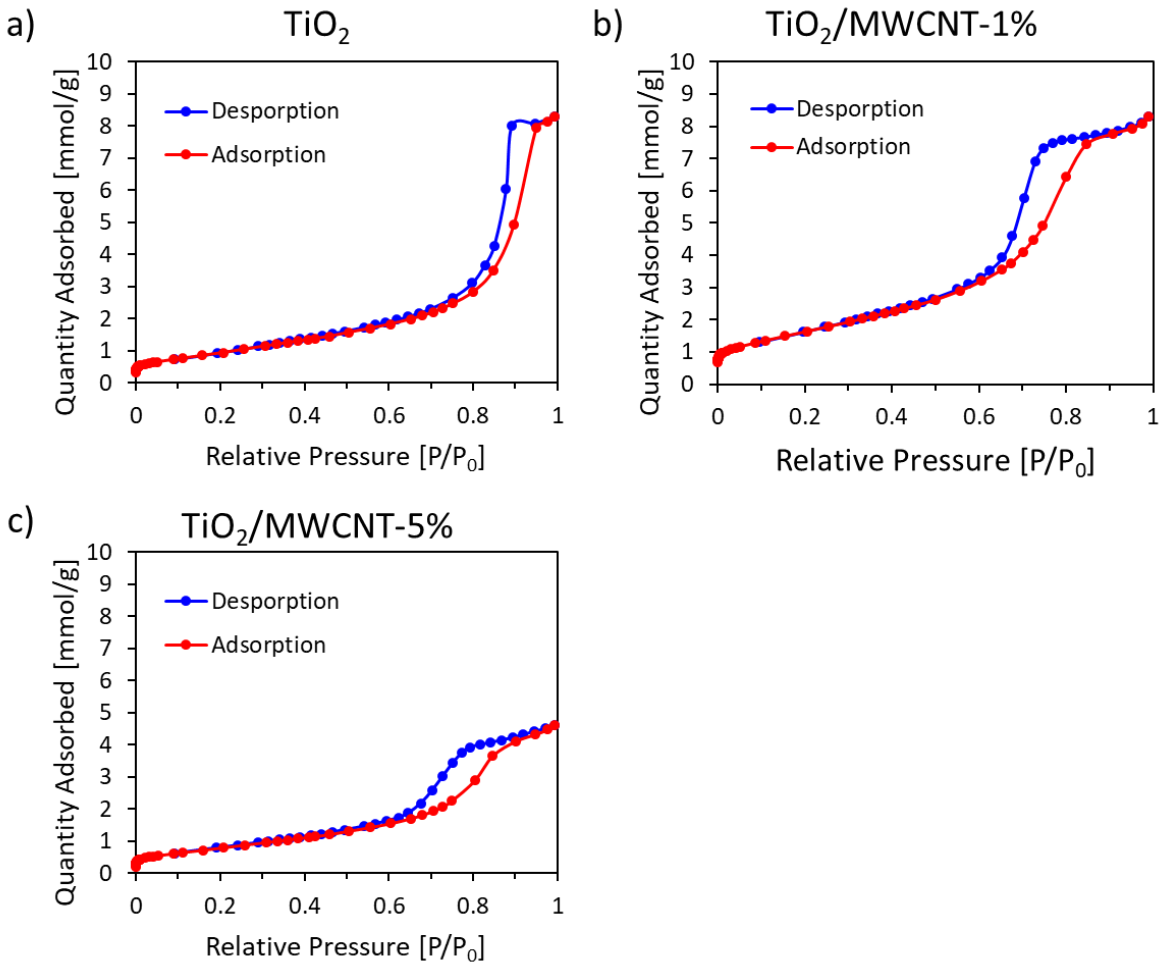

Figure C4.2. Adsorption-desorption isotherms of TiO_2, TiO_2/MWCNT-1%, and TiO_2/MWCNT-5% photocatalysts.

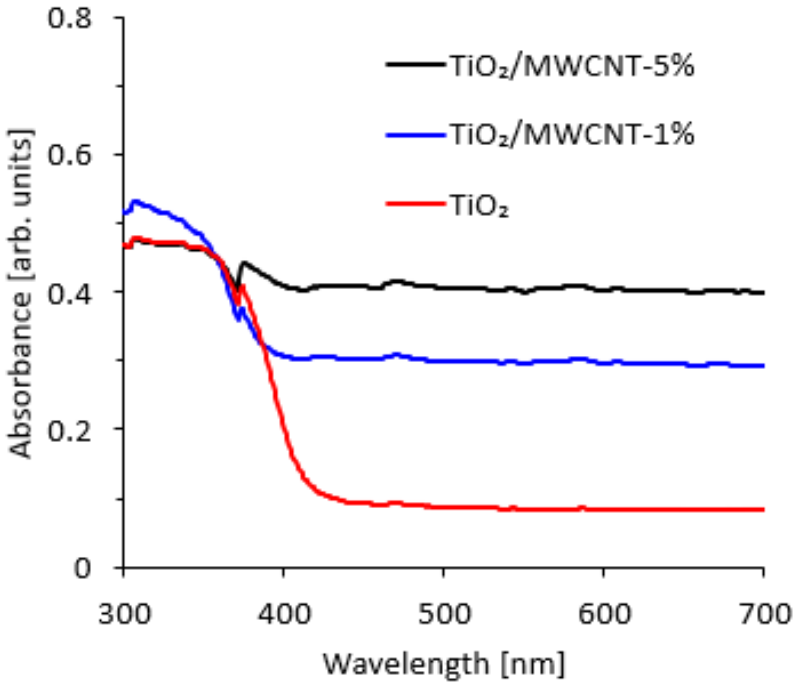

Figure C4.3. UV-Vis absorbance spectra of TiO_2, TiO_2/MWCNT-1%, TiO_2/MWCNT-5%, and P25 as a reference sample.

REFERENCES

1. Hubbard, C. R.; Snyder, R. L., RIR - Measurement and Use in Quantitative XRD. *Powder Diffr.* **1988,** *3* (2), 74-77.

Appendix D – Supplementary Information for Chapter 5

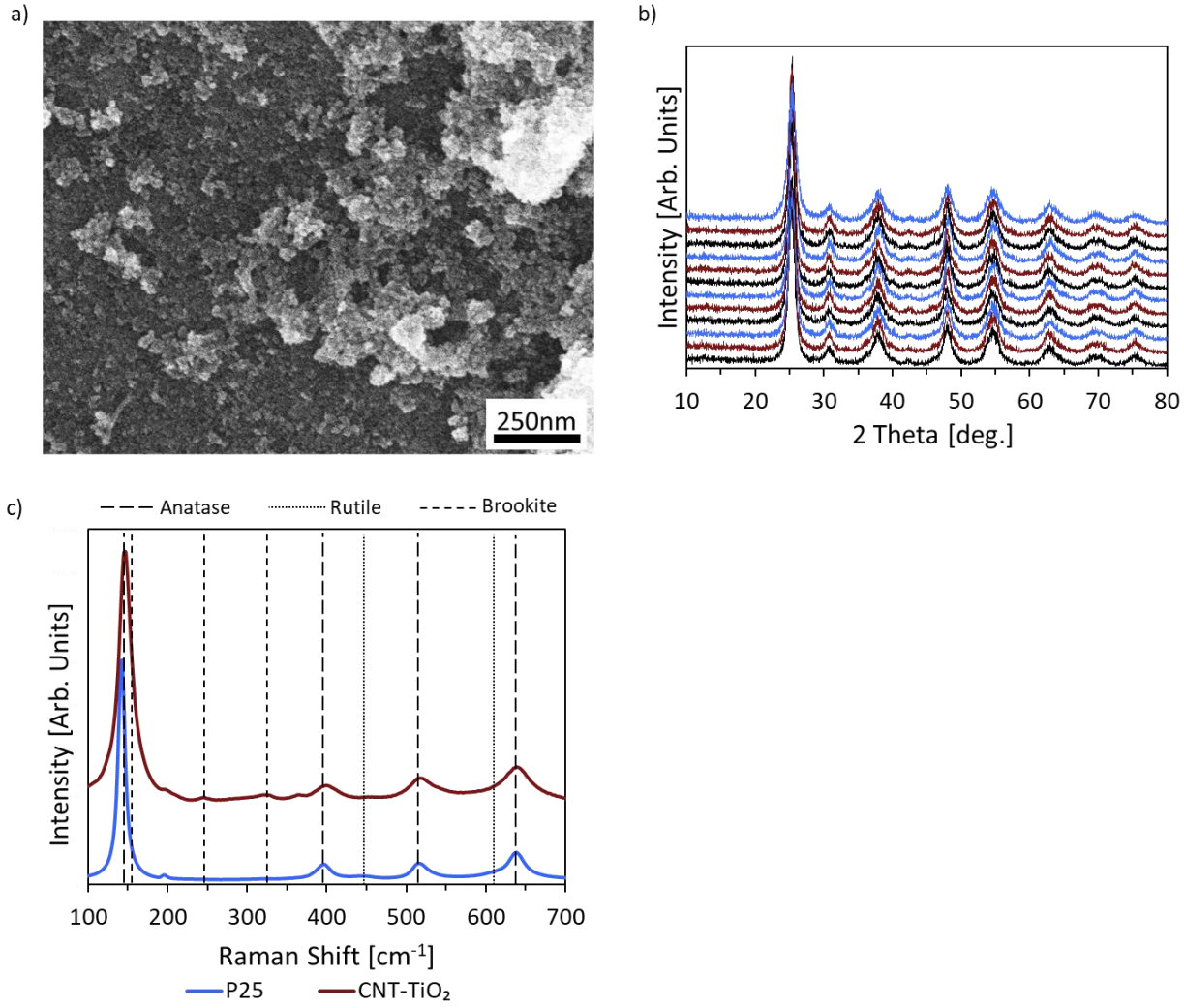

Figure D5.1. (a) An SEM image of CNT-TiO_2 microstructure. (b) XRD profiles of individual CNT-TiO_2 batches prior to mixing. (c) Raman spectra confirming the presence of the crystal phases observed in XRD.

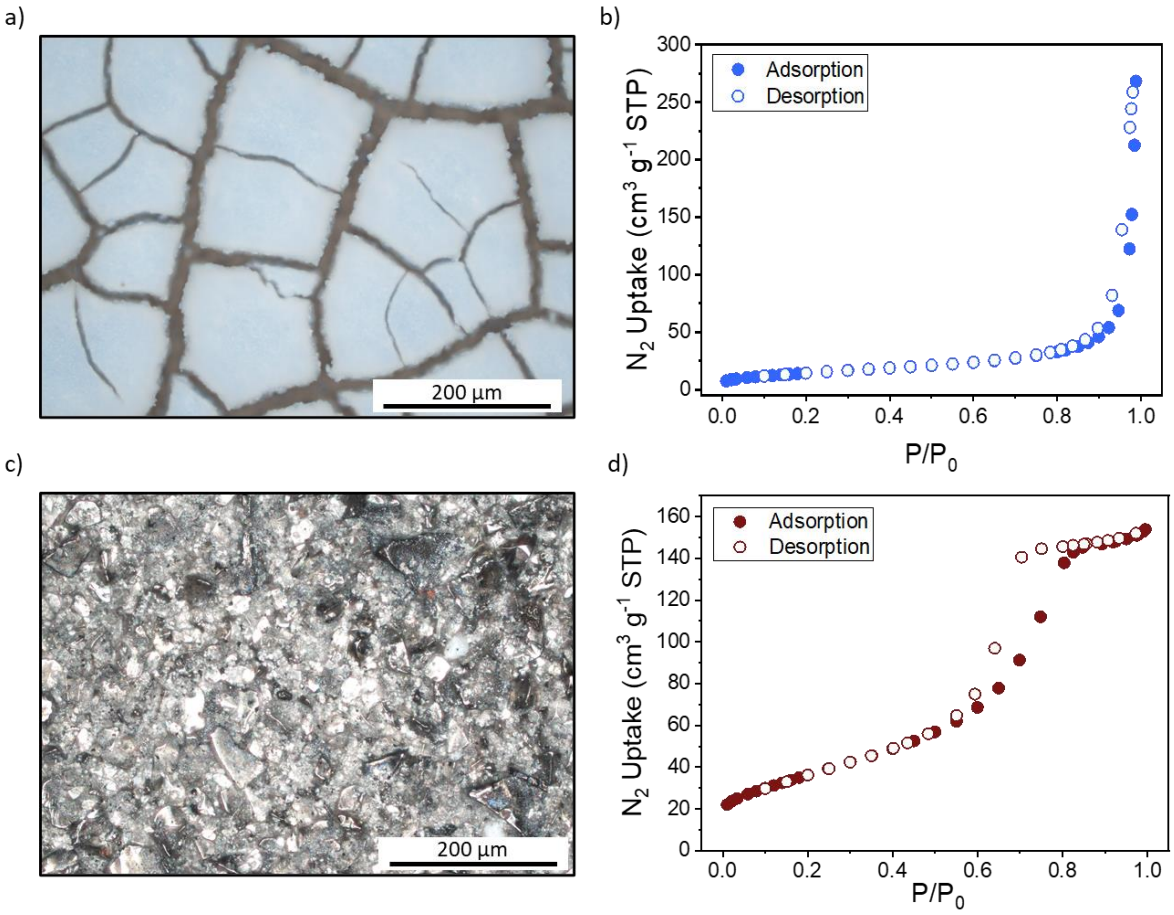

Figure D5.2. Optical microscopic images and N_2 adsorption-desorption isotherms for P25 and CNT-TiO_2 catalysts.

Table D5.1. Thickness measurements for P25 and CNT-TiO_2 catalyst films using optical microscopy.

Measurement	P25	CNT-TiO_2
	Thickness [µm]	Thickness [µm]
1	51	61
2	41	23
3	45	50
4	23	36
5	18	51
6	26	20
Average	34	40
Std. Dev.	12	14

Table D5.2. Total catalyst mass for P25 and CNT-TiO_2 catalyst films.

Catalyst Slide	P25	CNT-TiO_2
	mass [g]	mass [g]
1	0.123	0.086
2	0.129	0.158
3	0.123	0.071
4	0.106	0.133
5	0.080	0.180
6	0.120	0.087
7	0.137	0.055
8	0.124	0.138
9	0.121	0.168
Average	0.118	0.120
Std. Dev.	0.011	0.040

Table D5.3. Relative NO, NO_2, and NO_x degradation percentages for P25 and CNT-TiO_2 catalysts at different humidity levels, shown in Figure 4.

Rel. Humidity [%]	Catalyst	Rel. Degradation [%]		
		NO	NO_2	NO_x
70	P25	53	0	47
	CNT-TiO_2	49	29	45
50	P25	55	-12	42
	CNT-TiO_2	49	28	45
30	P25	52	9	44
	CNT-TiO_2	49	40	48
10	P25	51	44	50
	CNT-TiO_2	51	50	51

Table D5.4. Relative NO, NO_2, and NO_x degradation percentages for P25 and CNT-TiO_2 catalysts at different initial concentration for a) 50% and 10% relative humidity, shown in Figure 5.

a)

Initial NOx Conc. [ppb]	% Degradation at 50% Relative Humidity			
	Catalyst	NO	NO_2	NO_x
1000	P25	55	-12	42
	CNT-TiO_2	49	29	45
500	P25	55	13	47
	CNT-TiO_2	53	35	49
250	P25	59	27	53
	CNT-TiO_2	55	36	51
100	P25	63	29	55
	CNT-TiO_2	58	39	54

b)

Initial NOx Conc. [ppb]	% Degradation at 10% Relative Humidity			
	Catalyst	NO	NO_2	NO_x
1000	P25	51	44	50
	CNT-TiO_2	50	49	50
500	P25	54	54	54
	CNT-TiO_2	51	51	51
250	P25	57	56	57
	CNT-TiO_2	56	55	56
100	P25	63	61	63
	CNT-TiO_2	59	58	59

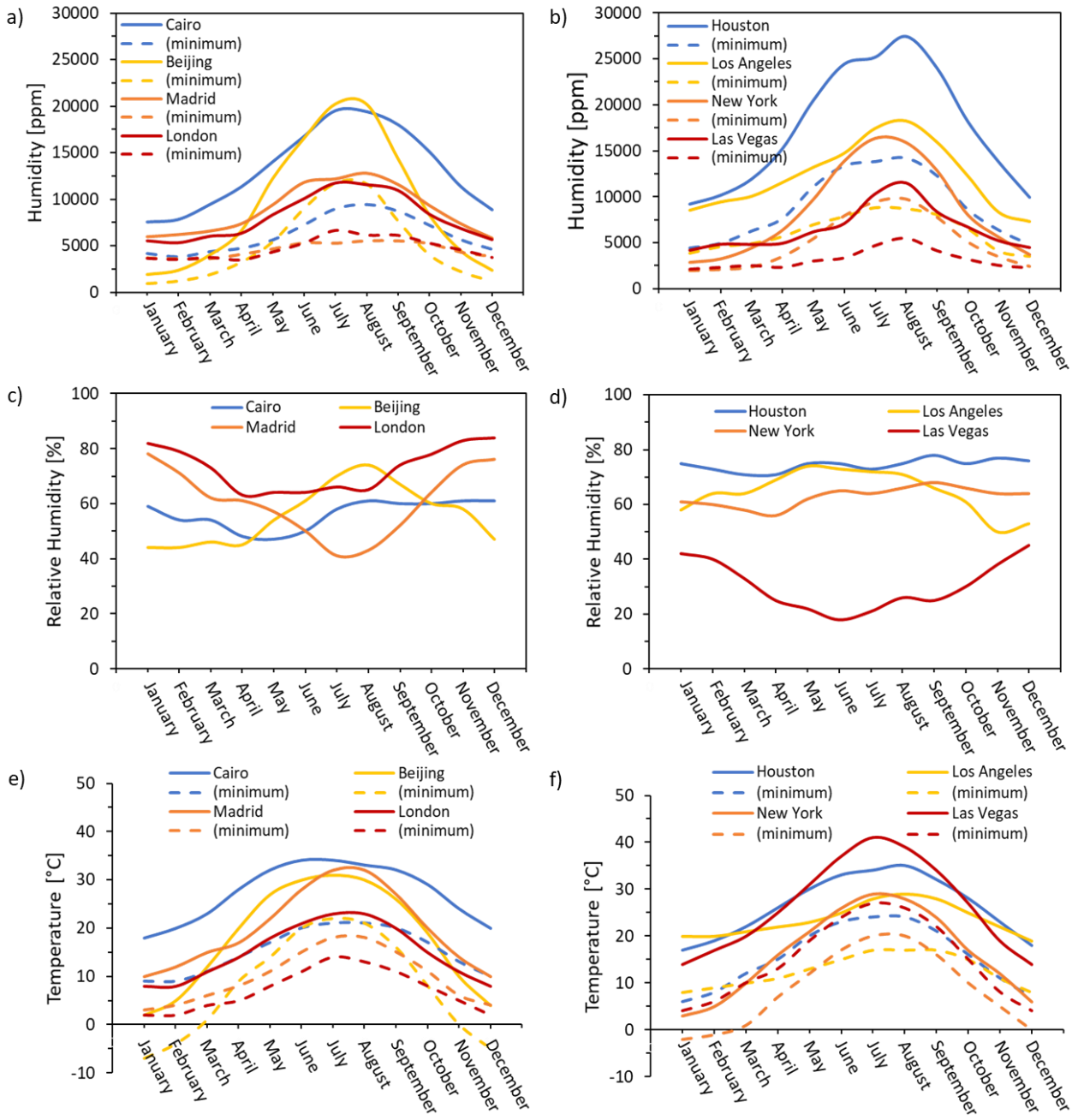

Figure D5.3. Absolute (a-b) and relative (c-d) humidity of major cities across the globe and in the US specifically. Temperature data used to convert relative humidity to absolute values has been included in (e-f).

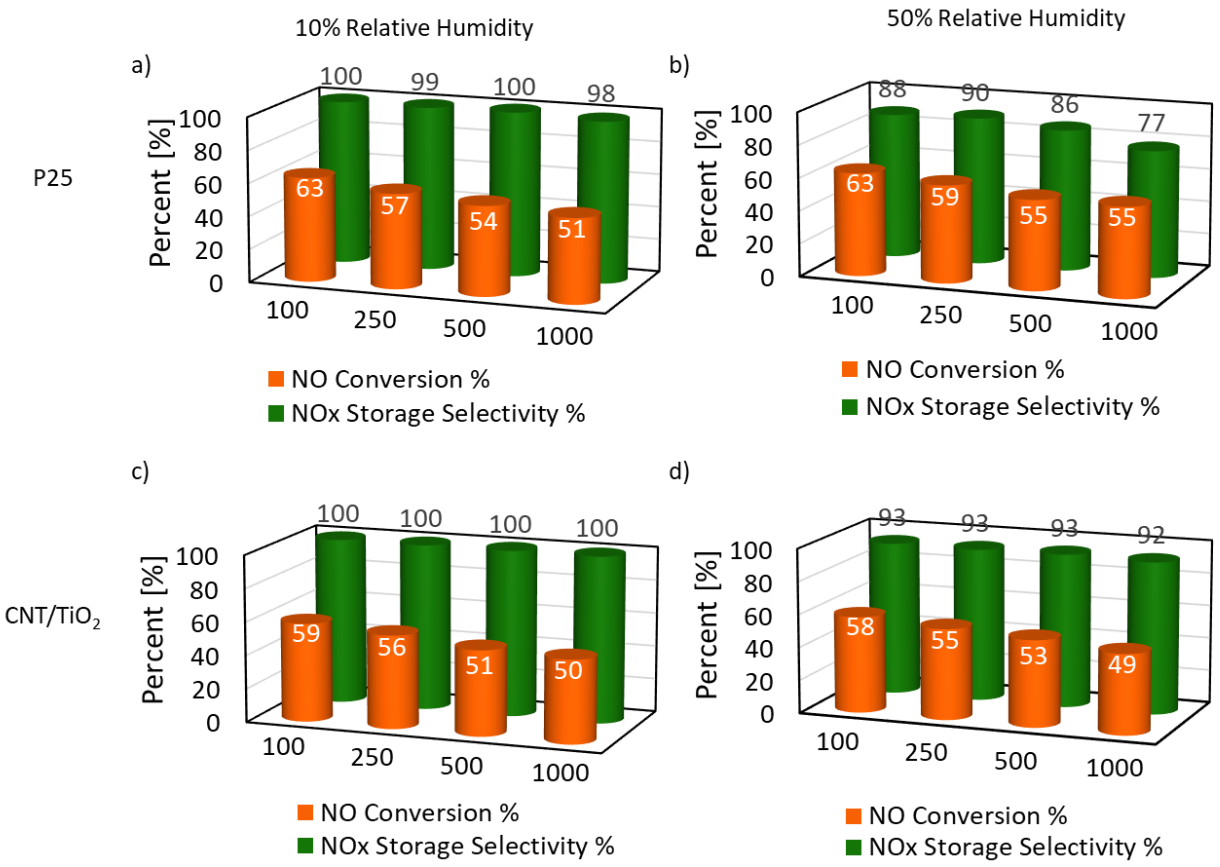

Figure D5.4. NO conversion and NOx storage selectivity for both P25 and CNT-TiO2 as a function of initial NOx concentration for low humidity (a) and (c) as well as high humidity (b) and (d). These figures show that NO conversion is dependent on initial concentration.

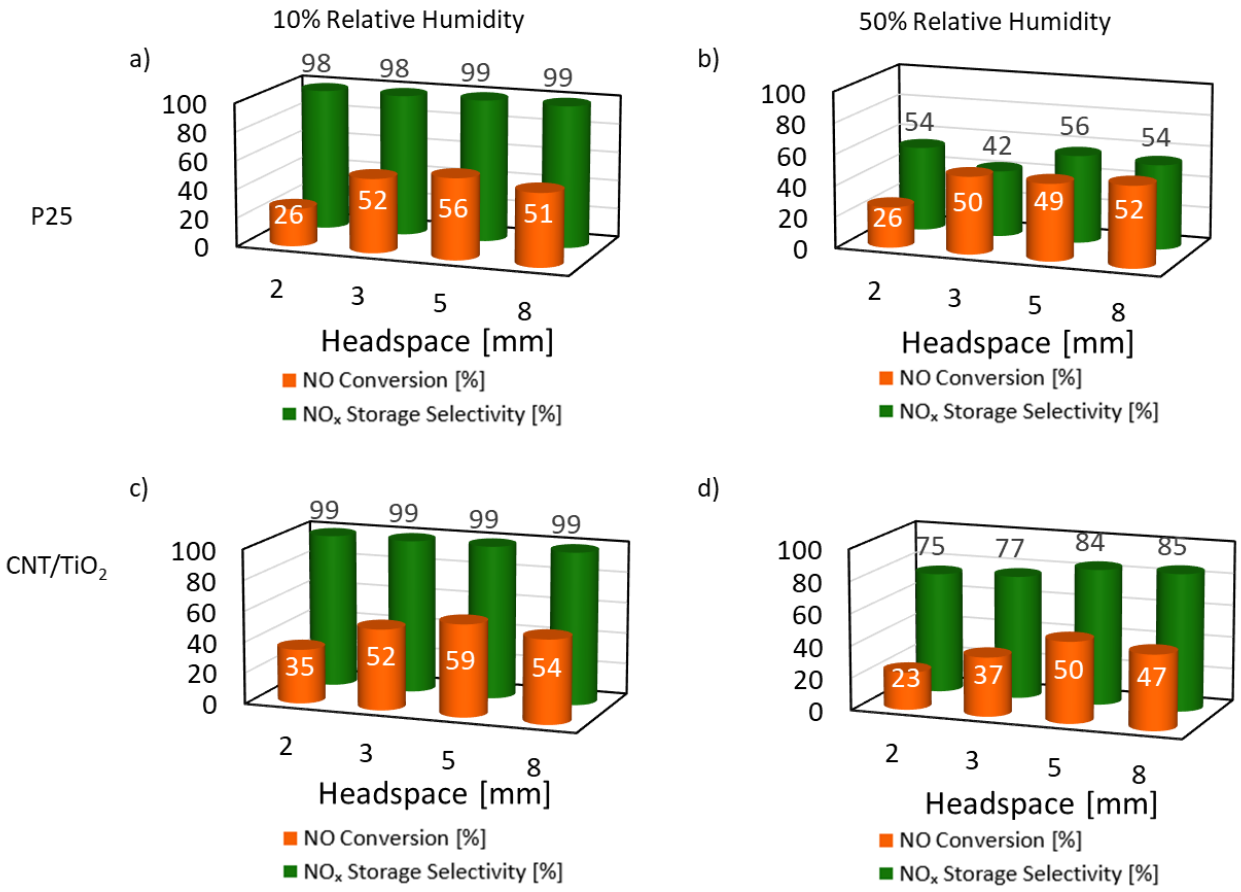

Figure D5.5. NO conversion and NOx storage selectivity for both P25 and CNT-TiO2 as a function of reactor headspace for low humidity (a) and (c) as well as high humidity (b) and (d). These figures show that NO conversion is highly dependent on reactor headspace, with a maximum conversion occurring at 5mm.

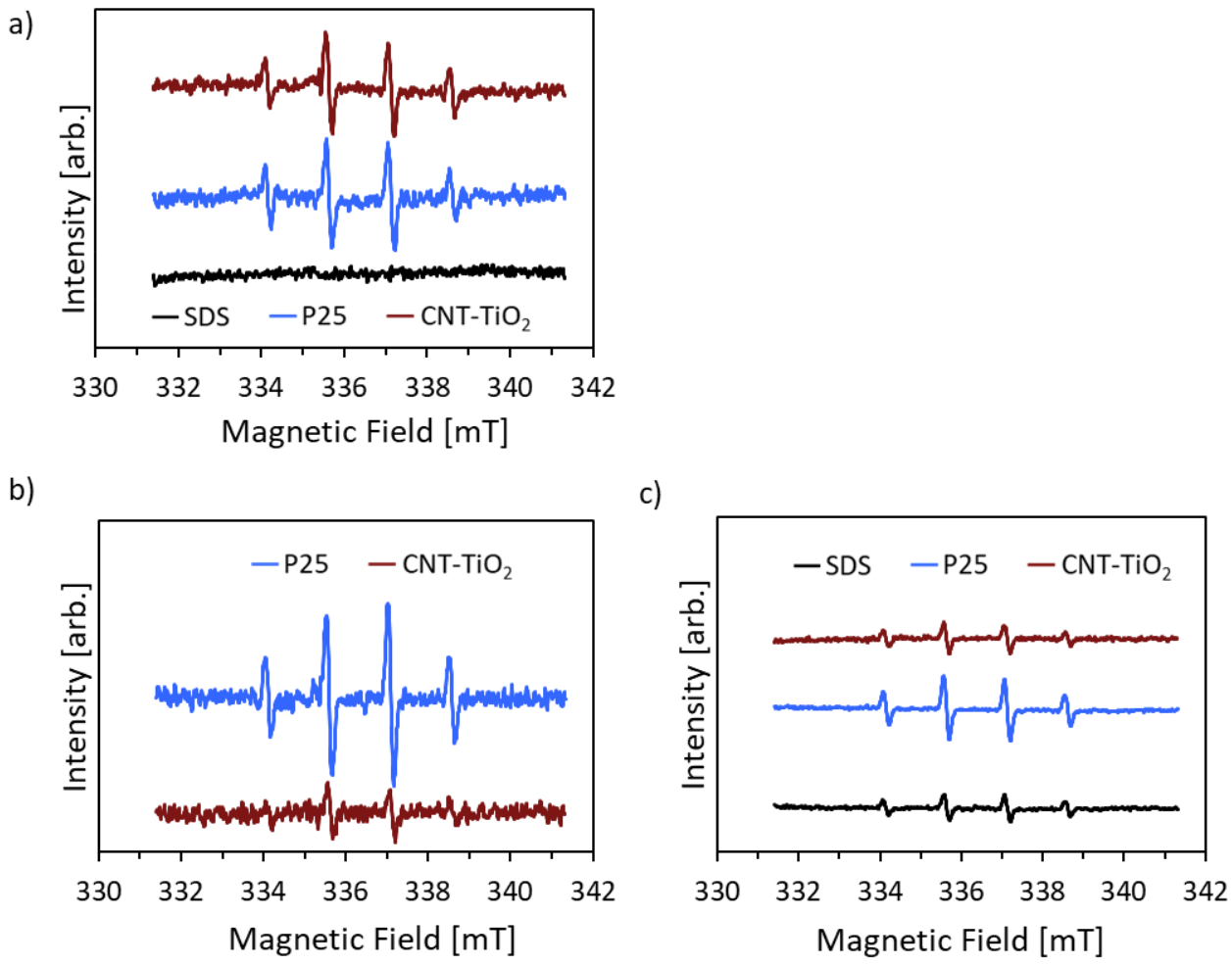

Figure D5.6. EPR results for P25 and CNT-TiO2 using (a) 0.2 mg/mL SDS surfactant and 15 minutes of sonication time. Results indicate that SDS does not contribute to the DMPO-OH radical measurement. Figure (b) shows EPR results without the addition of SDS. Figure (c) shows EPR results using SDS and long sonication times (120 minutes).

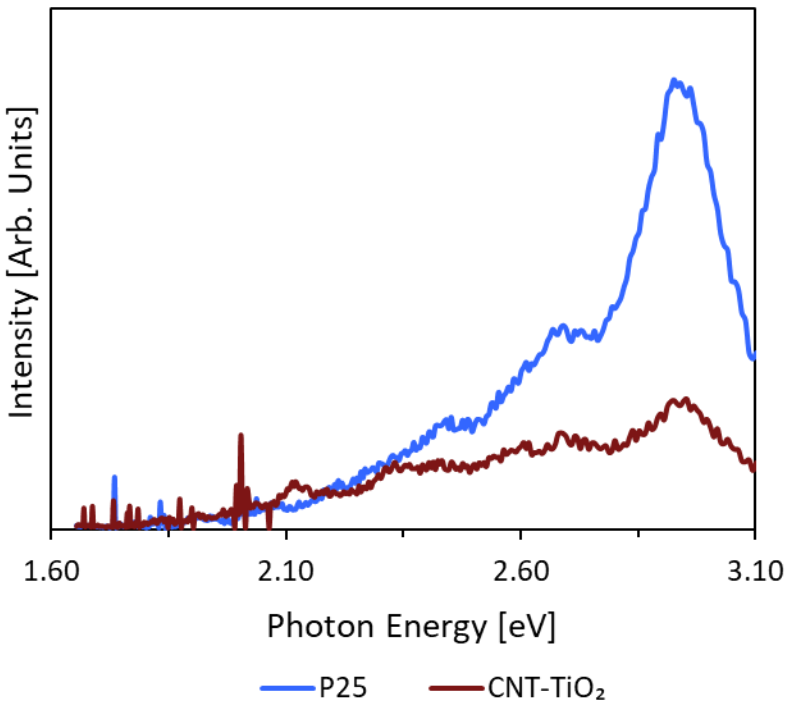

Figure D5.7. Photoluminescence spectra of P25 and CNT-TiO_2 catalyst powders.

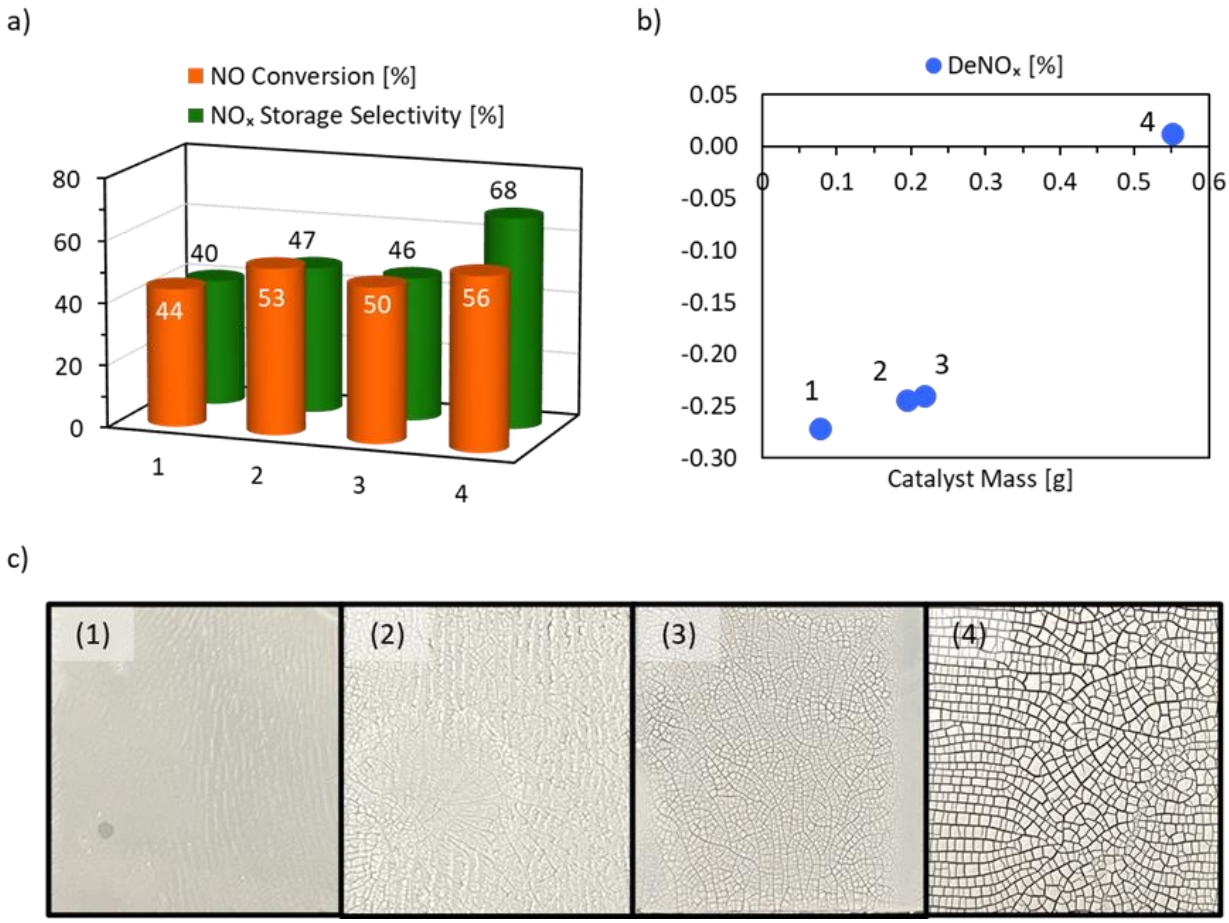

Figure D5.8. (a) NO conversion, storage selectivity, and (b) $DeNO_x$ of catalyst films containing different amounts of P25. (c) low magnification images of the respective catalyst films.